

ORIGINS OF (SUB)MILLIMETER DISK POLARIZATION

Haifeng Yang
Inner Mongolia, China

B.S. in Physics, Peking University, 2011

M.S. in Astronomy, University of Virginia, 2014

A Dissertation Presented to the Graduate
Faculty of the University of Virginia
in Candidacy for the Degree of
Doctor of Philosophy

Department of Astronomy

University of Virginia
August, 2018

Committee Members:

Zhi-Yun Li
Roger A. Chevalier
Phil Arras
Peter Arnold

© Copyright by

Haifeng Yang

All rights reserved

August, 2018

Abstract

Magnetic fields are believed to play a crucial role in the dynamics and evolution of protoplanetary disks. Polarized (sub)millimeter dust emission has been established as a reliable tool to probe the magnetic field on the relatively large scales of molecular clouds, dense star-forming cores and protostellar envelopes, based on the well-known mechanism of magnetically aligned grains. However, this canonical mechanism fails to explain the first spatially resolved disk polarization detected in a T Tauri star, HL Tau, through the Combined Array for Research in Millimeter-wave Astronomy (CARMA). We are thus motivated to search for alternative explanations. The goal of this thesis is to explore the origins of the disk polarization, with an emphasis on dust scattering.

We start by developing a semi-analytic theory for the dust scattering-induced polarization in a disk inclined to the line of sight under the simplification that the disk is both optically and geometrically thin. We show that dust scattering can naturally explain the two main features of the HL Tau disk polarization observed by CARMA: (1) the polarized intensity distribution is elongated along the major axis, and (2) the polarization orientation is along the minor axis. Both are unavoidable consequences of a simple geometric effect. The broad agreement between the simplified theory and the CARMA data played an important role in establishing dust scattering as a viable alternative to magnetic grain alignment for producing disk polarization. Furthermore, in order to produce polarization at the observed level of about 1%, the scattering grains must have sizes of order several tens of μm , which are much larger than those in the general interstellar medium (of order $0.1 \mu\text{m}$ or less). The dust polarization is thus a powerful tool for probing the grain growth in the disk, the crucial first step towards the formation of planetesimals and ultimately planets.

We then study the interplay between the polarization produced by dust scattering and that by magnetically aligned (ellipsoidal) grains under the same simplification. The scattering of (sub)millimeter light by aligned ellipsoidal grains is computed through the so-called “electrostatic approximation.” We show that the interplay can produce polarization patterns that are very different from those produced by the two mechanisms individually, including a “butterfly-shaped” pattern with two “null” (zero polarization) points. We find tentative evidence for this composite pattern in the Very Large Array (VLA) 8 mm polarization data of the deeply embedded protostar NGC 1333 IRAS 4A1. If confirmed, it would imply not only that magnetic fields exist on the disk scale but also that they are strong enough to align the large grains responsible for the 8 mm emission.

We quantify the effects of the optical depth on the scattering-induced polarization through a combination of analytic illustration, approximate semi-analytic modeling using formal solutions to the radiative transfer equation, and Monte Carlo simulations. We find that for an inclined, optically thick disk with a finite geometric thickness, the near side will be brighter than the far side in polarized intensity. It is a robust signature that can be used to distinguish the scattering-induced polarization from that by other mechanisms, such as aligned grains. This asymmetry is weaker in a well-settled (dust) disk with a smaller thickness. As such, it can be used to probe the dust settling, a process important for the grain growth and dust dynamics.

The last part of the thesis presents ongoing work on another mechanism for disk polarization, the radiative alignment. It was recently proposed as an explanation of the elliptical polarization pattern observed by the Atacama Large Millimeter/submillimeter Array (ALMA) in the HL Tau disk at 3 mm. We show that the radiative alignment produces a circular (or concentric), rather than elliptical, polar-

ization pattern. An elliptical pattern can be produced if the dust grains are aligned aerodynamically. However, both mechanisms predict a strong azimuthal variation in the polarized intensity, which is not observed. We conclude that neither of these two mechanisms alone can explain the data and the origin of the ALMA 3 mm polarization in HL Tau remains a mystery. The flood of ALMA data and relatively early stage of theoretical development should make the field of disk polarization an exciting area of research that is poised for rapid growth.

Acknowledgements

First and foremost, I would like to express my sincere gratitude to my advisor, Zhi-Yun Li, for his continuous support and supervision. It was his insight that led to this thesis project. He is always very inspiring, and discussions with him have been fruitful. He is very supportive, not only on research and travel, but also on my personal life and family affairs. He gives great advice when it comes to my career development and always thinks ahead for me. These years of study in Charlottesville wouldn't have been enjoyable and fruitful without him.

I would also like to thank Roger Chevalier for his supervision during the first couple of years of my Ph.D. study, and for providing me with good projects to work on. Thanks to Roger, I was exposed to various topics on theoretical astrophysics, especially through the meeting of his group, including Xiaping Tang, Chris Irwin and Chenliang Huang. It was a great place to hear interesting ideas. It was very educational for me to see how their ideas evolved over time.

I thank Phil Arras, who taught me in the fundamental astrophysics class with a wide range of interesting topics and lots of helpful homework problem sets. He is always very responsive to random questions from me and is willing to dig through books to best answer my questions and provide me with relevant references. I would like to thank Peter Arnold for being on my committee and reading through my thesis, and for teaching me in the Quantum Field Theory classes. He provided a very enjoyable and memorable year of classes. He was even willing to listen to me on what I expected and wanted to learn in his classes.

I want to thank my collaborators, especially Ian Stephens, Leslie Looney, and Chat Hull. The collaboration with them has been very enjoyable and fruitful. They provide a different view as observers. They help sharpen the arguments in our papers

and make them more understandable.

I want to thank my office mates, Chenliang Huang, Dom Pesce, Meng Sun, Scott Suriano, Nick Troup, and Apurva Oza, especially Scott because he is the coolest¹. I really enjoyed the atmosphere of our office, and they were always available to bounce ideas and to share great moments. I want to express my special gratitude to Dom. He was willing to spend time reading a lot of my writings over the years, especially during the job application season. He was always there to learn my premature ideas and help sharpen them.

I acknowledge support from ALMA SOS, which supported one year of my study.

Last, but definitely not least, my sincere gratitude and love goes to my family. I thank my parents, Aimin Sun and Tiandong Yang, for their continuous support over my entire life. They always have faith in me and always support my interests and choices. I thank Yangyang and Anna. You enlighten my world in a way I never expected. Although you bring much interruption to my schedule, your cuteness is always a great charging dock for me. And finally, thank you for everything, Echo. The last decade with your company is the best part of my life. You help take care of me and our kids. You are an angel that always shines in my world. I could never have done all this without you.

¹Thanks Scott for the editing suggestion.

Table of contents

Abstract	ii
Acknowledgements	v
List of Figures	xix
List of Tables	xx
1 Introduction	1
1.1 Outline of the thesis	1
1.2 Protoplanetary disks and importance of magnetic field	3
1.2.1 Classification and evolution stages	3
1.2.2 Importance of the magnetic field in the evolution of protostellar systems	4
1.3 Polarization as a probe of the magnetic field	8
1.3.1 Polarized starlight and alignment of foreground dust grains	9
1.3.2 Polarized thermal emission as a probe of the interstellar magnetic field.	10
1.4 Polarimetry observations of disks	15
1.4.1 Theoretical expectations from magnetic alignment	15
1.4.2 Polarization observations on disk scales	16
1.4.3 ALMA and well resolved disk polarimetric observations	19
1.5 Basics of scattering-induced polarization	21
1.5.1 Polarized scattered light under dipole approximation	21
1.5.2 Astrophysical examples of scattering-induced polarization	23
1.5.3 Strong dependency of polarization on grain sizes	24
1.6 Evolution of dust grains and the formation of planetesimals	27
1.6.1 Three steps of planet formation	27
2 Inclination-induced polarization of scattered millimetre radiation from protoplanetary disks	31
2.1 Introduction	32
2.2 Polarized Radiation from Dust Scattering	36

2.2.1	Formulation of the Problem	37
2.2.2	Inclination-Induced Polarization	41
2.2.3	Intrinsic Polarization from Azimuthally Anisotropic Radiation: an Example	43
2.2.4	Interplay Between Intrinsic and Inclination-Induced Polarization	48
2.3	Total Intensity and Polarization Fraction	52
2.4	Implications for Grain Size	55
2.4.1	Scattering Opacity and the Need for Large Grains	55
2.4.2	Opacity Spectral Index β and the Need for Larger Grains? . .	58
2.5	Polarization from dust scattering in the IM Lup protoplanetary disk .	62
2.6	Other Sources and Future Directions	66
2.7	Conclusions	70
3	Disk Polarization From Both Emission and Scattering of Magneti- cally Aligned Grains: The Case of NGC 1333 IRAS4A1	74
3.1	Introduction	75
3.2	Competition between scattering and direct emission of non-spherical grains: analytic results	78
3.2.1	Electrostatic approximation	79
3.2.2	Inclination-induced polarization from scattering by oblate grains	81
3.2.3	Competition between scattering and direct emission	84
3.3	Competition between scattering and direct emission in young star disks: numerical examples	89
3.3.1	Problem setup	90
3.3.2	Numerical examples of disk polarization pattern from both scat- tering and emission	92
3.4	The Case of NGC1333 IRAS4A1	100
3.5	Implications and Future Refinements	107
3.6	Conclusion	111
4	Scattering-Produced (Sub)millimeter Polarization in Inclined Disks: Optical Depth Effects, Near-Far Side Asymmetry, and Dust Settling	119
4.1	Introduction	120
4.2	Analytical Illustration of Optical Depth Effects	124
4.2.1	Polarization from scattering	124
4.2.2	Polarization from direct emission	132
4.3	Near-far side asymmetry in the polarization of inclined disks	136
4.3.1	Formal solution under single scattering approximation	136
4.3.2	Monte Carlo radiative transfer and the effects of multiple scat- tering	149
4.4	Disk polarization as a probe of dust settling	154
4.4.1	Dependence of near-far side asymmetry on dust settling	154

4.4.2	Evidence for evolution of dust settling over time	156
4.5	Distinguishing mechanisms of disk polarization	161
4.5.1	Scattering vs emission by aligned grains	161
4.5.2	The Near-Far Side Asymmetry as Signpost for Scattering-Induced Polarization	163
4.6	Conclusion	164
5	Does HL Tau Disk Polarization in ALMA Band 3 Come from Radiatively or Aerodynamically Aligned Grains?	168
5.1	Introduction	169
5.2	Polarization orientation	175
5.2.1	Polarization pattern from radiative alignment in an inclined disk is circular, not elliptical	175
5.2.2	Differences between circular and elliptical patterns	177
5.2.3	Aerodynamic alignment can produce elliptical polarization pattern	182
5.3	Azimuthal variation of polarization degree	183
5.3.1	Polarization dependence on the inclination of grain alignment axis to the line of sight	183
5.3.2	Azimuthal variation of polarization degree in inclined disks	184
5.4	HL Tau Band 3 polarization: neither radiative nor aerodynamic alignment	188
5.5	Discussion	192
5.5.1	More complex models for HL Tau Band 3 polarization: scattering by aerodynamically aligned grains?	192
5.5.2	Polarization spectrum of HL Tau disk: a potential problem for aligned grains?	196
5.6	Summary and conclusions	197
6	Conclusions and outlook	200
6.1	Major Achievements	201
6.1.1	Scattering-induced polarization in inclined disks	201
6.1.2	Interplay between scattering and magnetic alignment	203
6.1.3	The near-far side asymmetry in optically thick disks	205
6.1.4	The radiative alignment mechanism in HL Tau Band 3	207
6.2	Discussions and outlook	209
6.2.1	Probing grain sizes and the tension with other methods	210
6.2.2	The near-far side asymmetry and dust settling in protoplanetary disks	213
6.2.3	Radiative alignment: open questions and observational test	215

Appendix A Radiative transfer of polarized light	218
A.1 Formulation of the vector radiative transfer problem	219
A.2 The formal solution to the problem	220
A.3 Non-grid based numerical calculation with single scattering approximation	224
Appendix B Calculation of optical properties of dust grains	226
B.1 Conventions and basic definitions	227
B.1.1 The amplitude scattering matrix	227
B.1.2 The scattering matrix	228
B.2 The electrostatic approximation	230
B.2.1 The spherical case	230
B.2.2 The ellipsoid case	232
B.3 The Mie theory	234
B.4 The Discrete Dipole Approximation	238

List of Figures

1.1	A cartoon showing the different stages during the formation of a Sun-like low-mass star. Panel (c) is roughly a Class 0/I disk. Panel (d) is called T Tauri star and is roughly a Class II disk. Panel (e) shows a debris disk where planets are already formed. The disks in these three stages are called “protoplanetary disks”, and are the systems we are studying in this thesis. Credit: NASA/JPL: Greene, American Scientist, Jul-Aug 2001.	5
1.2	A snapshot in a typical MHD turbulent protoplanetary disk simulation, taken from Fromang (2013). Image courtesy Mario Flock.	8
1.3	Illustration of polarization in two different scenarios, adapted from Lazarian (2007). (a) The polarization of background star light. Due to the dichroic extinction, the star light becomes polarized with E vectors parallel to the B field. (b) The polarization of dust thermal emission. Due to the dichroic emission, the thermal emission is polarized with E vectors perpendicular to the B field.	10
1.4	The polarization of star light in our galaxy, taken from Fosalba et al. (2002). The orientations of the polarization are very coherent and represent the magnetic field structure in our galaxy.	11
1.5	The polarization of dust thermal emission taken by PLANCK at 0.85 mm wavelength (Planck Collaboration et al. 2015). The vectors shown here are the B vectors of the light to represent the underlying magnetic field structure. Left: the Pipe Nebula. Right: Chamaeleon-Musca regions. These regions are known to host star formation (Alves et al. 2008; Alcala et al. 1995), and are the birth place of extraterrestrial solar systems.	12
1.6	The Stokes I map with the inferred magnetic field overlaid as “drapery” image of the Vela C Molecular Cloud (Fissel et al. 2016).	13
1.7	The polarization of dust thermal emission of the protostellar system NGC 1333 IRS 4A taken by Girart et al. (2006) with the Submillimeter Array (SMA) at 0.88 mm wavelength. It is the first textbook example of the theoretically expected “hour-glass” shaped magnetic field structures.	14

1.8	The expected polarization pattern in a T Tauri disk. The left panel is taken from Cho & Lazarian (2007). The right panel shows a preliminary calculation using my own radiative transfer code (see Chap. 3 and App. A for more detail).	16
1.9	The polarization observation of the disk around HL Tau, taken from Stephens et al. (2014). The color map represents the polarized intensity. The contour shows the total flux, or Stokes I. The line segments represent the orientations of the polarization (rotated by 90° to show the inferred magnetic field direction).	18
1.10	Examples of ALMA protoplanetary disk polarization observations to date. a: L 1527 (Band 7, Harris et al. 2018); b: VLA 1623W (Band 7, Harris et al. 2018); c: HL Tau (Band 7, Stephens et al. 2017); d: Per-emb-50 (Band 7, Cox et al. 2018); e: HH 111 (Band 7, Lee et al. 2018); f: IM Lup (Band 7, Hull et al. 2018); g: HD 142527 (Band 7, Kataoka et al. 2016b); h: BHB 07-11 (Band 7, Alves et al. 2018); i: HH 80-81 (Band 6, Girart et al. 2018).	20
1.11	A schematic illustration of dipole scattering. The unpolarized incoming light will be polarized in the 1-direction after the scattering, and the polarization fraction depends on the scattering angle θ . The polarized light in the special case of $\theta = \pi/2$ is fully (maximally) polarized. . .	22
1.12	Subaru/CIAO K band ($2.2 \mu\text{m}$) polarimetric observation of the envelope of the R Mon star, taken from Murakawa et al. (2008). The colormap represents the polarization degree, which can go up to $\sim 50 - 60\%$. The line segments represent the orientations of the polarization, with length proportional to the polarization degree.	25
1.13	The product of the polarization fraction P and the albedo ω plotted as a function of grain size at different wavelengths, taken from Kataoka et al. (2015). The wavelengths chosen here are the representative wavelengths at different ALMA bands.	26
1.14	The size ladder from dust to planets, taken from Chiang & Youdin (2010). Various related processes are circled on the ladder as well as their relevant linear scales. The disk polarization can probe grain growth to (sub)millimeter sizes, which is the first step towards the formation of planets (see Chap. 2), as well as the dust settling (see Chap. 4), the second step of the ladder.	30
2.1	Observed 1.3 mm polarization pattern of the HL Tau disk. Plotted are total intensity (contours), polarized intensity (color map, $> 2\sigma$), and polarization vectors ($> 3\sigma$), with length proportional to the polarization fraction. Adapted from Stephens et al. (2014). The major axis determined from the ALMA data (ALMA Partnership et al. 2015) is tilted by 10° clockwise with respect to the vertical direction.	34

- 2.2 Effects of disk inclination on the polarization of scattered millimeter radiation. Shown are the intensity of the polarized radiation (color map, in units of $2\Sigma_0^2\kappa_{abs}\kappa_{sca}\nu^2kT_0/c^2$) and polarization vectors (line segments, with length proportional to the polarization fraction $p_{s,\infty}$ defined in eq.(2.24)), for $i = 0^\circ, 30^\circ, 45^\circ$ and 60° . As the disk becomes more tilted, both the polarized intensity and polarization directions become more dominated by those induced by inclination. The elongation of the polarized intensity along the major axis and orientations of the polarization vectors along the minor axis in the high intensity region in the inclined cases are broadly consistent with the observed pattern in HL Tau (see Fig. 2.1). The numbers 0.5, 1.0, 1.5 and 2.0 in each panel measure the de-projected distances from the center in units of the characteristic radius R_c . The x' -axis and y' -axis defined in the plane of the sky are shown in the lower-right panel for reference. . . . 47
- 2.3 Dimensionless quantity p_Q defined in eq. (2.25). Plotted are the distributions of p_Q along the major and minor axes, denoted by the subscript “maj” and “min” respectively, as a function of de-projected distance from the origin for the face-on $i = 0^\circ$ case (solid and dashed black) and the $i = 45^\circ$ case (solid and dashed blue). Its polarization fraction $|p_Q|$ approaches 20% in the central region and, at larger distances from the origin, is substantially larger along the major axis than along the minor axis. 49
- 2.4 Ratio of the near-field and far-field contributions to the intensity of the scattered radiation, $I_{s,0}/I_{s,\infty}$, for the $i = 45^\circ$ case. The far-field contribution $I_{s,\infty}$ dominates the near-field contribution $I_{s,0}$ everywhere, especially in the central region and near the outer edge. 53
- 2.5 Model for the polarization of HL Tau disk. Plotted are the polarized intensity (color map, in units of $2\Sigma_0^2\kappa_{abs}\kappa_{sca}\nu^2kT_0/c^2$) and polarization vectors (line segments, with length proportional to the polarization fraction of the total intensity) for $i = 45^\circ$. A characteristic scattering optical depth $\Delta\tau_{s,c} \approx 0.07$ is needed to bring the high polarization fraction of tens of percent relative to the scattered intensity (shown in the lower-left panel of Fig. 2.2) down to the observed level of $\sim 1\%$ relative to the total intensity. 56
- 2.6 Comparison of the distributions of the degree of polarization (see text for definition) as a function of scattering angle for three cases: the Rayleigh limit (blue line) and two cases with MRN-like power-law grain size distribution with $a_{max} = 72 \mu\text{m}$ (green) and 4 mm (red). The Rayleigh and $a_{max} = 72 \mu\text{m}$ cases are almost indistinguishable. The negative “peak” around 130° in the $a_{max} = 4 \text{ mm}$ case is an example of the so-called “polarization reversal,” which may provide a way to probe large, mm/cm sized, grains through scattering-induced polarization. . . 60

- 2.7 Scattering-induced polarization by large grains. As in Fig. 2.5, plotted are the polarized intensity (color map) and polarization vectors (line segments, with length proportional to the polarization fraction). Note the strong asymmetric with respect to the major axis in both the polarized intensity and the polarization vectors. The polarization along the major axis in the central region is due to polarization reversal, which may be a robust indicator of scattering by large, mm/cm-sized, grains. The near side of the disk is on the right. 62
- 2.8 870 μm ALMA observations of the Class II protoplanetary disk IM Lup. The grayscale represents the polarized intensity, plotted starting at $3\sigma_P$, with $\sigma_P = 22 \mu\text{Jy beam}^{-1}$. The contours are the total emission, plotted at 3, 8, 16, 32, 64, 128, 512, $1024 \times \sigma_I$, with $\sigma_P = 100 \mu\text{Jy beam}^{-1}$. Line segments represent the orientation and degree of the polarization, with 1% scale shown at the lower right corner. The lower left corner represents the interferometric beam, which measures $0''.50 \times 0''.40$ at a position angle of 76.9° , corresponding to a linear resolution of $\sim 72 \text{ AU}$ 64
- 2.9 Best-fit model to the ALMA 870 μm polarization observations of IM Lup. The colormap represents the polarized intensity, plotted starting $3\sigma_P = 66 \mu\text{Jy beam}^{-1}$. The contours represent the Stokes I, which is logarithmically scaled with a minimum value of $3\sigma_I = 300 \mu\text{Jy beam}^{-1}$. The line segments represent both the orientation and the degree of polarization. 65
- 3.1 Degree of polarization at a location on the disk major axis for scattered light (p_{sca} , solid lines) and direct emission (p_{abs} , dashed) for oblate grains with representative axis ratio $s = 1.0, 1.1, 1.5, \text{ and } 2.0$ as a function of disk inclination angle i , assuming perfect grain alignment. Note that p_{sca} and p_{abs} start from the same positive value at $i = 0^\circ$ (the face-on limit), but decrease to $-1/3$ and 0 , respectively, as the edge-on ($i = 90^\circ$) limit is approached. 86
- 3.2 Transition lines that divide the parameter space where the polarization is dominated by direct emission (to the upper left of each line) from that dominated by scattering (the lower right), for 6 representative values of the grain axis ratio $s = 1.01, 1.1, 1.3, 1.5, 1.8 \text{ and } 2.0$. The horizontal line marks $\sigma_{abs} B_\nu / \sigma_{sca} J_\nu = 2$, the fiducial value obtained in the flared disk model of Cho & Lazarian (2007). 88
- 3.3 Polarized intensity (in units of $B_\nu(T_0)$, color map) and polarization vectors with length proportional to polarization fraction for scattering only (left panels), emission only (middle), and the two combined (right), for three inclinations $i = 0^\circ$ (upper panels), 45° (middle), and 70° (lower). 95

3.4	Polarization observed in IRAS4A1 at 8.1 mm (adapted from Cox et al. 2015). Plotted are the total intensity (contours), polarized intensity (color map), and polarization (rather than magnetic) vectors with length proportional to the polarization fraction. The molecular outflows near the source are roughly in the north-south direction, which implies an approximately east-west orientation for the major axis (Santangelo et al. 2015; Ching et al. 2016).	101
3.5	Lines of constant contrast η in polarization fraction between the minor and major axes (the nearly vertical lines, with values labeled) and constant maximum polarization p_{\max} (horizontal) for direct emission in the plane of inclination angle i and grain axis ratio s . Note that λ depends weakly on s , and approaches $1/\cos^2 i$ as $s \rightarrow 1$	103
3.6	Polarization models with and without scattering. Plotted are the polarized intensity (in units of $B_\nu(T_0)$, color map) and polarization vectors with length proportional to polarization fraction for emission only (upper panel) and for both emission and scattering (lower panel). The lower panel resembles the observed polarization in IRAS4A1 shown in Fig. 3.4 more closely than the upper panel (see text for discussion).	105
3.7	Scattering (solid line) and absorption (dashed) opacities at 1 mm as a function of grain size for oblate grains with $s = 1.5$ computed using the discrete dipole approximation (green lines) and under the electrostatic approximation for small particles (blue lines). Note that the scattering opacity obtained under the electrostatic approximation is valid up to a grain size of ~ 0.2 times the wavelength λ , and it exceeds the absorption opacity for grains larger than $\sim 0.05\lambda$. Opacities computed from Mie theory for spherical grains of the same size are also shown (red lines) for comparison.	109
3.8	Effects of imperfect grain alignment, parametrized by the value of $\langle \cos^2(\theta) \rangle$, on the relative importance of scattering and direct emission for polarization for the case of $\sigma_{\text{abs}} B_\nu / \sigma_{\text{sca}} J_\nu = 2$. For each value of axis ratio s , the polarization is dominated by direct emission in the parameter space to the upper-left of the corresponding curve, and by scattering to the lower right.	117
4.1	Coordinate system centered on a scattering particle located in the optically thin layer near the surface of the semi-infinite model. The dashed blue line denotes the direction of the local minor axis as viewed by the observer when the surface of the semi-infinite slab represents a local patch on the disk surface and the local major axis is along the y-axis. The circle indicates a sphere considered in the text around the scattering particle.	126

4.2	Maximum degree of polarization from scattering by spherical grains in a semi-infinite slab as a function of the slab inclination angle i with respect to the line of sight ($i = 0$ means face-on) under the single scattering approximation. The polarization peaks at 1.4% for an inclination angle $i = 78^\circ$. The extinction opacity is assumed to be dominated by the scattering.	131
4.3	Variation of the degree of polarization from dust scattering (blue line) and direct emission from aligned grains (dashed green line) with the total optical depth τ_{\max} of an isothermal slab with an inclination angle of 45° . The polarization degree from aligned grains is assumed to be 3% at small optical depth. Note the contrasting behaviors of the two curves at both small and large optical depth limits. See text for discussion.	133
4.4	Distributions of the total intensity (left panels), polarized intensity (middle) and polarization vectors (right panels, with length proportional to the polarization degree) for three disk models with increasing density scale $\rho_0 = 1.13 \times 10^{-16}$ (Model A; top panels), 1.13×10^{-15} (Model B; middle), and $1.13 \times 10^{-14} \text{ g cm}^{-3}$ (Model C; bottom). Intensities are in unit of $\text{erg} \cdot \text{s}^{-1} \cdot \text{sr}^{-1} \cdot \text{cm}^{-2} \cdot \text{Hz}^{-1}$	140
4.5	Left panel shows the polarization degree along the minor axis for the three models with different density scales, with the near side to the right of the central vertical line and the far side to the left. Positive polarization degree indicate a polarization along minor axis, whereas a negative value corresponds to a polarization along major axis. Right panel shows the difference in polarization degree for pairs of points along minor axis plotted against distance from the center of the disk for the same three models. Note the increasing near-far side asymmetry as the density (and thus optical depth) increases.	143
4.6	Illustration of the “local inclination angle” of the disk surface to the line of sight. The gray shaded region represents the disk. The line of sight makes a larger angle to the normal of the disk surface on the near side (denoted by i') than that on the far side (i''). This difference in local inclination angle is the main reason for the near-far side asymmetry in the polarized intensity for optically thick disks.	145
4.7	Bifurcation in polarization orientation along the major axis. Plotted are the offset angle θ_{offset} between the polarization vectors and the direction of the minor axis as a function of distance from the center along the major axis for the three models with different density scales (Models A-C). The blue dashed line shows the expectation based on the shape of the disk surface at one scale height.	148

- 4.8 Comparison of the results from formal solution under single scattering approximation (top panels) and Monte Carlo simulations including multiple scattering (bottom panels). Plotted are the polarized intensity for a representative disk inclined by an angle $i = 45^\circ$ to the line of sight, with three different grain sizes: $10 \mu\text{m}$ (Model E; left panels), $37.5 \mu\text{m}$ (Model D; middle) and $100 \mu\text{m}$ (Model C; right). From left to right, the scattering optical depth at the characteristic radius R_c are 1.04×10^{-2} , 0.56, and 11.7, respectively. Intensities are in unit of $\text{erg} \cdot \text{s}^{-1} \cdot \text{sr}^{-1} \cdot \text{cm}^{-2} \cdot \text{Hz}^{-1}$. The color scales were adjusted to best show the morphology of the polarized intensity. 151
- 4.9 Quantitative comparison of the results from formal solution under single scattering approximation (blue curves) and Monte Carlo simulations including multiple scattering (red curves). Plotted are the total intensity I along both the major and minor axis (top panels), the polarization degree p along the minor axis (middle), and the offset angle θ_{offset} between the polarization orientation and the minor axis along the major axis (bottom), for three grain sizes: $10 \mu\text{m}$ (Model E; left panels), $37.5 \mu\text{m}$ (Model D; middle), and $100 \mu\text{m}$ (Model C; right). Results on major axis and minor axis are plotted in solid lines and dashed lines, respectively. 152
- 4.10 Total intensity (left), polarized intensity (middle), and polarization vectors (right) for geometrically thin but optically thick disk model (Model F). Intensities are in unit of $\text{erg} \cdot \text{s}^{-1} \cdot \text{sr}^{-1} \cdot \text{cm}^{-2} \cdot \text{Hz}^{-1}$ 155
- 5.1 HL Tau disk polarization detected by ALMA in Band 3 (panel a) and Band 7 (b). The panels are adopted from Kataoka et al. (2017) and Stephens et al. (2017), respectively. Plotted are the polarization orientations (line segments), polarized flux (color map) and total flux (contours). 172
- 5.2 Elliptical vs circular polarization pattern. The red solid line segments are for polarization orientations, and green dashed line segments for the direction of the required radiative flux projected into the sky plane in the case of radiative alignment. 176
- 5.3 Upper panel: expected polarization angle for circular (θ_{cir} ; solid line) and elliptical (θ_{ell} ; dashed) pattern as a function of the azimuthal angle θ_{sky} in the sky plane for a disk inclined by 45° to the line of sight. Lower panel: the difference in polarization orientations between the two patterns, which can be as large as $\sim 20^\circ$ for this disk inclination. 178

5.4	The difference in polarization angle between the circular and elliptical patterns as a function of the azimuthal angle in the sky plane θ_{sky} between 0° (major axis) and 90° (minor axis), for disks inclined by different angles ($i = 0^\circ$ for face-on view). The difference is larger for a more inclined disk.	179
5.5	Large difference in polarization orientation between the elliptical (upper panel) and circular (lower) pattern for a nearly edge-on disk (with an inclination angle $i = 85^\circ$). Such disks are ideal for distinguishing the two patterns.	180
5.6	Polarization degree as a function of the azimuthal angle in the sky plane θ_{sky} for different alignment mechanisms and different inclination angles. The polarization degrees from the magnetic alignment (dotted line) and aerodynamic alignment (solid) have a similar angular dependence, both peaking on the minor axis ($\theta_{\text{sky}} = 90^\circ$). This is opposite to that of the radiative alignment (dashed), which peaks on the major axis ($\theta_{\text{sky}} = 0^\circ$) instead. Different inclination angles are represented by different colors. Note that the polarization degree on the minor axis decreases monotonically with increasing inclination angle for the case of radiative alignment (dashed lines), vanishing completely in the edge-on case with $i = 90^\circ$	185
5.7	Large difference in not only polarization orientation but also azimuthal variation of polarization degree between the aerodynamic (upper panel) and radiative (lower) alignment for a nearly edge-on disk (with an inclination angle $i = 85^\circ$). Such disks are ideally suited for distinguishing the two alignment mechanisms.	188
5.8	Histogram of the difference in polarization orientation between the ALMA Band 3 data and the models based on the aerodynamic (upper panel) and radiative (lower) alignment. The two dashed vertical lines are at $\pm 19.5^\circ$, the maximum difference expected between the circular and elliptical polarization pattern for an inclined disk of $i = 45^\circ$, as shown in Fig. 5.3.	190
5.9	Comparison between the ALMA Band 3 data (left panel) and the models based on radiative (middle) and aerodynamic (right) alignment. The colormap shows the polarized flux, in mJy/beam, and the contours are for Stokes I, with a logarithmic scale. The line segments denote the polarization orientations. They are plotted only in regions with polarized intensity above $34.5 \mu\text{Jy}/\text{beam}$, which corresponds to 5σ noise level in Kataoka et al. (2017). The ellipse at the lower corner represents the interferometric beam.	191

- 5.10 Two intrinsically elliptical polarization models with different azimuthal variations. The left column assumes uniform azimuthal polarization fraction, whereas the right column has polarization peaking at major axis, in the same way as the radiative alignment model. The upper panels show the histogram of the difference in polarization orientation with data for the two models, and the lower panel show the simulated polarization observation. 194
- 6.1 Scattering properties for aggregates resembling cometary dust, taken from Shen et al. (2009). The size parameters $2\pi a/\lambda$ is about $10 \sim 15$. The bottom panels are to be compared with Fig. 2.6. Unlike the scattering phase functions for large *spherical* grains calculated with Mie theory, represented with the red curve in Fig. 2.6, the large aggregates have a better behaved scattering phase function. See Shen et al. (2008) and Shen et al. (2009) for details. 212
- 6.2 Dust evolution and near-far asymmetry. Upper left: HH 80-81 (Girart et al. 2018), a massive protostar. Lower left: HH 111 (Lee et al. 2018), a deeply embedded Class I source. Upper right: HL Tau (Stephens et al. 2017), Class I/II source. Lower right: IM Lup (Hull et al. 2018), a weak-line T Tauri star and Class II source. We see a tentative trend that younger systems to the left show a prominent near-far side asymmetry, which disappears in the older systems to the right. This is an indication of dust settling based on our theory of scattering-induced polarization. 214

List of Tables

4.1	Parameters for the disk model.	138
4.2	Different models used in this chapter.	139

Chapter 1

Introduction

1.1 Outline of the thesis

The origin of stars and planets is among the most important questions in astronomy. Stars are observed to form in dense molecular clouds André et al. (2014). They are formed when cloud materials collapse when the self-gravity overwhelms the cloud support by thermal pressure and other means (such as magnetic fields) Li et al. (2014). Due to conservation of angular momentum, a disk structure is formed together with the star Shu et al. (1987). This disk is believed to be the birth place for planets. In this thesis, we will study the light from such disks at (sub)millimeter wavelengths, with a focus on its polarization. The structure of this thesis is as follows.

In Chapter 1, I give a brief introduction to the problem of star and planet formation, summarizing the important evolution stages and discussing the important roles played by the magnetic field in them. I summarize the efforts towards probing the magnetic field using polarization on various scales, and the problems with this method in the protoplanetary disk environments. This leads to the search for alternative mechanisms in producing disk polarization, which is the main focus of this

thesis. I also give a brief introduction on grain growth. It serves as a background for probing grain sizes in disks using our method.

In Chapter 2, I introduce an alternative mechanism in producing disk polarization. I provide a semi-analytic approach to this problem that illustrates the basic physics. The scattering of dust thermal emission by dust grains themselves, the so-called “self-scattering”, is very efficient at producing polarization at (sub)millimeter wavelengths for disks significantly inclined to the line of sight. This chapter is based on Yang et al. (2016a).

In Chapter 3, I study the interplay between two existing mechanisms in producing polarization, namely magnetic grain alignment and dust self-scattering. I use an “Electrostatic Approximation” to calculate the optical properties of aspherical dust grains and show how the polarization may transit from being dominated by one mechanism to the other in a single system when both are operating. This chapter is based on Yang et al. (2016b).

In Chapter 4, I relax the constraints imposed by the optical thin assumption used in previous works to study the effects of the optical depth on disk polarization. I show that from a simple geometric effect, the polarization will have a near-far side asymmetry if the disk is both optically thick and geometrically thick. This effect can be a powerful tool to probe the settling of dust grains in protoplanetary disks, and help us understand the formation of planetesimals. This chapter is based on Yang et al. (2017).

In Chapter 5, I describe some observations and ongoing efforts on modeling the polarization from disks. I discuss the current understanding of the origins of polarization from protoplanetary disks and the problems associated with different mechanisms, with a focus on the HL Tau system. This chapter is based on a draft of a

paper to be submitted to MNRAS before the end of Summer 2018.

I summarize the main points of this thesis in Chapter 6, and give an outlook of this new field. I introduce some of the ongoing observations, and discuss what kind of observations will be crucial in fully understanding the roles of various mechanisms in producing polarization from protoplanetary disks.

I include the technical details relevant for this thesis in two Appendices. App. A introduces the radiative transfer of polarized light, as well as its formal solution. We also discuss our numerical approach for treating such radiative transfer problems, which is employed in Chap. 4. In App. B, I discuss the three methods employed throughout this thesis to calculate the optical properties of dust grains.

1.2 Protoplanetary disks and importance of magnetic field

Circumstellar disks are inevitable outcomes during the formation of stars due to the conservation of angular momentum Li et al. (2014). Such disks are believed to be the birth place of planets. They produce coplanar planetary systems like the one we live in. In this section, we will briefly introduce the evolution stages and classification of protoplanetary disks (PPDs), and the important role that the magnetic field is playing during their evolution.

1.2.1 Classification and evolution stages

Fig. 1.1 is a cartoon showing the different stages in the formation of a low-mass star like the Sun (see, e.g., Shu et al. 1987; Williams & Cieza 2011). Stars are formed out of molecular clouds (Fig. 1.1a, see also Fig. 1.5). Certain regions (dense cores)

have higher densities and become gravitationally unstable. They become the seeds of star formation and undergo gravitational collapse (Fig. 1.1b). During the collapse, a protostar is formed, as well as a protostellar disk (Fig. 1.1c). During this stage, there is still some envelope material surrounding the central protostar. After the envelope is cleared through further accretion and/or interaction with protostellar outflow, we enter the T Tauri star stage, a low-mass young star with a disk but little or no envelope (Fig. 1.1d). On the timescale of $\sim 1\text{--}10$ Myrs, planets are formed in this disk. As the disk is depleted by accretion onto the star and planet formation, it becomes a debris disk (Fig. 1.1e) before it finally disappears (Fig. 1.1f), leaving behind a fully formed young stellar system.

In this thesis, we focus on the protoplanetary disk stages (Fig. 1.1c,d, and maybe Fig. 1.1e). Observationally, such systems are classified based on their spectral energy distribution (SED), specifically the slope α_{IR} in the infrared part ($2\ \mu\text{m} \sim 25\ \mu\text{m}$) (Lada 1987; Greene et al. 1994). In the early stage, the system has a heavy surrounding envelope. They typically have $\alpha_{\text{IR}} > 0.3$ and their optical and near-IR emission is generally obscured. These systems are classified as Class 0/I systems (Fig. 1.1c). After the envelope is cleared, the system still shows infrared excess comparing to just the black-body spectrum from the star. Typically such systems have $-1.6 < \alpha_{\text{IR}} < -0.3$ and are classified as Class II systems. Systems with $\alpha_{\text{IR}} < -1.6$ are called Class III systems.

1.2.2 Importance of the magnetic field in the evolution of protostellar systems

An object orbiting around the central star will never fall onto it without losing its angular momentum first. From the UV excess from young stellar objects (YSOs), we

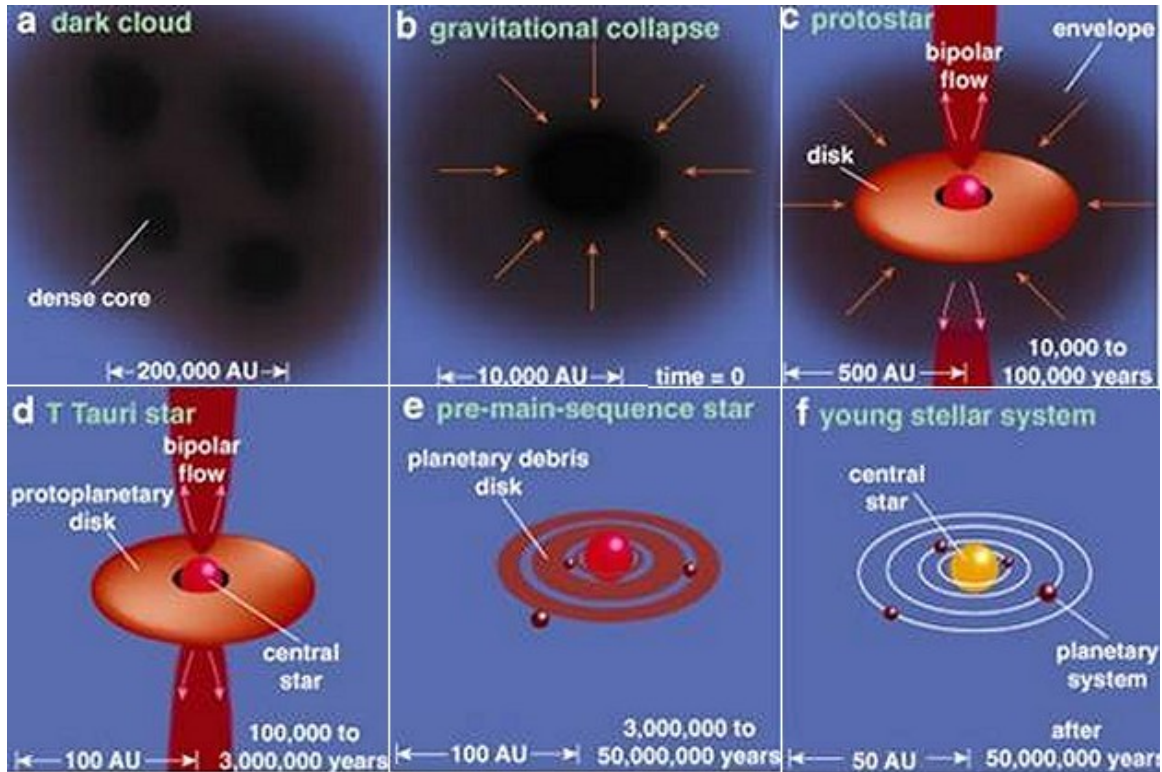


Fig. 1.1.— A cartoon showing the different stages during the formation of a Sun-like low-mass star. Panel (c) is roughly a Class 0/I disk. Panel (d) is called T Tauri star and is roughly a Class II disk. Panel (e) shows a debris disk where planets are already formed. The disks in these three stages are called “protoplanetary disks”, and are the systems we are studying in this thesis. Credit: NASA/JPL: Greene, American Scientist, Jul-Aug 2001.

can infer that PPDs are often actively accreting (Calvet & Gullbring 1998; Gullbring et al. 2000). During the evolution of young stellar systems and the protoplanetary disks, outward angular momentum transport is essential in order to maintain this active accretion. Theoretically, magnetic fields can play a very important role in angular momentum transport through either magnetorotational instability, or a magnetically driven wind. An excellent review on this topic is Turner et al. (2014), where the reader can find more details.

Magnetorotational instability

One of the fundamental ways to transport angular momentum is through viscous interaction between the annuli in the disk. An inner annulus with a higher angular velocity gives kinetic energy to an outer annulus, which in turn causes the inner annulus to slow down. As a result, the material in the inner annulus will fall toward the central star whereas the angular momentum gets transported outward. Because molecular viscosity is too weak to produce a strong enough angular momentum transport, disks usually rely on some sort of turbulent viscosity, and the canonical model to describe such a process is the so-called α -disk model (Shakura & Sunyaev 1973).

The Magnetorotational Instability (MRI) is one of the most promising ways to produce turbulence in disks. MRI in an ideal MHD Couette flow was discovered in the late 1950s (Velikhov 1959; Chandrasekhar 1960). Its importance under the astrophysical context, especially in accretion disks, was pointed out by Balbus & Hawley (1991). MRI arises naturally for a Keplerian rotating disk threaded by vertical magnetic field lines. Consider a fluid parcel under epicyclic motion, which oscillates radially inward and outward. When this parcel moves inward, it will move faster. However, it is still connected with materials attached to the same field line at its initial locations, within the ideal MHD regime. This differential motion creates a magnetic force between this parcel and others along the same field line, which slows down this parcel. As a result, this parcel will move even further inward after losing angular momentum. The same works for outward motion as well. This is a run-away process that causes the MRI and creates turbulence in accretion disks.

Magnetically driven winds

Disk winds are another process that can potentially transport angular momentum to enable accretion in disks. When a large-scale magnetically driven wind is launched on the surface of the disk, it can interact with the surface of the disk and take away angular momentum from the disk, which in turn facilitates the accretion through the disk.

One of the most studied launching mechanisms, known as the magnetocentrifugal mechanism, was initially proposed by Blandford & Payne (1982). In the co-rotating frame of the disk, fluid parcels experience the gravity and the centrifugal force. With a razor-thin disk model under the self-similar assumption, Blandford & Payne (1982) proved that if the magnetic field line attached to the surface of the disk has an inclination angle θ with respect to the disk normal direction that is larger than 30° , the effective potential along such a magnetic field line will *decrease* with increasing radius and height. As a result, fluid parcels will move upward and outward from the disk and launch a disk wind. The fluid moving along such a field line has constant angular velocity to begin with. As a result, their specific angular momentum will be increasing as they move radially outward, and the rotation of the disk will be braked by the disk wind, which enables the accretion through the disk.

In either scenario, the magnetic field plays a crucial role in the angular momentum transport in protoplanetary disks and greatly impacts the dynamics and the evolution of protoplanetary disks. Due to the differential rotation of the disk, the magnetic field inside the disk is usually expected to be in a toroidal configuration (see Fig. 1.2), which plays an important role in our discussion in Chap. 3. However, there is no clear observational evidence for magnetic fields in protoplanetary disks yet. Whether dynamically significant magnetic fields exist or not is one of the most important open

questions in astrophysical disk research.

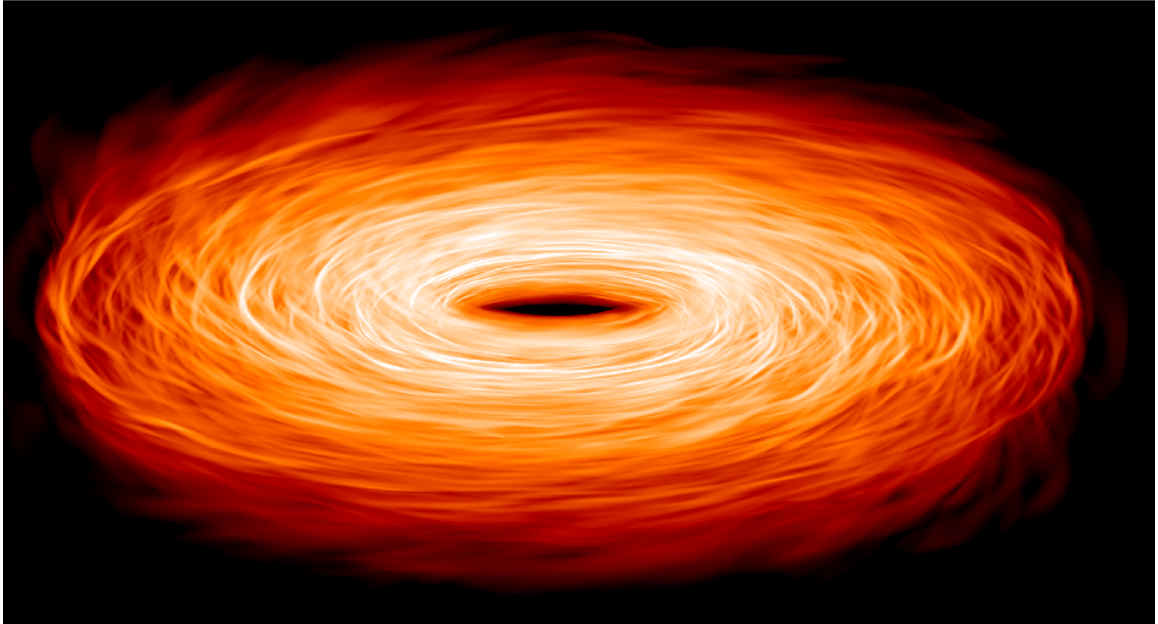


Fig. 1.2.— A snapshot in a typical MHD turbulent protoplanetary disk simulation, taken from Fromang (2013). Image courtesy Mario Flock.

1.3 Polarization as a probe of the magnetic field

Due to the importance of the magnetic field in the evolution of protostellar and protoplanetary systems, searching for evidence for magnetic fields and studying their structures and influence are among the most important tasks in star formation studies. Techniques to probe the magnetic field in celestial systems include the Zeeman effect (Feynman 1965; Zeeman 1897), the Chandrasekhar-Fermi method (Chandrasekhar & Fermi 1953; Crutcher et al. 2004), polarization from aligned dust grains (Andersson et al. 2015), the Goldreich-Kylafis effect (Goldreich & Kylafis 1981, 1982), and the Velocity Gradient Technique (Lazarian et al. 2002), etc. Since this thesis is on the origins of polarization in protoplanetary disks, we will focus on the polarization from

aligned dust grains as a way to probe magnetic fields next.

1.3.1 Polarized starlight and alignment of foreground dust grains

In 1949, the optical light from stars was found to be polarized (Hall 1949; Hiltner 1949a). Because the thermal radiation from stars is not polarized to begin with, the polarization of star light was soon recognized to be coming from the foreground dust grains in the ISM (Hiltner 1949b). To produce polarization, these grains must be aligned along some preferred direction, at least to a substantial degree. It turns out that the magnetic field is most likely responsible for such alignment.

When dust grains are aligned with respect to an external magnetic field, we expect them to have their long axis perpendicular to the magnetic field (Fig. 1.3). In the case of the polarization of the star light (Fig. 1.3a), the black body radiation from stars is not polarized to begin with. When such light propagates through foreground dust grains in the interstellar medium, its component with polarization along the long axis of the dust grains (the part represented by the blue wavy curve) will be preferentially absorbed by these aligned dust grains. As a result, we are left with polarized light with polarization along the short axis of the dust grains (the part represented by the red wavy curve).

Fig. 1.4 shows the polarization from stars in our galaxy. We can see that the orientations of the polarization are very coherent, and they represent the local magnetic field in the foreground diffuse interstellar medium (Fosalba et al. 2002). This technique has been very successful in the study of the magnetic field structure in our galaxy.

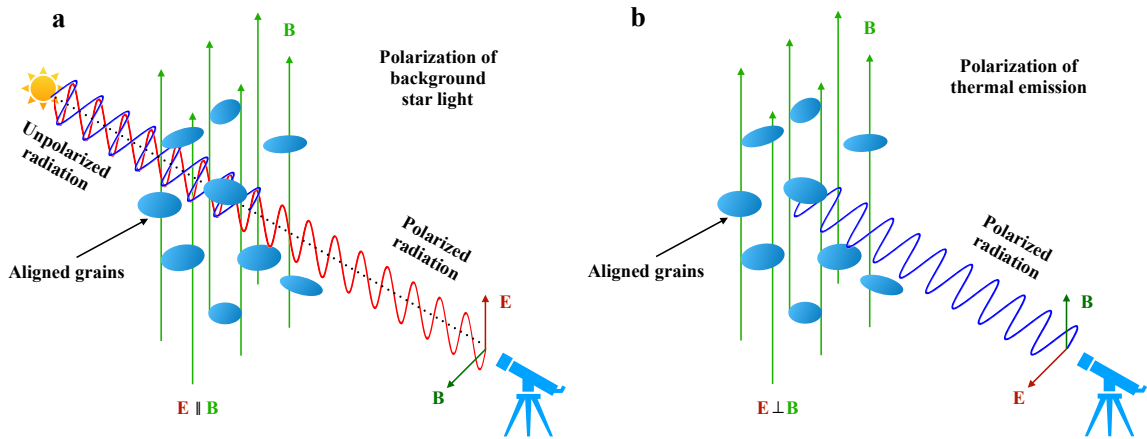


Fig. 1.3.— Illustration of polarization in two different scenarios, adapted from Lazarian (2007). (a) The polarization of background star light. Due to the dichroic extinction, the star light becomes polarized with E vectors parallel to the B field. (b) The polarization of dust thermal emission. Due to the dichroic emission, the thermal emission is polarized with E vectors perpendicular to the B field.

1.3.2 Polarized thermal emission as a probe of the interstellar magnetic field.

Just as the dichroic extinction from aligned grains causes the background star light to be polarized, the thermal emission from such aligned grains is also polarized (Fig. 1.3b). In this case, the dust grains preferentially emit light with polarization along their long axes, i.e., the blue wavy curve shown in the figure. As a result, the thermal emission is polarized with their E vectors perpendicular to the underlying magnetic field direction.

Usually, the dust thermal emission peaks around $0.1 \sim 1$ mm, and dominates the radiation in (sub)millimeter wavelengths. Through polarimetric observations at these wavelengths, astronomers are able to probe the magnetic field structure on multiple scales, even in the absence of any background star light.

Fig. 1.5 shows the polarization map observed by Planck Collaboration et al. (2015) at 0.85 mm wavelength. The left panel shows the result of the Pipe Nebula, whereas

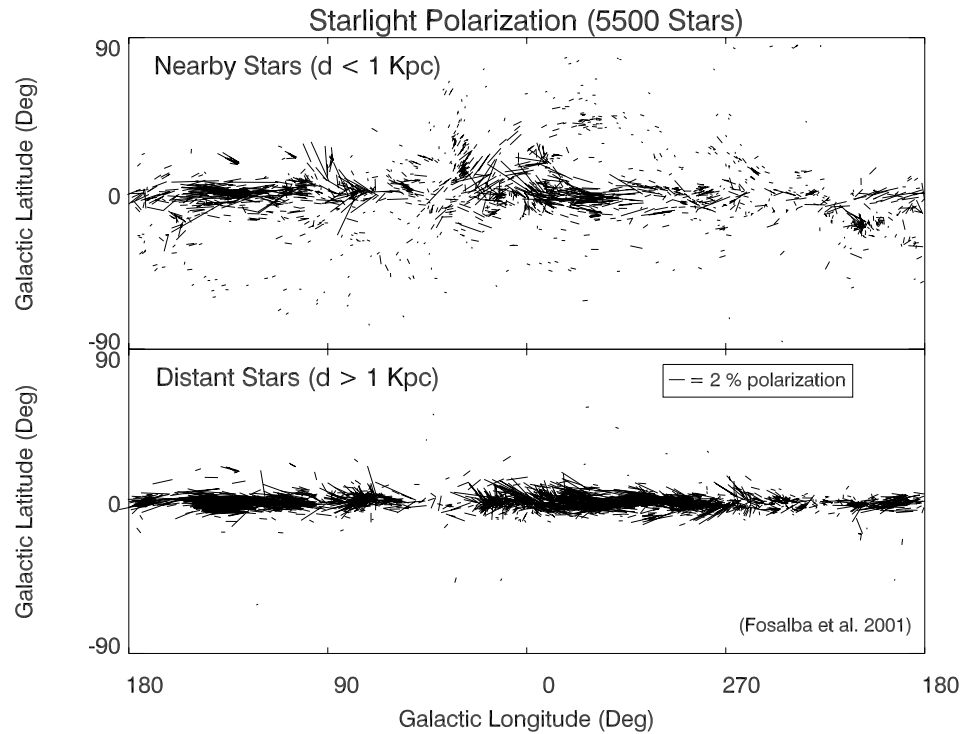


Fig. 1.4.— The polarization of star light in our galaxy, taken from Fosalba et al. (2002). The orientations of the polarization are very coherent and represent the magnetic field structure in our galaxy.

the right panel shows the result of the Chamaeleon-Musca regions. The vectors shown in the images are the polarization of the light rotated by 90 degrees (or the so-called “B-vectors”) to represent the underlying magnetic field structure. These regions are called “dense molecular clouds” which are known to host active star formation (Alves et al. 2008; Alcalá et al. 1995). The typical scale is of order \sim pc or larger. They are the birth place of extraterrestrial solar systems. Fig. 1.6 is the result from the Balloon-borne Large Aperture Submillimeter Telescope for Polarimetry (BLAST-Pol) on a similar scale at 0.5 mm wavelength.

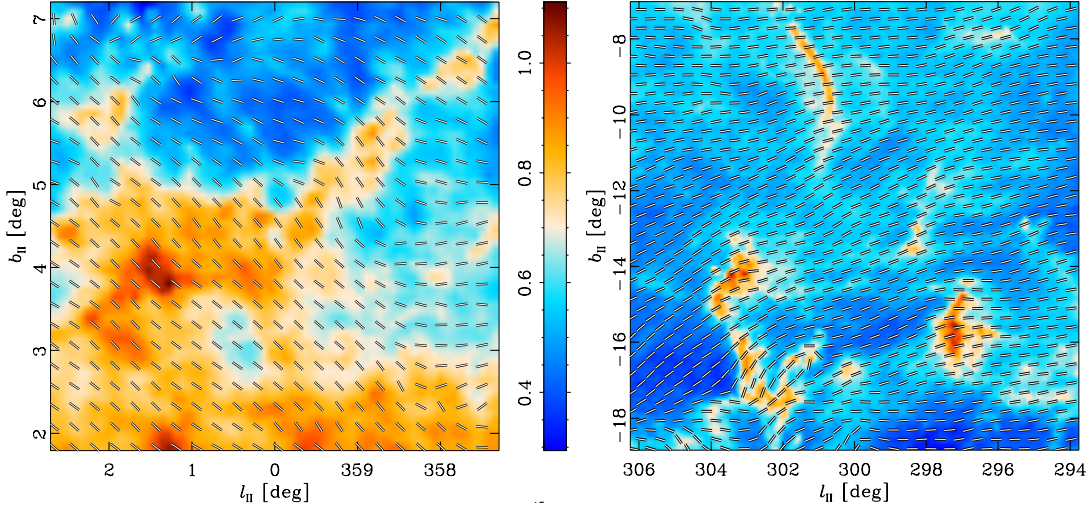


Fig. 1.5.— The polarization of dust thermal emission taken by PLANCK at 0.85 mm wavelength (Planck Collaboration et al. 2015). The vectors shown here are the B vectors of the light to represent the underlying magnetic field structure. Left: the Pipe Nebula. Right: Chamaeleon-Musca regions. These regions are known to host star formation (Alves et al. 2008; Alcalá et al. 1995), and are the birth place of extraterrestrial solar systems.

From the above, we can see that stars are formed out of turbulent magnetized clouds. Some dense substructures of the molecular clouds, called star forming cores, will collapse gravitationally once they become dense enough. Due to the conservation of angular momentum, these collapsing material will likely form a flattened structure (a so-called “pseudo-disk”), because it is easier for the material to collapse along the field lines towards the mid-plane than to collapse across the field lines. As the material in the pseudodisk collapses inward, it will drag the magnetic field lines with it due to the “flux freezing” if the matter and field are well coupled (i.e., in the ideal MHD limit). As a result, we expect the magnetic field to be pinched in the mid plane of the pseudodisk, and open up and down from it, and form an “hour-glass” shaped structure. The very first spatially resolved polarization observation on the protostellar envelope scale of ~ 1000 au was done by Girart et al. (2006) with the Submillimeter Array (SMA) at 0.88 mm wavelength towards the protostellar system NGC 133 IRS

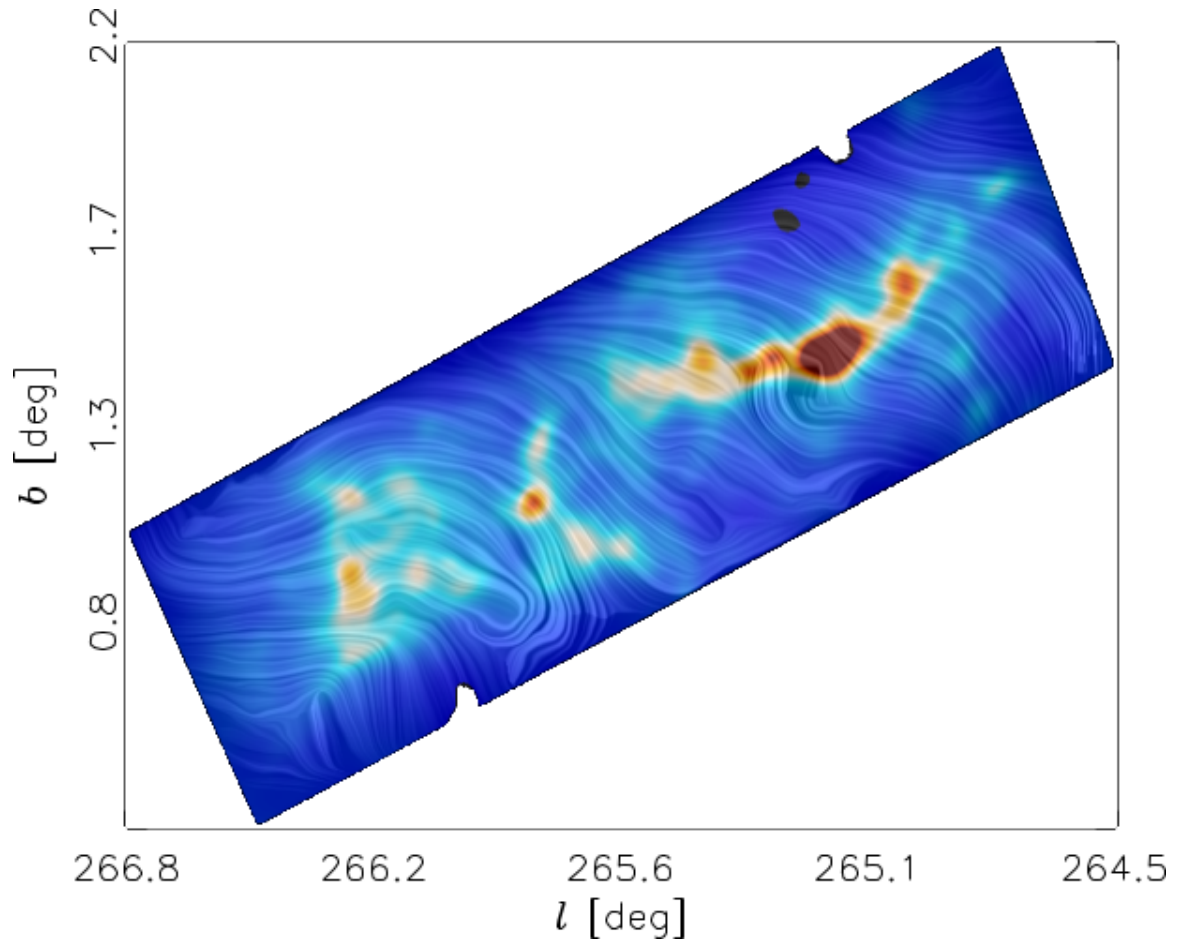


Fig. 1.6.— The Stokes I map with the inferred magnetic field overlaid as “drapery” image of the Vela C Molecular Cloud (Fissel et al. 2016).

4A (see Fig. 1.7). The observed magnetic field structure matches very well with our theoretical expectations. There are now many other polarized thermal emission observations at ~ 100 – 1000 AU scales towards protostellar cores (Rao et al. 2009; Hull et al. 2013, 2014, 2017b,a; Stephens et al. 2013; Cox et al. 2018). The polarized thermal emission has been very successful in probing magnetic field structures so far.

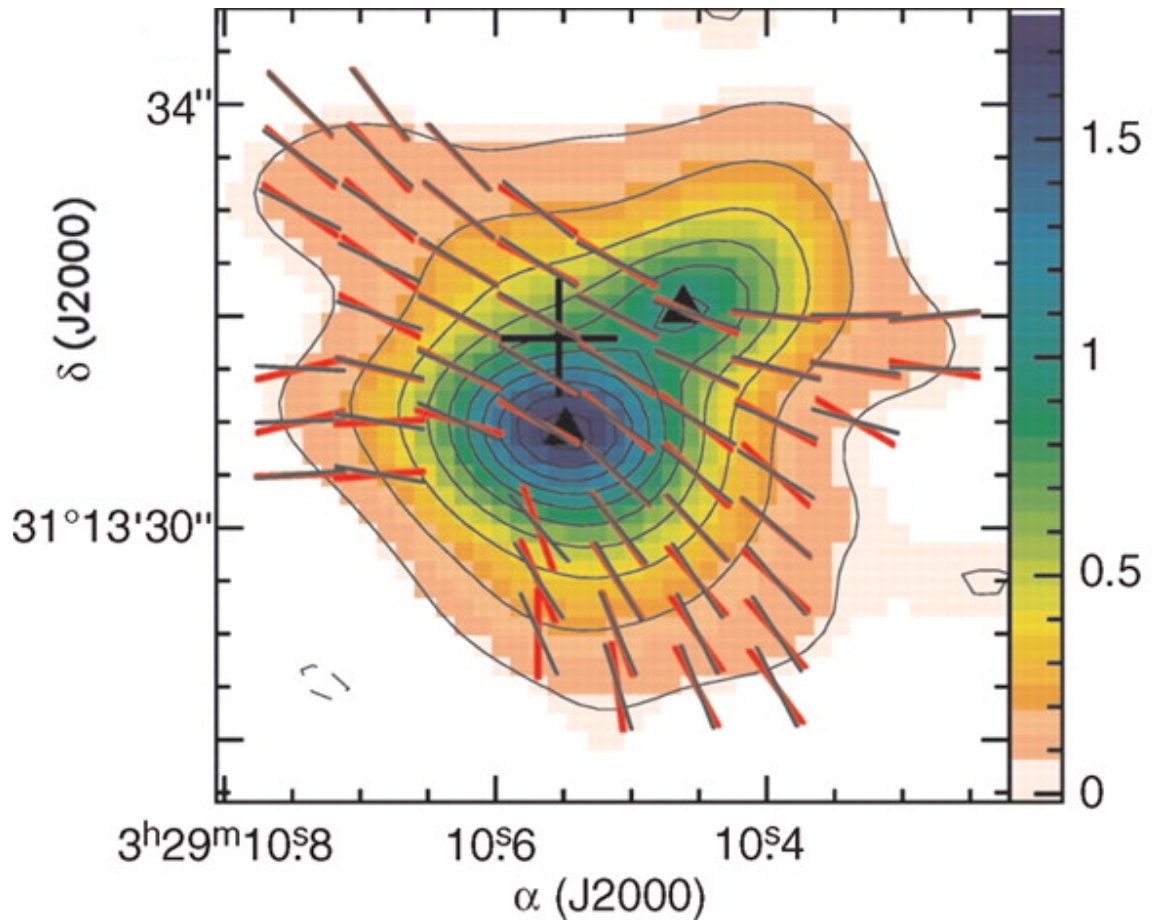


Fig. 1.7.— The polarization of dust thermal emission of the protostellar system NGC 1333 IRS 4A taken by Girart et al. (2006) with the Submillimeter Array (SMA) at 0.88 mm wavelength. It is the first textbook example of the theoretically expected “hour-glass” shaped magnetic field structures.

1.4 Polarimetry observations of disks

In Sec. 1.2, we have discussed the important role that the magnetic field is playing in the dynamics and evolution of protoplanetary disks from a theoretical point of view. Given its importance, it is crucial to find observational evidence for the magnetic field in protoplanetary disks. The polarized dust thermal emission has long been the “go-to” method to reveal the presence of a magnetic field.

1.4.1 Theoretical expectations from magnetic alignment

Before jumping into the polarimetric observations of disks, we will briefly discuss the theoretical expectations first. Cho & Lazarian (2007) was the first to study the polarization features in T Tauri disks. Within the frame of radiative torque (RAT) grain alignment theory for magnetic alignment (Lazarian 2007; Lazarian & Hoang 2007), they were able to calculate synthetic polarization maps for their adopted passive flared disk models (Chiang & Goldreich 1997; Chiang et al. 2001).

There are two major predictions in Cho & Lazarian (2007)’s work. Firstly, at mid-IR ($\sim 10\text{--}100\ \mu\text{m}$), the polarized emission is dominated by the small dust grains in the surface layer of the disk. The polarization fraction at these wavelengths can be as high as $\sim 10\%$ for unresolved disks. Secondly, at (sub)millimeter wavelengths ($\gtrsim 100\ \mu\text{m}$), the settled large dust grains at the mid plane dominates the radiation and the polarization fraction is around the $2 \sim 3\%$ level.

Due to the differential rotation of the disk, we expect a mostly toroidal magnetic field configuration (Flock et al. 2015). The synthetic polarization is shown in Fig. 1.8 (see also Bertrang & Wolf 2017). We can see that the polarization is perpendicular to the toroidal magnetic field and forms a “fan-like” structure. At the same time, the polarized intensity is higher along the minor axis of the disk (see Chap. 5 for a more

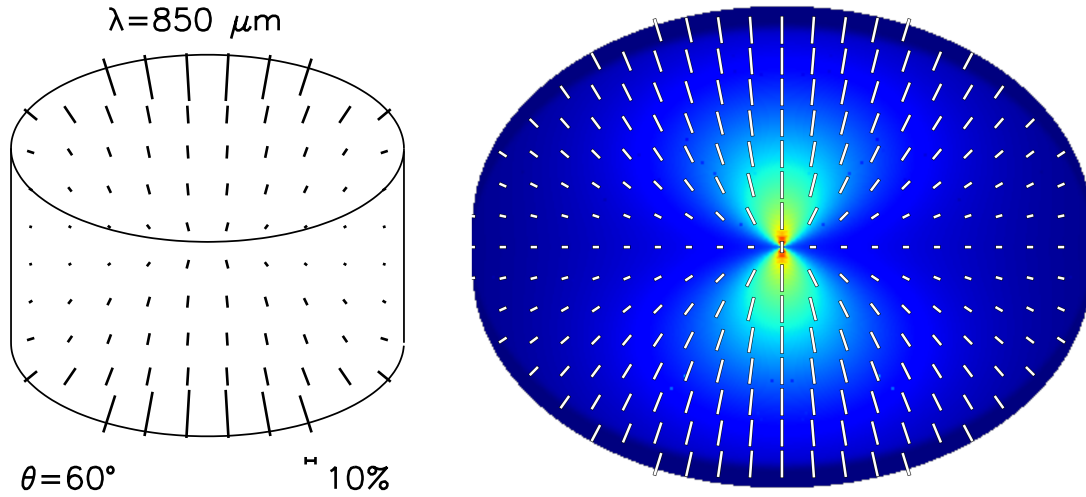


Fig. 1.8.— The expected polarization pattern in a T Tauri disk. The left panel is taken from Cho & Lazarian (2007). The right panel shows a preliminary calculation using my own radiative transfer code (see Chap. 3 and App. A for more detail).

detailed discussion on this).

1.4.2 Polarization observations on disk scales

Guided by the predictions of Cho & Lazarian (2007), several groups have searched for polarization signals in protostellar systems. The earliest work by Hughes et al. (2009) used the Submillimeter Array (SMA) to probe the continuum polarization in two systems, HD 163296 and TW Hya at 0.88 mm. However, they failed to detect any polarization and put a stringent upper limit for polarization fraction of 1.0% and 1.5% for HD 163296 and TW Hya, respectively. Such limits ruled out Cho & Lazarian (2007)’s model at the 10σ and 7σ level respectively. Later, Hughes et al. (2013) combined SMA with the Combined Array for Research in Millimeter-wave Astronomy (CARMA) to conduct polarimetry observations towards three other similar systems, DG Tau, GM Aur, and MWC 480. Again, they failed to detect any polarization signatures and put a polarization fraction limit of about 1% which rules

out Cho & Lazarian (2007)’s model at the $5 \sim 7\sigma$ level. The negative results cast doubt on the magnetic alignment models.

The first spatially resolved polarization in a T Tauri disk was detected by Stephens et al. (2014)¹. However, the observed pattern was very surprising (see Fig. 1.9). If we rotate the polarization by 90° to show the magnetic field orientations (the red lines in the figure), we get a rather uniform magnetic field direction. Such an interpretation has two major problems:

1. The inferred uniform magnetic field pattern is very unphysical. Considering the fact that the disk is rotating differentially around the center star, any unidirectional magnetic field configuration would be wound into a toroidal configuration, as illustrated in Fig. 1.2 (see, e.g., Flock et al. 2015). The time scale for such a process is expected to be the dynamical time scale of $\sim 10^3$ yr at a 100 au radius, much shorter than the typical disk life time of $\sim 10^6$ yr or more.
2. The polarized intensity is concentrated along the major axis of the disk. This is the opposite of what is expected of magnetically aligned grains (see Fig. 1.8).

These problems raise serious doubts about the magnetically aligned grain interpretation of the observed polarization. We are thus motivated to search for alternative explanations, which are the main focus of this thesis.

¹ There was an earlier detection towards a Class 0 protostar, IRAS 16293B, by Rao et al. (2014). However, it is unclear whether the emission is from a rotationally supported disk or not, since the emitting region appears to be optically thick, which makes it hard to obtain kinematic information through molecular line observations. In this thesis, we will not include polarization from evolved, transition disks, such as the HD 142527 observed by Kataoka et al. (2016b). Such disks tend to have complex substructures, such as (partial) rings and gaps, and their polarization patterns remain poorly understood.

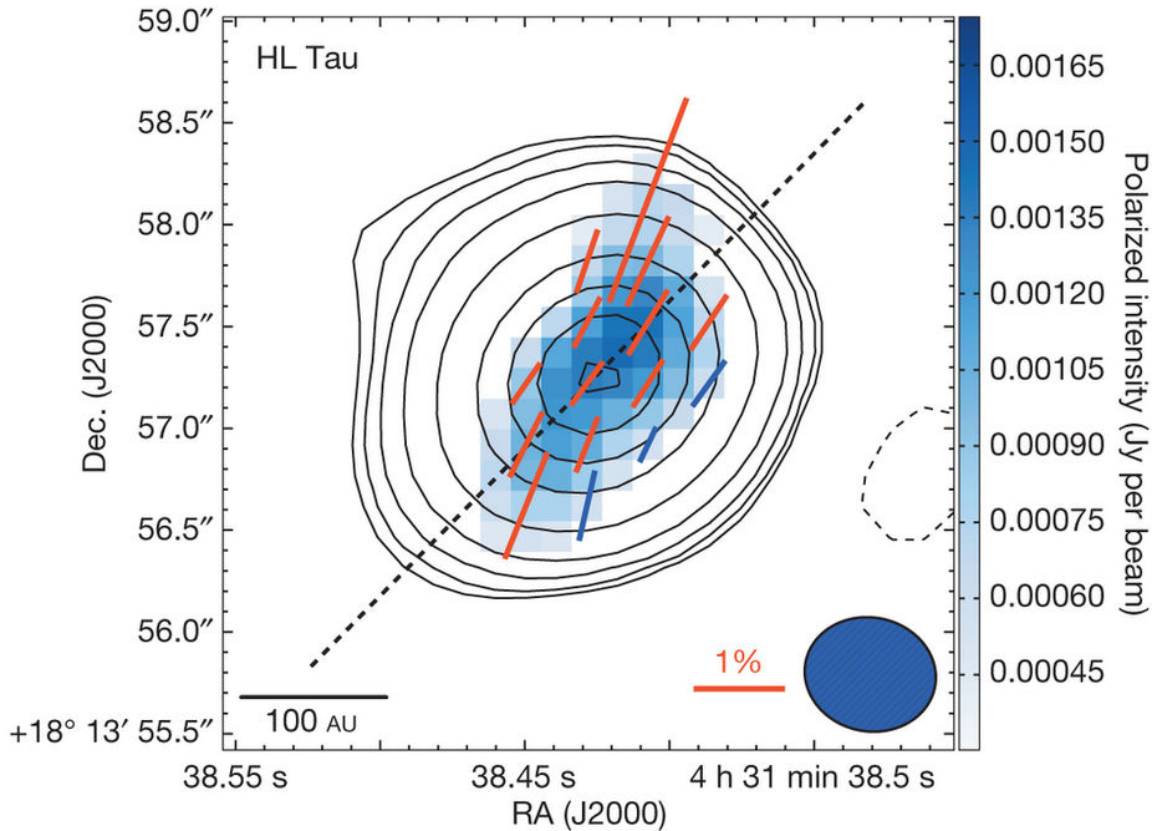


Fig. 1.9.— The polarization observation of the disk around HL Tau, taken from Stephens et al. (2014). The color map represents the polarized intensity. The contour shows the total flux, or Stokes I. The line segments represent the orientations of the polarization (rotated by 90° to show the inferred magnetic field direction).

1.4.3 ALMA and well resolved disk polarimetric observations

Recently, the Atacama Large Millimeter/submillimeter Array (ALMA) has fully calibrated its polarization system and becomes a game-changer in this field². ALMA is an interferometric array of radio telescopes built on the Atacama desert in Chile. It is an international partnership of the European Southern Observatory (ESO), the U.S. National Science Foundation (NSF) and the National Institutes of Natural Sciences (NINS) of Japan, together with NRC (Canada), NSC and ASIAA (Taiwan), and KASI (Republic of Korea), in cooperation with the Republic of Chile. ALMA is the most advanced radio interferometric array at (sub)millimeter wavelengths to date, with 66 high-precision dish antennas and about 6600 square meters of collecting area.

With ALMA, many disks have been observed with polarization information at a high angular resolution (of order 0.5 arcsec or better). Some examples are shown in Fig. 1.10. Relatively uniform polarization patterns are common, such as L1527 (panel a, Harris et al. 2018), VLA 1623W (panel b, Harris et al. 2018), Per-emb-50 (panel d, Cox et al. 2018), and especially HL Tau (panel c, Stephens et al. 2017; see also Chap. 2 and 5), IM Lup (panel f, Hull et al. 2018; see also Chap. 2), and IRS 63 (Sadavoy et al. 2018, unpublished). There are other systems that show more complicated polarization patterns, such as HH 80-81 (panel i, Girart et al. 2018; see also Chap. 4), HH 111 (panel e, Lee et al. 2018), HD 142527 (panel g, Kataoka et al. 2016b), and BHB 07-11 (panel h, Alves et al. 2018). This collection is incomplete, but it provides an indication that disk polarization is an exciting new field being revolutionized by ALMA. A detailed physical understanding of its origins is needed

²<http://www.almaobservatory.org/en/home/>

in order to turn the hard-fought data into effective probes of the disk properties.

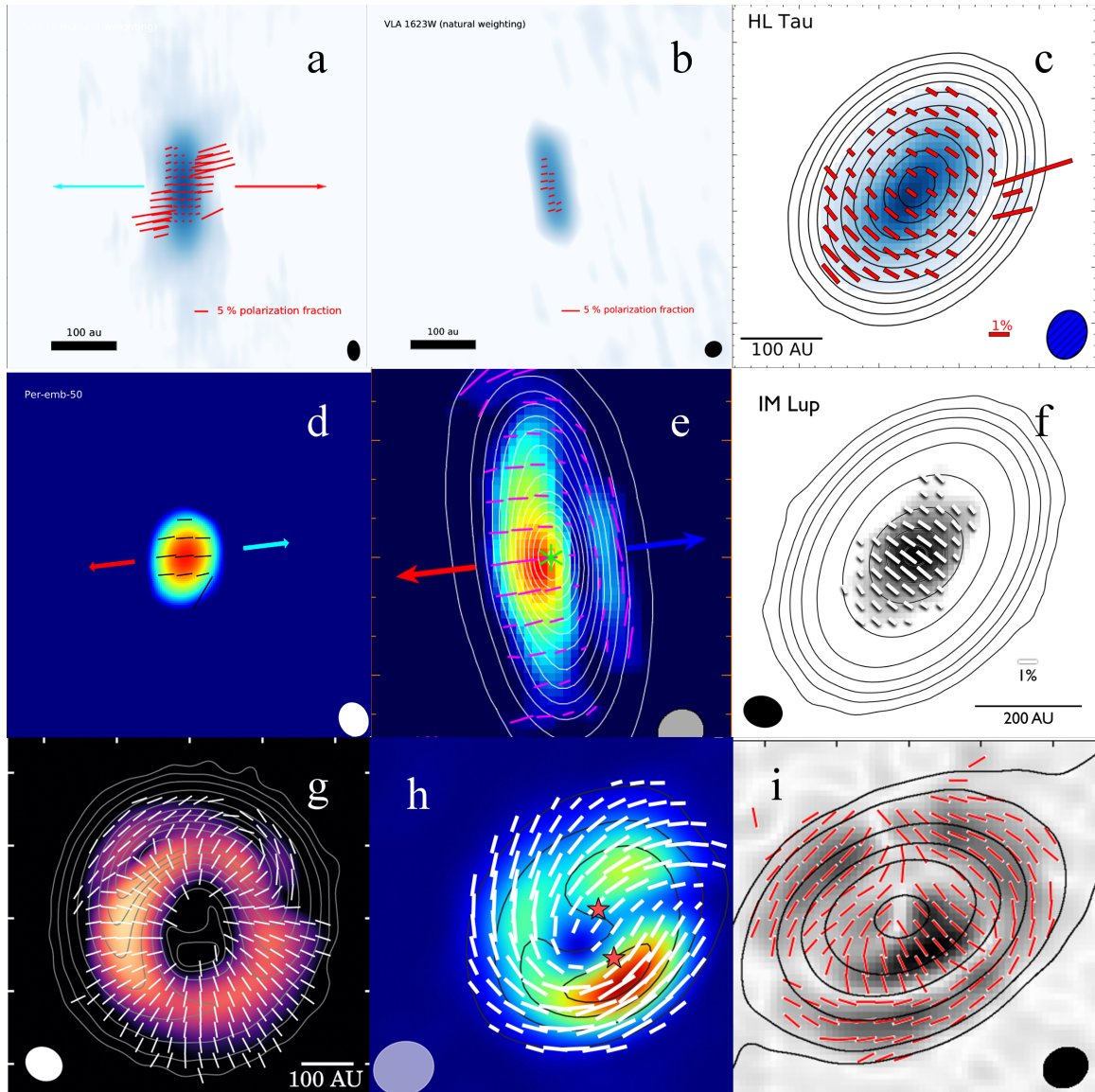


Fig. 1.10.— Examples of ALMA protoplanetary disk polarization observations to date. a: L 1527 (Band 7, Harris et al. 2018); b: VLA 1623W (Band 7, Harris et al. 2018); c: HL Tau (Band 7, Stephens et al. 2017); d: Per-emb-50 (Band 7, Cox et al. 2018); e: HH 111 (Band 7, Lee et al. 2018); f: IM Lup (Band 7, Hull et al. 2018); g: HD 142527 (Band 7, Kataoka et al. 2016b); h: BHB 07-11 (Band 7, Alves et al. 2018); i: HH 80-81 (Band 6, Girart et al. 2018).

1.5 Basics of scattering-induced polarization

An alternative to magnetically aligned grains is the scattering by dust grains, a theory developed by Kataoka et al. (2015). Before diving into the more detailed discussion in Chap. 2, we will discuss the basic physics behind scattering and why it can produce polarization.

1.5.1 Polarized scattered light under dipole approximation

For the sake of simplicity, we shall consider scattering by spherical particles much smaller than the wavelength of the incident light here (the so-called “Rayleigh Scattering”). Specifically, we assume that the size parameter $x = 2\pi a/\lambda$ to be much smaller than unity, where λ is the wavelength of the light and a is the linear size of the particle. It turns out that such a particle can be well treated as a dipole with an induced electric dipole moment of (Jackson 1999)³

$$\mathbf{p} = \alpha \mathbf{E} \tag{1.1}$$

where \mathbf{E} is the external electric field. In the case of small spherical particles, the polarizability α is a scalar. The scattering of unpolarized light by such a dipole is depicted in Fig. 1.11.

For an unpolarized incident light, we can decompose it into two fully polarized components in 1- and 2-direction. These two components excite two dipoles in the scattering particle, \mathbf{p}_1 and \mathbf{p}_2 , independently. The re-radiation from these two dipoles is the scattered light. We know that the dipole radiation in the far-field satisfies

³The small-particle dipole approximation allows us to capture the basic physics of scattering-induced polarization and will be used for most of the quantitative calculations in this thesis. We will relax the assumption of spherical particles in Chap. 3. Methods for calculating scattering by large (non)spherical grains are presented in App. B.

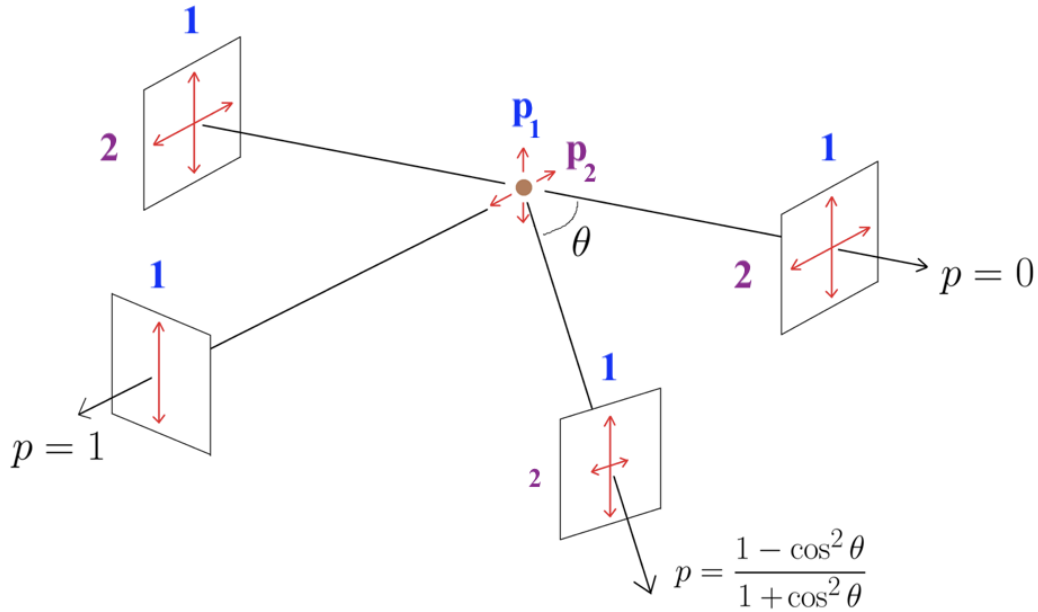


Fig. 1.11.— A schematic illustration of dipole scattering. The unpolarized incoming light will be polarized in the 1-direction after the scattering, and the polarization fraction depends on the scattering angle θ . The polarized light in the special case of $\theta = \pi/2$ is fully (maximally) polarized.

(Jackson 1999):

$$\langle \mathbf{S} \rangle \propto \frac{\sin^2(\theta_d)}{r^2}, \quad (1.2)$$

where $\langle \mathbf{S} \rangle$ is the time-averaged Poynting vector. The dipole radiation is also polarized. The radiation from \mathbf{p}_1 is polarized in 1-direction, whereas the polarization of the radiation from \mathbf{p}_2 is in the perpendicular, 2-direction. For the forward scattering with $\theta = 0$, the light propagation direction is perpendicular to both of the two dipoles ($\theta_{d1} = \theta_{d2} = \pi/2$). So in this case, the net polarization is 0 and the scattered light is unpolarized. For the case with $\theta = \pi/2$, we have $\theta_{d1} = \pi/2$, but $\theta_{d2} = 0$. As a result, the 2-component of the scattered light completely vanishes, and we are left with a fully polarized light in the 1-direction.

Using the same argument, it is straightforward to show that the light is partially polarized in the 1-direction with a polarization fraction:

$$p(\theta) = \frac{1 - \cos^2(\theta)}{1 + \cos^2(\theta)}, \quad (1.3)$$

where θ is the scattering angle between the incident and outgoing light.

To sum up, there are two most important features for polarization from scattering by small spherical dust grains:

1. The direction of the polarization is perpendicular to the scattering plane, the plane defined by the incoming radiation direction and outgoing radiation direction. In the example shown in Fig. 1.11, this direction is in the 1-direction.
2. The polarization is maximized with 90 degree scattering angle. The scattered light is fully polarized in this case.

These will be the keys to understand why the scattering of dust grains can explain the disk polarization observed in HL Tau and other sources.

1.5.2 Astrophysical examples of scattering-induced polarization

The scattering-induced polarization is a very common phenomenon and is widely used in fields such as photography, biophysics (Bickel et al. 1976), etc. Astronomers also use the polarization from scattered light to study celestial systems, especially at optical and near infrared wavelengths.

One well-known example is reflection nebulae. They are bright in the optical/near-IR wavelengths. They have similar spectra with nearby stars, indicating that the

illumination from these stars is responsible for the brightness of the reflection nebulae (Slipher 1912).

Fig. 1.12 is the K band polarimetric observation of the envelope of the R Mon star, taken with Subaru/CIAO (Murakawa et al. 2008). The polarization forms a circular pattern around the illuminating star. This is the 1-direction discussed above (see Fig. 1.11), which is perpendicular to both the incoming radiation from the star and the outgoing radiation towards the observer along the line of sight. Also, the polarization degree can be as high as $\sim 50 - 60\%$.

1.5.3 Strong dependency of polarization on grain sizes

The scattering efficiency has a strong dependency on the grain sizes. For (small-particle) Rayleigh scattering, the opacity for scattering (which is the cross-section for scattering per unit mass) (Bohren & Huffman 1983):

$$\kappa_{\text{sca}} = \frac{32\pi^4 a^3}{\rho_d \lambda^4} \left| \frac{m^2 - 1}{m^2 + 2} \right|^2, \quad (1.4)$$

where ρ_d is the density of the dust grain, a is the grain size, and λ is the wavelength of the photons. $m = n + ik$ is the complex refractive index of the material. We can see that the scattering opacity depends on the grain size strongly, with $\kappa_{\text{sca}} \propto a^3$. For comparison, the absorption opacity of the grains is given by

$$\kappa_{\text{abs}} = \frac{6\pi}{\rho_d \lambda} \text{Im} \left\{ \frac{m^2 - 1}{m^2 + 2} \right\}, \quad (1.5)$$

which does not depend directly on the grain size a . The $\text{Im}\{\dots\}$ here denotes the imaginary part of the quantity inside the brackets. Fig. 3.7 in Chap. 3 shows the dependency of the scattering and absorption opacities on the grain size beyond the

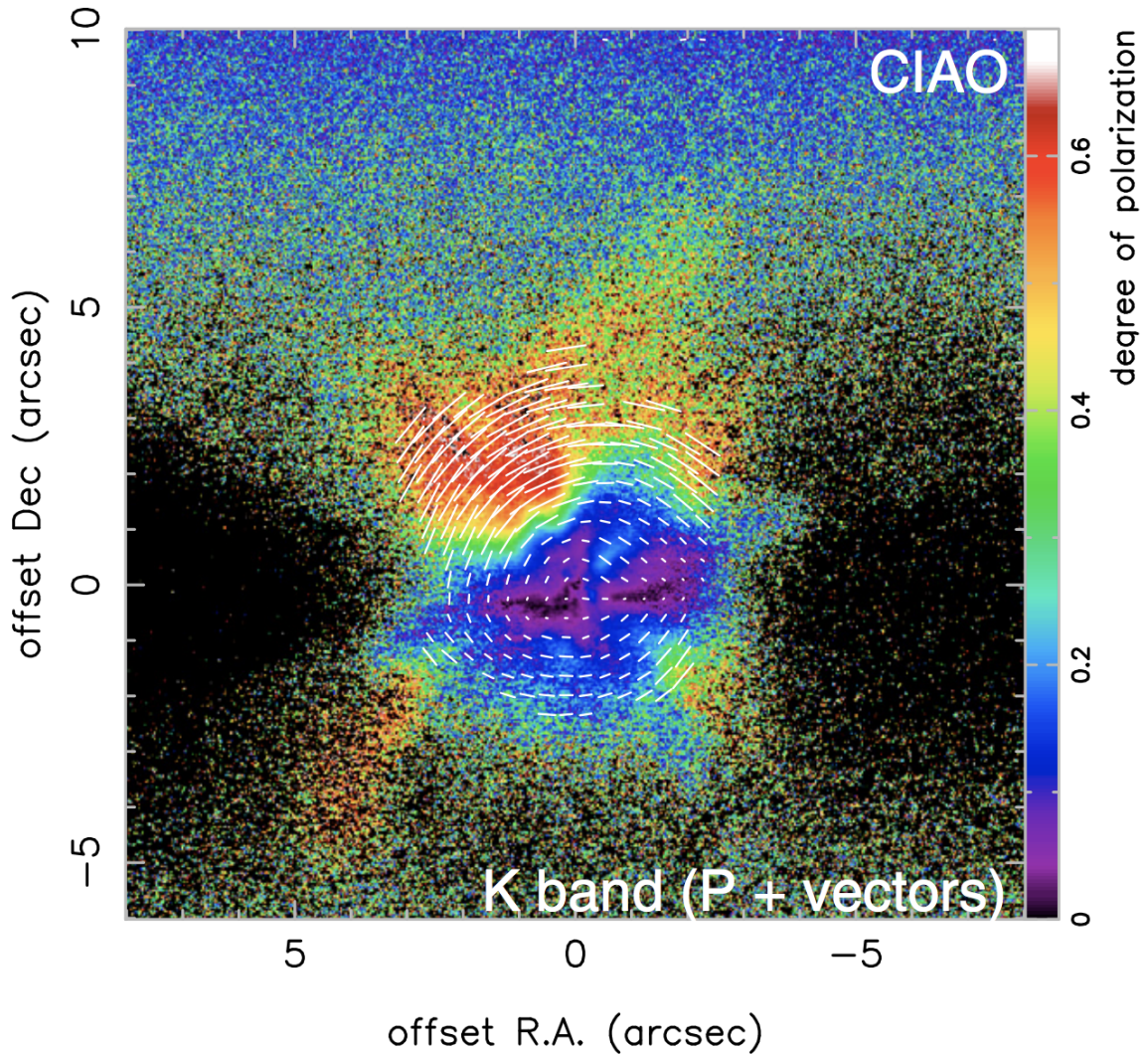


Fig. 1.12.— Subaru/CIAO K band ($2.2\ \mu\text{m}$) polarimetric observation of the envelope of the R Mon star, taken from Murakawa et al. (2008). The colormap represents the polarization degree, which can go up to $\sim 50 - 60\%$. The line segments represent the orientations of the polarization, with length proportional to the polarization degree.

small-particle regime.

Kataoka et al. (2015) proposed a metric $P\omega$ to measure the sensitivity of polarimetry observations on the size of dust grains responsible for the polarization within the scattering mechanism. Here P is the polarization fraction at 90 degree scattering an-

gle. $\omega \equiv \kappa_{\text{sca}}/(\kappa_{\text{sca}} + \kappa_{\text{abs}})$ is the albedo, which describes how important the scattering is relative to the total extinction by the particle. The dependency of $P\omega$ on the grain size at different wavelengths is shown in Fig. 1.13. We can see that at each wavelength, there is one narrow range of grain sizes that the polarimetry observation is most sensitive to. Because of this, we will see that the scattering-induced polarization is a potentially powerful tool to study the grain sizes in protoplanetary disks.

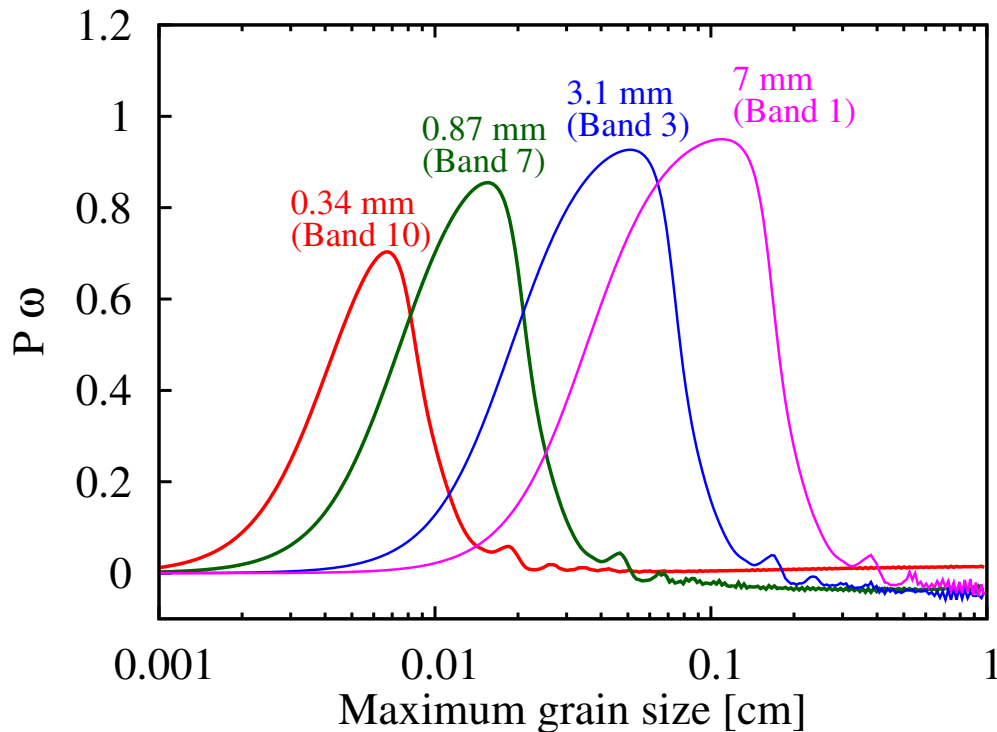


Fig. 1.13.— The product of the polarization fraction P and the albedo ω plotted as a function of grain size at different wavelengths, taken from Kataoka et al. (2015). The wavelengths chosen here are the representative wavelengths at different ALMA bands.

1.6 Evolution of dust grains and the formation of planetesimals

We have discussed briefly the dependence of scattering opacity on the grain size, and will discuss in more detail how disk polarization can be a powerful tool to study the sizes of dust grains in Chap. 2. The evolution of grain sizes, especially in the protoplanetary disk environment, is an important topic in understanding the formation of planets. Planets are about 10^3 km or more in sizes, whereas the dust grains in diffuse ISM are usually on the order of $0.1 \mu\text{m}$. These (sub)micron-sized dust grains must grow in size by roughly 13 orders of magnitude in order to become a planet.

1.6.1 Three steps of planet formation

In general, the process of small dust grains growing bigger and eventually forming planets can be broadly divided into three steps: growth by sticking, planetesimal formation, and accretion by the planetesimals.

Growth by sticking

Due to the Van der Waals force, dust particles may stick together when they collide (Chiang & Youdin 2010; Blum & Wurm 2008). The speed of the collision cannot be too high. When the colliding kinetic energy exceeds the surface potential energy or the deformation potential energy, the grain particles will shatter rather than sticking together. For micron-sized ice particles, the maximum sticking velocity is on the order of 1 m/s (Chokshi et al. 1993). For micron-sized spherical silicate particles, the maximum sticking velocity is measured experimentally to be of order only $\sim 10 - 100$ cm/s (Blum & Wurm 2008).

However, the grain growth by sticking only works for grains with sizes $\lesssim 1$ cm (Testi et al. 2014). In what follows, I will use 1 cm to divide big and small grains. Experimentally, when two big grains collide, they will *fragment* to smaller ones. When we use one small grain to hit a big one, *erosion* will take place and the small grain will abrade part of the material off the bigger one rather than sticking onto it. As such, it is unlikely that grains can grow all the way up to kilometer-sized planetesimals (Blum & Wurm 2008), although some caveats need to be sorted out before we are finally certain about this, such as the potential direct path through “growth by mass transfer” (Testi et al. 2014), the effects of ice mantles (Okuzumi et al. 2012), etc. See Testi et al. (2014) for more detailed discussions on this.

Accretion by the planetesimals

When an object becomes large (and thus massive) enough, it will start to accrete other objects through gravity. Objects reaching this limit are called planetesimals, and are considered the building blocks for planets.

We can make a very rough estimate of the required size for planetesimals in the following way. Let’s consider a test particle with velocity v . When the gravitational binding energy of this test particle around a planetesimal is comparable or larger than its kinetic energy, it would be accreted gravitationally by the planetesimal. This condition yields:

$$R \sim 700 \text{ m} \times \left(\frac{v}{1 \text{ m/s}} \right) \left(\frac{\rho_d}{3 \text{ g/cm}^3} \right)^{-1/2}, \quad (1.6)$$

where $\rho_d = 3 \text{ g/cm}^3$ is the typical density for compact silicate dust. The typical velocity v is the most uncertain quantity. If we take the thermal sound speed for 30 K Hydrogen gas particle, $\sim 500 \text{ m/s}$, we get $R \sim 350 \text{ km}$. In reality, the typical velocity for dust particles is much smaller than this. As a result, the initial sizes

of planetesimals can be anywhere between 10 m \sim 10 km; 1 km is usually taken as a fiducial value⁴. More massive objects tend to accrete other objects faster, which increases their gravity which in turn makes it easier for them to accrete. The runaway growth eventually leads to the formation of planets.

Formation of planetesimals

This is the most challenging stage to study during the planet formation. For dust particles with sizes between centimeter and kilometer, collisions tend to shatter bigger grains and they are not big enough for self-gravity to play a role yet. Current understanding is that if the dust density is enhanced to a certain level, kilometer-sized planetesimals would form directly. The characteristic density for this to happen is the so-called “Roche density.” An incompressible fluid orbiting around a central star will be able to resist the tidal disruption of this star if it is denser than the Roche density. For a star with mass M_* , the Roche value is about $3.5M_*/r^3$ (Chandrasekhar 1987). Even though self gravity can be important at lower densities, the Roche density still serves as a good benchmark value (Chiang & Youdin 2010).

There are a couple of potential ways to enhance the local density to bring an ensemble of small dust grains together to seed planetesimals, such as gravitational instabilities (Goldreich & Ward 1973), streaming instabilities (Youdin & Goodman 2005), secular dust layer instability (Goodman & Pindor 2000). Detailed discussion on this topic is beyond the scope of this thesis and readers are encouraged to read the excellent review by Chiang & Youdin (2010).

Fig. 1.14 shows the ladder of grain growth and various stages during the formation of planets. The disk polarization discussed in this thesis is able to probe the very

⁴For example, Schlichting et al. (2013) inferred a favored initial planetesimal size of about 2 km by modeling the observed Kuiper Belt size distribution.

first step on this ladder, as well as the dust settling, the second step of the ladder.

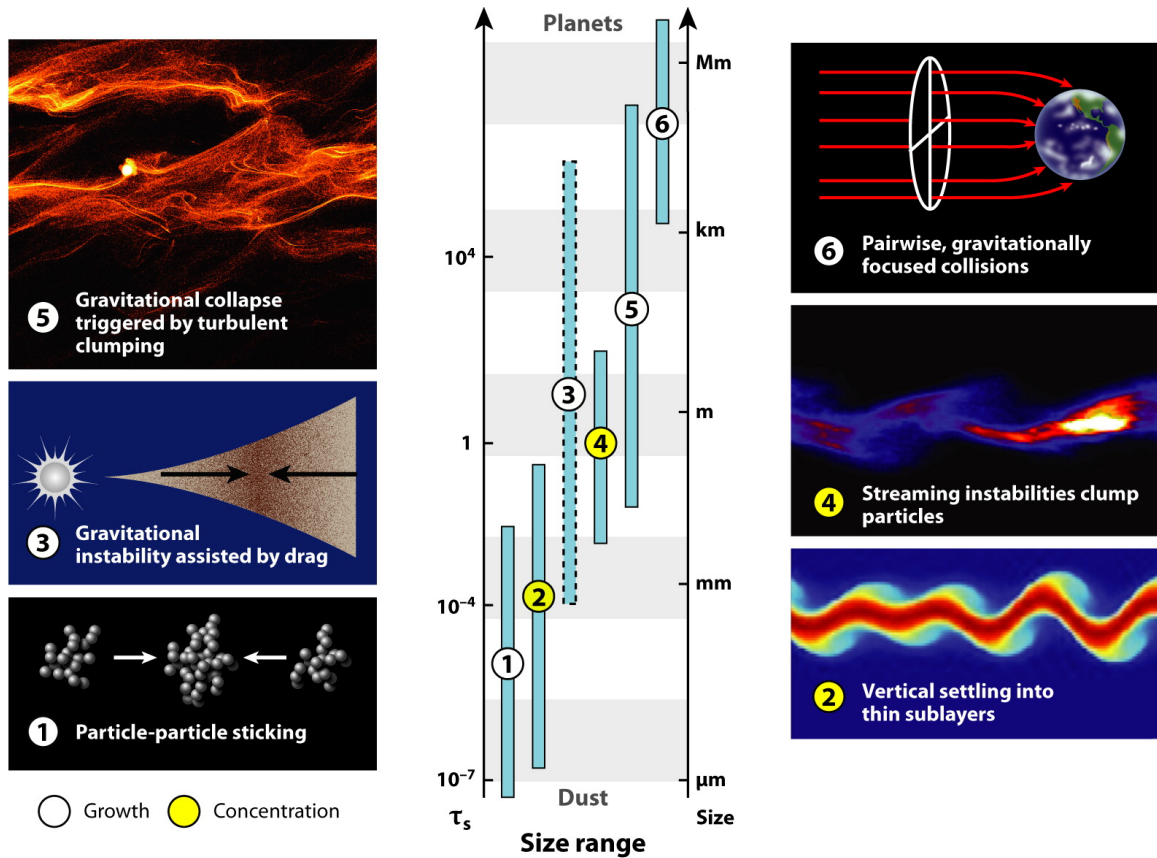


Fig. 1.14.— The size ladder from dust to planets, taken from Chiang & Youdin (2010). Various related processes are circled on the ladder as well as their relevant linear scales. The disk polarization can probe grain growth to (sub)millimeter sizes, which is the first step towards the formation of planets (see Chap. 2), as well as the dust settling (see Chap. 4), the second step of the ladder.

Chapter 2

Inclination-induced polarization of scattered millimetre radiation from protoplanetary disks

This chapter is based on Yang et al. (2016a) with minimal modifications, except for Sec. 2.5 on the modeling for the IM Lup system that I did for Hull et al. (2018), on which I am a second author.

Abstract

Spatially resolved polarized millimeter/submillimeter emission has been observed in the disk of HL Tau and two other young stellar objects. It is usually interpreted as coming from magnetically aligned grains, but can also be produced by dust scattering, as demonstrated explicitly by Kataoka et al. (2015) for face-on disks. We extend their work by including the polarization induced by disk inclination with respect to the line of sight. Using a physically motivated, semi-analytic model, we show that

the polarization fraction of the scattered light increases with the inclination angle i , reaching $1/3$ for edge-on disks. The inclination-induced polarization can easily dominate that intrinsic to the disk in the face-on view. It provides a natural explanation for the two main features of the polarization pattern observed in the tilted disk of HL Tau ($i \sim 45^\circ$): the polarized intensity concentrating in a region elongated more or less along the major axis, and polarization in this region roughly parallel to the minor axis. This broad agreement provides support to dust scattering as a viable mechanism for producing, at least in part, polarized millimeter radiation. In addition, we carry out detailed Monte Carlo simulations of scattering-induced polarization to model the ALMA data observed in the protoplanetary disk around the Class II source IM Lup. The close agreement between the model and data adds confidence to scattering as an important origin of the disk polarization at millimeter/submillimeter wavelengths. In both HL Tau and IM Lup disks, in order to produce polarization at the observed level ($\sim 1\%$), the scattering grains must have grown to a maximum size of tens of microns. However, such grains may be too small to produce the opacity spectral index of $\beta \lesssim 1$ observed in both HL Tau and IM Lup, as well as other sources; another population of larger, millimeter/centimeter-sized, grains may be needed to explain the bulk of the unpolarized continuum emission.

2.1 Introduction

Polarized millimeter/sub-millimeter emission has been observed in the disks around several young stellar objects with CARMA and especially ALMA (see Fig. 1.10 for a collection of examples). It is usually interpreted as coming from magnetically aligned dust grains (e.g., Cho & Lazarian 2007; Bertrang & Wolf 2017). This interpretation appears consistent with the data on some systems, such as IRAS 16293-2422B and

L1527, where the observed polarization patterns are broadly similar to those expected from grains aligned by a predominantly toroidal magnetic field (Rao et al. 2014; Segura-Cox et al. 2015; see § 2.6 for more discussion). In contrast, the polarization vectors in the disk of HL Tau (Stephens et al. 2014; Stephens et al. 2017) (which is inclined with respect to the line of sight by $\sim 45^\circ$, ALMA Partnership et al. 2015; Kwon et al. 2011) are all roughly parallel to the minor axis (see Fig. 2.1), which is not compatible with the pattern expected of grains aligned by a toroidal disk field, although more complicated field configurations cannot be ruled out (Stephens et al. 2014). Another drawback of the toroidal field-aligned grain model is that it predicts a lower polarization fraction along the major axis than along the minor axis (Cho & Lazarian 2007, see also Fig. 1.8), which is the opposite of what is observed (Fig. 2.1). A much better fit is provided by a uni-directional magnetic field approximately (within $\sim 10^\circ$) along the disk major axis. However, such a field configuration would be difficult to maintain against the disk differential rotation. Furthermore, there is growing evidence for grain growth in protoplanetary disks, up to millimeter or even centimeter sizes (e.g., Pérez et al. 2012; Testi et al. 2014). It is unclear whether such large grains would be aligned with respect to the magnetic field through the currently favored mechanism of radiative torque because their magnetic moments may not be large enough to provide the fast precession needed (Lazarian 2007) and their slow internal relaxation makes the alignment less efficient (Hoang & Lazarian 2009). These difficulties provide a motivation to investigate other potential mechanisms for producing, at least in part, the polarized mm emission from the HL Tau disk.

One possibility, first investigated in detail by Kataoka et al. (2015), is that the polarized millimeter disk emission comes from scattering of large dust grains. Kataoka et al. stressed the need for anisotropic radiation field for this mechanism to work

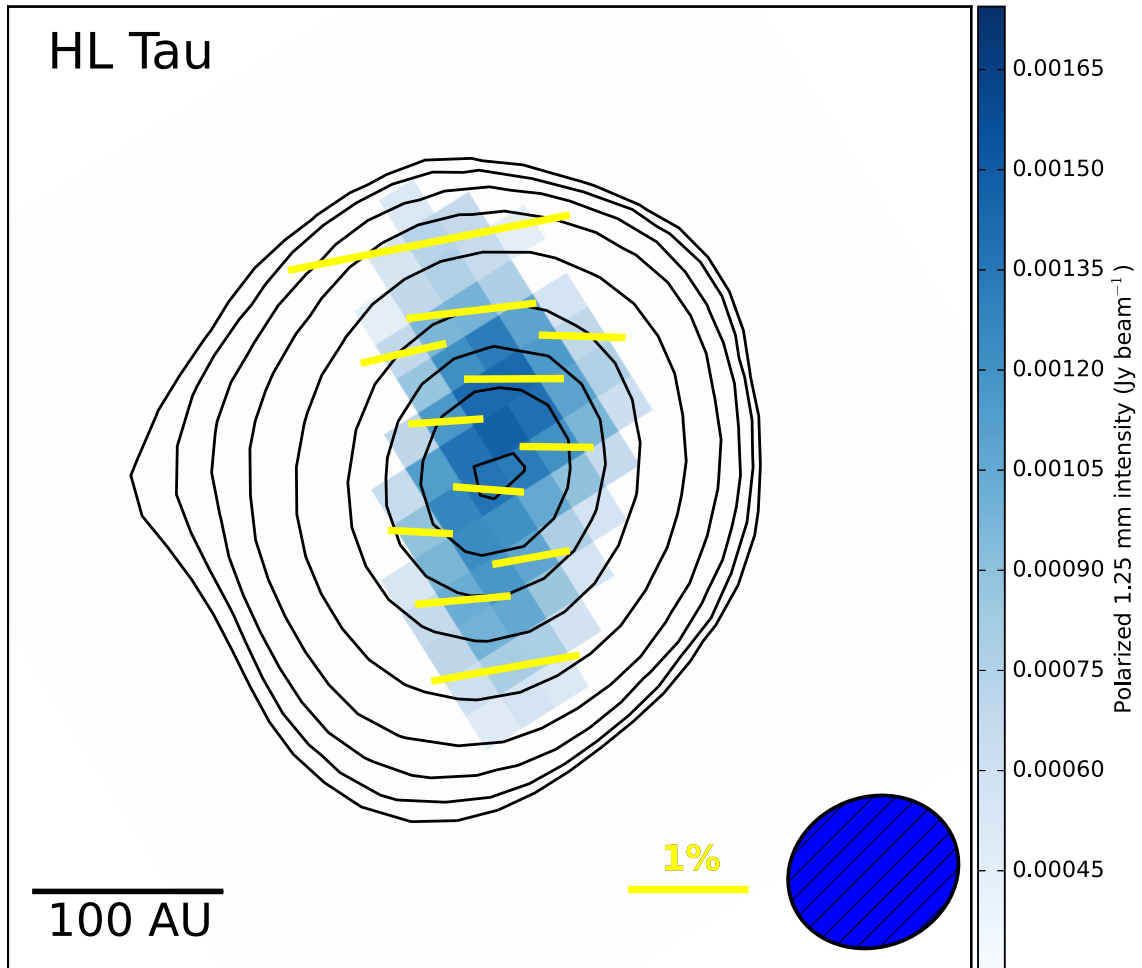


Fig. 2.1.— Observed 1.3 mm polarization pattern of the HL Tau disk. Plotted are total intensity (contours), polarized intensity (color map, $> 2\sigma$), and polarization vectors ($> 3\sigma$), with length proportional to the polarization fraction. Adapted from Stephens et al. (2014). The major axis determined from the ALMA data (ALMA Partnership et al. 2015) is tilted by 10° clockwise with respect to the vertical direction.

efficiently. As examples of this requirement, they considered radiation from structured disks with either an axisymmetric ring or a non-axisymmetric lobe, both viewed face-on. Here, we extend Kataoka et al. (2015)’s work to show that significant polarization is produced even in a smooth disk, as long as the disk axis is tilted away from the line of sight by a large enough angle. The physical reason can be understood most easily in the limits of optically and geometrically thin dust emission and Rayleigh

scattering, where the degree of polarization is peaked near a scattering angle of 90° . In these limits, the radiation field to be scattered by dust grains becomes essentially two dimensional, concentrated in the disk plane. In such a case, only the radiation propagating along the disk major axis would be scattered by 90° to reach the observer and be maximally polarized, with a polarization direction along the minor axis in the plane of the sky. This simple geometric effect provides a natural explanation for the two main features of the polarization pattern observed in the HL Tau disk (see Fig. 2.1): (1) polarized emission concentrating in an elongated region more or less along the major axis, and (2) polarization vectors in this region roughly parallel to the minor axis. These are the features that are difficult to explain in the current models of polarization from magnetically aligned grains¹. They provide a strong motivation to explore in more detail the polarization pattern produced by dust scattering. It is a first step toward disentangling the contributions of dust scattering and grain alignment to the disk polarization, which is needed in order to take full advantage of the high resolution ALMA and JVLA polarization observations that will become available soon for probing the grain growth and/or magnetic field in protoplanetary disks.

In the remainder of the Chapter, we will put the above qualitative picture on a more quantitative ground by computing the scattered radiation from an inclined disk (such as the HL Tau disk) semi-analytically using the so-called “thin-disk” approximation that brings out the essential physics transparently (§ 2.2); a more complete treatment of the radiative transfer problem will be postponed to a future investigation. The effects of disk inclination on the polarization pattern will be emphasized. The scattered radiation is compared with the direct dust emission in § 2.3, where the

¹Grains aligned by a toroidal magnetic field can explain the orientations of the polarization vectors near the center, but not at larger distances (see the left panel of Fig. 2 of Stephens et al. 2014).

fractional polarization of the total intensity is computed. In § 2.4, we comment on the implications of the polarization fraction observed in HL Tau on the grain size distribution. In § 2.5, we model the polarization from disk around the IM Lup protostar with inclination-induced polarization. We discuss the possibility of dust scattering-induced polarization for other sources and future model refinements in § 2.6 and conclude in § 2.7.

2.2 Polarized Radiation from Dust Scattering

In this section, we develop a semi-analytic model for polarization from dust scattering under the simplifying assumptions that the dust emission is optically thin and that the dust disk is geometrically thin, with a local scale height much less than the radius. The latter would be a particularly good approximation if the relatively large grains responsible for the emission and scattering of millimeter radiation are settled toward the disk mid-plane. To isolate the polarization due to dust scattering from that caused by grain alignment, we further assume that the grains are not aligned, so that the radiation directly emitted by dust is unpolarized. Under these assumptions, the incoming radiation field seen by the scattering dust grains at a given point inside the disk can be decomposed into two components: a local, roughly isotropic, component emitted by the (non-aligned) grains in a region of size comparable to the (dust) scale height surrounding the point, and an anisotropic component coming from the grains in the rest of the disk beyond the local region. The former does not lead to significant polarization after scattering because scattering of isotropic radiation by non-aligned grains does not have any preferred direction. It is the latter that is mainly responsible for the polarized radiation after scattering. The computation of this component will be drastically simplified by the thin-disk approximation, as we show below.

2.2.1 Formulation of the Problem

To facilitate the computation of the scattered light from dust grains at a location \mathbf{r} inside a disk with axis inclined by an angle i with respect to the line of sight, we define two coordinate systems, both centered on the scatterer's location \mathbf{r} . The first is fixed in the observer's frame, with horizontal x' - and vertical y' - axes in the plane of the sky, and z' -axis pointing toward the observer. The second is fixed on the disk, with the y -axis coinciding with the y' -axis, and the z - and x -axis rotating around the y' -axis counter-clockwise (viewed along the minus y' -axis) from the z' - and x' -axis, respectively, by the inclination angle i . We align the major axis of the disk in the plane of the sky along the y - (and y' -) axis, and the disk normal direction along the z -axis.

Since the scattered radiation is linearly polarized, we will compute the three Stokes parameters I_s , Q and U defined in the observer's frame (x', y', z') separately, starting with the intensity I_s (we drop the subscript s for Q and U since, in our model, they are assumed to be produced only by the scattered radiation, without any contribution from the direct radiation, unlike the total intensity I). In the optically thin limit, the intensity of the scattered radiation along the line of sight I_s is given by an integration of the source function of the scattered radiation, $S_{s,z'}$, along the z' -axis. The source function $S_{s,z'}$ at any location \mathbf{r} inside the disk is given by

$$S_{s,z'}(\mathbf{r}) = \frac{1}{\sigma_s} \int \frac{d\sigma}{d\Omega} I(\mathbf{r}, \theta, \phi) d\Omega \quad (2.1)$$

where $I(\mathbf{r}, \theta, \phi)$ is the intensity of the unpolarized incoming radiation seen by the scattering dust grains at the location \mathbf{r} along the direction of polar angle θ (measured from the z -axis or the disk normal direction) and azimuthal angle ϕ (measured

counter-clockwise from the x -axis on the disk), σ_s is the solid angle Ω -integrated (total) scattering cross section, and $d\sigma/d\Omega$ is the differential cross section for scattering the radiation $I(\mathbf{r}, \theta, \phi)$ into the line of sight (i.e., along the z' -axis).

The intensity $I(\mathbf{r}, \theta, \phi)$ is given by an integration of the source function for thermal dust emission, the Planck function $B_\nu(T)$, over the optical depth $d\tau_{abs} = \kappa_{abs}\rho dl$ (where κ_{abs} is the thermal dust absorption opacity and ρ the mass density at a source location \mathbf{r}_1) along a line in the direction (θ, ϕ) up to the scatterer at \mathbf{r} (the quantity l is the distance between \mathbf{r}_1 and \mathbf{r}):

$$I(\mathbf{r}, \theta, \phi) = \int_0^\infty \kappa_{abs}(\mathbf{r}_1) \frac{2\nu^2 k T(\mathbf{r}_1)}{c^2} \rho(\mathbf{r}_1) dl, \quad (2.2)$$

where we have assumed that the photon energy $h\nu$ is substantially less than kT so that the Rayleigh-Jeans law $B_\nu(T) = 2\nu^2 k T / c^2$ is applicable; we have checked that, for the HL Tau model to be discussed below in § 2.2.3, the results will not change significantly if the Planck function is used instead.

Substituting the above expression for $I(\mathbf{r}, \theta, \phi)$ into Eq.(2.1) and reorder the integrals, we can rewrite the source function for the scattered radiation into:

$$S_{s,z'} = \frac{2\nu^2 k}{c^2 \sigma_s} \int_0^{2\pi} d\phi \int_0^\infty dl \int_0^\pi d\theta \frac{d\sigma}{d\Omega} \kappa_{abs}(\mathbf{r}_1) \rho(\mathbf{r}_1) T(\mathbf{r}_1) \sin \theta \equiv S_0 + S_\infty, \quad (2.3)$$

where

$$S_0 \equiv \frac{2\nu^2 k}{c^2 \sigma_s} \int_0^{2\pi} d\phi \int_0^H dl \int_0^\pi d\theta \frac{d\sigma}{d\Omega} \kappa_{abs}(\mathbf{r}_1) \rho(\mathbf{r}_1) T(\mathbf{r}_1) \sin \theta, \quad (2.4)$$

and

$$S_\infty \equiv \frac{2\nu^2 k}{c^2 \sigma_s} \int_0^{2\pi} d\phi \int_H^\infty dl \int_0^\pi d\theta \frac{d\sigma}{d\Omega} \kappa_{abs}(\mathbf{r}_1) \rho(\mathbf{r}_1) T(\mathbf{r}_1) \sin \theta. \quad (2.5)$$

The two quantities, S_0 and S_∞ , denote the contributions to the unpolarized incoming

radiation to be scattered at the location \mathbf{r} from two conceptually distinct regions respectively. For a geometrically thin dust disk, the unpolarized radiation coming from a region within a distance on the order of the local (dust) scale height H is expected to be more or less isotropic. This near-field contribution, denoted by S_0 , produces little polarized radiation after scattering; it will be discussed in the next section, together with the unpolarized direct dust emission. In contrast, the thermal dust emission coming from well outside this local region (i.e., $l \gg H$) is mostly confined close to the disk plane. This far-field contribution, denoted by S_∞ , is highly anisotropic, with the bulk of the radiation beamed into a narrow range of polar angle near $\theta = \pi/2$ along any azimuthal direction ϕ . Specifically, the vertical column of disk material passing through the source location \mathbf{r}_1 at a distance l from the scatterer contributes radiation only within a range of polar angle $\delta\theta \sim 2H(\mathbf{r}_1)/l \ll 1$, where $H(\mathbf{r}_1)$ is the (dust) scale height at \mathbf{r}_1 . Replacing the integral over angle θ in the expression for S_∞ (eq. (2.5)) by this rough estimate and making use of $\theta \approx \pi/2$, we have approximately

$$S_\infty \approx \frac{2\nu^2 k \kappa_{abs}}{c^2 \sigma_s} \int_0^{2\pi} d\phi \frac{d\sigma}{d\Omega} \Lambda(\mathbf{r}, \phi), \quad (2.6)$$

where we have assumed a spatially constant absorption opacity κ_{abs} for simplicity. The auxiliary quantity $\Lambda(\mathbf{r}, \phi)$ is a line integral along the direction of constant ϕ in the disk plane defined as

$$\Lambda(\mathbf{r}, \phi) \equiv \int_H^\infty dl \frac{\Sigma(\mathbf{r}_1) T(\mathbf{r}_1)}{l}, \quad (2.7)$$

where $\Sigma(\mathbf{r}_1) = 2\rho(\mathbf{r}_1)H(\mathbf{r}_1)$ is the column density at the source location \mathbf{r}_1 .

One can determine the distance between the source location \mathbf{r}_1 and the center of

the disk through

$$r_l = \sqrt{r^2 + l^2 - 2rl \cos(\phi - \phi_{\mathbf{r}})}, \quad (2.8)$$

where r and $\phi_{\mathbf{r}}$ are the radius and azimuthal angle of the scatterer in an (x, y, z) coordinate system that centers on the star (rather than the scatterer at \mathbf{r}). For the axisymmetric disk that we will consider below, the radius r_l uniquely determines the column density Σ and temperature T that appear in eq.(2.7).

Once the integral $\Lambda(\mathbf{r}, \phi)$ is computed, the only term that is left to determine in eq.(2.6) is the differential cross section for scattering $d\sigma/d\Omega$. For illustrative purposes, we will consider the dust scattering under the Rayleigh approximation, which is valid when the grain sizes are smaller than the wavelength divided by 2π (see, e.g., Fig. 10 of Canovas et al. 2013 and Fig. 2.6 below); we will check in § 2.4.1 that this condition is satisfied for the HL Tau model to be discussed in the next section. In this limit, the differential cross section is given by

$$\frac{d\sigma}{d\Omega} = \frac{3\sigma_s}{16\pi} (1 + \cos^2 \theta_s), \quad (2.9)$$

where θ_s is the scattering angle between the incoming radiation along the direction (θ, ϕ) and the outgoing radiation along the line of sight (i.e., the z' -axis), given by

$$\cos \theta_s = \sin i \cos \phi. \quad (2.10)$$

After scattering, a fraction of the initially unpolarized incoming radiation becomes polarized. The polarization fraction is

$$p = \frac{1 - \cos^2 \theta_s}{1 + \cos^2 \theta_s}, \quad (2.11)$$

which peaks at $\theta_s = \pi/2$.

The polarization direction is perpendicular to the scattering plane formed by the incoming direction (θ, ϕ) and the z' -axis. It lies in the x' - y' plane of the sky, at an angle $\phi' + \pi/2$ measured counter-clockwise from the x' -axis, with the angle ϕ' given by

$$\cos \phi' = \frac{\cos i \cos \phi}{\sqrt{\sin^2 \phi + \cos^2 i \cos^2 \phi}}. \quad (2.12)$$

This linearly polarized radiation is the source of the observed polarized radiation in the plane of the sky, through the source functions for the Stokes parameter Q and U :

$$S_{Q,\infty} \approx -\frac{2\nu^2 k \kappa_{abs}}{c^2 \sigma_s} \int_0^{2\pi} d\phi \frac{d\sigma(\theta_s)}{d\Omega} \Lambda(\mathbf{r}, \phi) p(\theta_s) \cos(2\phi'), \quad (2.13)$$

and

$$S_{U,\infty} \approx -\frac{2\nu^2 k \kappa_{abs}}{c^2 \sigma_s} \int_0^{2\pi} d\phi \frac{d\sigma(\theta_s)}{d\Omega} \Lambda(\mathbf{r}, \phi) p(\theta_s) \sin(2\phi'). \quad (2.14)$$

For the optically thin radiation that we are considering, Q and U along the line of sight passing through any location \mathbf{r} in the disk is simply given by their respective source functions, multiplied by the optical depth for scattering $\Delta\tau_s \approx \kappa_{sca} \Sigma(\mathbf{r}) / \cos i$ (where κ_{sca} is the scattering opacity) through the disk: $Q = S_{Q,\infty} \Delta\tau_s$ and $U = S_{U,\infty} \Delta\tau_s$.

2.2.2 Inclination-Induced Polarization

As a simple illustration of polarization from scattered light induced by disk inclination, we consider the limiting case where the incoming radiation field seen by the scatterer at the location \mathbf{r} is confined to an infinitely thin disk plane (so that the near-field contribution to the scattering source function, S_0 , can be ignored compared to the far-field contribution S_∞) and is isotropic in the azimuthal (ϕ) direction (but highly anisotropic in polar angle θ). In this case, the integral $\Lambda(\mathbf{r}, \phi)$ defined

in eq. (2.7) is independent of ϕ and can be moved outside the integral over ϕ in the source functions for the total scattered intensity I_s (eq. (2.6)), Q (eq. (2.13)) and U (eq. (2.14)), so that

$$\begin{aligned} S_\infty &= \frac{2\nu^2 k \kappa_{abs} \Lambda}{c^2} \int_0^{2\pi} d\phi \frac{3}{16\pi} (1 + \sin^2 i \cos^2 \phi) \\ &= C \int_0^{2\pi} d\phi (1 + \sin^2 i \cos^2 \phi) = \pi C (2 + \sin^2 i), \end{aligned} \quad (2.15)$$

where $C = 3\nu^2 k \kappa_{abs} \Lambda / (8\pi c^2)$ is a constant independent of the angles i and ϕ , and

$$S_{Q,\infty} = -C \int_0^{2\pi} d\phi (1 - \sin^2 i \cos^2 \phi) \frac{\cos^2 \phi \cos^2 i - \sin^2 \phi}{\cos^2 \phi \cos^2 i + \sin^2 \phi} = \pi C \sin^2 i, \quad (2.16)$$

$$S_{U,\infty} = -C \int_0^{2\pi} d\phi (1 - \sin^2 i \cos^2 \phi) \frac{\cos i \sin(2\phi)}{\cos^2 \phi \cos^2 i + \sin^2 \phi} = 0. \quad (2.17)$$

The fact that $S_{U,\infty}$ is zero and $S_{Q,\infty}$ is positive (for $i \neq 0$) means that the inclination-induced polarization is always along the x' -axis (or the minor axis of the disk) in the plane of the sky for Rayleigh scattering (see eq. (2.23) below for the relation between the Stokes parameters Q and U , and polarization angle α). This is expected physically because, in a tilted disk, the light coming from different directions in the disk plane will be scattered by different angles toward the observer. In particular, the light coming from a direction along the major axis will always be scattered by $\pi/2$. In the Rayleigh limit, this part of the light will be fully polarized along the minor axis of the disk. In contrast, the light coming from a direction along the minor axis will be scattered by either $\pi/2 - i$ or $\pi/2 + i$. This part of the light will be partially polarized along the major axis, with a polarization fraction of $\cos^2 i / (1 + \sin^2 i)$. The difference in the fraction of polarization leads to more scattered light polarized along the minor axis than along the major axis, despite the fact that the scattering cross

section is less for the former than the latter (see eq. (2.9)). This generic tendency for the inclination-induced polarization to align with the minor axis provides a natural explanation for the polarization directions observed in HL Tau (see Fig. 2.1).

It is easy to determine the fraction of the total scattered light that is polarized along the minor axis:

$$p_s(i) \equiv \frac{\sqrt{Q^2 + U^2}}{I_s} = \frac{\sqrt{S_{Q,\infty}^2 + S_{U,\infty}^2}}{S_\infty} = \frac{\sin^2 i}{2 + \sin^2 i}. \quad (2.18)$$

This same expression can be obtained if one considers only the radiation coming from directions along the major and minor axes. Note that the maximum degree of polarization reaches 1/3 when the disk is viewed edge-on ($i = 90^\circ$). For the inclination angle $i = 0^\circ, 30^\circ, 45^\circ$ and 60° to be considered in the next subsection, the fractional polarization is $p_s = 0, 1/9, 1/5,$ and $3/11,$ respectively. The analytically obtained polarization fraction in this simple limiting case will be used to interpret the results obtained numerically in more general cases.

2.2.3 Intrinsic Polarization from Azimuthally Anisotropic Radiation: an Example

As emphasized by Kataoka et al. (2015), the radiation field in the disk plane is not isotropic in general, and the anisotropy in the azimuthal (ϕ) direction leads to polarized scattered light even in the face-on case. In a tilted disk, the observed polarization pattern is expected to be shaped by the interplay between those produced by anisotropy in ϕ -direction and disk inclination (which relies on strong anisotropy in θ direction). To illustrate this interplay, we adopt Kwon et al. (2011) model of the HL Tau disk, where the distributions of temperature and column density as a

function of the cylindrical radius R are parametrized as

$$T = T_0 \left(\frac{R}{R_c} \right)^{-q}, \quad (2.19)$$

$$\Sigma = \Sigma_0 \left(\frac{R}{R_c} \right)^{3/2-p-q/2} \exp \left[- \left(\frac{R}{R_c} \right)^{7/2-p-q/2} \right], \quad (2.20)$$

where R_c is a characteristic disk radius beyond which the column density drops off exponentially, and p is an exponent that, together with the exponent q , controls the column density distribution; it is not to be confused with the polarization fraction.

The temperature profile yields a thermal scale height for the gas

$$H = H_0 \left(\frac{R}{R_c} \right)^{3/2-q/2}. \quad (2.21)$$

Although higher resolution ALMA observations have revealed substructures (rings) on the disk (ALMA Partnership et al. 2015), the above is still the best model at the CARMA resolution that was used to detect the polarization in HL Tau. Adopting $q = 0.43$, Kwon et al. found a set of parameters that best fit their CARMA observations at 1.3 and 2.7 mm: $R_c \approx 79$ AU, $p \approx 1$, and a scale height for gas at R_c of $H_0 \approx 16.8$ AU (see also Kwon et al. 2015). Since the relatively large grains responsible for the scattered radiation may settle toward the midplane, the scaling factor H_0 in eq.(2.21) may need to be reduced by some (potentially large) factor (Kwon et al. 2011). We have experimented with reduction factors of 1, 10, 50 and 100, and found very similar results. In what follows, we will focus on the case where the scale height is the same for the dust and gas.

With the disk structure specified, we can now compute the Stokes parameters Q , U and $I_{s,\infty}$ from their source functions given by eqs. (2.13), (2.14) and (2.6). In this

section, we consider the contribution $I_{s,\infty}$ to the total observed intensity from the far-field scattering source function S_∞ only, in order to facilitate comparison with the analytic results obtained in the preceding subsection; the contributions from S_0 and direct dust emission would lower the polarization fraction, and will be considered in the next section. From these three Stokes parameters, we can determine the total intensity of the polarized radiation

$$I_p = \sqrt{Q^2 + U^2}, \quad (2.22)$$

the polarization angle α (measured counter-clockwise from the x' -axis in the plane of the sky)

$$\alpha = \frac{1}{2} \text{atan2} \left(\frac{U}{Q} \right), \quad (2.23)$$

where the function `atan2` returns the appropriate quadrant of the computed angle based on the signs of Q and U , and the polarization fraction

$$p_{s,\infty} = \frac{I_p}{I_{s,\infty}}, \quad (2.24)$$

which can be compared directly with that given analytically in eq. (2.18).

In Fig. 2.2, we show the polarization vectors and the spatial distribution of the polarized intensity I_p for $i = 0^\circ, 30^\circ, 45^\circ$, and 60° . The intensity is measured in units of $2\Sigma_0^2\kappa_{abs}\kappa_{sca}\nu^2kT_0/c^2$, where Σ_0 and T_0 are the characteristic column density and temperature of the disk, and κ_{abs} and κ_{sca} the absorption and scattering opacity. In the face-on ($i = 0^\circ$) case, the fraction of polarization of the scattered light is zero at the center because the light to be scattered there comes isotropically along all azimuthal directions for the prescribed axisymmetric disk. The radiation seen by the scatterer becomes more and more beamed in the radial direction as the radius

increases, because of the drop in temperature and column density. As a result, the light is polarized in the azimuthal direction and the polarization degree increases outward. We will refer to the polarization induced by anisotropic radiation in the azimuthal direction in the face-on case as the “intrinsic” polarization. Note that although the polarization fraction $p_{s,\infty}$ can reach a value as high as 50% or more near the outer edge, the total scattered polarized intensity I_p is rather low. As a result, the intrinsic polarization from dust scattering can be easily modified, indeed dominated, by the inclination-induced polarization.

When the disk is tilted away from the line of sight, both the polarized intensity and orientations of the polarization vectors change drastically compared to the face-on case. As Fig. 2.2 shows, the polarized intensity peaks at a ring in the face-on case, with the inward decrease caused by radiation becoming more isotropic in the azimuthal direction and the outward decrease from the exponential drop-off in column density. In contrast, the polarized intensity in the $i = 30^\circ$ case peaks in the central region, as a result of the inclination-induced polarization. The polarization vectors in this (central) region (within $\sim 0.5 R_c$ of the origin) lie more or less along the minor axis, consistent with the analytic results for the inclination-induced polarization derived in the last subsection. Outside the central region, the polarization directions are broadly similar to those in the face-on case, indicating that the intrinsic polarization remains important there. A difference is that the axisymmetric polarization pattern in the face-on case becomes highly non-axisymmetric in this moderately tilted case, with both the polarized intensity and the polarization fraction significantly higher along the major axis than along the minor axis.

As the disk tilt angle increases further, the polarization pattern becomes more dominated by that induced by inclination. Going from $i = 30^\circ$ to 45° to 60° , we see

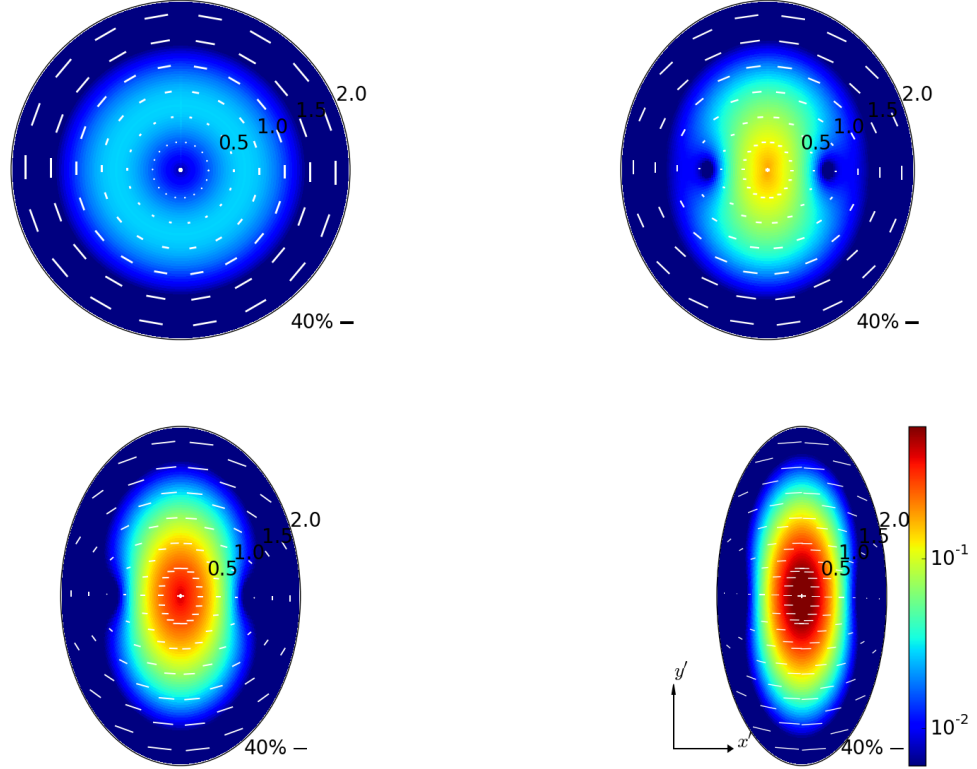


Fig. 2.2.— Effects of disk inclination on the polarization of scattered millimeter radiation. Shown are the intensity of the polarized radiation (color map, in units of $2\Sigma_0^2\kappa_{abs}\kappa_{sca}\nu^2kT_0/c^2$) and polarization vectors (line segments, with length proportional to the polarization fraction $p_{s,\infty}$ defined in eq.(2.24)), for $i = 0^\circ, 30^\circ, 45^\circ$ and 60° . As the disk becomes more tilted, both the polarized intensity and polarization directions become more dominated by those induced by inclination. The elongation of the polarized intensity along the major axis and orientations of the polarization vectors along the minor axis in the high intensity region in the inclined cases are broadly consistent with the observed pattern in HL Tau (see Fig. 2.1). The numbers 0.5, 1.0, 1.5 and 2.0 in each panel measure the de-projected distances from the center in units of the characteristic radius R_c . The x' -axis and y' -axis defined in the plane of the sky are shown in the lower-right panel for reference.

a clear trend for increasing polarized intensity in the central region, a larger fraction of the polarization vectors parallel to the minor axis, and more elongation of the polarized intensity along the major axis (see Fig. 2.2). The elongation is a generic feature of the interplay between the intrinsic polarization and inclination-induced polarization. It provides a natural explanation for the distribution of polarized intensity observed in HL Tau², which has an inclination angle of $i \sim 45^\circ$ (ALMA Partnership et al. 2015; Kwon et al. 2011).

2.2.4 Interplay Between Intrinsic and Inclination-Induced Polarization

To understand the interplay between the intrinsic polarization and inclination-induced polarization more quantitatively, we plot in Figure 2.3 the distribution of a dimensionless quantity

$$p_Q \equiv \frac{Q}{I_{s,\infty}} \quad (2.25)$$

along the major and minor axes for the $i = 45^\circ$ case. Since $U = 0$ along the major and minor axes, this quantity is essentially the polarization fraction $p_{s,\infty}$ defined in eq.(2.24), except that it retains the sign of the Stokes parameter Q . A positive (negative) p_Q means that the polarization is along the x' -axis (y' -axis) in the plane of the sky.

In the face-on case ($i = 0^\circ$), the intrinsic polarization fraction increases monotonically from zero to a large value approaching unity as the distance from the origin increases along the major (or y' -) axis, with the polarization vectors parallel to the

²The observed direction of elongation does not lie exactly along the major axis, but is offset by a small angle of $\sim 10^\circ$ (see Stephens et al. (2014) and Fig. 2.1). This offset is not explained in our model under thin-disk approximation, and may require full 3D models and/or additional physics, such as grain alignment.

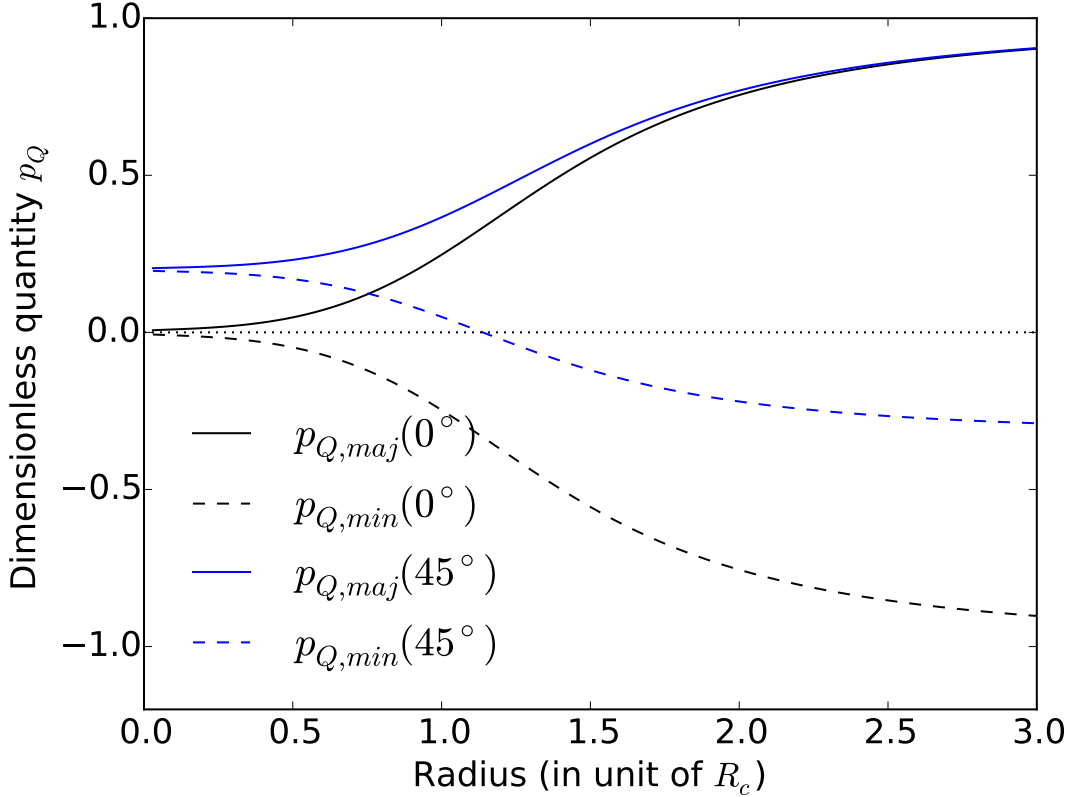


Fig. 2.3.— Dimensionless quantity p_Q defined in eq. (2.25). Plotted are the distributions of p_Q along the major and minor axes, denoted by the subscript “maj” and “min” respectively, as a function of de-projected distance from the origin for the face-on $i = 0^\circ$ case (solid and dashed black) and the $i = 45^\circ$ case (solid and dashed blue). Its polarization fraction $|p_Q|$ approaches 20% in the central region and, at larger distances from the origin, is substantially larger along the major axis than along the minor axis.

x' -axis in the plane of the sky. The quantity p_Q is thus positive, as shown in Fig. 2.3 (solid black line). Along the minor axis, the fractional polarization is the same, but the polarization direction is along the y' -axis, with a negative p_Q (dashed black line). For comparison, we plot in the same figure the numerically computed distribution of p_Q along the major and minor axes as a function of the (de-projected) distance from the origin for the $i = 45^\circ$ case. Clearly, the inclination has shifted the curves for the

intrinsic ($i = 0^\circ$) p_Q along both major and minor axes upward, which is not surprising since inclination tends to produce polarization along the x' -direction (corresponding to a positive Q , see eq.2.16). The amount of upward shift is different at different locations, however. In the central region where the intrinsic polarization fraction is relatively low (within about $0.5 R_c$), the shift is by ~ 0.2 along both the major and minor axes; it is the value expected from the analytic results for an azimuthally isotropic radiation field given in eq. (2.18). The behavior in the central region where the intrinsic polarization is weak is therefore easy to understand; it is dominated by the inclination-induced polarization.

The behavior outside the central region where the intrinsic polarization fraction is higher is more complicated. It can be reproduced exactly, however, by the formula

$$p_Q = \frac{\sin^2 i}{2 + \sin^2 i} + \frac{p_{Q,in}}{(1 + \sin^2 i/2)[1 + (1 - p_{Q,in}) \sin^2 i/2]}, \quad (2.26)$$

along both the major and minor axes. Note that the first term on the right hand side is simply the inclination-induced polarization given by eq. (2.18), and the second term is the intrinsic polarization fraction $p_{Q,in}$ (the face-on case) modified by the inclination. This formula can be derived heuristically under the assumption that the radiation seen by the scatterer comes from only two directions: the x - and y -axes in the disk plane.

In the limit where the intrinsic polarization fraction $|p_{Q,in}| \rightarrow 0$, we have

$$p_Q \rightarrow \frac{\sin^2 i}{2 + \sin^2 i}. \quad (2.27)$$

In the opposite limit where the intrinsic polarization fraction $|p_{Q,in}| \rightarrow 1$, we need to consider the major and minor axes separately. Along the major axis where p_Q is

positive, we have $p_{Q,in} \rightarrow 1$, which yields

$$p_Q \rightarrow 1. \quad (2.28)$$

Along the minor axis where p_Q is negative, we have $p_{Q,in} \rightarrow -1$, so that

$$p_Q \rightarrow -\frac{1 - \sin^2 i}{1 + \sin^2 i}, \quad (2.29)$$

which, for $i = 45^\circ$ shown in Fig. 2.3, approaches $-1/3$. The difference in the asymptotic behavior of p_Q , particularly the polarization fraction $|p_Q|$, highlights one of the major differences between the polarization patterns along the major and minor axes. It becomes more extreme as the inclination angle i approaches 90° .

Another difference is that there exists a point of zero polarization on the minor axis across which p_Q changes sign (or the polarization direction changes by 90°). This null point occurs at a location where

$$p_{Q,in} = -\frac{\sin^2 i}{2 - \sin^2 i}, \quad (2.30)$$

which has a value of $-1/3$ for $i = 45^\circ$. Indeed, if the inclination angle i is known independently, one can in principle deduce the intrinsic value of p_Q along the major and minor axes from the value of $p_{Q,in}$ through

$$p_{Q,in} = \frac{p_Q - \sin^2 i / (2 + \sin^2 i)}{[(2 - \sin^2 i) + p_Q \sin^2 i] / (2 + \sin^2 i)}. \quad (2.31)$$

However, it is difficult to infer the value of p_Q from observation directly because it is the observed Stokes Q parameter normalized by the scattered intensity from the far-field, $I_{s,\infty}$, which cannot be measured directly. What can be measured is the total

intensity, which we discuss next.

2.3 Total Intensity and Polarization Fraction

The total intensity I of the radiation along the line of sight is the sum of the direct dust emission I_d , the scattered radiation from near-field $I_{s,0}$, and the scattered radiation from far-field $I_{s,\infty}$. The source function for the near-field contribution at a location \mathbf{r} inside the disk can be estimated approximately assuming isotropic incoming radiation from within a uniform sphere of radius H , the local scale height:

$$S_0 \approx \frac{\nu^2 k \kappa_{abs} \Sigma(\mathbf{r}) T(\mathbf{r})}{c^2}, \quad (2.32)$$

which is multiplied by the scattering optical depth $\Delta\tau_s \approx \kappa_{sca} \Sigma(\mathbf{r}) / \cos i$ to yield the intensity

$$I_{s,0} \approx \frac{\nu^2 k \kappa_{abs} \kappa_{sca} \Sigma^2(\mathbf{r}) T(\mathbf{r})}{c^2 \cos i}. \quad (2.33)$$

For the HL Tau disk model discussed in § 2.2.3, the intensity of the scattered radiation $I_{s,0}$ from the near-field is weaker than that from the far-field $I_{s,\infty}$ everywhere for $i = 45^\circ$, as can be seen from Fig. 2.4, where the ratio of the two is plotted. The ratio peaks in a ring between $\sim 0.5R_c$ and $\sim 1R_c$ (where R_c is the characteristic radius of the disk), with a maximum value of $\sim 60\%$. Near the peak, the unpolarized scattering intensity $I_{s,0}$ reduces the polarization fraction by a factor of ~ 1.6 , from $\sim 20\%$ to $\sim 12\%$. Going outward from the ring, the ratio drops rapidly because the near-field intensity $I_{s,0}$ is determined by the local column density, which drops off exponentially with radius, whereas the far-field intensity $I_{s,\infty}$ is determined globally, including contributions from the bright central region that decrease with radius more slowly than exponential. Inside the ring, the ratio decreases with decreasing radius

because of a smaller scale height H , which decreases the size of the region where the incoming radiation for the near-field source function S_0 comes from relative to that for the far-field source function S_∞ . In any case, the polarization fraction of the scattered radiation remains high, of order 10% or more, after both the near- and far-field contributions are taken into account. It is much higher than observed in HL Tau (of order 1%), and needs to be further reduced, by the unpolarized direct dust emission³.

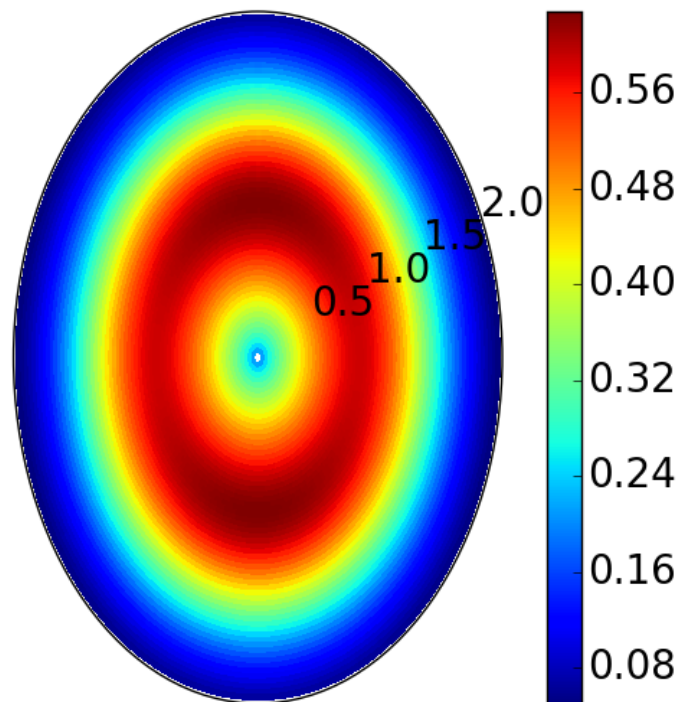


Fig. 2.4.— Ratio of the near-field and far-field contributions to the intensity of the scattered radiation, $I_{s,0}/I_{s,\infty}$, for the $i = 45^\circ$ case. The far-field contribution $I_{s,\infty}$ dominates the near-field contribution $I_{s,0}$ everywhere, especially in the central region and near the outer edge.

³Direct emission can be polarized, due to, for example, grain alignment. Polarized direct emission needs to be included in a more complete model (as discussed in § 2.6).

The source function for the direct emission is simply the Planck function $B_\nu(T) \approx 2\nu^2 kT/c^2$. The optical depth for dust absorption along the line of sight passing through a location \mathbf{r} in the disk is $\Delta\tau_a \approx \kappa_{abs}\Sigma(\mathbf{r})/\cos i$ under the thin disk approximation. Together, they yield the intensity for the direct emission

$$I_d \approx \frac{2\nu^2 k \kappa_{abs} \Sigma(\mathbf{r}) T(\mathbf{r})}{c^2 \cos i}. \quad (2.34)$$

This estimate allows us to evaluate the ratio of the intensities of the scattered and direct emission:

$$\begin{aligned} \frac{I_s}{I_d} &= \frac{I_{s,0} + I_{s,\infty}}{I_d} \\ &\approx \kappa_{sca} \Sigma_0 \frac{\Sigma(\mathbf{r})}{\Sigma_0} \left[\frac{1}{2} + \frac{3}{16\pi} \int_0^{2\pi} d\phi (1 + \sin^2 i \cos^2 \phi) \int_H^\infty \frac{dl}{l} \frac{\Sigma(\mathbf{r}_l) T(\mathbf{r}_l)}{\Sigma(\mathbf{r}) T(\mathbf{r})} \right]. \end{aligned} \quad (2.35)$$

Note that the ratio $\Sigma(\mathbf{r})/\Sigma_0$ and the second term inside the square bracket are dimensionless quantities that depend only on the shape of the column density and temperature profiles. The overall scaling is set by the characteristic scattering optical depth $\Delta\tau_{s,c} = \kappa_{sca}\Sigma_0$. In order to reduce the high polarization fraction of the scattered radiation at 1.3 mm to the observed value of about 1%, we need a rather small value of $\Delta\tau_{s,c} \approx 0.07$, so that the scattered radiation is heavily diluted by the unpolarized direct emission.

We stress that the inclusion of the unpolarized radiation $I_{s,0}$ and I_d changes neither the polarized intensity nor the polarization direction shown in Fig. 2.2 (the lower-left panel). What is changed is the polarization fraction. In Fig. 2.5, we plot the distribution of the polarized intensity for the $i = 45^\circ$ case, as in the lower-left panel of Fig. 2.2, but with the length of the overlaid polarization vectors scaled by the new polarization fraction (relative to the total intensity). This figure represents our

final model for the HL Tau disk. It has three features that are broadly consistent with observations: (1) the region of high polarized intensity is elongated along the major axis, (2) the polarization vectors in this region are nearly parallel to the minor axis, and (3) the polarization fraction in the region is about 1%. Along the ridge of detectable polarized intensity, the observed polarization fraction appears to be somewhat higher toward the edge of the disk (at a distance of $\sim R_C \approx 80$ AU) than near the center, although it is unclear how significant the trend is in view of the low polarized intensity near the edge. This trend was present in our model when only the scattered radiation was considered (see Fig. 2.2 and 2.3), but was washed out by the total intensity in Fig. 2.5.

The semi-analytic theory that we have developed so far under the assumption of geometrically thin disk, optically thin emission, and only Rayleigh scattering is independent of the detailed properties of dust grains. This independence makes the broad agreement between our model and the main polarization features observed in HL Tau rather robust. In the next section, we will try to put constraints on the grain size distribution in the HL Tau disk, which is much more uncertain.

2.4 Implications for Grain Size

2.4.1 Scattering Opacity and the Need for Large Grains

The main free parameter of the final model for the HL Tau disk polarization discussed in § 2.3 is the characteristic scattering optical depth $\Delta\tau_{s,c}$, which controls the polarization fraction. In order to produce the observed polarization fraction of $\sim 1\%$, a value of $\Delta\tau_{s,c} \approx 0.07$ is required. This value yields a scattering opacity $\kappa_{sca} \approx 10^{-3} \text{ cm}^2 \text{ g}^{-1}$ (cross section per unit total, rather than dust, mass) at 1.3 mm

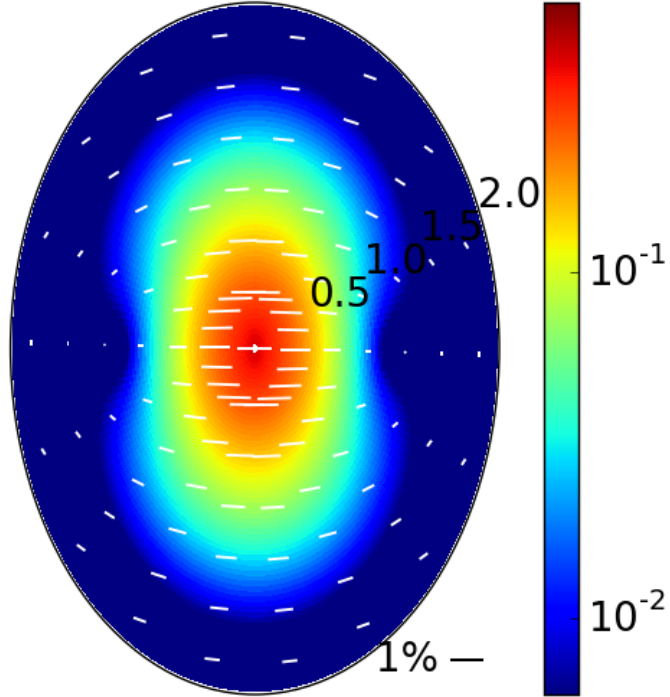


Fig. 2.5.— Model for the polarization of HL Tau disk. Plotted are the polarized intensity (color map, in units of $2\Sigma_0^2\kappa_{abs}\kappa_{sca}\nu^2kT_0/c^2$) and polarization vectors (line segments, with length proportional to the polarization fraction of the total intensity) for $i = 45^\circ$. A characteristic scattering optical depth $\Delta\tau_{s,c} \approx 0.07$ is needed to bring the high polarization fraction of tens of percent relative to the scattered intensity (shown in the lower-left panel of Fig. 2.2) down to the observed level of $\sim 1\%$ relative to the total intensity.

(the wavelength of the HL Tau disk polarization observation), using the characteristic column density $\Sigma_0 = 68 \text{ g cm}^{-2}$ from the best-fit disk mass of $0.13 M_\odot$ of Kwon et al. (2011). This scattering opacity can put constraints on the grain size distribution, although they depend on the dust composition, which is uncertain. As an illustration, we consider the model of dust grains adopted by Kataoka et al. (2015), which are spheres with a mixture of silicate (8%), water ice (62%) and organics (30%). All

fractional abundances are in volume and are taken from Pollack et al. (1994). We assume a canonical gas-to-dust mass ratio of 100, and use the Mie theory to calculate the absorption and scattering opacities (Bohren & Huffman 1983). The inferred scattering opacity corresponds to a grain radius $a = 37 \mu\text{m}$ for grains of a single size. For the MRN-type power-law distribution $n(a) \propto a^{-3.5}$ (Mathis et al. 1977), we obtain a maximum grain size of $a_{max} = 72 \mu\text{m}$. The increase of this maximum over the single size case comes from averaging over the grain size. In both cases, the dimensionless parameter $x = 2\pi a/\lambda \ll 1$, so that the Rayleigh limit used for treating the scattering in the previous sections is self-consistent (see Fig. 2.6 below). The maximum size inferred for the grains responsible for the scattered dust emission in the HL Tau disk is much larger than that of the grains in the diffuse interstellar medium. This is consistent with other lines of evidence for grain growth in disk environments (e.g., Pérez et al. 2012; Testi et al. 2014).

We note that Kataoka et al. (2016a) independently modeled the HL Tau disk polarization using dust scattering through Monte Carlo radiative transfer simulations. They obtained disk polarization patterns that are very similar to ours. They inferred a maximum grain size that ranges from $70 \mu\text{m}$ to $350 \mu\text{m}$, which is broadly consistent with our value of $72 \mu\text{m}$.

In summary, to reproduce the $\sim 1\%$ polarization fraction observed in the disk of HL Tau through dust scattering, the grains must have grown to tens of microns (the exact value depends on the assumed grain size distribution and composition). However, this picture is complicated by the opacity spectral index β inferred for HL Tau, as we discuss next.

2.4.2 Opacity Spectral Index β and the Need for Larger Grains?

Kwon et al. (2011) obtained a best-fit value 0.73 for the spectral index β of the dust opacity $\kappa_{abs} \propto \nu^\beta$ for the HL Tau disk based mostly on CARMA observations at 1.3 and 2.7 mm. It is in agreement with the spatially averaged value obtained from ALMA observations from 0.87 to 2.9 mm (ALMA Partnership et al. 2015). This value is significantly lower than the typical ISM value of $\beta \sim 1.5 - 2$. The difference is usually taken as evidence for grain growth to millimeter size or larger (Testi et al. 2014), although other interpretations are possible. For example, Ricci et al. (2012) showed that a value of $\beta \sim 1$ or lower can be obtained without mm/cm sized grains if part of the disk is optically thick. Some support for this possibility is provided by the spatially resolved distribution of β derived from the ALMA data, which shows $\beta \sim 0$ indicative of optically thick emission at the central continuum peak and two rings (B1 and B6, ALMA Partnership et al. 2015, see their Fig. 3). Another possibility is that the index β is sensitive to not only the size but also the shape of the grains. Indeed, Verhoeff et al. (2011) was able to reproduce the spectral energy distribution (SED) of the disk of HD 142527 (with $\beta \sim 1$ in the millimeter regime) with irregular grains of sizes up to only $2.5 \mu\text{m}$; the grain shape was treated with the distribution of hollow spheres Min et al. (2005). The grains inferred in our model of dust scattering-induced polarization for the HL Tau disk have a significantly larger maximum size (of order tens of microns). They may still be able to reproduce the observed (averaged) opacity spectral index of $\beta \sim 0.73$ if the grains are irregular and/or part of the disk is optically thick. Detailed exploration of this possibility is beyond the scope of the present work.

If large, mm/cm sized, grains are responsible for the relatively low value of β observed in the HL Tau disk, it is natural to ask whether they can produce a po-

larization pattern that matches the observed one through scattering. It is unlikely, because the key to producing the observed pattern is the polarization degree of the scattered light peaking near 90° (as in the Rayleigh limit), and this requirement is not satisfied for mm/cm sized grains. For example, for the grain model adopted by Kataoka et al. (2015), the polarization degree (defined as the ratio of the two elements in the scattering matrix, $-Z_{12}/Z_{11}$, which is essentially the polarization fraction but can be either positive or negative) is nearly zero at 0.87 mm for all scattering angles except around 135° , where it reaches a (negative) “peak” value of ~ -0.2 for $a_{max} = 1$ mm and 1 cm (see the right panel of their Fig. 2). The negative value is known as the polarization reversal (e.g., Murakawa 2010; Kirchschrager & Wolf 2014) which, together with the shift of the polarization “peak” away from 90° , is expected to produce a polarization pattern very different from the Rayleigh scattering case.

As an illustration, we repeat the computation of the scattering-induced polarization at $\lambda = 1.3$ mm in § 2.3, but with an MRN-type power-law size distribution up to $a_{max} = 4$ mm (instead of $72 \mu\text{m}$), using the dust model of Kataoka et al. (2015) and Mie theory. The maximum grain size is chosen such that $a_{max} \approx 3\lambda$, which is roughly the minimum value required to yield an opacity spectral index of $\beta \sim 1$ according to Draine (2006). The distribution of the polarization degree with scattering angle in this case is shown in Fig. 2.6. It is very similar to that obtained by Kataoka et al. at 0.87 mm, except that the “peak” is slightly lower (-0.17) and is shifted to a slightly smaller angle of $\sim 130^\circ$.

In Fig. 2.7, we plot the distribution of the polarized intensity together with polarization vectors for the large grain case of $a_{max} = 4$ mm. There are several features that are worth noting. First, unlike the Rayleigh scattering case, the polarized intensity is no longer symmetric with respect to the major axis. This is because large, mm/cm

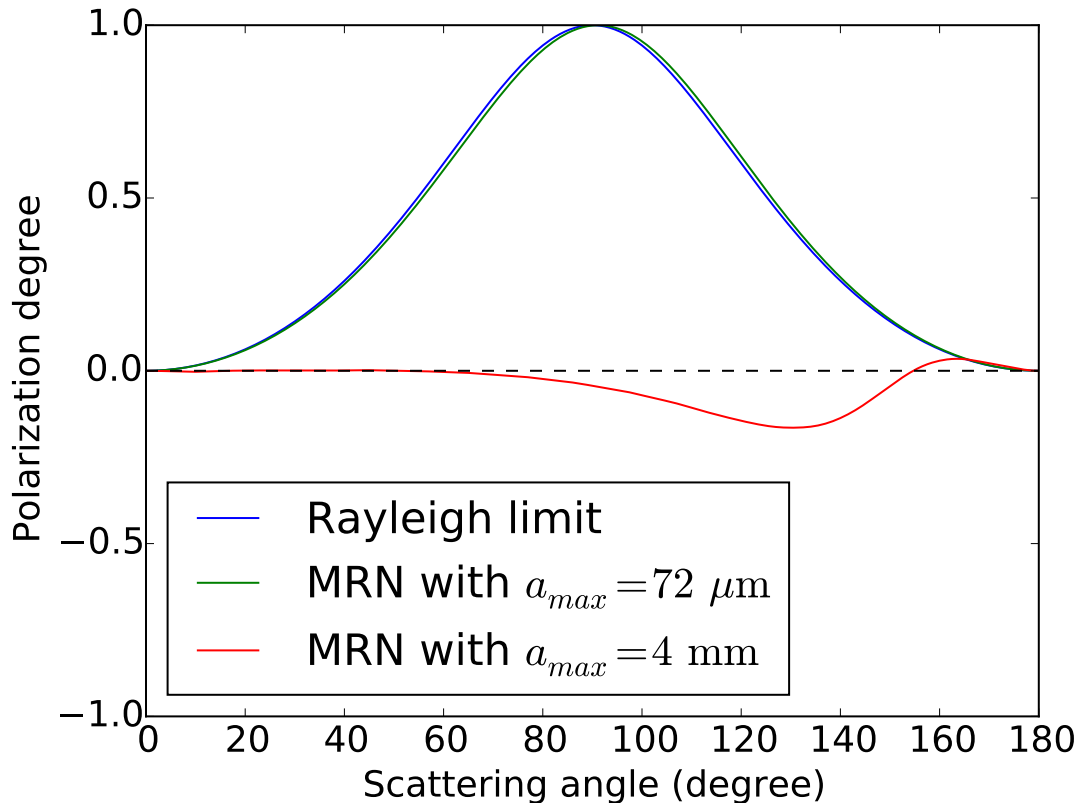


Fig. 2.6.— Comparison of the distributions of the degree of polarization (see text for definition) as a function of scattering angle for three cases: the Rayleigh limit (blue line) and two cases with MRN-like power-law grain size distribution with $a_{max} = 72 \mu\text{m}$ (green) and 4 mm (red). The Rayleigh and $a_{max} = 72 \mu\text{m}$ cases are almost indistinguishable. The negative “peak” around 130° in the $a_{max} = 4 \text{ mm}$ case is an example of the so-called “polarization reversal,” which may provide a way to probe large, mm/cm sized, grains through scattering-induced polarization.

sized, grains preferentially scatter light in the forward direction (e.g., Bohren & Huffman 1983), making the side of the disk closer to the observer (the right half) brighter. The polarization fraction is, however, higher on the far side (especially toward the outer part of the disk) because the polarization degree of the scattered light is higher for backward scattering than for forward scattering (see Fig. 2.6). The most striking difference between this case and the Rayleigh scattering case shown in Fig. 2.5 lies in

the polarization direction. The difference comes from the polarization reversal in the large grain case, which yields an intrinsic (or face-on) polarization direction in the radial (as opposed to azimuthal) direction and an inclination-induced polarization along the major (rather than minor) axis. The interplay between the intrinsic and inclination-induced polarization leads to polarization directions in the region of high polarized intensity (the most easily observable part) completely different from those observed in HL Tau (see Fig. 2.1).

We are therefore left with an interesting conundrum. The polarization pattern in the HL Tau disk is suggestive of Rayleigh scattering by relatively small dust grains (although still much larger than the typical ISM grains), but such grains may have difficulty reproducing the observed opacity spectral index β ($\lesssim 1$). The index can be reproduced more easily with larger, mm/cm sized, grains, but it is difficult to generate the observed polarization pattern with such grains through scattering. It is conceivable that there are two populations of dust grains, with one responsible for polarization, the other for β . The two populations do not have to be located co-spatially in the disk; for example, large grains responsible for the bulk of the unpolarized continuum (and thus β) may have settled close to the midplane, whereas smaller grains that dominate the polarized millimeter radiation may remain floating higher up above the midplane (e.g., Dullemond & Dominik 2004; Tanaka et al. 2005; Balsara et al. 2009). If this speculation turns out to be correct, polarized emission in millimeter would provide a powerful probe of not only grain growth, but also the expected vertical stratification of grain sizes, especially in conjunction with observations of optical/IR polarization, which probe even smaller, micron-sized, grains that are higher up still above the disk midplane.

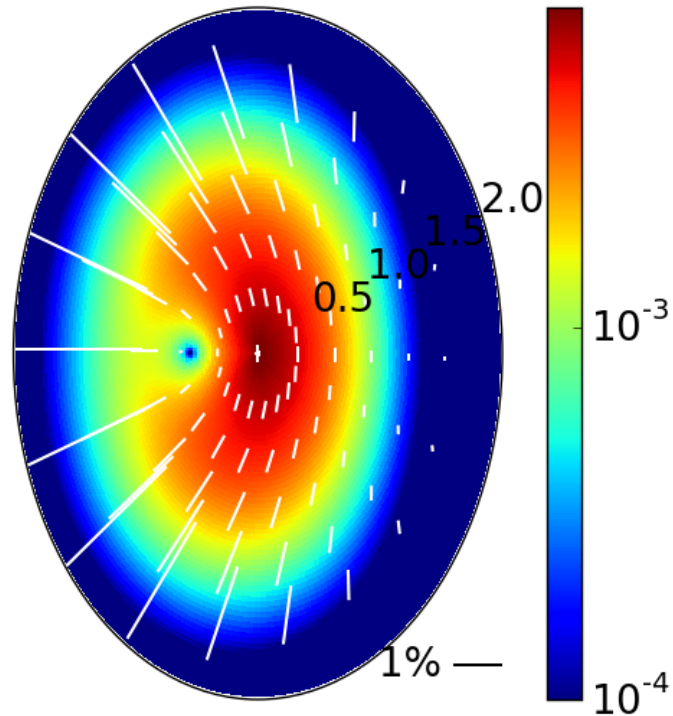


Fig. 2.7.— Scattering-induced polarization by large grains. As in Fig. 2.5, plotted are the polarized intensity (color map) and polarization vectors (line segments, with length proportional to the polarization fraction). Note the strong asymmetric with respect to the major axis in both the polarized intensity and the polarization vectors. The polarization along the major axis in the central region is due to polarization reversal, which may be a robust indicator of scattering by large, mm/cm-sized, grains. The near side of the disk is on the right.

2.5 Polarization from dust scattering in the IM Lup protoplanetary disk

IM Lup is a Class II source that is more evolved than HL Tau. It was classified as weak-line T Tauri star (Finkenzeller & Basri 1987; Martin et al. 1994). Pinte et al. (2008) showed that there is substantial grain growth in the IM Lup disk, up

to millimeter in sizes. These large grains can potentially produce significant polarization according to our theory. In Hull et al. (2018), we used ALMA to observe dust polarization with Band 7 ($870 \mu\text{m}$) toward IM Lup. The full polarization results are shown in Fig. 2.8. The grayscale represents the polarized intensity. The total intensity is represented by the contours. The line segments represent the orientations of polarization, with their lengths proportional to the local polarization degree. The interferometric beam is shown in the lower left corner. Both the scale for polarization degree and the linear spatial scale are shown at the lower right corner, assuming a distance of 161 ± 10 pc (Gaia Collaboration et al. 2016).

We can see that the polarization forms a very uniform pattern oriented along the minor axis of the IM Lup disk. This is very similar to our model prediction (see Fig. 2.5). In order to model this source in detail and get an estimate of the sizes of the dust grains responsible for the observed scattering polarization, we adopted a physical (gas and temperature) model for IM Lup disk model based on Cleeves et al. (2016), who included two grain populations for computing the thermal structure: a (large) millimeter-sized and a (small) micron-sized population. The model is one of a viscous disk (Lynden-Bell & Pringle 1974) with a column density of dust $\Sigma_c = 0.25 \text{ g cm}^{-2}$ at a radius $R_c = 100$ au. The scale height of the millimeter grains is $H_c = 3$ au at R_c , which is $0.25\times$ the scale height of the gas and the micron-sized grains. The surface-density power-law index is set to $\gamma = 1.0$, so that the surface density is roughly inversely proportional to the radius, except near the outer edge where it drops off exponentially. To model the scattering-induced polarization in this disk, we adopted the same dust grain model as described above in § 2.4.1, with an MRN-type power law distribution $n(a) \propto a^{-3.5}$ (Mathis et al. 1977), with a fixed minimum grain size $a_{\text{min}} = 0.25 \mu\text{m}$. The optical properties are calculated with Mie theory (Bohren & Huffman 1983;

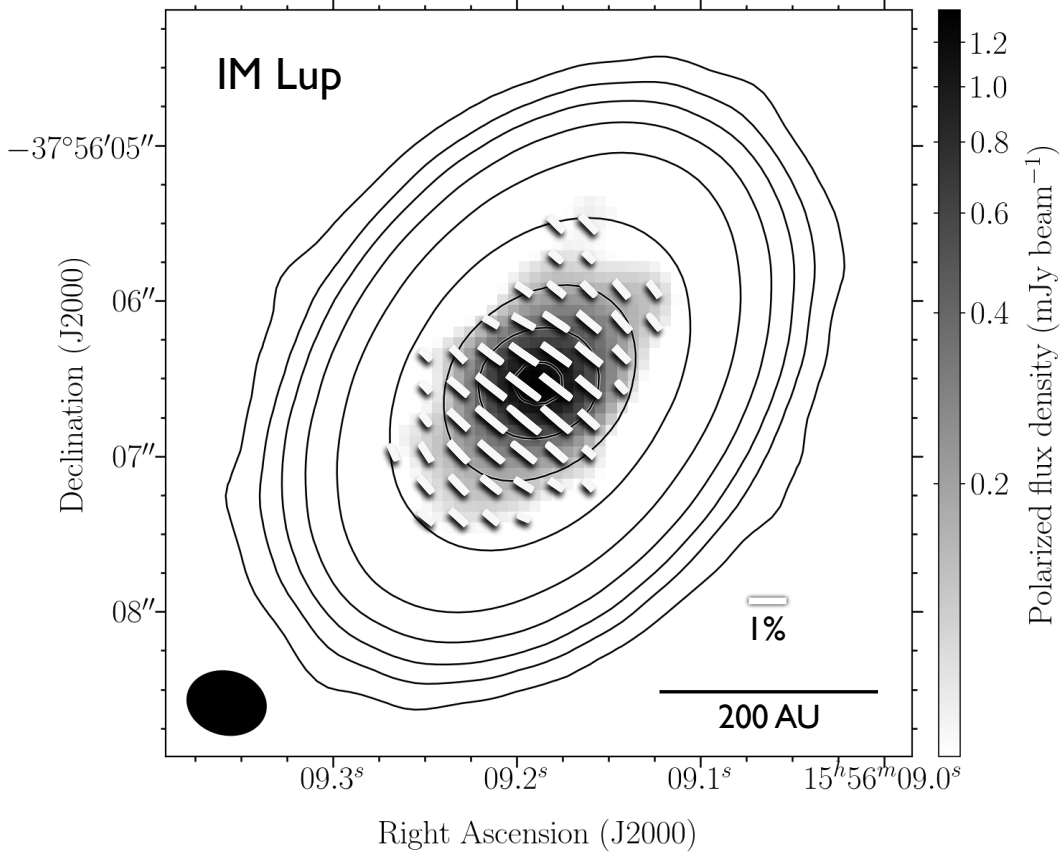


Fig. 2.8.— 870 μm ALMA observations of the Class II protoplanetary disk IM Lup. The grayscale represents the polarized intensity, plotted starting at $3\sigma_P$, with $\sigma_P = 22 \mu\text{Jy beam}^{-1}$. The contours are the total emission, plotted at 3, 8, 16, 32, 64, 128, 512, $1024 \times \sigma_I$, with $\sigma_I = 100 \mu\text{Jy beam}^{-1}$. Line segments represent the orientation and degree of the polarization, with 1% scale shown at the lower right corner. The lower left corner represents the interferometric beam, which measures $0''.50 \times 0''.40$ at a position angle of 76.9° , corresponding to a linear resolution of $\sim 72 \text{ AU}$.

see also App. B). We then use the Monte Carlo Radiative Transfer code RADMC-3D (Dullemond et al. 2012) to calculate the polarization from this disk model with varying maximum grain sizes. We then convolve the fully resolved theoretical model with the interferometric beam applied to the real observation. We found that the observed IM Lup polarization can be best reproduced with $a_{\text{max}} = 61 \mu\text{m}$. The result for this model is shown in Fig. 2.9.

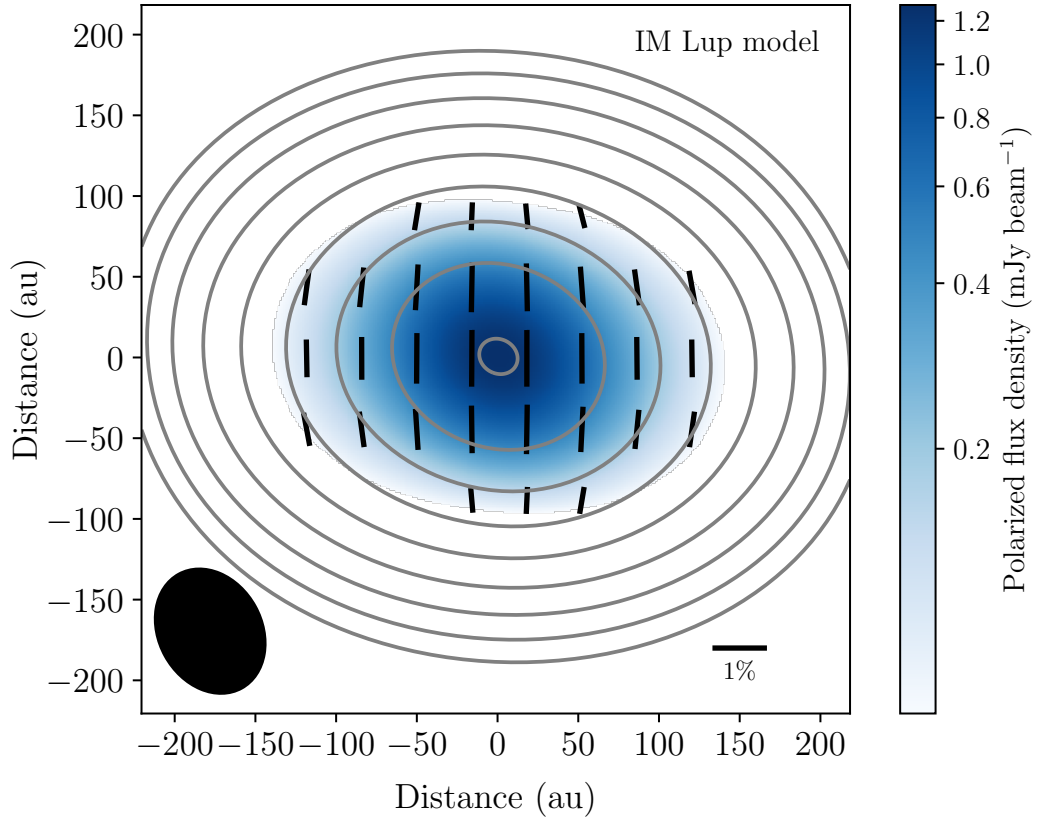


Fig. 2.9.— Best-fit model to the ALMA $870\ \mu\text{m}$ polarization observations of IM Lup. The colormap represents the polarized intensity, plotted starting $3\sigma_P = 66\ \mu\text{Jy beam}^{-1}$. The contours represent the Stokes I, which is logarithmically scaled with a minimum value of $3\sigma_I = 300\ \mu\text{Jy beam}^{-1}$. The line segments represent both the orientation and the degree of polarization.

We can see that our best-fit model (Fig. 2.9) is in good agreement with the observation (Fig. 2.8). To be more specific, (1) the distribution of the polarization orientations is well reproduced (not shown here, see Hull et al. 2018 for more details). (2) The polarized intensity is at the same level as the observation. (3) The polarization degree is in good agreement with the observation in both the peak value of $\sim 1.1\%$, and the dependency on the distance from the center along both major and minor axes (not shown here, see Hull et al. 2018 for more details). The level of agreement adds confidence to the scattering mechanism as an important origin of

the polarization in protoplanetary disks. IM Lup, as a relatively clean system, is an ideal target for further detailed modeling, which can help us understand how different properties of the dust grains, such as their size distribution and shape, affect the polarization signatures.

2.6 Other Sources and Future Directions

As mentioned in § 2.1, spatially resolved polarized sub-mm/mm emission was observed in two other sources besides HL Tau: IRAS 16293-2422B (Rao et al. 2014) and L1527 (Segura-Cox et al. 2015), using SMA and CARMA respectively (at the time of our first paper on the subject, Yang et al. 2016a, on which this Chapter is based). We discuss whether the polarization in these two sources is compatible with an origin in dust scattering.

The L1527 disk is nearly edge-on, with an inclination angle $i \approx 90^\circ$. Its 1.3 mm dust emission was observed to be polarized at $\sim 2.5\%$ level, with a direction roughly perpendicular to the disk (i.e., along the minor axis). This pattern is consistent with that expected from dust grains aligned by a predominantly toroidal magnetic field (Segura-Cox et al. 2015). It is also the pattern expected of scattering by relatively small dust grains in the Rayleigh limit because the polarization induced by disk inclination is along the minor axis (as illustrated vividly in the lower right panel of Fig. 2.2). Indeed, the fraction of the scattered radiation that is polarized due to disk inclination increases with the inclination angle, reaching a maximum value of $1/3$ for edge-on disks, as we showed analytically in § 2.2.2 (see eq. (2.18)). This trend makes it more likely for L1527-like disks to show scattering-induced polarization than face-on disks. Indeed, the median polarization fraction of L1527 is the highest among the three sources with spatially resolved sub-mm/mm polarized emission so

far. However, whether such polarization can actually be observed or not depends on the polarized intensity, which in turn depends on the total intensity and the polarization fraction (relative to the total intensity). The latter is sensitive to the scattering opacity κ_{sca} , which depends on the dust properties, especially the grain size, which can vary greatly from one source to another. To produce the observed polarization fraction of $\sim 2.5\%$ in L1527 through scattering, the grains must have grown well beyond μm size; otherwise, the scattering opacity would be too small. The scattering cannot be dominated by large, mm/cm sized grains either. Such grains would produce polarization along, rather than perpendicular to, the edge-on disk because of polarization reversal (see § 2.4.2 and Figs. 2.6 and 2.7). Large cm-sized grains are inferred in the L1527 disk from the small opacity spectral index $\beta \sim 0$ (Tobin et al. 2013). If the observed polarization is due to scattering by sub-mm sized grains, then two grain populations may again be needed, as in the HL Tau case discussed in § 2.4.2.

The disk in IRAS 16293-2422B appears to be nearly face-on (Rodriguez et al. 2005; Zapata et al. 2013). Its 0.88 mm emission was observed to be polarized at $\sim 1.5\%$ level, with the polarization directions showing a swirling pattern that is neither strictly radial nor purely azimuthal (Rao et al. 2014). Rao et al. showed that the pattern is broadly consistent with the polarized emission expected from grains aligned by a magnetic field that is warped into a spiral configuration by disk rotation, although the rotation is hard to measure directly because of the face-on orientation. It is inconsistent with the simplest dust scattering model for axisymmetric face-on disks, where the polarization directions are expected to be perfectly azimuthal, as illustrated in the upper left panel of Fig. 2.2. However, the observed polarized intensity is arc-shaped which, for face-on systems, requires intrinsically non-axisymmetric disk

models, such as those constructed by Kataoka et al. (2015). Indeed, the observed intensity distribution is reminiscent of the lopsided ring models of Kataoka et al. (see their Fig. 6 and 7), although the polarization direction in the models changes sharply from radial in the inner part of the ring to azimuthal in the outer part. It is conceivable that dust scattering models with more complicated disk structures, such as spiral arms, may match the observation better, but this remains to be demonstrated. One worry is that the dust emission in this source may be optically thick at sub-mm wavelengths (Zapata et al. 2013), which would reduce the degree of anisotropy in the unpolarized radiation to be scattered, and thus the degree of polarization in the scattered radiation (Kataoka et al. 2015). Another is that the polarized emission detected in this deeply embedded source may be contaminated by the protostellar envelope. Higher resolution ALMA polarization observations should become available in the near future. They will provide more stringent tests of the dust scattering model of polarized mm/sub-mm emission.

As stressed by Kataoka et al. (2015), polarized radiation at mm/sub-mm wavelengths provides a powerful probe of grain growth, if it is produced by dust scattering. A robust prediction of the scattering model is that large, mm/cm-sized, grains should produce millimeter polarization along the major axis of an inclined disk due to polarization reversal, especially in the central region where the intrinsic (face-on) polarization is expected to be weak and the observed polarization pattern is more easily dominated by that induced by disk inclination (see Fig. 2.7 for an illustration). This effect should be searched for with high resolution ALMA observations, especially in high-inclination systems. Another way to probe large grains is to observe polarization at longer, centimeter, wavelengths using, for example, JVLA and the future SKA. At such wavelengths, the scattering by mm-sized grains would still be in the Rayleigh

regime, with a high degree of polarization of the scattered light. Given the sensitive dependence of the scattering opacity κ_{sca} (which controls the polarization fraction of the total intensity) on the grain size relative to the wavelength, it is important to carry out high-resolution polarization observations at multiple wavelengths to determine whether the polarization is indeed due to dust scattering and, if yes, to constrain the grain size distribution. With the polarization capability of JVLA, and that of ALMA coming online soon, the prospect for using sub-mm/mm/cm polarization to probe grain properties in disks is bright on the observational side.

On the theoretical side, much work remains to be done. In this chapter, we have limited our treatment to the simplest case of optically and geometrically thin disk, to bring out the essential features of the disk inclination-induced polarization transparently through a semi-analytic model. As noted earlier, there is indication from the spatial distribution of the opacity spectral index β that part of the HL Tau disk is optically thick at sub-mm/mm wavelength, including the central continuum peak, B1 and B6 rings, at radii of ~ 0 , 20, and 81 AU, respectively (ALMA Partnership et al. 2015). Since the B6 ring is rather narrow, and the bulk of polarized emission is detected interior to it, it should not affect our HL Tau model much. The continuum peak and B1 ring are not resolved by the polarization observation, but they can potentially lower the polarization fraction in the central pixel relative to the outer part, which is expected to bring the dust scattering model presented in § 2.3 and Fig. 2.5 into closer agreement with observation⁴. The effects of optically thick regions, as well as substructures on the disk such as rings and gaps, need to be quantified in future calculations in order to compare with higher resolution ALMA polarization observations that should become available soon.

⁴The polarization fraction of millimeter emission in the central region can also be lowered if the grains there grow to centimeter sizes, which can contribute significantly to the total but little to the polarized intensity.

Another future improvement is to relax the thin disk approximation. While the approximation is adequate for large grains that have settled close to the disk midplane, it would be less so for smaller grains that remain higher up above the midplane. It is likely that there is a gradient in dust grain concentration and size distribution in all three (radial, vertical and azimuthal) directions through grain growth, inward drift, vertical settling, and trapping (see Testi et al. 2014 for a recent review, and Pérez et al. 2012 for an example of gradient in grain size). Such gradients should be taken into account in more complete models of scattering-induced polarization, perhaps using 3D radiative transfer codes such as RADMC3D. As noted earlier, in HL Tau and L1527, the observed opacity spectral index β and polarization pattern in millimeter, if originating from dust scattering, appear to require two grain populations of different size distributions. Whether they can arise naturally through grain evolution in the disk warrants further investigation. In addition, a complete model of disk polarization at sub-mm/mm/cm will need to include both the polarized emission by aligned, non-spherical grains (particularly grains of tens of microns in size or larger, although it is unclear whether such grains can be aligned with respect to the magnetic field or not, as discussed in § 2.1) and dust scattering, and possible interplay between the two.

2.7 Conclusions

Motivated by the recent spatially resolved millimeter polarization observations of the HL Tau disk, we have developed a simple semi-analytic model for the dust scattering-induced polarization in the limit of optically and geometrically thin disk and Rayleigh scattering, with an emphasis on the effects of the disk inclination to the line of sight. The main results are summarized as follows:

1. We developed an efficient approximate method for computing disk polarization

from dust scattering by dividing the source region of the millimeter radiation to be scattered at a location inside the disk into two conceptually distinct parts: a near-field region centered on the location with a size comparable to the local dust scale-height, and a far-field region outside. Radiation from the near-field region is more or less isotropic, and does not contribute significantly to the polarization of the scattered light. Radiation from the far-field region is concentrated toward the disk plane. It is strongly polarized after scattering in an inclined disk. The polarization fraction of the scattered light increases with the inclination angle, reaching a maximum value of $1/3$ for edge-on disks if the incoming radiation to be scattered is azimuthally isotropic in the disk plane (eq. (2.18)). The polarization induced by disk inclination is parallel to the minor axis. It can easily dominate the intrinsic polarization of the disk in the face-on view (see Fig. 2.2).

2. We developed a simple model for the polarization of the HL Tau disk, based on the Kwon et al. (2011) model of disk physical structure and polarization induced by a disk inclination of 45° (see Fig. 2.5). The model naturally reproduces two main features of HL Tau: (1) the region of high polarized intensity is elongated along the major axis, and (2) the polarization vectors in this region are roughly parallel to the minor axis. Both are the consequences of a simple geometric effect: only the radiation propagating along the major axis of a tilted disk would be scattered by 90° to reach the observer and be maximally polarized, with a polarization direction along the minor axis in the plane of the sky. The broad agreement is robust because it does not depend on the detailed properties of dust grains (which are uncertain) as long as the scattering is in the Rayleigh limit. It provides support for the millimeter polarization observed in this particular case originating at least in part from dust scattering, although polarized emission from magnetically aligned dust grains cannot

be ruled out, especially if the disk field is more complex than toroidal.

3. For the other two cases with observed mm/sub-mm polarization, L1527 and IRAS 16293-2242B, the situation is less clear. The observed polarization pattern in the nearly edge-on disk of L1527 is compatible with that expected of either toroidal field-aligned grains or dust scattering. The pattern observed in the possibly face-on disk of IRAS 16293-2242B is more consistent with that expected of grains aligned by a rotationally warped magnetic field than with the simplest case of dust scattering. Higher resolution observations of more disks with different inclination angles are needed to better differentiate the grain-alignment and dust-scattering models. The observational situation should improve drastically with ALMA and JVLA.

4. To reproduce the polarization fraction of $\sim 1\%$ observed at 1.3 mm in the HL Tau disk, a maximum size of tens of microns is needed for the scattering grains. Detailed Monte Carlo simulation of the IM Lup system yields similar grain sizes. Such grains are generally thought to be too small to produce an opacity spectral index β of order 1 or less that is observed in HL Tau and other sources; larger, mm/cm sized grains may be needed. However, mm/cm sized grains tend to produce polarization parallel (rather than orthogonal) to the major axis due to polarization reversal (see Figs. 2.6 and 2.7), which is not observed in HL Tau; nevertheless, this pattern should be searched for in other sources as a robust indicator for large grains. In any case, the dust scattering model for polarization and the relatively low β produce an interesting conundrum that needs to be resolved in the future, perhaps with more complete models that include grain evolution and 3D radiative transfer, as well as polarized direct emission from aligned grains. Such models, together with the high resolution ALMA/JVLA polarization observations that will soon become available, should make it possible to disentangle the contributions of grain alignment and dust scattering to

the disk polarization, which is needed in order to provide robust constraints on the magnetic field that is generally thought to be crucial to the dynamics and evolution of protoplanetary disks and/or the grain growth that may eventually lead to planet formation.

Chapter 3

Disk Polarization From Both Emission and Scattering of Magnetically Aligned Grains: The Case of NGC 1333 IRAS4A1

This chapter is based on Yang et al. (2016b) with minimal modifications.

Abstract

Dust polarization in millimeter (and centimeter) has been mapped in disks around an increasing number of young stellar objects. It is usually thought to come from emission by magnetically aligned (non-spherical) grains, but can also be produced by dust scattering. We present a semi-analytic theory of disk polarization that includes both the direct emission and scattering, with an emphasis on their relative importance and how they are affected by the disk inclination. For face-on disks, both emission

and scattering tend to produce polarization in the radial direction, making them difficult to distinguish, although the scattering-induced polarization can switch to the azimuthal direction if the incident radiation is beamed strongly enough in the radial direction in the disk plane. Disk inclination affects the polarizations from emission and scattering differently, especially on the major axis where, in the edge-on limit, the former vanishes while the latter reaches a polarization fraction as large as $1/3$. The polarizations from the two competing mechanisms tend to cancel each other on the major axis, producing two low polarization “holes” (one on each side of the center) under certain conditions. We find tantalizing evidence for at least one such “hole” in NGC1333 IRAS4A1, whose polarization observed at 8 mm on the 100 AU scale is indicative of a pattern dominated by scattering close to the center and by direction emission in the outer region. If true, it would imply not only that a magnetic field exists on the disk scale, but that it is strong enough to align large, possibly mm-sized, grains.

3.1 Introduction

It is generally expected that magnetic fields play a crucial role in the dynamics and evolution of young star disks, through magneto-rotational instability (Balbus & Hawley 1991) and magneto-centrifugal disk wind (Blandford & Payne 1982; see Turner et al. 2014 and Armitage 2015 for recent reviews). This expectation, based mostly on theoretical studies, provides a strong motivation to search for the putative disk field observationally. To date, the observational effort has been concentrated on detecting and characterizing the polarized dust continuum emission, which has long been interpreted as coming from magnetically aligned grains (Lazarian 2007; Andersson et al. 2015), using the Submillimeter Array (SMA; Hughes et al. 2009; Rao et al. 2014)

and Combined Array for Research in Millimeter-wave Astronomy (CARMA; Hughes et al. 2013; Stephens et al. 2014; Segura-Cox et al. 2015). More recently, Cox et al. (2015) opened a new front for this line of research by detecting dust polarization at 8 mm and 1 cm on the 100-AU scale around the protostar NGC1333 IRAS4A1 using the Karl G. Jansky Very Large Array (VLA), as part of the VLA Nascent Disk and Multiplicity (VANDAM) survey (Tobin et al. 2015; see also Liu et al. 2016). If the detected (sub)mm and cm polarization is indeed produced by magnetically aligned grains, it would provide the long sought-after evidence that young stellar disks are magnetized, which is a pre-requisite for MRI and magneto-centrifugal disk winds to operate.

However, Kataoka et al. (2015) recently discovered an alternative mechanism for producing polarized millimeter emission in disks that relies on dust scattering of anisotropic incident radiation rather than the alignment of asymmetric grains. Yang et al. (2016a, Paper I hereafter) showed that, in the best observed case of HL Tau disk (Stephens et al. 2014), the polarization pattern is broadly consistent with that produced by dust scattering in an inclined disk (see also Kataoka et al. 2016a), although grain alignment cannot be ruled out completely, especially if the magnetic field structure of the disk is more complex than a purely toroidal configuration (Stephens et al. 2014). If the dust scattering interpretation is correct, the grains responsible for the scattering in the HL Tau disk must be orders of magnitude larger than the classical ISM size of $0.1 \mu\text{m}$ (at least several tens of microns; Paper I and Kataoka et al. 2016a). The inferred (relatively large) grain size would add to other lines of evidence for substantial grain growth in protoplanetary disks (e.g., Pérez et al. 2012; Guidi et al. 2016; see Testi et al. 2014 for a recent review), which provides a first step toward planets.

Whether large (non-spherical) grains can be aligned with respect to the magnetic field inside a protoplanetary disk remains uncertain. In the context of the currently favored mechanism for grain alignment through radiative torque, their magnetic moments may not be large enough to provide the fast precession needed (Lazarian 2007; although it depends on the disk field strength, which is uncertain), and their slow internal relaxation makes the alignment less efficient (Hoang & Lazarian 2009). More work is needed to address this important issue. In this chapter, we will adopt the conventional view that the grains are aligned with respect to the magnetic field (Andersson et al. 2015), at least to some extent in the disk, and treat the (currently uncertain) degree of alignment as a free parameter¹. This treatment allows us to focus on the following question: how would the polarization pattern produced by direct emission from magnetically aligned grains be modified by scattering by the same aligned grains? It is a step beyond Paper I and Kataoka et al. (2015, 2016a), because the grains are no longer assumed to be spherical and the polarization from direct dust emission is included together with that from scattering. Our goal is to delineate the conditions under which one of the two competing mechanisms would dominate over the other and vice versa, and to determine the composite polarization pattern when both are important. This delineation of the parameter space and the determination of polarization pattern will benefit the physical interpretation of disk polarization observations, especially those to be conducted with the Atacama Large Millimeter/submillimeter Array (ALMA).

As a first step toward a comprehensive theory of disk polarization including both emission and scattering from magnetically aligned grains, we will adopt the well-known “electrostatic approximation” to simplify the computation of the optical prop-

¹The parametrization is also needed because of the uncertainty in the grain shape, which greatly affects the degree of polarization but cannot be determined from the grain alignment theory.

erties of non-spherical grains. This approximation is discussed in § 3.2, together with an *analytic* model to illustrate the relative importance of the scattering and direct emission in producing polarization, which turns out to depend strongly on the disk inclination. In § 3.3, we compute numerically the polarization patterns of a model disk produced by the scattering and direct emission individually and in combination, to illustrate the diverse outcomes of the competition between the two mechanisms, especially for disks of different inclinations. Our results are used to explain the polarization detected in NGC1333 IRAS 4A1 in § 3.4. We discuss the implications of our results and their limitations in § 3.5, and conclude in § 3.6.

3.2 Competition between scattering and direct emission of non-spherical grains: analytic results

In order to determine how a non-spherical dust grain scatters light, one needs to know how it interacts with an external electromagnetic wave. The interaction can be very complicated in general, since each grain can be considered as a collection of polarizable parts, and each part responds to its local electric field inside the grain and may have a different polarization and phase. The grain-light interaction can in principle be treated numerically using, for example, the Discrete Dipole Approximation (e.g., Draine & Flatau 1994). However, such numerical treatments tend to be computationally expensive, and are not optimal for an initial exploration of the problem at hand: competition between the scattering and direct emission of non-spherical, magnetically-aligned grains in determining the polarization pattern. For such a purpose, we have decided to employ the well-known “electrostatic approximation” (e.g., Bohren & Huffman 1983), which greatly simplifies the computation of the scattering

cross sections without sacrificing the essential physics. The limitations of this approximation and its future refinements are discussed in section § 3.5 (see Fig. 3.7). Our discussion below follows closely that in Chapter 5 of Bohren & Huffman 1983, to which we refer the readers for details.

3.2.1 Electrostatic approximation

The basic requirement for the electrostatic approximation is that the grain size is smaller than the wavelength of the external electromagnetic wave. In such a case, the electric field varies little across the grain, and the field can be approximated as having the same time dependence throughout the region of interest. The approximation simplifies the calculation of the polarization of the (small) grain using the electrostatic equations with only spatial derivatives.

The scattering cross sections depend on both the size and shape of the dust grain. The grain shape is not well constrained. For illustration purposes, we model the grain as an ellipsoid, for which analytic solutions are available. For an ellipsoid composed of isotropic material with a complex dielectric constant ϵ , the governing electrostatic equations can be solved analytically using ellipsoidal coordinates. The dielectrics will respond to the external field linearly and develop a dipole moment. Since the grains are not spherical, the polarizability $\bar{\alpha}$ that relates the electric dipole moment \mathbf{p} induced in the grain to the external electric field \mathbf{E} is not a single number but rather a matrix, i.e., $\mathbf{p} = \bar{\alpha}\mathbf{E}$. In a coordinate system with axes along the three principle axes of the dust grain, the polarizability matrix $\bar{\alpha}$ is diagonal, i.e., $\bar{\alpha} = \text{diag}\{\alpha_1, \alpha_2, \alpha_3\}$. Its diagonal element can be expressed as:

$$\alpha_i = r_e^3 \frac{\epsilon - 1}{3 + 3L_i(\epsilon - 1)}, \quad (3.1)$$

where r_e is the radius of the sphere that has the same volume as the ellipsoid, and L_i ($i = 1, 2, 3$) is a geometric parameter determined solely by the shape of the grain, subjected to the constraint $L_1 + L_2 + L_3 = 1$. In the simplest case of a spherical grain, L_i is $1/3$. For an ellipsoidal grain, L_i can be expressed as an integral that includes the length of the corresponding principle axis as a parameter. For an spheroid, which is an ellipsoid obtained by rotating an ellipse along one of its principle axis, the integral can be done analytically. Following the convention $L_1 \leq L_2 \leq L_3$ (which corresponds to the convention for the semi-diameters $a_1 \geq a_2 \geq a_3$ and diagonal matrix elements $|\alpha_1| \geq |\alpha_2| \geq |\alpha_3|$), we have for a prolate spheroid ($a_1 > a_2 = a_3$):

$$L_1 = \frac{1 - e^2}{e^2} \left(-1 + \frac{1}{2e} \ln \frac{1 + e}{1 - e} \right), \quad e^2 = 1 - s^2, \quad (3.2)$$

where $s = a_2/a_1 < 1$ is the axis ratio. The other two geometric parameters are both equal to $(1 - L_1)/2$.

For an oblate spheroid ($a_1 = a_2 > a_3$), we have:

$$\begin{aligned} L_1 &= \frac{g(e)}{2e^2} \left[\frac{\pi}{2} - \tan^{-1} g(e) \right] - \frac{g^2(e)}{2}, \\ g(e) &= \left(\frac{1 - e^2}{e^2} \right)^{1/2}, \quad e^2 = 1 - \frac{1}{s^2}, \end{aligned} \quad (3.3)$$

where the axis ratio is defined as $s = a_1/a_3 > 1$. The other two geometric parameters are given by $L_2 = L_1$ and $L_3 = 1 - 2L_1$.

As the external electric field varies over time, the dipole induced inside the grain also oscillates, which results in dipole radiation. It is straightforward to compute the scattering matrix and phase matrix of the induced dipole radiation and, through the optical theorem, obtain the absorption cross section. The resultant scattering and absorption cross sections will be used to compute numerically the polarization due

to direct emission and scattering of (small) ellipsoidal grains in a young star disk in § 3.3. Before doing so, we will first illustrate the main features of the polarization produced by the scattering of non-spherical grains analytically in a limiting case, which will also allow us to compare with previous work and build physical intuition of how the scattering of non-spherical grains depends on the disk inclination, a focus of this investigation.

3.2.2 Inclination-induced polarization from scattering by oblate grains

In Paper I, we showed that the disk inclination with respect to the line of sight plays an important role in the polarization produced by the scattering of spherical grains. The inclination-induced polarization was illustrated analytically in the limiting case where the disk is geometrically thin and the incoming radiation to be scattered by the grains is locally isotropic in the disk plane (see their § 2.2). Under these conditions, the polarization fraction of the scattered light by small spherical grains goes from zero for the face-on view to $1/3$ for the edge-on case. Here, we extend this analysis to oblate grains with the semi-diameters $a_1 = a_2 > a_3$ (Hildebrand & Dragovan 1995); the case of prolate grains will be discussed in the Appendix A at the end of this chapter.

To be specific, let us consider the polarization of the light scattered by oblate grains at a location O inside a disk that is inclined with respect to the line of sight by an angle i ($i = 0^\circ$ corresponds to the face-on case). We will adopt a Cartesian coordinate system centered on the location O , with the x -axis pointing radially away from the center of the disk, and y -axis tangential to the circle in the disk plane that is centered at the origin and passes through the point O . For simplicity, we assume

that the disk magnetic field is purely toroidal, so that the only non-zero component is along the y -direction. In the case of perfect grain alignment, the y -axis is also the direction of the minor axis of the oblate grain (with the smallest semi-diameter a_3). The z -axis of the coordinate system is perpendicular to the disk plane. In this coordinate system, the polarizability is diagonal: $\bar{\alpha} = \text{diag}\{\alpha_x, \alpha_y, \alpha_z\}$, with $\alpha_x = \alpha_z \equiv \alpha_1$, $\alpha_y \equiv \alpha_3$ and $|\alpha_1| > |\alpha_3|$. We let the x -axis lie in the plane of the sky, so that the line of sight to the location O of interest is perpendicular to the x -axis and is thus in the yOz plane. In this coordinate system, the disk inclination angle i is simply the angle between the z axis and the line of sight, and the x -axis is along the major axis of the inclined disk projected in the plane of the sky. For this initial analysis, we focus on the disk locations on the major rather than the minor axis for two reasons. First, the polarization produced by direct emission from the oblate grains on the minor axis is independent of the inclination angle because these grains are aligned with the (toroidal) magnetic field in such a way that they always appear “edge-on” to the observer. More importantly, the polarization pattern is expected to be simpler on the minor axis because both direct emission and scattering there tend to produce polarization along the minor axis (although not always, see Fig. 3.3), so that they generally add to, rather than cancel, each other.

Our goal is to determine the polarization properties of the light that is scattered into our line of sight. In general, the Stokes parameters of the scattered light (I_s , Q_s , U_s and V_s) are related to those of the incident radiation (I_i , Q_i , U_i and V_i) through a 16-element scattering matrix (see Bohren & Huffman 1983, p65). We assume that the incident light is non-polarized (i.e., $Q_i = U_i = V_i = 0$), so that only 4 of the matrix elements are relevant, namely: $I_s \propto S_{11}I_i$, $Q_s \propto S_{21}I_i$, $U_s \propto S_{31}I_i$, and $V_s \propto S_{41}I_i$. We assume further that the incident radiation to be scattered at the location O is confined

in the disk plane (i.e., the thin (dust) disk approximation), so that its direction is uniquely described by the azimuthal angle ϕ from the x -axis. In the limiting case that the incident radiation is independent of the azimuthal angle ϕ , it is straightforward to average the scattering matrix elements over ϕ , which yields the following results:

$$\langle S_{11} \rangle = \frac{1}{2}k^6 \left(|\alpha_1|^2 \sin^2 i + \frac{1}{2}|\alpha_3|^2 \cos^2 i + \frac{1}{2}|\alpha_1|^2 \right), \quad (3.4)$$

$$\langle S_{21} \rangle = -\frac{1}{2}k^6 \left(|\alpha_1|^2 \sin^2 i + \frac{1}{2}|\alpha_3|^2 \cos^2 i - \frac{1}{2}|\alpha_1|^2 \right), \quad (3.5)$$

where $k = 2\pi/\lambda$ is the wave-number of the scattered light. In addition, $\langle S_{31} \rangle = \langle S_{41} \rangle = 0$, as expected from the symmetry of the problem. It means that the scattered light will be polarized either in the x -direction or perpendicular to it, and that there is no circular polarization. Since $\langle S_{11} \rangle$ and $\langle S_{21} \rangle$ are essentially the differential scattering cross sections for the Stokes parameter I and Q , respectively, the degree of polarization of the scattered light is simply given by their ratio:

$$p_{sca} = \frac{\langle S_{21} \rangle}{\langle S_{11} \rangle} = \frac{|\alpha_1|^2 - 2|\alpha_1|^2 \sin^2 i - |\alpha_3|^2 \cos^2 i}{|\alpha_1|^2 + 2|\alpha_1|^2 \sin^2 i + |\alpha_3|^2 \cos^2 i}, \quad (3.6)$$

which can be either positive or negative; a positive (negative) p_{sca} means that the polarization direction is parallel (perpendicular) to the x -axis in the plane of the sky.

In order to obtain numerical values for p_{sca} , a grain model is needed to calculate the values of α_1 and α_3 . This will be done in the next subsection. Here, we will make a couple of interesting points that are independent of the detailed grain properties. First, since $|\alpha_1| > |\alpha_3|$ for oblate grains, we have $p_{sca} > 0$ in the face-on case with $i = 0^\circ$, which means that the scattered light will be polarized in the x -direction. This is different from the case of spherical grains, where the polarization in the face-on

case is zero. The difference makes physical sense because, for non-spherical grains, the scattering cross sections for incident light coming from different directions are no longer the same. In particular, for oblate grains with the short axis aligned with the y -axis, light propagating along the y -direction will be scattered more efficiently into our line of sight, producing polarization in the x -direction. The degree of polarization will depend on the degree of the grain non-sphericity, as we show below. Second, in the opposite limit of edge-on view ($i = 90^\circ$), we have $p_{sca} = -1/3$. This is expected because, when viewed edge-on, the grain is axisymmetric with respect to the line of sight. It means that the polarization in this limit is determined completely by the inclination effect, which is known to produce a fractional polarization of $1/3$ perpendicular to the x -axis in the plane of the sky (i.e., along the minor axis of the inclined disk, Paper I). In the limit $\alpha_1 = \alpha_3$, we have $p_{sca} = -\sin^2 i / (2 + \sin^2 i)$, which recovers the previous analytic results for spherical grains².

3.2.3 Competition between scattering and direct emission

In this subsection, we will compute the polarization from the scattering of oblate grains at a location O in an inclined disk adopting a specific grain model. The model allows us to determine diagonal elements of the polarizability matrix, α_1 and α_3 , and, through Equation 3.6, the degree of polarization, p_{sca} . The polarization from scattering will be compared with that from the direct emission from the same magnetically aligned oblate grains at the location O (with the shortest axis along the y -direction). To determine the latter, the absorption cross sections along the major axis of the inclined disk in the plane of the sky, the x -axis, and the minor

²Note that the Stokes parameters in Paper I were defined in a plane-of-sky coordinate system $x'-y'$, with x' along the minor axis of the inclined disk. In this chapter, the x -axis lies in the plane of the sky and is along the major axis of the disk. This difference introduces a sign difference between these two results

axis (denoted by y' hereafter), are needed. They are related to the polarizability, especially the imaginary part, through the optical theorem:

$$\sigma_{\text{abs},x} = 4\pi k \text{Im} [\alpha_1], \quad (3.7)$$

$$\sigma_{\text{abs},y'} = 4\pi k \text{Im} [\alpha_3 \cos^2 i + \alpha_1 \sin^2 i], \quad (3.8)$$

where $\text{Im}[x]$ stands for the imaginary part of any variable x . These absorption cross sections yield the following degree of polarization for the direct emission:

$$p_{\text{abs}} = \frac{\text{Im} [\alpha_1 - \alpha_3] \cos^2 i}{\text{Im} [\alpha_3 \cos^2 i + \alpha_1 (1 + \sin^2 i)]}. \quad (3.9)$$

We follow Kataoka et al. (2015) in adopting the grain model of Pollack et al. (1994), where grains are composed of silicate (8% in volume), water ice (62%) and organics (30%). This type of dust grains has a complex dielectric constant of $\epsilon = 3.78 + 0.04j$ (where j is the imaginary unit $\sqrt{-1}$) at 1 mm. In Fig. 3.1, we plot the degree of polarization for scattered light and direction emission, p_{sca} and p_{abs} , for several representative values of the axis ratio of the oblate grain, $s = 1.0, 1.1, 1.5$ and 2.0 , as a function of the disk inclination angle i . Several features are immediately apparent. First, in the limit of spherical grains with $s = 1.0$, we recover the known (analytic) results that the direct emission is not polarized, and the polarization from scattering is along the minor axis, with a polarization fraction that goes from zero to $1/3$ as the inclination angle i increases from 0° to 90° . Second, as anticipated analytically in the last subsection, the polarization of the light scattered by the oblate grains aligned with a toroidal magnetic field (along the y -direction) is along the x -axis (with a positive p_{sca}) in the face-on case. As the inclination angle increases, the polarization along the major (or x -) axis is gradually weakened by that from the polarization induced

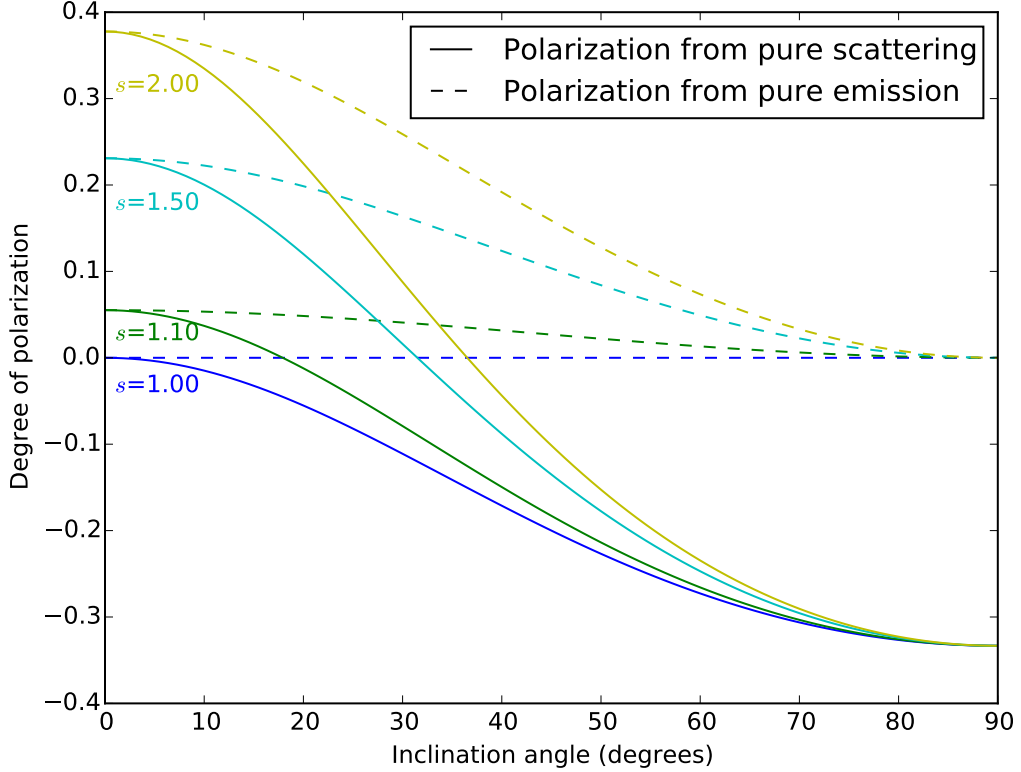


Fig. 3.1.— Degree of polarization at a location on the disk major axis for scattered light (p_{sca} , solid lines) and direct emission (p_{abs} , dashed) for oblate grains with representative axis ratio $s = 1.0, 1.1, 1.5,$ and 2.0 as a function of disk inclination angle i , assuming perfect grain alignment. Note that p_{sca} and p_{abs} start from the same positive value at $i = 0^\circ$ (the face-on limit), but decrease to $-1/3$ and 0 , respectively, as the edge-on ($i = 90^\circ$) limit is approached.

by the inclination, which is along the minor (or y' -) axis. At a critical inclination angle i_c , the polarization direction switches from the major axis to the minor axis; the angle i_c increases with the axis ratio s . In all cases, the scattering degree of polarization asymptotes to the limiting value $p_{sca} = -1/3$ as the inclination angle i approaches 90° , as we showed analytically above. Third, the polarization of the direct emission by the aligned oblate grains is always along the major (or x -) axis of the disk, which is the direction of the long axis of the grain. The polarization degree p_{abs}

peaks in the face-on case, where the grain appears most elongated to the observer. Interestingly, the peak value is exactly the same as that of the scattering polarization degree p_{sca} in the face-on case, which can be proven analytically for oblate grains. Lastly, the emission polarization degree p_{abs} decreases smoothly with the inclination angle i , reaching zero in the edge-on limit, when the oblate grains appear circular to the observer and thus there is no preferred direction for polarization. The vanishing of p_{abs} as $i \rightarrow 90^\circ$ means that the polarization will be dominated sooner or later by scattering, as long as the inclination angle i is large enough.

The relative contribution of scattering and direct emission to the polarization depends on not only the degree of polarization (p_{sca} and p_{abs}), but also the ratio of $\sigma_{sca}J_\nu$ and $\sigma_{abs}B_\nu$, where J_ν is mean intensity at the location under consideration, B_ν is the local source function for thermal dust emission, and σ_{sca} and σ_{abs} are the scattering and absorption cross sections. The ratio J_ν/B_ν depends on the detailed disk model and temperature structure, while the ratio of scattering and absorption cross sections, $\sigma_{sca}/\sigma_{abs}$, depends on the dust composition and especially grain size. Roughly speaking, the cross section ratio is of the order $(2\pi r_e/\lambda)^3$. In order for the scattering to be competitive, the grain size r_e cannot be much smaller than the wavelength λ . On the other hand, the electrostatic approximation that we adopted is valid only when the grain is relatively small compared to the wavelength. As we show in § 3.5 below, the scattering opacity exceeds the absorption opacity as long as the grains are bigger than $\sim 0.05\lambda$, while the electrostatic approximation remains valid for grain sizes up to $\sim 0.2\lambda$. For larger grains, the scattering opacity remains larger than the absorption opacity, but their optical properties need to be computed numerically; we postpone such a treatment to a future investigation. In what follows, we will leave the ratio $\sigma_{abs}B_\nu/\sigma_{sca}J_\nu$ as a free parameter, and explore the parameter

space where the polarization from scattering becomes important relative to that from direction emission.

Since the polarization from direct emission at a location on the major axis is always along the major axis (for a purely toroidal magnetic field), one way to measure the importance of the scattering is to determine the transition inclination angle i_t beyond which the polarization is forced to align with the minor axis instead. In Fig. 3.2, we plot the angle i_t as a function of the ratio $\sigma_{\text{abs}}B_\nu/\sigma_{\text{sca}}J_\nu$ for a representative set of

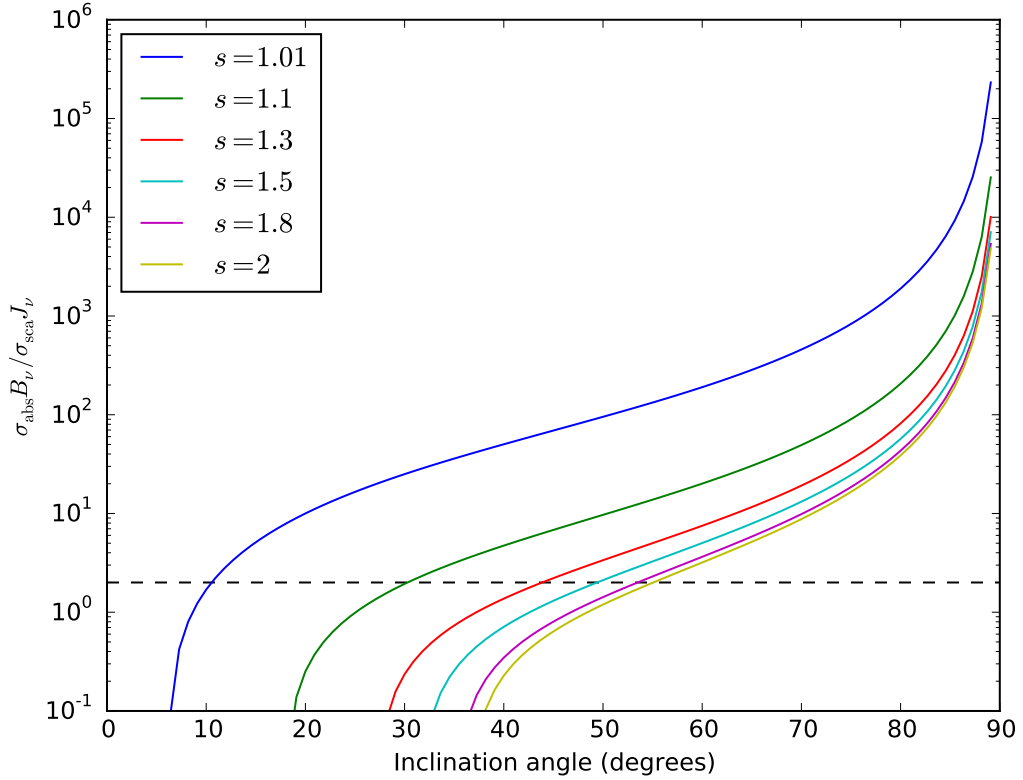


Fig. 3.2.— Transition lines that divide the parameter space where the polarization is dominated by direct emission (to the upper left of each line) from that dominated by scattering (the lower right), for 6 representative values of the grain axis ratio $s = 1.01, 1.1, 1.3, 1.5, 1.8$ and 2.0 . The horizontal line marks $\sigma_{\text{abs}}B_\nu/\sigma_{\text{sca}}J_\nu = 2$, the fiducial value obtained in the flared disk model of Cho & Lazarian (2007).

values for the axis ratio s . Roughly speaking, for each value of s , the polarization is dominated by direct emission in the parameter space to the upper left of the corresponding curve, and by scattering to the lower right of the curve. Also shown in the plot is the fiducial value of $\sigma_{\text{abs}}B_{\nu}/\sigma_{\text{sca}}J_{\nu} = 2$ derived in the flared disk model of Cho & Lazarian (2007). For this fiducial value, the polarization is dominated by scattering for i greater than approximately 55° as long as the grain axis ratio is not too extreme ($s < 2$, see Hildebrand & Dragovan 1995). For larger ratios of $\sigma_{\text{abs}}B_{\nu}/\sigma_{\text{sca}}J_{\nu}$, a more extreme inclination is required for the scattering to become dominant, unless the grains are nearly spherical (i.e., with s close to 1). In what follows, we will evaluate this ratio self-consistently with the help of a specific disk model. The effects of two potential complications, imperfect grain alignment and non-oblate grain shape, are discussed in the Appendix A at the end of this chapter.

3.3 Competition between scattering and direct emission in young star disks: numerical examples

So far, we have limited our (analytic) discussion of the interplay between the polarizations produced by non-spherical grains through scattering and direct emission to the limiting case where the incident radiation field is both planar and isotropic in the disk plane. While the planar approximation is usually a good one, especially for large grains that tend to settle to the disk mid-plane, the isotropic assumption is adopted mainly for the purposes of illustrating the competition between scattering and emission as simply as possible. In this section, we will relax this assumption with the help of a specific model for the disk structure, which enables a self-consistent computation of the angular distribution of the incident radiation field, as done in Paper I. More

importantly, the disk model allows for a determination of the polarization pattern over the entire disk, which is needed for direct comparison with spatially resolved polarization observations, especially those with ALMA. We will keep the “thin-disk” approximation adopted in Paper I, which has been shown to greatly speed up the computation of the scattering-induced polarization in an inclined disk by spherical grains without compromising the essential physics of the problem. Our treatment here is essentially a generalization of Paper I to the case of non-spherical grains, where both scattering and direct emission contribute to the polarization. It turns out that the combined polarization pattern resembles that observed recently in NGC1333 IRAS4A with VLA at 8 mm and 1 cm (Cox et al. 2015). The application of our results to this specific source will be discussed in § 3.4.

3.3.1 Problem setup

We will compute the polarizations due to the direct thermal emission and scattering by non-spherical grains separately. The former can be done through straightforward integration along each line of sight once the grain properties, magnetic field configuration, and degree of grain alignment are specified. The latter is more complicated because, along each line of sight, it involves the computation of the incident radiation field to be scattered at all locations and the integration of the scattered light. To treat the scattering-induced polarization, we will adopt the same basic problem setup as in Paper I (see § 2.2.1). Particularly important for their formulation of the scattering problem is the assumption that the disk is both geometrically and optically thin. This simplification enabled us to relate the source function of the radiation scattered into the line of sight at any target location \mathbf{r} on the (thin, inclined) disk to the column density and temperature at a source location \mathbf{r}_1 (which supplies the

photons to be scattered at \mathbf{r}), $\Sigma(\mathbf{r}_1)$ and $T(\mathbf{r}_1)$, through their equations (6)-(7), which are reproduced here for easy reference:

$$S \approx \frac{2\nu^2 k \kappa_{\text{abs}}}{c^2 \sigma_s} \int_0^{2\pi} d\phi \frac{d\sigma}{d\Omega} \Lambda(\mathbf{r}, \phi) \quad (3.10)$$

where ν is the frequency of the scattered light, k is the Boltzmann constant, κ_{abs} the absorption opacity, c the speed of light, σ_s the solid angle-integrated (total) scattering cross section, $d\sigma/d\Omega$ the differential scattering cross section, and the quantity $\Lambda(\mathbf{r}, \phi)$ is an integral along a straight line on the disk that passes through the target location \mathbf{r} along a constant azimuthal angle ϕ :

$$\Lambda(\mathbf{r}, \phi) \equiv \int_H^\infty dl \frac{\Sigma(\mathbf{r}_1)T(\mathbf{r}_1)}{l}, \quad (3.11)$$

where H is the local disk scale-height at \mathbf{r}_1 and l is the separation between the target and source locations, \mathbf{r} and \mathbf{r}_1 .

In the simpler case of (small) spherical grains considered previously in Paper I, the differential scattering cross section $d\sigma/d\Omega$ in equation (3.10) is simply given by Rayleigh scattering. For non-spherical grains, there are two potential complications. The first is that the incident radiation to be scattered at a given location is already polarized before scattering because it is emitted by non-spherical grains. In principle, one needs to determine the polarization state of the incident radiation carefully, taking into account of the grain orientation at each source location \mathbf{r}_1 along the line of integration in equation (3.11). For simplicity, we shall assume that the incident light is unpolarized before scattering. This approximation should not change the polarization produced by scattering qualitatively, as explained in the Appendix B.

The second complication is that, for non-spherical grains, the scattering matrix

(see equations 3.4 and 3.5), which determines the differential cross section $d\sigma/d\Omega$ in equation (3.10), will depend on two angles, the incident radiation direction and line of sight direction in the frame of the dust grains, rather than a single scattering angle, as it is in Rayleigh scattering. These matrix elements can be computed easily once the grain properties and degree of grain alignment are specified. For illustrative purposes, we will adopt the same grain model of Kataoka et al. (2015) used in the last section (§ 3.2) and assume that the grains are oblate spheroids perfectly aligned with a purely toroidal magnetic field in the disk; grains of other shapes (e.g., prolate) and/or imperfectly aligned should produce qualitatively similar results after averaging around the field direction (see Appendix A at the end of this chapter). We adopt a volume-equivalent radius $r_e = 100 \mu\text{m}$ to maximize the effects of the scattering of radiation at 1 mm wavelength and a rather large axis ratio of $s = 1.5$, so that the direct emission is significantly polarized. Other choices of r_e and s would not change the polarization patterns produced by scattering and direct emission individually, but will affect their relative importance in a simple way: increasing r_e (s) tends to make scattering (direct emission) more important.

3.3.2 Numerical examples of disk polarization pattern from both scattering and emission

For our numerical examples, we adopt the column density distribution of the viscous disk model of Pringle (1981):

$$\Sigma(R) = \Sigma_0 \left(\frac{R}{R_c} \right)^{-\gamma} \exp \left[- \left(\frac{R}{R_c} \right)^{2-\gamma} \right], \quad (3.12)$$

which is often used for modeling disk continuum observations (e.g., Testi et al. 2014; Kwon et al. 2015). The prescribed disk profile has an inner part with a power-law distribution and an outer part dominated by an exponential cutoff. Most observed disks have an inferred value of the power index γ between ~ 0.5 and ~ 1 (Andrews et al. 2009; Segura-Cox et al. 2016). We have experimented with different values of γ in this range and found similar polarization patterns. Only the results for the $\gamma = 0.5$ case will be shown below.

The size of the model disk is set by the characteristic radius R_c . It provides an overall scaling for the polarization pattern, but does not change the pattern itself. For definitiveness, we choose $R_c = 50$ AU, and truncate the disk beyond an outer radius $R_{\text{out}} = 3R_c = 150$ AU. The inner radius of the disk is set to $R_{\text{in}} = 1$ AU in order to prevent the column density from going to infinity at the origin. For the temperature profile, we adopt the simple prescription

$$T(R) = T_0 \left(\frac{R}{R_c} \right)^{-1/2}, \quad (3.13)$$

which is approximately valid for disks heated by the central stellar radiation (e.g., Hartmann et al. 1998). We will assume the radiation is in the Rayleigh-Jeans regime and all the intensities will be presented in unit of the Planck function $B_\nu(T_0)$; the dimensionless intensities are independent of T_0 . As a concrete illustrative example, we set the scale factor for the total (gas and dust) column density to $\Sigma_0 = 17 \text{ g/cm}^2$ (with a gas-to-dust-ratio of 100), so as to prevent the optical depth for direct emission from becoming too large, especially at small radii, on the one hand and to make the optical depth for scattering large enough that the scattering can compete with direct emission in producing polarization on the other. The key parameter that we will focus on is the inclination angle i , which is expected to change the balance between

the polarization produced by scattering and that by direct emission, based on the analytic results described in § 3.2.

We will start with the simplest, face-on case ($i = 0^\circ$), which is free of any disk inclination effect. In this case, the polarization pattern for the direct emission from the oblate grains that are perfectly aligned with a purely toroidal magnetic field is trivial: the polarization direction is radial everywhere (see upper-middle panel of Fig. 3.3). The pattern for the scattered light is more structured. The polarization direction is radial inside a radius of ~ 20 AU (this radius depends on the disk mass and temperature distributions), and becomes azimuthal outside (see upper-left panel). This is very different from the pattern in the case of spherical grains (see the top-left panel of Fig. 2.2), where the polarization direction is azimuthal everywhere, including at small radii, where the polarization fraction is small, because the incident radiation field at these radii is more or less isotropic in the disk plane. In contrast, for non-spherical grains, the scattered light can be significantly polarized even for (planar) isotropic incident radiation, as we demonstrated analytically in the last section (see Fig. 3.1). Since the oblate grains are aligned with their shortest axes along the azimuthal (B-field) direction, incident light coming from the radial direction (with an electric field \mathbf{E} along the azimuthal direction) is scattered less efficiently than that from the azimuthal direction (with \mathbf{E} along the radial direction), leading to polarization along the radial direction at small radii where the incident radiation field in the disk plane is more or less isotropic. As the radius increases, the incident radiation field becomes more beamed in the radial direction, which leads to the polarization along the azimuthal direction in the outer part of the disk. Indeed, the incident radiation near the outer edge of the disk shown in Fig. 3.3 is so beamed in the radial direction that the polarization fraction of the scattered light is more than 50%.

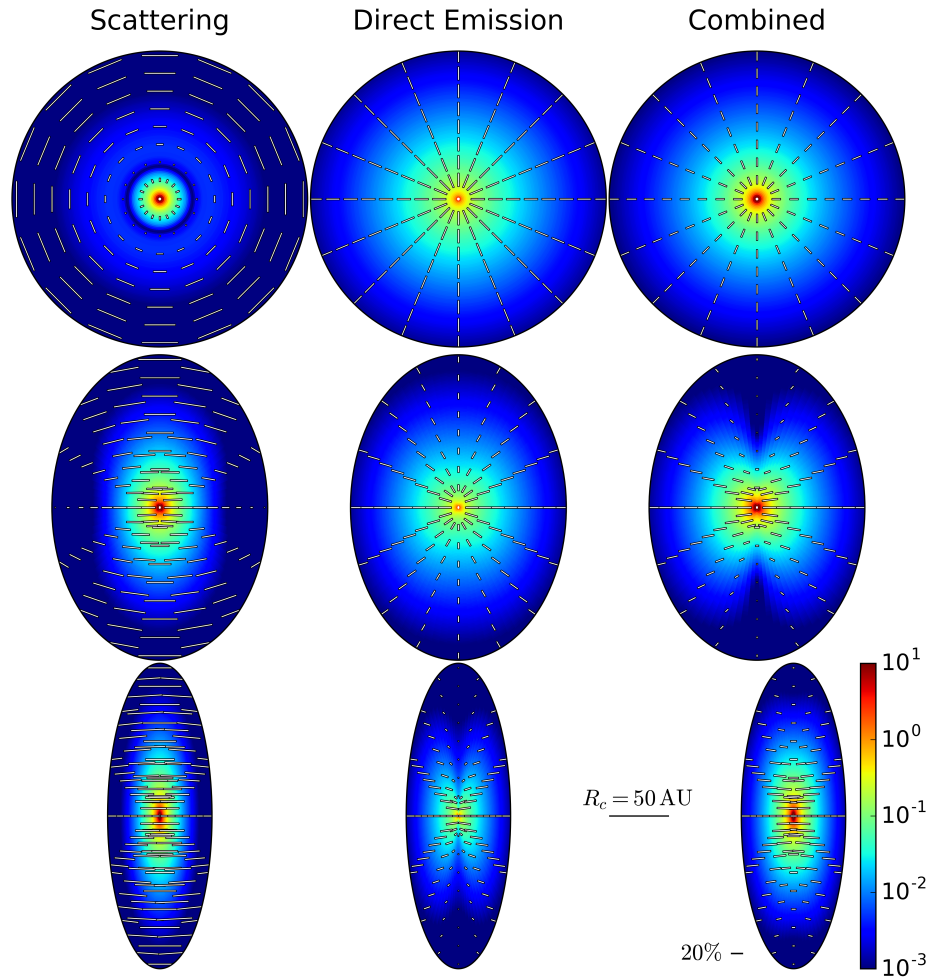


Fig. 3.3.— Polarized intensity (in units of $B_\nu(T_0)$, color map) and polarization vectors with length proportional to polarization fraction for scattering only (left panels), emission only (middle), and the two combined (right), for three inclinations $i = 0^\circ$ (upper panels), 45° (middle), and 70° (lower).

Despite the high polarization fraction, the polarized intensity of the scattered light is relatively low in the outer part in this particular example, so that the polarization of the combined light from both direct emission and scattering is in the radial direction everywhere (see the upper right panel). The radial polarization pattern does

not mean that the direct emission dominates the polarization everywhere. Indeed, close to the center, the polarization is dominated by scattering³. This illustrates the potential danger of automatically identifying radial polarization with the direct emission from grains aligned with a toroidal magnetic field in a face-on disk. Other pieces of information, such as grain properties and disk radiation field, are needed to help determine unambiguously which polarization mechanism dominates.

As the angle i increases, the inclination-induced polarization in the scattered light becomes more important, which reduces the difference between the spherical and non-spherical grain cases (compare the lower-left panel of Fig. 2 of Paper I with the middle-left panel of Fig. 3.3 for the $i = 45^\circ$ case). In particular, in the inner part of the disk where the incident radiation field in the disk plane is not far from being isotropic, the scattered light is polarized more or less along the minor axis of the disk, which is the hallmark of the inclination-induced polarization; it is very different from the radial pattern seen in the face-on case (see the upper-left panel). In addition, both the ring of null polarization and the azimuthal polarization pattern in the outer part of the disk of the face-on case disappear, again because of the inclination-induced polarization.

As emphasized in Paper I for spherical grains, the tendency for the inclination-induced polarization in the scattered light to lie along the minor axis is a simple consequence of the (thin) disk geometry and maximum polarization at 90° scattering angle for small grains. For locations on the major axis of a disk of inclination angle i , the incident radiation coming from the radial direction is scattered by 90° into the line of sight, whereas that from the locally azimuthal direction (i.e., perpendicular to the local radial direction in the disk plane) is scattered by $90^\circ + i$ or $90^\circ - i$.

³The exact size of the scattering dominated central region depends on the disk structure and dust properties, and will require more elaborate models to determine if the region becomes optically thick.

This difference in scattering angle makes the polarization from the former, which is along the minor axis, more important relative to that from the latter. Similarly, for locations along the minor axis, the incident light along the locally azimuthal direction is scattered by 90° , and that along the radial direction (in the disk plane) by $90^\circ + i$ or $90^\circ - i$. The difference increases the relative importance of the polarization from the former, which is again along the minor axis. This basic picture is qualitatively similar for both spherical and non-spherical grains.

The polarization produced by direct emission is also affected by the disk inclination. Although the polarization vectors remain perpendicular to the local toroidal magnetic field projected onto the plane of the sky (see the middle-middle panel for the $i = 45^\circ$ case), the polarization fraction is changed significantly by the inclination, especially at locations on the major axis, where it is reduced compared to the face-on case, by a factor of about 2 for $i = 45^\circ$ for the particular grain model with $s = 1.5$ adopted here (see Fig. 3.1). As mentioned earlier, for locations on the minor axis, the aligned oblate grains appear “edge-on” to the observer independent of the inclination angle, and their polarization fraction remains unchanged. Therefore, a generic feature of the polarization produced by the direct thermal emission of magnetically aligned oblate (or effectively “oblate”, see Appendix A for a discussion) grains is that, as the inclination angle i increases, the distribution of the polarization fraction becomes more non-uniform azimuthally, with the radiation on the minor axis becoming increasingly more polarized compared to that on the major axis. The degree of the contrast between the two axes depends sensitively on the grain axis ratio s , which is unfortunately uncertain in general.

The inclination-induced contrast between the polarizations produced by the direct emission on the major and minor axes is further increased when the scattering is also

included (see the middle-right panel). The main reason is that, for our particular grain model, the polarizations produced by direct emission and scattering are in orthogonal directions at locations on the major axis (see the middle-left and middle-middle panels, see Fig. 3.1). It leads to a null point at a radius ~ 50 AU on the major axis where the polarization from the scattering cancels that from the direct emission exactly. Closer to the center, the polarization is dominated by the scattering (which produces a higher polarized intensity in this particular example), with a direction along the minor axis; the opposite is true beyond the null point (although this is hard to see clearly in the middle-right panel because of low polarization fraction). In contrast, at locations on the minor axis, the polarizations from both direct emission and scattering are along the same direction; they add to, rather than cancel, each other. The net result is a “butterfly-shaped” pattern for the polarized intensity.

Besides the strong azimuthal variation in the polarization fraction, there is also a significant radial dependence in the direction of the combined polarization. At relatively small radii (within $\sim R_c = 20$ AU), the polarization is dominated by scattering with direction more or less along the minor axis. At larger radii, the direct emission becomes more important, turning the polarization morphology into a more fan-like pattern. This example illustrates the potential richness of the interplay between the polarizations produced by scattering and direct emission in an inclined disk, even though the underlying magnetic field is simple (purely toroidal): the combined polarization varies both radially and azimuthally and in both direction and polarization fraction. In particular, it includes a polarization “hole,” where the polarizations from the two competing mechanisms cancel each other. We should stress that, for this intriguing composite pattern to appear, the polarized intensities from the direct emission and scattering must be comparable. Whether it can happen naturally is

uncertain. In the discussion section, we will return to this and other issues, including the fact that the patterns of the polarization vectors appear very different in the scattering and emission cases for this intermediate inclination $i = 45^\circ$, which should be distinguished observationally.

In the lower panels of Fig. 3.3, we show the case of an even more inclined disk, with $i = 70^\circ$. Not surprisingly, the inclination effect becomes more prominent for the polarizations produced by both scattering and direction emission. Specifically, the polarization from scattering has a direction nearly parallel to the minor axis everywhere, and a polarization fraction close to the maximum value of $1/3$ (see the lower-left panel). This pattern is similar to the highly inclined case with spherical grains, indicating that the effect of grain non-sphericity is largely masked by that of inclination. For the direct emission, the polarization near the major axis is greatly reduced relative to that near the minor axis (the lower-middle panel), producing a much more pronounced “butterfly” pattern than the $i = 45^\circ$ case (the middle-middle panel). The patterns of the polarized intensity are so distinct in the scattering and emission cases that one should be able to tell them apart observationally in principle. In practice, the characteristic “butterfly” pattern would be smeared out in disks with large inclination angles such as $i = 70^\circ$ unless the distribution of the polarized intensity along the minor axis is well resolved spatially. Such well resolved observations should also be able to reveal the difference in the polarization direction and thus help distinguish the two cases.

The total polarization pattern for the highly inclined $i = 70^\circ$ case including both emission and scattering is shown in the lower-right pattern. It appears very different from that of the intermediate inclination ($i = 45^\circ$) case (the middle-right panel). In the $i = 45^\circ$ case, the “butterfly” pattern in the polarized intensity is barely recogniz-

able for the emission only case, but becomes much more prominent in the combined case, because the polarization produced by the emission along the major axis is largely canceled out by that produced by the scattering. In contrast, in the $i = 70^\circ$ case, the “butterfly” pattern is much more prominent for the emission only case, but completely disappears in the combined case, because the low polarized intensity region along the major axis (the gap between the two “wings of the butterfly”) is filled in by the scattering-produced polarization. In any case, the systematic change in polarization pattern from $i = 0^\circ$ to 45° to 70° is driven mainly by the expected decrease of the polarization from emission along the major axis and the increase of that from scattering at the same time.

3.4 The Case of NGC1333 IRAS4A1

IRAS4A is a well studied protobinary system in the NGC1333 region of the Perseus molecular clouds. It is the first protostellar system where a dust polarization pattern corresponding to an “hourglass-shaped” magnetic field is detected on the 1000-AU, inner protostellar envelope (Girart et al. 2006). Given the relatively large scale (and the relatively low corresponding volume and column densities), it is unlikely for the scattering to dominate the observed polarization; the required grain size and column density are too large for the envelope. On this scale, the conventional interpretation involving direct emission by non-spherical grains aligned with respect to a (pinched) magnetic field appears secure.

On the smaller scale of 100 AU, Cox et al. (2015) recently detected polarization at 8.1 and 10.3 mm with VLA for the brighter component, A1, of the protobinary system. The polarization at 8.1 mm, which is significant for more independent beams than that at 10.3 mm, is reproduced in Fig. 3.4 for easy reference.

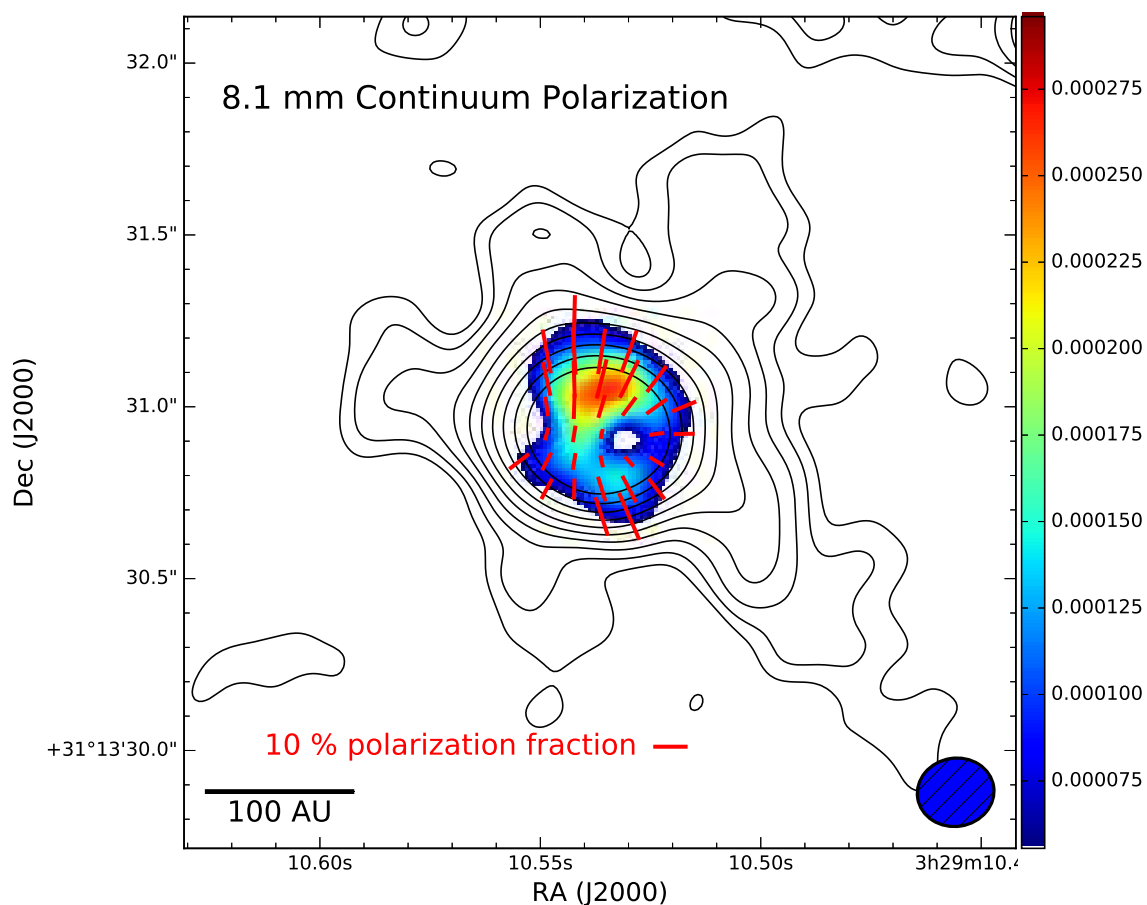


Fig. 3.4.— Polarization observed in IRAS4A1 at 8.1 mm (adapted from Cox et al. 2015). Plotted are the total intensity (contours), polarized intensity (color map), and polarization (rather than magnetic) vectors with length proportional to the polarization fraction. The molecular outflows near the source are roughly in the north-south direction, which implies an approximately east-west orientation for the major axis (Santangelo et al. 2015; Ching et al. 2016).

As stressed by Cox et al., the polarization pattern on the 100 AU scale appears very different from that on the 1000-AU scale. It broadly resembles the pattern expected from direct emission by grains aligned with respect to a toroidal magnetic field in a face-on disk. It is unclear, however, whether a sizable rotationally supported disk exists in this source. The VLA continuum images appear marginally resolved, which may be indicative of a disk not much smaller than the resolution limit (~ 50 AU).

There is, however, little kinematic data on this scale to confirm or reject the possibility of a Keplerian rotation. If the disk is indeed nearly face-on, the disk rotation would be difficult to measure directly. However, the red- and blue-shifted lobes of its bipolar molecular outflows are cleanly separated spatially on the few 100 to few 1000 AU scale (Santangelo et al. 2015; Ching et al. 2016), indicating that the outflows are not exactly along the line of sight and, by implication, the disk is unlikely viewed face-on. If this interpretation is correct, the roughly north-south orientation of the molecular outflows would imply a disk major axis along approximately the east-west direction.

Additional support for an inclined disk comes from modeling of the 8 mm dust continuum emission, which is consistent with an inclination angle of $\sim 35^\circ$. Further evidence for significant inclination may come from the detected polarization pattern itself. The polarization fraction is significantly smaller along the east-west direction than along the north-south direction; such a contrast is not expected in a face-on disk (see the upper panels of Fig. 3.3). It is, however, qualitatively consistent with the polarization pattern produced by direct emission from an inclined disk with the major axis along the east-west direction, as indicated by the molecular outflow orientation. As stressed earlier and illustrated in Fig. 3.3, the polarization fraction is reduced along the major axis relative to that along the minor axis by disk inclination. The magnitude of the contrast, denoted by η , increases with the inclination angle i , and has a weak dependence on the degree of grain non-sphericity (characterized in our model by the grain axis ratio s), as illustrated in Fig. 3.5. It is easy to show, from Equation 3.9, that the contrast is given analytically

$$\lambda \equiv \frac{p_{\text{abs,minor}}}{p_{\text{abs,major}}} \rightarrow \frac{1}{\cos^2 i}, \quad (3.14)$$

in the limit $s \rightarrow 1$ (i.e., as the oblate spheroid approaches a sphere, with $\alpha_3 \rightarrow \alpha_1$).

The above expression provides a good estimate for η for the range of s (between 1 and 2) shown in Fig. 3.5.

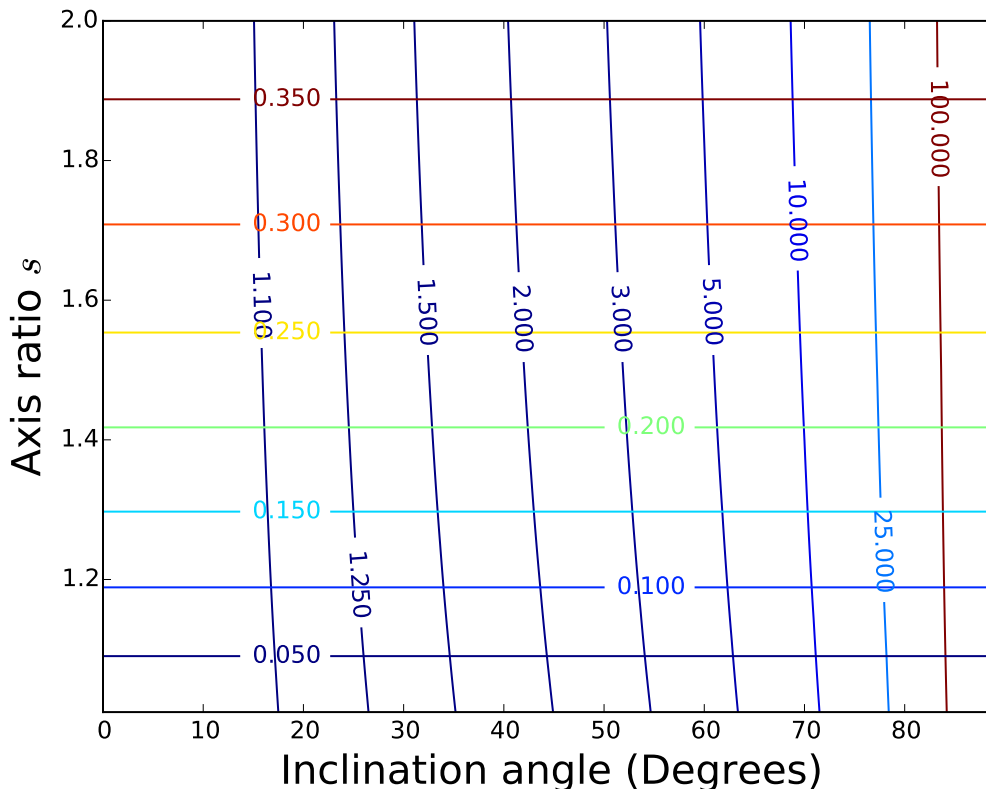


Fig. 3.5.— Lines of constant contrast η in polarization fraction between the minor and major axes (the nearly vertical lines, with values labeled) and constant maximum polarization p_{\max} (horizontal) for direct emission in the plane of inclination angle i and grain axis ratio s . Note that λ depends weakly on s , and approaches $1/\cos^2 i$ as $s \rightarrow 1$.

Also plotted in the figure are lines of constant maximum polarization fraction p_{\max} . This maximum value depends on the grain axis ratio s but not the inclination angle, and is reached at locations along the minor axis (i.e., $p_{\text{abs,minor}} = p_{\max}$). This diagram can help evaluate whether the polarization observed in a particular source comes from direct emission or not.

In the case of IRAS4A1, the polarization fraction is the highest along the minor

axis in the north-south direction (see Fig. 3.4), consistent with the direct emission interpretation. The maximum value in the north is $\sim 18\%$, which is somewhat larger than that in the south ($\sim 12\%$). In the grain model adopted in this chapter, these degrees of polarization correspond to a grain axis ratio s of ~ 1.4 and ~ 1.2 respectively in this interpretation. The upper limit on the inclination angle was set by fitting the 8 mm continuum data to a disk model in the uv -plane, following the method used in Segura-Cox et al. (2016). The shortest baselines ($< 350 \text{ k}\lambda$) were omitted from the data to better exclude envelope emission for the modeling. Since the inclination angle is likely less than ~ 45 degrees based on the continuum modeling⁴, the contrast η should be less than $\sim 1/\cos^2 45^\circ = 2$. This expectation is confirmed in the left panel of Fig. 3.6, where we show the polarization pattern at 8 mm from emission by perfectly aligned oblate grains of 0.6 mm in size and $s = 1.3$ in axis ratio (adopting the same grain material as in § 3.3, which has a complex dielectric constant $\epsilon = 3.78 + 0.0075j$ at 8 mm). The inclination angle was set to $i = 40^\circ$, which is on the high side of the range preferred by the continuum modeling. As expected, there is some contrast between the minor and major axes in the polarization fraction (and polarized intensity). The contrast appears less than that suggested by observation: roughly 12-18% along the (minor) north-south axis and approximately 3-4% along east-west. That is, the contrast η is at least a factor of 3, and likely significantly higher. In order to produce such a high contrast, a disk inclination angle of $\sim \arccos(1/\sqrt{3}) \approx 55^\circ$ or more is needed according to Equation (3.14). Such a large inclination, although cannot be ruled out completely, is unlikely based on the continuum modeling.

Another, perhaps more severe, drawback of the emission only model is that it predicts a purely east-west orientation for the polarization vectors on the major axis,

⁴Ching et al. (2016) suggested a larger inclination angle of $\sim 70 - 80^\circ$ based on outflow modeling, although the inferred angle depends strongly on their model assumptions. If the inclination is indeed this high, the scattering would be more important relative to direct emission.

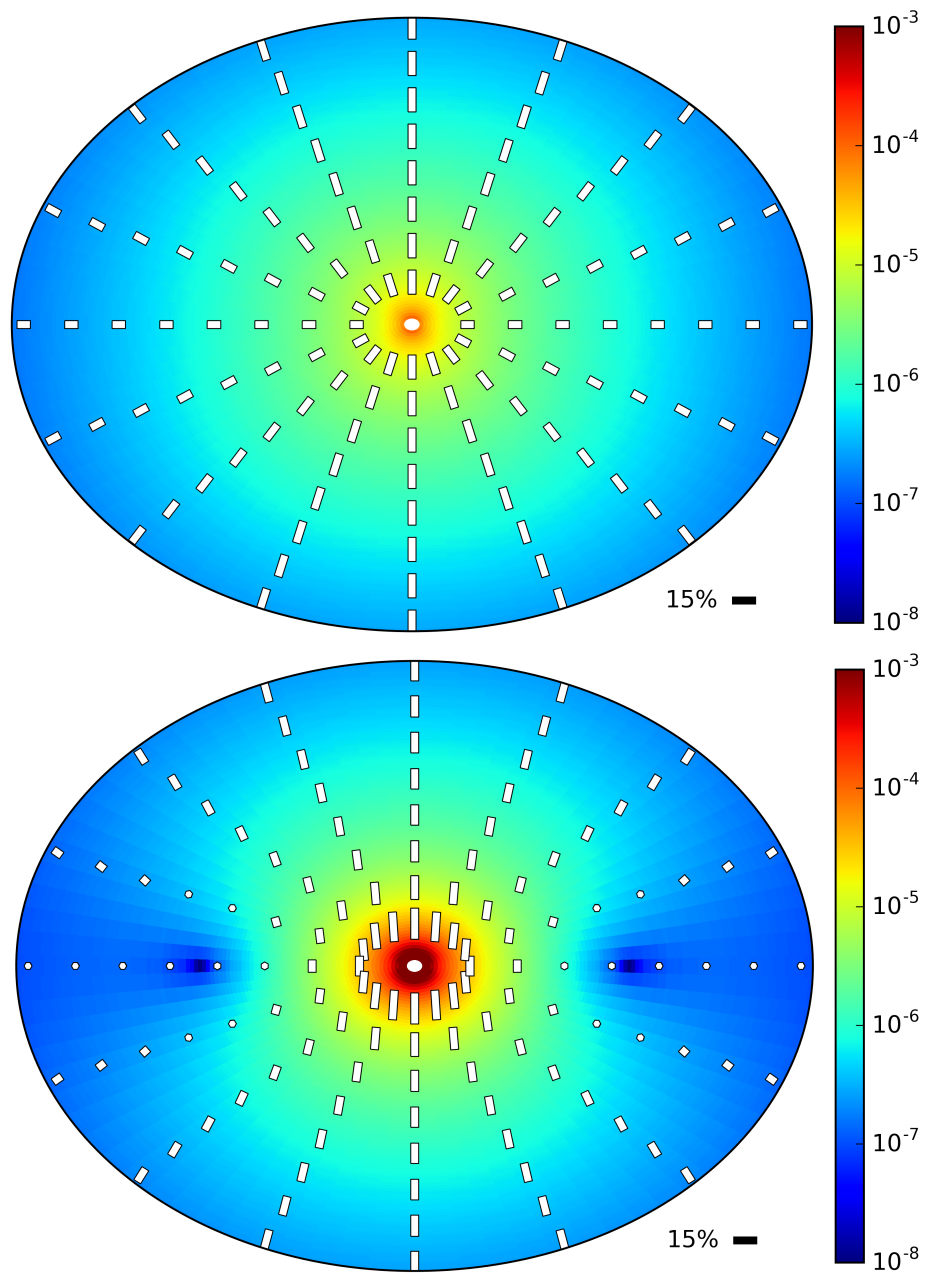


Fig. 3.6.— Polarization models with and without scattering. Plotted are the polarized intensity (in units of $B_\nu(T_0)$, color map) and polarization vectors with length proportional to polarization fraction for emission only (upper panel) and for both emission and scattering (lower panel). The lower panel resembles the observed polarization in IRAS4A1 shown in Fig. 3.4 more closely than the upper panel (see text for discussion).

which matches the observed vectors near the western edge but not those closer to the center, which are oriented more or less north-south (i.e., along the minor axis). The orientations of these central vectors can naturally arise from scattering, which has the added advantage of canceling out some of the polarization produced by emission on the major axis and thus bringing the contrast η closer to the observed level. This is illustrated in the right panel of Fig. 3.6, where we include the contributions to the polarization from both emission and scattering. In this particular example, the scattering dominates the emission near the center and *visa versa* near the edge. Two polarization “holes” are produced at a distance of ~ 25 AU along the major axis, one on each side of the origin. They broadly resemble the polarization “hole” to the west of the center⁵ and, to a lesser extent, the low-polarization “bay” to the east. The inclusion of scattering appears to have improved the agreement between the model and observations significantly, at least in some broad features.

The inclusion of scattering does not improve the agreement in other observed features, however. For example, the north-south asymmetry in the polarized intensity (see Fig. 3.4) cannot be accounted for in our simple semi-analytic model that assumes an axisymmetric disk structure. Asymmetry in the disk properties, such as the dust distribution, could be a culprit. Another discrepancy is that the polarized intensity is peaked at the center in the model but not in the observed map. However, the central region may be optically thick, which would reduce the polarization fraction for both the directly emitted and scattered light (Liu et al. 2016). In any case, more detailed models will be needed to explain these features, especially when they become better quantified with higher resolution and sensitivity observations in the future.

⁵We checked that the polarization “hole” is not where the emission at longer wavelengths (1 and 4 cm) peaks, and is therefore unlikely caused by unpolarized free-free emission.

3.5 Implications and Future Refinements

We have found suggestive evidence that the dust scattering may have contributed significantly to the polarization observed in NGC1333 IRAS4A1 on the 50 AU scale, especially in the central region and along the major axis. However, the concentration of the polarized light along the minor axis and the “fanning out” of most of the polarization vectors point to a polarization pattern dominated by the direct emission from grains aligned with respect to a toroidal magnetic field as the dominant mechanism, especially in the outer regions, with the strong implication that the disk is indeed magnetized. This is very different from the case of HL Tau disk, where the polarized light is concentrated along the major axis, and all polarization vectors are more or less parallel to the minor axis (Stephens et al. 2014). As emphasized in Paper I (see also Kataoka et al. 2016a), these features are explained more naturally by dust scattering than direct emission. These two examples illustrate the diversity of the polarization pattern on the disk scale and the need to include both scattering and direct emission for interpreting the observations. The need will only increase in the near future as ALMA disk polarization observations with higher spatial resolution and sensitivity become available.

There are several factors that determine the relative importance of the scattering and emission in disk polarization, including the grain properties, disk structure and inclination. A key factor is the grain size, to which the scattering opacity κ_{sca} is highly sensitive. This sensitivity is illustrated in Fig. 3.7, where we plot the scattering and absorption opacities as a function of the grain size r_e for oblate grains with an axis ratio $s = 1.5$, obtained using both the electrostatic approximation and discrete dipole approximation (Draine & Flatau 1994, DDSCAT) at wavelength $\lambda = 1$ mm. Also plotted for comparison is the opacity for spherical grains of the same size computed

from the Mie theory. As mentioned earlier, the scattering opacity $\kappa_{sca} \propto r_e^3$ for grains smaller than about $\lambda/(2\pi)$. It starts to exceed the absorption opacity κ_{abs} only for grains larger than $\sim 0.05\lambda$. The sensitive dependence of κ_{sca} on r_e is a double-edged sword. It implies a relatively narrow range in grain size, from $\sim 0.05\lambda$ to $\sim 0.2\lambda$, for the scattering to be competitive with direct emission and the electrostatic approximation adopted in this chapter to hold⁶. Scattering may still dominate direct emission for grains above this size range, but its polarization patterns will likely be quite different from those discussed in this chapter (including, e.g., polarization reversal, Paper I) and will need more elaborated methods, such as the Discrete Dipole Approximation (e.g., Draine & Flatau 1994), to determine; we will postpone such a treatment to a future investigation.

On the other hand, if the polarization pattern observed in a disk requires dust scattering to explain, the size of the scattering grains must lie in a relatively narrow range. The case of IRAS4A1 is particularly interesting in this context. To produce significant polarization at 8 mm by dust scattering, the grains must be roughly millimeter-sized (or larger). In this source, there is evidence for polarization from direct emission as well. If the polarized emission is dominated by the same grains that are responsible for the scattering, it would imply that large, millimeter-sized, grains can indeed be aligned with respect to the magnetic field inside the disk. This inference is important because, compared to the micron-sized (or smaller) grains that are more commonly discussed in the grain-alignment literature, the much larger, millimeter-sized, grains are more difficult to align by radiative torque because of their slower internal relaxation (Hoang & Lazarian 2009) and slower Larmor precession around the field (Lazarian 2007). The latter obstacle can in principle be overcome with a strong

⁶Note that the grain sizes used in § 3.3 and § 3.4 are in this range, so our treatment is self-consistent.

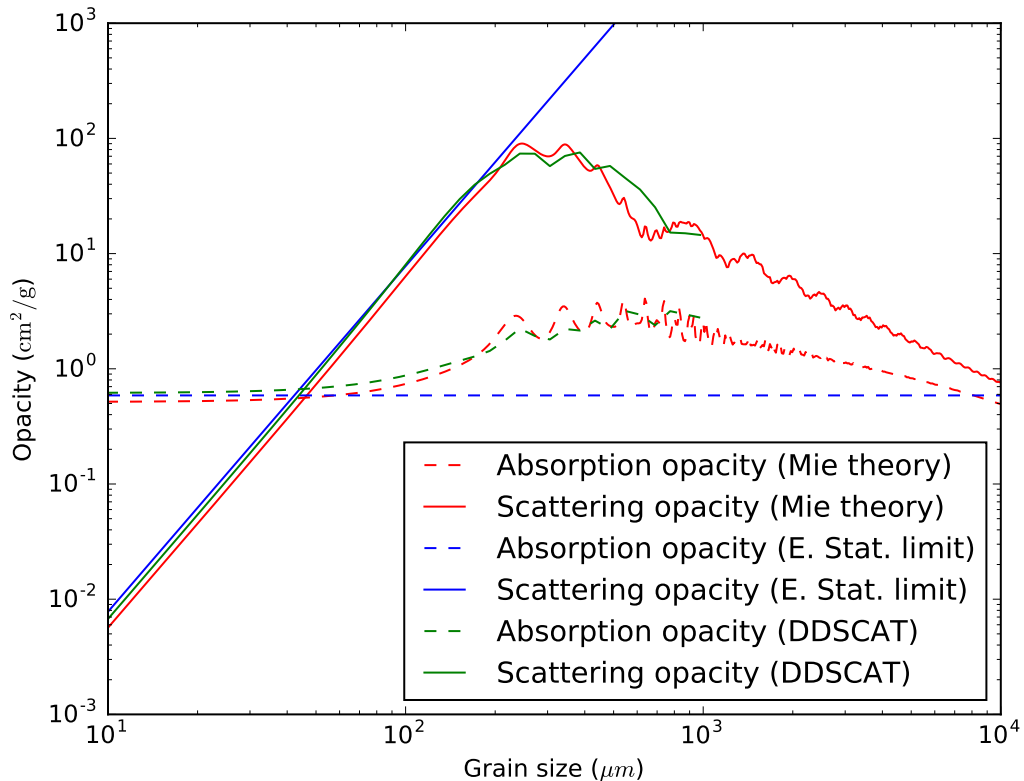


Fig. 3.7.— Scattering (solid line) and absorption (dashed) opacities at 1 mm as a function of grain size for oblate grains with $s = 1.5$ computed using the discrete dipole approximation (green lines) and under the electrostatic approximation for small particles (blue lines). Note that the scattering opacity obtained under the electrostatic approximation is valid up to a grain size of ~ 0.2 times the wavelength λ , and it exceeds the absorption opacity for grains larger than $\sim 0.05\lambda$. Opacities computed from Mie theory for spherical grains of the same size are also shown (red lines) for comparison.

enough magnetic field. Therefore, alignment of large grains can potentially provide an indirect estimate of the lower limit to the field strength that is all-important to the disk dynamics; we will postpone the quantification of this limit to a future investigation.

A potential complication is that the grains responsible for the scattering and direct emission may not have the same sizes. For example, in the case of IRAS4A1,

the central part of the disk where scattering appears to dominate the polarization may have large grains while the direct emission-dominated outer part could have smaller grains. Indeed, there is evidence for such a spatial gradient, with the grain size increasing toward the center, from the distribution of opacity spectral index β in a number of (relatively evolved) disks (e.g., Pérez et al. 2012; Testi et al. 2014; Guidi et al. 2016). The gradient is also expected on theoretical grounds (e.g., Birnstiel et al. 2012). The inward increase in grain size tends to make the scattering-induced polarization more important at smaller radii (in addition to a higher column density there), as appears to be the case in IRAS 4A, although the optical depth close to the center could be substantial, which may invalidate the optical thin approximation and single scattering assumption adopted in the paper. These effects should be treated self-consistently in more refined models in the future, together with the expected spatial variation of grain properties. Another refinement is to include the polarization of the incident light in treating the scattering.

If the observed polarization is dominated by direct emission from magnetically aligned grains, the polarization fraction may provide a handle on the grain shape. For perfectly aligned oblate spheroids, there is a one-to-one relation between the grain axis ratio s and the maximum polarization fraction p_{max} (see Fig. 3.5). For example, values of $p_{max} = 15\%$ and 30% would imply axis ratios of $s \approx 1.3$ and 1.7 , respectively. However, the polarization could also be produced by prolate grains, whose optical properties are similar to those of the oblate grains when averaged around the magnetic field direction (see Appendix A). Furthermore, alignment with the magnetic field may not be perfect, especially for large grains with Larmor precession time scales longer than the disk lifetime. For imperfectly aligned grains, larger deviation from spherical shape is needed to produce the same degree of polarization. Therefore,

there is a degeneracy between different grain shapes (oblate vs prolate) and between the grain shapes and their degrees of alignment that is difficult to break with the observed polarization fraction alone. Grain growth models and detailed grain alignment calculations, together with higher resolution and sensitivity data, may be needed to break the degeneracy.

3.6 Conclusion

Using the electrostatic approximation, we have taken a first step toward developing a general theory for disk polarization in millimeter and centimeter that includes both direct emission from magnetically aligned, non-spherical grains and scattering by the same grains, with an emphasis on the relative importance of these two mechanisms and how they are affected by disk inclination. We have adopted the approximation of unpolarized incident light for scattering, which could affect the polarization produced by scattering at a level up to a few tens of percent (see Appendix B). With this caveat in mind, the main results are as follows:

1. The polarizations produced by scattering and direct emission both depend strongly on the disk inclination, which changes the relative importance of the two, especially along the (projected) disk major axis in the plane of the sky. This change was illustrated analytically with a simple case where oblate grains are perfectly aligned with a purely toroidal magnetic field at a location on the major axis where the incident radiation field is assumed isotropic (see Fig. 3.1). For a nearly face-on disk, both scattering and direct emission produce polarization along the major axis (or radial direction) at the location; they tend to reinforce each other. As the inclination angle i increases, the direction of the scattering-induced polarization switches to the minor axis, with the polarization fraction increasing to $1/3$ as $i \rightarrow 90^\circ$. In contrast, the

polarization produced by direct emission remains along the major axis, with the polarization fraction decreasing monotonically to zero as $i \rightarrow 90^\circ$. Therefore, for large disk inclinations, the polarizations from scattering and direct emission tend to cancel each other on the major axis, with the scattering dominating the direct emission in the limit of edge-on disks. For less extreme disk inclinations, the relative importance of the two competing mechanisms depends on the properties of the dust grains, especially their size and degree of non-sphericity, and the ratio of the Planck function $B_\nu(T)$ for thermal dust emission and the mean intensity J_ν of the incident radiation field to be scattered by the grains.

2. The scattering and direct emission by magnetically aligned, non-spherical grains produce polarization patterns that should be easily distinguishable in general but not always. This was illustrated with a geometrically and optically thin dust disk of a prescribed column density and temperature distribution and a purely toroidal magnetic field (see Fig. 3.3). For significantly inclined disks, the difference between the two mechanisms is most pronounced at locations on the major axis, where the polarized intensity is enhanced relative to that on the minor axis and the polarization direction is along the minor axis for scattering while the opposite is true for direct emission. For nearly face-on disks, the direction of the scattering-induced polarization near the disk center where the radiation field is more or less isotropic in the disk plane is the same as that from direct emission, making it hard to distinguish the two (both radial). At larger radii where the radiation field in the disk plane is more radially beamed, the scattering-induced polarization switches to the azimuthal direction, which is orthogonal to that from the emission. The interplay between these two competing mechanisms can yield interesting new polarization patterns, especially when their polarized intensities are comparable. Particularly intriguing is the pattern

produced in a disk of intermediate inclination with the scattering dominating the inner region of the disk and the emission the outer: the polarization directions are nearly uniform (along the minor axis) at small radii, and become increasingly radial at larger distances, with two “null” points located on the major axis (one on each side of the origin) where the polarizations from scattering and direct emission cancel out exactly. The “null” points serve as a signpost for both mechanisms contributing significantly to the polarization.

3. There is suggestive evidence that the polarization pattern observed in NGC1333 IRAS4A1 at 8 mm is shaped by a combination of direct emission and scattering. The scattering and direct emission naturally account for, respectively, the relatively uniform polarization directions observed in the central region and the roughly radial pattern at larger distances (see Fig. 3.4). Most interestingly, there is clear evidence for at least one “null” point in the observed polarization map, which can naturally be interpreted as the location on the major axis of an inclined disk where the polarizations from the scattering and direct emission cancel each other. The implied disk orientation matches that required for launching the observed molecular outflows.

4. If both direct emission and scattering from the same magnetically aligned grains indeed contribute significantly to the polarization observed in IRAS 4A1, it would imply not only that a magnetic field exists on the disk scale, but that it is strong enough to align large, possibly millimeter-sized, grains, at least in this source, with potentially far reaching consequences for the disk dynamics and evolution. This inference remains tentative, however, in this early stage of observations and modeling of disk polarization. The situation should be greatly improved in the near future with the higher resolution and sensitivity ALMA observations and model refinements.

Appendix

A. Prolate grains and imperfect alignment

In § 3.2.2 and 3.2.3, we have considered in detail only oblate grains. For non-oblate grains that have their shortest axes aligned with the local magnetic field, the situation is qualitatively similar to the oblate grain case, as a result of either rapidly grain rotation around the field line or averaging over an ensemble of grains. For example, consider prolate grains with the semi-diameters $a_1 > a_2 = a_3$ and intrinsic polarizability $|\alpha_1| > |\alpha_2| = |\alpha_3|$. Let the minor axis a_3 be aligned with the magnetic field. The polarizability along the field direction remains unchanged (i.e., $\alpha_{\parallel,3} = \alpha_3$, where the subscript \parallel denotes "parallel" to the local magnetic field), whereas the two components perpendicular to the field become $\alpha_{\perp,1} = \alpha_{\perp,2} = (1/2)(\alpha_1 + \alpha_2)$, which is the average over the azimuthal angle around the field line (see e.g., Lee & Draine 1985a). Therefore, the effective (averaged) polarizabilities for the prolate grains become $|\alpha_{\perp,1}| = |\alpha_{\perp,2}| > |\alpha_{\parallel,3}|$, which have the same ordering as the oblate grain case. In other words, the averaging makes the prolate grains behave effectively as "oblate" grains as far as the polarization is concerned, although their efficiency in producing polarization is reduced somewhat compared to the oblate grains that have the same long-to-short axis ratio (see, e.g., Hildebrand & Dragovan 1995).

Another potential complication is that the grains may not be perfectly aligned with respect to the magnetic field. For example, it is likely for the grains to wobble around the field line (see e.g. Hoang & Lazarian 2012). The wobbling is expected to be more important for larger grains, since their alignment is made less efficient by the longer Larmor precession time. Determining the degree of alignment requires a detailed study of the grain alignment mechanism, which is beyond the scope of this chapter.

Here we illustrate the effects of imperfect alignment through parametrization.

For simplicity, let us consider oblate grains with the symmetric axis along the shortest axis a_3 . Let the grain's shortest axis wobble around the local magnetic field, which is fixed in space, with an instantaneous polar angle θ and azimuthal angle ϕ with respect to the field direction. With a simple frame rotation, we can obtain the polarizability matrix in the lab frame, i.e., the frame fixed with respect to the magnetic field (rather than the wobbling grains). Since the system is symmetric with respect to the field direction, we can average over the azimuthal angle ϕ , which leaves the elements of the polarizability matrix in the lab frame depending only on the polar angle θ :

$$\bar{\alpha} = \text{diag} \left\{ \frac{1}{2}(\alpha_1 + \alpha_3) + \frac{1}{2}(\alpha_1 - \alpha_3) \langle \cos^2(\theta) \rangle, \right. \\ \left. \frac{1}{2}(\alpha_1 + \alpha_3) + \frac{1}{2}(\alpha_1 - \alpha_3) \langle \cos^2(\theta) \rangle, \alpha_1 - (\alpha_1 - \alpha_3) \langle \cos^2(\theta) \rangle \right\} \quad (3.15)$$

where $\text{diag}\{\}$ represents a diagonal matrix and $\langle \cos^2(\theta) \rangle$ is an ensemble average. We can see that the matrix preserves the form of polarizability matrix of oblate grains with two equal components bigger than the third one. When $\langle \cos^2(\theta) \rangle = 1$, we recover the perfect alignment result. In the opposite limit of completely random grain orientation, we have $\langle \cos^2(\theta) \rangle = 1/3$, which yields $\bar{\alpha} = (1/3)(2\alpha_1 + \alpha_3)\bar{I}$, where \bar{I} is the identity matrix. As expected, there would be no polarization from direct dust emission in this case, and the polarization would be completely dominated by scattering. This limiting case is an example of the general trend that imperfect grain alignment tends to increase the importance of scattering relative to direct emission.

To illustrate the above trend further, we consider how imperfect grain alignment, as parametrized by the value of $\langle \cos^2(\theta) \rangle$, affects the transition inclination angle

i_t (discussed in § 3.2.3 and Fig. 3.2) where the polarization produced by scattering cancels that from direct emission completely, for the fiducial value of the ratio $\sigma_{\text{abs}}B_\nu/\sigma_{\text{sca}}J_\nu$. The results are shown in Fig. 3.8. Clearly, for each value of the axis ratio s , the scattering starts to become important at a smaller inclination angle as the grain alignment becomes worse (i.e., as the parameter $\langle \cos^2(\theta) \rangle$ decreases). Another way to interpret the curve for each s in the figure is that, in order for the direct emission to dominate the total polarization, two conditions must be satisfied: (1) the inclination angle i must be less than a critical value (the value of the transition angle i_t in the perfectly aligned limit), and (2) the grains must be sufficiently aligned so that the parameter $\langle \cos^2(\theta) \rangle$ is larger than the value at the intersection of the curve and the vertical line passing through the angle i).

In summary, in the presence of a magnetic field, the local field direction serves as a symmetry axis for the system. Averaging around this axis makes non-oblate grains behave effectively as oblate grains regardless of their shape and degree of alignment. It provides a strong motivation to concentrate on oblate grains with different values of axis ratio s , since the results in the more general cases will be qualitatively similar. The downside of the averaging is that there is a strong degeneracy between the degree of alignment, characterized by the quantity $\langle \cos^2(\theta) \rangle$, and the degree of the grain nonsphericity, characterized by s . In particular, imperfectly aligned “needles” might have similar optical properties as perfectly aligned “pancakes,” making it difficult to tell them apart based on polarization observations.

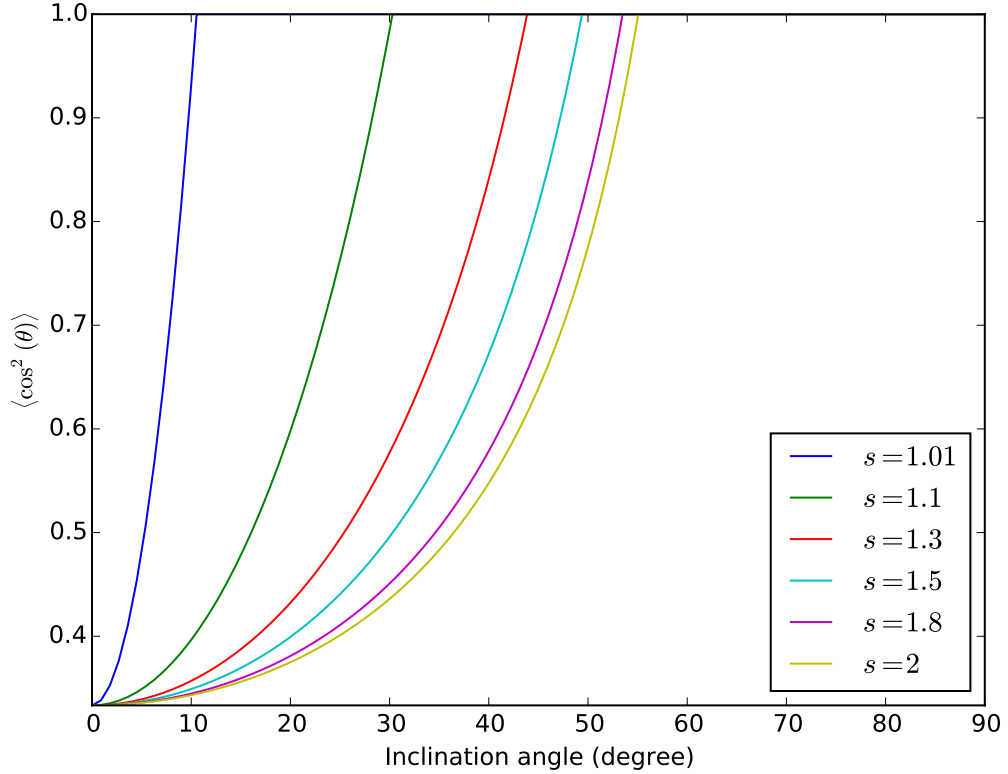


Fig. 3.8.— Effects of imperfect grain alignment, parametrized by the value of $\langle \cos^2(\theta) \rangle$, on the relative importance of scattering and direct emission for polarization for the case of $\sigma_{\text{abs}} B_\nu / \sigma_{\text{sca}} J_\nu = 2$. For each value of axis ratio s , the polarization is dominated by direct emission in the parameter space to the upper-left of the corresponding curve, and by scattering to the lower right.

B. Approximation of unpolarized incident light for scattering

Here we evaluate the effect of the approximation of unpolarized incident light on the polarization produced by scattering. For a disk with a purely toroidal magnetic field, the incident radiation will be polarized along the z direction, i.e., the normal direction of the disk (see the Cartesian coordinate system defined in the second paragraph of § 3.2.2), so that is Stokes parameters $U = V = 0$. In this case, the polarization

fraction of the scattered light can be estimated roughly as:

$$p \sim \frac{\langle I \rangle \langle S_{21} \rangle + \langle Q \rangle \langle S_{22} \rangle}{\langle I \rangle \langle S_{11} \rangle + \langle Q \rangle \langle S_{12} \rangle} \sim \frac{\langle S_{21} \rangle}{\langle S_{11} \rangle} \frac{1 + \tilde{p} \frac{\langle S_{22} \rangle}{\langle S_{12} \rangle}}{1 + \tilde{p} \frac{\langle S_{12} \rangle}{\langle S_{11} \rangle}} \quad (3.16)$$

where $\tilde{p} \equiv \langle Q \rangle / \langle I \rangle$, and the brackets denote angle-averaging. The dust polarization fraction observed in young star disks is of order $\sim 10\%$ (Cox et al. 2015) or less (typically of order 1%; Stephens et al. 2014). If such low values are representative of the polarization fraction of the direct thermal emission, we would expect \tilde{p} to be of this order as well, i.e., $\tilde{p} \sim 1 - 10\%$. The factor $\langle S_{12} \rangle / \langle S_{11} \rangle$ in the denominator of the above equation is of the same order as \tilde{p} , so we expect the correction term $\tilde{p} \frac{\langle S_{12} \rangle}{\langle S_{11} \rangle}$ in the denominator to be of order $\tilde{p}^2 \sim 10^{-2} - 10^{-4}$, which is negligible.

The correction term in the numerator of equation (3.16) is expected to be larger, because the ratio $\langle S_{22} \rangle / \langle S_{12} \rangle$ is typically of order a few (rather than the much smaller \tilde{p}). It is expected to affect the intensity of the scattering-produced polarized radiation at a few to a few tens of percent level.

We do not expect the approximation of unpolarized incident light to significantly affect the polarization pattern produced by scattering, especially in the central region of an axisymmetric disk, where the incident radiation is nearly isotropic in the disk plane. In this case, the same angle-averaging as in Section § 3.2.2 yields $\langle S_{32} \rangle = \langle S_{42} \rangle = 0$, which implies that the scattering of incident light polarized perpendicular to the disk will not produce any U or V component, just as in the case of unpolarized incident light.

Chapter 4

Scattering-Produced (Sub)millimeter Polarization in Inclined Disks: Optical Depth Effects, Near-Far Side Asymmetry, and Dust Settling

This chapter is based on Yang et al. (2017) with minimal modifications.

Abstract

Disk polarization at (sub)millimeter wavelengths is being revolutionized by ALMA observationally, but its origin remains uncertain. Dust scattering was recently recognized as a potential contributor to polarization, although its basic properties have yet to be thoroughly explored. Here, we quantify the effects of optical depth on the

scattering-induced polarization in inclined disks through a combination of analytical illustration, approximate semi-analytical modeling using formal solution to the radiative transfer equation, and Monte Carlo simulations. We find that the near-side of the disk is significantly brighter in polarized intensity than the far-side, provided that the disk is optically thick *and* that the scattering grains have yet to settle to the midplane. This asymmetry is the consequence of a simple geometric effect: the near-side of the disk surface is viewed more edge-on than the far-side. It is a robust signature that may be used to distinguish the scattering-induced polarization from that by other mechanisms, such as aligned grains. The asymmetry is weaker for a geometrically thinner dust disk. As such, it opens an exciting new window on dust settling. We find anecdotal evidence from dust continuum imaging of edge-on disks that large grains are not yet settled in the youngest (Class 0) disks, but become more so in older disks. This trend is corroborated by the polarization data in inclined disks showing that younger disks have more pronounced near-far side asymmetry and thus less grain settling. If confirmed, the trend would have far-reaching implications for grain evolution and, ultimately, the formation of planetesimals and planets.

4.1 Introduction

Polarized (sub)millimeter emission has been observed in an increasing number of disks around young stellar objects. The original motivation for such observations is to detect magnetic fields through linear dichroism of magnetically aligned grains (Cho & Lazarian 2007; Bertrang & Wolf 2017; Andersson et al. 2015); the magnetic fields are widely believed to play a crucial role in the disk dynamics and evolution, through magnetorotational instability (Balbus & Hawley 1991) and magnetocentrifugal disk wind (Blandford & Payne 1982; see Turner et al. 2014 and Armitage 2015 for recent

reviews). The initial searches for disk polarization yielded only upper limits (Hughes et al. 2009, 2013). These were soon followed by detections in IRAS 16293B (Rao et al. 2014) using the Submillimeter Array (SMA), in HL Tau (Stephens et al. 2014), L1527 (Segura-Cox et al. 2015), and Cepheus A HW2 (Fernández-López et al. 2016) using the Combined Array for Research in Millimeter-wave Astronomy (CARMA), and in NGC 1333 IRAS 4A at 8 mm and 1 cm (Cox et al. 2015; Liu et al. 2016) using the Karl G. Jansky Very Large Array (VLA). Most excitingly, there are a large number of approved disk polarization programs using Atacama Large Millimeter/submillimeter Array (ALMA), with some results already published (Kataoka et al. 2016b; Stephens et al. 2017; Lee et al. 2018; Girart et al. 2018). With its unique combination of high resolution and sensitivity, ALMA ushers a new era of rapid growth in the observational study of disk polarization.

Theoretical interpretation of the disk polarization at (sub)millimeter remains uncertain, however. The conventional interpretation is that the disk polarization comes from magnetically aligned non-spherical grains, as on the larger scales of molecular clouds and dense cores (Andersson et al. 2015). Initial calculations of disk polarization from aligned grains assume a purely toroidal magnetic field (Cho & Lazarian 2007; Bertrang & Wolf 2017), as expected in a weakly magnetized disk (Fromang 2013). Such a configuration would produce a polarization pattern that appears inconsistent with the pattern observed in HL Tau (Stephens et al. 2014). The apparent inconsistency led Yang et al. (2016a) to propose that the disk polarization in HL Tau comes from dust scattering, based on Kataoka et al. (2015) theory of scattering-induced millimeter polarization (see also Kataoka et al. 2016a). Specifically, they show that dust scattering in a disk inclined to the line of sight can naturally explain why the observed polarization vectors are roughly parallel to the minor axis and the distri-

bution of polarized intensity is elongated along the major axis. This interpretation will be tested further in the near future with higher resolution ALMA observations at 3 mm and 0.87 mm (Kataoka et al. 2017; Stephens et al. 2017).

There is evidence that scattering may also play a role in producing polarization in other sources, including Cepheus A HW2 (Fernández-López et al. 2016) and HD 142527 (Kataoka et al. 2016b) at (sub) millimeter, NGC 1333 IRAS 4A at centimeter (Cox et al. 2015; Yang et al. 2016b), and AB Aur in mid-IR (Li et al. 2016). If dust scattering really contributes significantly to the observed disk polarization at (sub)millimeter and perhaps even centimeter wavelengths, the implication would be far-reaching: it would provide direct evidence for grain growth, to sizes of order $100 \mu\text{m}$ or larger (Kataoka et al. 2015; see also Pohl et al. 2016), which is the first step toward the formation of planetesimals and ultimately planets. However, although the physics of dust scattering-induced polarization appears sound, whether it indeed contributes significantly to the observed disk polarization is still not completely certain. For example, in the case of HL Tau, Matsakos et al. (2016) shows that magnetically aligned grains may still be able to explain the observation if the disk magnetic field is not dominated by a toroidal magnetic field, but rather has a substantial radial component from, e.g, centrifugal disk winds. The situation is further complicated by the possibility that large (non-spherical) grains may be aligned with the respect to the direction of the anisotropy in the disk radiation field rather than the magnetic field (Tazaki et al. 2017). These uncertainties highlight the need for finding additional distinguishing features of scattering-induced disk polarization. Such features are required in order to use the disk polarization to probe the grain growth and/or magnetic field with confidence.

In this chapter, we explore how the optical depth affects the disk polarization,

focusing on dust scattering. The primary motivation comes from the fact that circumstellar disks tend to be optically thick at relatively short (sub)millimeter wavelengths. For example, the famous HL Tau disk, for which multi-wavelength polarization data have been taken by ALMA, is known to be optically thick at ALMA Band 7 (0.87 mm), especially within a radius of ~ 50 AU (Carrasco-González et al. 2016). This is likely true for the disk around massive protostar HH 80-81 as well, for which polarization is also detected by ALMA (Girart et al. 2018). Such optically thick disks were not treated in our previous semi-analytical work on dust scattering, which was focused on the effects of disk inclination in the optically and geometrically thin limit. Here, we extend the treatment to include both a finite optical depth and a finite thickness for the emitting and scattering dust grains in the disk. We find that, in an optically thick disk of a finite angular thickness in (vertical) dust distribution that is inclined significantly to the line of sight, the polarization pattern becomes asymmetric, with the near-side of the disk significantly brighter than the far-side in polarized intensity. As we will show later, the near-far side asymmetry is a simple consequence of the fact that, in an optically thick disk, the light detected by an observer comes mostly from the surface layer of the disk, which is inclined to the line of sight by a larger angle on the near-side than on the far-side (see Fig. 4.6 below for a cartoon illustration). This generic asymmetry, if detected, would not only add weight to the dust scattering interpretation of disk polarization, but also provide evidence that the large grains ($\sim 100 \mu\text{m}$) responsible for the scattering are not completely settled to the mid-plane.

The rest of the Chapter is organized as follows. We will start with an analytical illustration of the optical depth effects in a one-dimensional (1D) plane-parallel slab in § 4.2, highlighting the difference between the polarization from scattering and

from direct emission from aligned grains. The analytical results lay the foundation for interpreting the results obtained numerically under more complicated geometries. This is followed by radiative transfer calculations to quantify the optical depth effects on the scattering-produced polarization, especially the near-far side asymmetry in an inclined disk, in § 4.3. We discuss the dependence of the near-far side asymmetry on the dust settling and observational evidence that large grains are less settled in younger disks in § 4.4, and the use of the near-far side asymmetry to distinguish the scattering-produced disk polarization from those from either magnetically or radiatively aligned grains in § 4.5. We conclude in § 4.6 with our main results.

4.2 Analytical Illustration of Optical Depth Effects

In order to illustrate how the optical depth affects the polarization analytically, we consider a slab of dust grains that is infinite in the x - and y -direction but has a finite thickness in the z -direction. The grains are assumed to be isothermal and uniformly distributed within the slab. Although our emphasis is on the scattering-produced polarization, we will discuss in this section the polarization produced by direct emission from aligned (non-spherical) grains as well, in order to contrast the optical depth effects in these two competing mechanisms.

4.2.1 Polarization from scattering

For simplicity, we will consider Rayleigh scattering by spherical grains in this subsection. We denote the total optical depth of the slab along the z -direction by τ_{\max} . The optical depth τ is defined as $d\tau = nC_{\text{ext}}ds$, where s is the distance along the light

path, n the number density of the grains, and C_{ext} the extinction cross section. The radiative transfer equation for the Stokes parameters vector $\mathbf{S} \equiv (I, Q, U, V)$ can be written as (see e.g. Tsang et al. 1985, Chapter 3):

$$\frac{d\mathbf{S}}{ds} = -nC_{\text{ext}}\mathbf{S} + nC_{\text{abs}} \begin{pmatrix} B_\nu(T) \\ 0 \\ 0 \\ 0 \end{pmatrix} + n \int d\Omega \bar{M}(\tilde{\phi}) \bar{Z}(\Theta) \mathbf{S}_{\text{in}}, \quad (4.1)$$

where C_{abs} is the absorption cross section, and $\bar{Z}(\Theta)$ is the scattering phase matrix, which takes only one argument, the scattering angle Θ between the incident and scattered light, because of the assumed spherical shape for the grains. The rotation matrix $\bar{M}(\tilde{\phi})$ transforms Stokes parameters from the scattering plane coordinate—the coordinate system used for Rayleigh scattering—to the lab frame. \mathbf{S}_{in} is the Stokes parameters vector for the incident light, which depends on the location of the scatterer and the direction of the light path in general.

The integral on the right hand side of Eq.(4.1) can be treated as the source function for the scattered light. In this case, scattering alone determines how the light is polarized since the direct emission from spherical grains is non-polarized, as indicated by the zeros in the second term. We will first consider an optically thick slab with $\tau_{\text{max}} \gg 1$. If a scattering particle is located deep within the opaque slab, it would see a roughly isotropic incident radiation field and would produce little polarization in its scattered light. In contrast, a scattering particle located within a (vertical) optical depth of order unity or less ($\tau \lesssim 1$) of the surface sees an anisotropic incident radiation field, and has the potential of producing scattered light that is polarized.

To quantify the polarization from the light scattered by particles in the optically

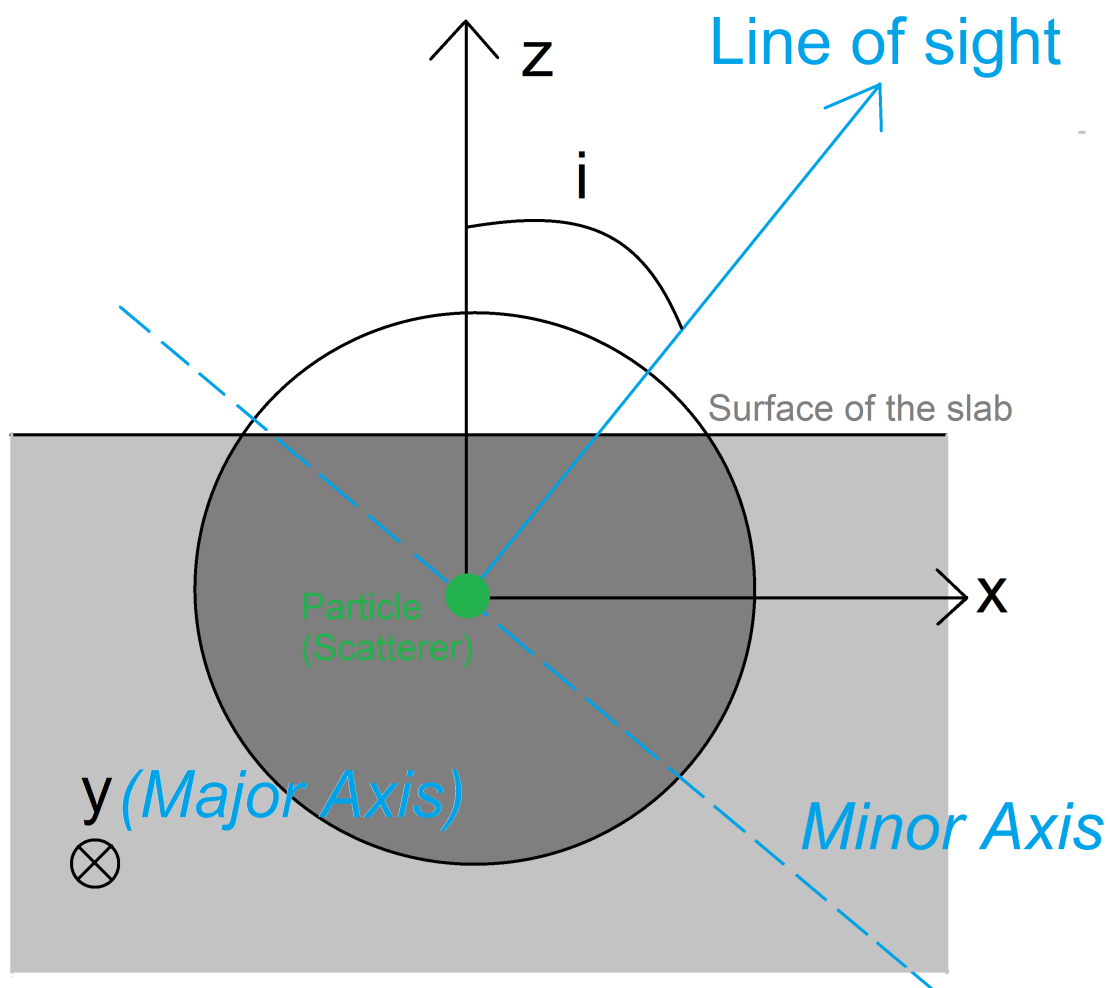


Fig. 4.1.— Coordinate system centered on a scattering particle located in the optically thin layer near the surface of the semi-infinite model. The dashed blue line denotes the direction of the local minor axis as viewed by the observer when the surface of the semi-infinite slab represents a local patch on the disk surface and the local major axis is along the y -axis. The circle indicates a sphere considered in the text around the scattering particle.

thin surface layer, we set up a coordinate system in the frame of the slab with z directed upwards perpendicular to the slab (see Fig. 4.1). The line of sight direction lies in the xz -plane, making an inclination angle i with respect to the z -axis. As viewed by the observer, the y -axis of the slab (pointing into the page in Fig. 4.1) lies in the

plane of the sky. If this slab represented a patch on the surface of an inclined disk, then the y -axis would correspond to the observed major axis; this will be important in § 4.3 below, and we will often refer to the y -axis as the “major axis direction.” The axis perpendicular to the y -axis within the plane of the sky (represented by the blue dashed line in Fig. 4.1) points along the intersection of the xz -plane with the plane of the sky, and it makes an angle i with respect to the x -axis. As viewed by the observer in the case of an inclined disk, this intersection would fall along the minor axis, and we will thus refer to it as the “minor axis direction.”

As we have previously made clear, the total polarization of this slab will be dominated by the radiation from the optically thin region. We will first argue that the polarization direction of this light will be along the minor axis direction, as defined in the previous paragraph. This can be demonstrated by considering the scattered radiation coming from a single scattering particle located at a vertical optical depth having $\tau < 1$. Roughly speaking, the incident radiation as seen by this particle will reside within a sphere of radius corresponding to an optical depth of unity (represented by the circle in Fig. 4.1), and if this sphere is centered on a particle within the optically thin region of the slab then a portion of the sphere will stick out above the upper surface. The net polarization of the scattered light from this particle will then be determined by the net polarization of the incident radiation field it sees from this partially-filled sphere of material.

To determine what this incident polarization will be, let’s first imagine that this sphere were completely filled with thermally-emitting dust grains. If this were the case then the radiation field incident on the central scattering particle would be isotropic, and it would thus retain no net polarization after being scattered by that particle. However, in the actual setup shown in Fig. 4.1, a portion of the sphere (a “cap,”

represented by the white unshaded segment) lies above the surface of the slab and does not contain any emitting dust grains. The net polarization from this partially-filled sphere will then be equal to what we would expect from a completely filled sphere (i.e., zero) minus whatever would have been produced by the missing cap of material. The radiation from the latter would primarily be directed along the $-z$ direction. Because the polarization direction in Rayleigh scattering is perpendicular to both the incident radiation direction and the scattered radiation direction, the radiation from the missing material in the cap would be preferentially polarized along the y -axis (i.e., the major axis direction as seen in the plane of the sky) after being scattered by the particle at the center of the coordinate system. Thus, after subtracting this component from the otherwise unpolarized scattered light that we would have from a completely filled sphere, the net result is a net polarization (for the setup shown in Fig. 4.1) that is along the minor axis direction. This is a key feature that we will use to interpret the numerical results presented in § 4.3 below.

To calculate this degree of polarization along the minor axis direction in an inclined slab in a quantitative way, we need to solve the integro-differential equation (4.1) iteratively. For illustrative purposes, we will make the standard single scattering approximation, which is also assumed below in § 4.3.1 but will be checked in § 4.3.2 using Monte Carlo simulations that include multiple scattering. Under this approximation, the incident radiation \mathbf{S}_{in} on a scattering particle located at a vertical optical depth τ below the surface is unpolarized and is given by the incident unpolarized intensity I_{in} :

$$\frac{I_{\text{in}}(\theta, \tau)}{(C_{\text{abs}}/C_{\text{ext}})B_{\nu}(T)} = \begin{cases} 1 - \exp\left[-\frac{\tau}{\cos(\theta)}\right] & 0 \leq \theta \leq \frac{\pi}{2} \\ 1 & \frac{\pi}{2} \leq \theta \leq \pi \end{cases}, \quad (4.2)$$

where θ is the polar angle measured from the z -axis. All other components of Stokes

parameters of the incident light are 0. With $\mathbf{S}_{\text{in}} = (I_{\text{in}}, 0, 0, 0)$, we can solve equation (4.1) numerically. For a semi-infinite slab ($\tau_{\text{max}} \rightarrow \infty$) inclined by a representative angle $i = 45^\circ$ to the line of sight, we have the Stokes Q :

$$Q_\infty = 0.012 \times \frac{C_{\text{sca}}}{C_{\text{ext}}} \times \left(\frac{C_{\text{abs}}}{C_{\text{ext}}} \right) B_\nu(T), \quad (4.3)$$

where Q is positive along the minor axis direction in the plane of the sky, and

$$I_\infty = \left(1 + 0.81 \times \frac{C_{\text{sca}}}{C_{\text{ext}}} \right) \frac{C_{\text{abs}}}{C_{\text{ext}}} B_\nu(T). \quad (4.4)$$

In the total intensity shown in Eq.(4.4), the first term comes from direct thermal emission. It differs from the Planck function $B_\nu(T)$ because of the scattering in the material. The second term comes from scattering and has the same dependence as Q_∞ shown in Eq.(4.3). The Stokes U and V are expected to be zero. If we take a ratio of Q_∞ and the second term of I_∞ , we get 1.47%. This is the polarization degree of the purely scattered light. It is much smaller than that in the geometrically and optically thin disk cases, which can be as high as $\sim 20\%$ (Yang et al. 2016a). The actual polarization degree (relative to the total intensity, not just the scattered intensity) can be expressed as:

$$p_{\text{sca},\infty} = \frac{0.012C_{\text{sca}}}{C_{\text{ext}} + 0.81C_{\text{sca}}}. \quad (4.5)$$

We can see that, for a given inclination angle i , the polarization degree depends only on the ratio of $C_{\text{ext}}/C_{\text{sca}}$, and that it reaches a maximum value when $C_{\text{ext}} \rightarrow C_{\text{sca}}$, i.e., the extinction is dominated by scattering rather than absorption. In this case, we have $p_{\text{sca},\infty} = 0.66\%$ for $i = 45^\circ$. In Fig. 4.2, we plot the maximum degree of

polarization for a semi-infinite slab as a function of the inclination angle under the single scattering approximation. It is clear that the degree of polarization increases with the inclination angle i except when the line of sight becomes so inclined that it is nearly parallel to the slab. The increase comes about because the light coming from the y -axis direction in the slab is always scattered by 90° by a particle located in the optically thin surface layer (where $\tau < 1$) into the line of sight (and it is thus full polarized for Rayleigh scattering) while that coming from the x -axis direction is scattered by an angle that becomes closer to 0 or 180° (and thus less polarized) as the inclination angle i increases. This is the same argument that we used in Yang et al. (2016a) to explain the increase of polarization degree with inclination angle in a geometrically and optically thin disk. The difference is that this trend continues all the way to $i = 90^\circ$ in Yang et al. (2016a) but not here, because of optical depth effects: the scattered light takes an increasingly longer path out of the slab and thus gets more attenuated as the line of sight becomes more parallel to the surface of the slab.

We can generalize equation (4.2) to the case of a finite slab of (vertical) optical depth τ_{\max} to:

$$\frac{I_{\text{in}}(\theta, \phi, \tau, \tau_{\max})}{(C_{\text{abs}}/C_{\text{ext}})B_{\nu}(T)} = \begin{cases} 1 - \exp\left[-\frac{\tau}{\cos(\theta)}\right] & 0 \leq \theta \leq \frac{\pi}{2} \\ 1 - \exp\left[-\frac{\tau_{\max}-\tau}{|\cos(\theta)|}\right] & \frac{\pi}{2} \leq \theta \leq \pi \end{cases}. \quad (4.6)$$

With the incident radiation field specified, it is again straightforward to integrate the radiative transfer equation (4.1) to determine the degree of polarization viewed from any inclination angle i . As an example, we show in Fig. 4.3 the degree of polarization as a function of the slab optical depth τ_{\max} for a representative angle $i = 45^\circ$. For an optically thin slab with $\tau_{\max} \lesssim 1$, the degree of polarization increases with the optical

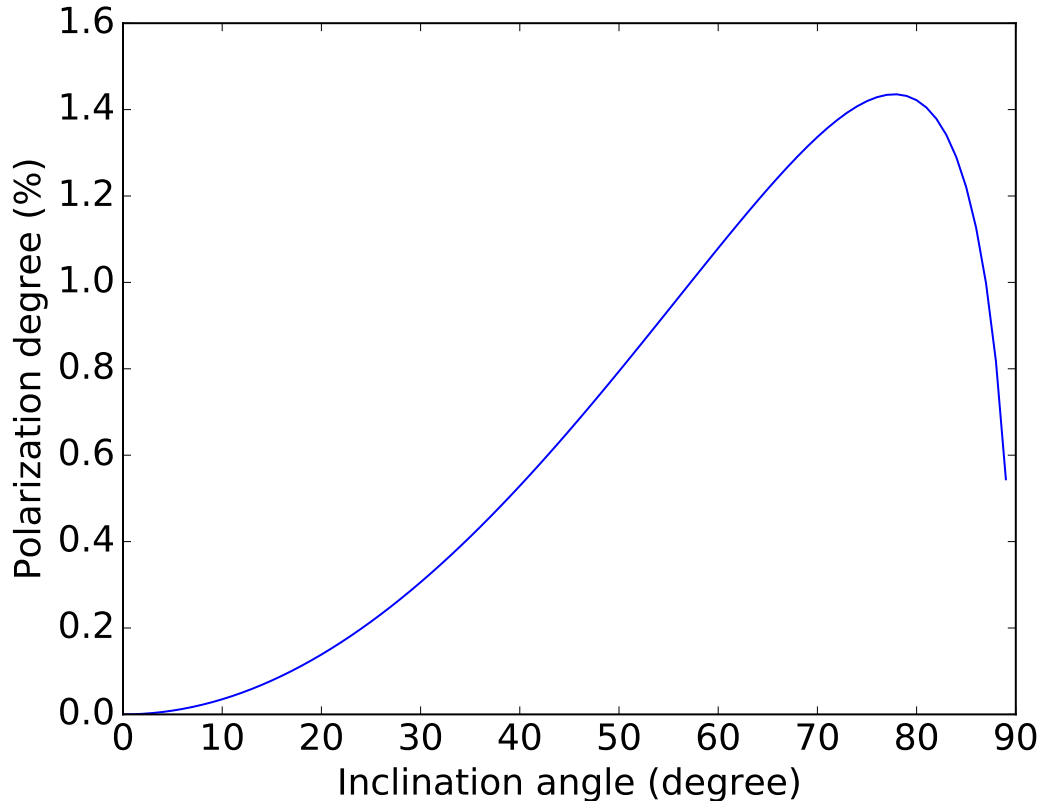


Fig. 4.2.— Maximum degree of polarization from scattering by spherical grains in a semi-infinite slab as a function of the slab inclination angle i with respect to the line of sight ($i = 0$ means face-on) under the single scattering approximation. The polarization peaks at 1.4% for an inclination angle $i = 78^\circ$. The extinction opacity is assumed to be dominated by the scattering.

depth of the slab for a fixed inclination angle. This is expected because, as already pointed out in Yang et al. (2016a), a higher slab optical depth τ_{\max} means more particles emitting more photons to be scattered *and* more scattering particles, the combination of which yields a larger increase in the intensity of the scattered light compared to that of the thermally emitted (non-polarized) light. In the opposite limit of a highly opaque slab ($\tau_{\max} \gg 1$), the polarization degree asymptotes to a constant value, which is 0.66% for the inclination angle adopted here ($i = 45^\circ$). Such opaque slabs are effectively semi-infinite, with a polarization degree approaching that

shown in Fig. 4.2. Note that the polarization degree peaks for a translucent slab with $\tau_{\max} \approx 1$, at a value of 1.44%, which is significantly above the asymptotic value. One can understand this result qualitatively with the help of a sphere of unit optical depth as before: most of the polarization observed outside the slab (from above, say) comes from the scattering particles located in the optically thin layer below the surface, and the unit optical depth sphere centered on such a particle would stick out of both the top and bottom surfaces of the translucent slab, leading to two missing caps (instead of just one) and thus a more anisotropic incident radiation field and a more polarized scattered light compared to the semi-infinite case.

4.2.2 Polarization from direct emission

So far we have only considered spherical dust grains. Light emitted by such dust grains is not polarized, which is also true for randomly oriented non-spherical dust grains. Direct emission from aligned non-spherical grains produces polarization that depends on the optical depth very differently from that from scattering. Non-spherical grains tend to rotate with their shortest principle axis parallel to the external “alignment axis”, which is usually taken to be the magnetic field direction, although other possibilities exist (e.g., Tazaki et al. 2017). Because of their linear dichroism, such grains have different optical depths for the light polarized parallel and perpendicular to the alignment axis, which are denoted by τ_{\parallel} and τ_{\perp} respectively. In the simplest case of uniform grain alignment orientation and isothermal condition, the expected polarization is (Andersson et al. 2015; Hildebrand et al. 2000):

$$p_{\text{emit}} = -\frac{e^{-\tau} \sinh(p_0\tau)}{1 - e^{-\tau} \cosh(p_0\tau)}, \quad (4.7)$$

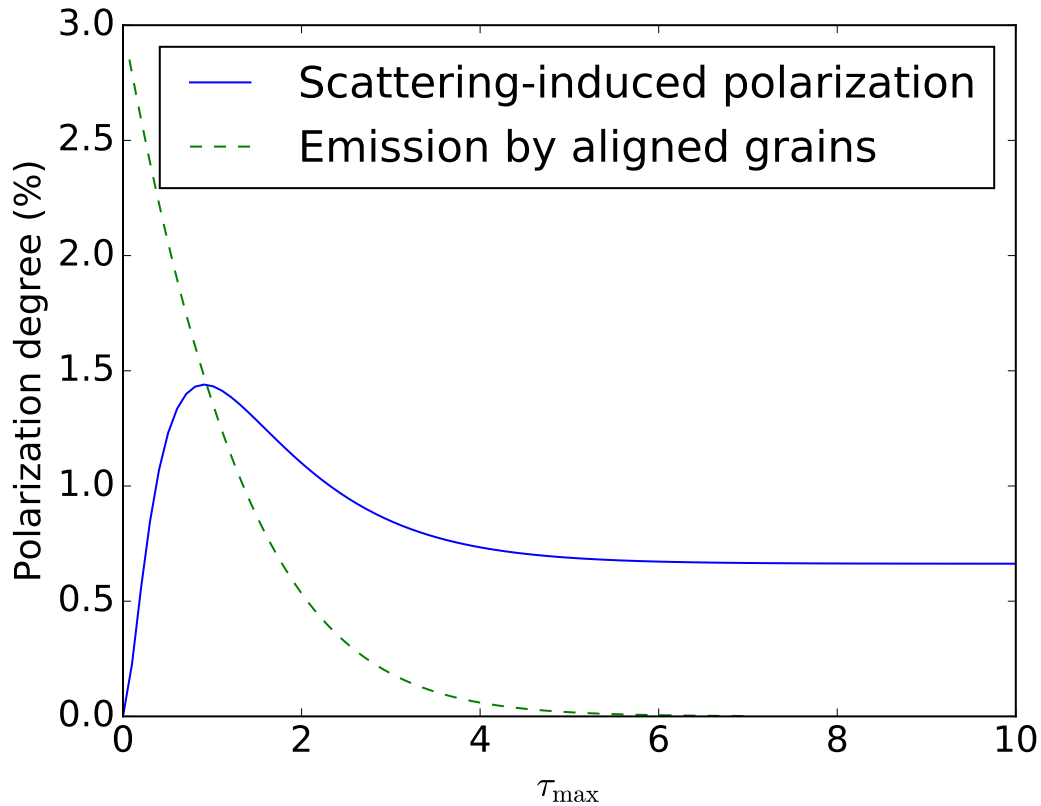


Fig. 4.3.— Variation of the degree of polarization from dust scattering (blue line) and direct emission from aligned grains (dashed green line) with the total optical depth τ_{\max} of an isothermal slab with an inclination angle of 45° . The polarization degree from aligned grains is assumed to be 3% at small optical depth. Note the contrasting behaviors of the two curves at both small and large optical depth limits. See text for discussion.

where $\tau = (\tau_{\perp} + \tau_{\parallel})/2$ is the (averaged) optical depth along line of sight, and the sign of the polarization degree is defined such that positive means polarization parallel to the alignment axis. Note that p_{emit} is always negative, which means that the polarization from direct emission in this isothermal case is, as expected, perpendicular to the alignment axis. The parameter p_0 is defined as

$$p_0 = \frac{\tau_{\perp} - \tau_{\parallel}}{\tau_{\perp} + \tau_{\parallel}}, \quad (4.8)$$

whose value depends on the intrinsic properties of the grain. In the slab model of a finite thickness that we discussed above, the total optical depth along line of sight is $\tau_{\max}/\cos(i)$, where i is the inclination angle. So we have:

$$p_{\text{emit}} = -\frac{e^{-\tau_{\max}/\cos(i)} \sinh(p_0 \tau_{\max}/\cos(i))}{1 - e^{-\tau_{\max}/\cos(i)} \cosh(p_0 \tau_{\max}/\cos(i))}, \quad (4.9)$$

It is clear that the polarization from direct emission is p_0 when $\tau_{\max} \ll 1$ and it decreases monotonically as the optical depth increases, approaching 0 exponentially for $\tau_{\max} \gg 1$. This behavior is very different from the polarization produced by scattering, which increases with the optical depth τ_{\max} of the slab initially, peaking around $\tau_{\max} \sim 1$, before asymptoting to a finite value. The polarization fraction for emission from aligned grains in the optically thin limit, p_0 , depends on many factors, including grain shape, composition and alignment efficiency. It can be quite high on parsec scales or larger (up to $\sim 20\%$; Planck Collaboration et al. 2015), although the (sub)millimeter polarization fraction detected on the scale of protoplanetary disks is typically on the order of a few percent or less (e.g., Stephens et al. 2014). For illustration purposes, we adopt $p_0 = 3\%$ in Fig. 4.3, where the polarization from direct emission by an isothermal slab is plotted as a function of τ_{\max} together with that produced by scattering for the same slab inclination of $i = 45^\circ$. Clearly, the polarization is more likely dominated by scattering than direct emission if the optical depth of the slab is large *and* the temperature is spatially constant.¹

For an optically thick slab with a vertical temperature gradient, the above result no longer holds. As an illustration, we adopt a temperature structure $T(\zeta) = T_0 + a\zeta$, where both T_0 and a are constant and ζ is the distance along line of sight with $\zeta = 0$

¹ The optical depth at which the polarization fractions from emission by aligned grains and scattering become equal depends on the choice of p_0 . For example, its value would change from $\tau_{\max} \approx 1$ to about 4 when p_0 is increased from 3% to 20%.

corresponding to the surface of the slab facing the observer. For a semi-infinite slab (with ζ going from 0 to ∞), the standard Eddington-Barbier relation in radiative transfer yields the intensity at the surface along a given direction, which is equal to the source function at an optical depth of 1 along that direction. However, since the opacity is different for light polarized parallel and perpendicular to the axis of grain alignment, differently polarized light reaches optical depth of 1 at different physical depths. In this non-isothermal case, the polarization degree is given by:

$$p'_{\text{emit}} = \frac{\frac{1}{2}a(\alpha_{\perp} - \alpha_{\parallel})}{T_0\alpha_{\perp}\alpha_{\parallel} + \frac{1}{2}a(\alpha_{\perp} + \alpha_{\parallel})}. \quad (4.10)$$

where we've assumed Rayleigh-Jeans limit for the thermal emission and $\alpha_{\parallel(\perp)} \equiv \tau_{\parallel(\perp)}/\zeta$ is the absorption coefficient for light with polarization parallel (perpendicular) to the alignment axis. In general, dust grains are aligned with their long axis perpendicular to the alignment axis, so that $\alpha_{\perp} > \alpha_{\parallel}$. As a result, the above expression gives a positive polarization degree, which means that the polarization is parallel to the alignment axis for a positive temperature gradient a . This is the opposite of the isothermal case, where the polarization is perpendicular to the alignment axis (see Eq. (4.7)). In the case of grains aligned by a magnetic field, the alignment axis will be the field direction. Although the general expectation is that the thermal dust emission is polarized perpendicular to the field direction, Equation (4.10) demonstrates that this may not be true in the presence of a temperature gradient along the line of sight. This simple exercise drives home the point that, in optically thick regions, the interpretation of polarization from aligned grains is not as straightforward as in the familiar optically thin limit, and can depend strongly on temperature distribution. We will postpone a more detailed exploration of this important point to a future investigation.

4.3 Near-far side asymmetry in the polarization of inclined disks

In this section, we aim to quantify the effects of optical depth on the scattering-induced polarization in an inclined disk of young stellar object, focusing on the difference between the near and far side of the disk. For simplicity, we will assume spherical grains as in § 4.2.1, and postpone a treatment of scattering by aligned non-spherical grains to a future investigation. We will solve the transfer equation (1) for the polarized light in two complementary ways: using formal solution under the approximation of single scattering (§ 4.3.1) and through Monte Carlo simulations (§ 4.3.2). The former is conceptually straightforward and mathematically simple, involving only direct integration along straight lines. It is well suited for illustrating the basic effects of optical depth. The latter is more general, with multiple scattering taken into account self-consistently, but produces noisier results that are harder to interpret physically.

4.3.1 Formal solution under single scattering approximation

In the presence of scattering, the radiative transfer equation (1) is an integro-differential equation that is difficult to solve in general. The solution is simplified by the single scattering approximation, where the incident radiation \mathbf{S}_{in} to be scattered by dust grains at any location is assumed to come solely from direct thermal emission. Since the dust grains are assumed to be spherical and thus emit only unpolarized light, \mathbf{S}_{in} can be written as $(I_{\text{in}}, 0, 0, 0)$, with I_{in} determined by:

$$\frac{dI_{\text{in}}}{ds'} = -nC_{\text{ext}}I_{\text{in}} + nC_{\text{abs}}B_{\nu}(T), \quad (4.11)$$

which has the following formal solution:

$$I_{\text{in}} = \int_0^\infty e^{-\int_0^{s'} n(s'') C_{\text{ext}} ds''} n(s') C_{\text{abs}} B_\nu(T(s')) ds'. \quad (4.12)$$

In the above expression, we have explicitly written the dependence of number density n and temperature T on the location, described by the distance s' from the scatterer along a given direction \mathbf{n}' . The cross sections C_{ext} and C_{abs} are taken to be constant for simplicity, although they could vary spatially in general, due to, e.g., variation in grain size distribution. Such additional complications will be explored in future investigations.

Once the incident radiation \mathbf{S}_{in} is determined, we can compute through straightforward integration the Stokes parameters for the scattered light \mathbf{S}_{sca} (the third term on the right hand side of equation [1]) which, together with the (non-polarized) thermal dust emission, serves as the source for the formal solution that determines the Stokes parameters along any line of sight through the disk.

Disk model

For illustration purposes, we will adopt the disk model used by Kwon et al. (2011) to fit the millimeter observations of the HL Tau disk. It is a standard viscous accretion disk model with a density profile for dust grains only (assuming a dust-to-mass ratio of 100):

$$\rho(R, z) = \rho_0 \left(\frac{R}{R_c} \right)^{-p} \exp \left[- \left(\frac{R}{R_c} \right)^{3.5-p-q/2} \right] \exp \left[- \left(\frac{z}{H(R)} \right)^2 \right], \quad (4.13)$$

where R and z are the coordinates for a cylindrical coordinate system, R_c a characteristic radius of the disk (dust) density distribution, and $H(R)$ the (dust) scale

height at a radius R , determined by hydrostatic equilibrium in the vertical direction in the case of no dust settling (the effects of dust settling will be discussed in § 4.4 below). The scale height scales with radius as $H(R) = H_0(R/R_c)^{1.5-q/2}$.

The q parameter is the temperature power law index $T \propto R^{-q}$. To account for the surface heating by stellar irradiation approximately, a two-component temperature distribution is adopted, with $T(R, z) = WT_m(R) + (1 - W)T_s(r)$, where $T_m(R) = T_0(R_0/R)^q$ and $T_s(r) = T_{s0}(r_{s0}/r)^q$ are the mid-plane and surface temperature distribution, respectively, $r = \sqrt{R^2 + z^2}$ is the spherical radius, and $W = \exp[-(z/3H(R))^2]$ is chosen to mimic the temperature profile computed self-consistently. The values for the parameters that Kwon et al. (2011) found to be the best fit to the HL Tau disk data are listed in Table 4.1. We leave the density scale ρ_0 as a free parameter, in order to explore the effects of the disk column density (and thus optical depth for a given grain size distribution). We will consider a range of values for ρ_0 , including an extreme case with $\rho_0 = 1.124 \times 10^{-14} \text{ g/cm}^3$, corresponding to a disk mass of about 1 solar mass (motivated by the ALMA polarimetric observations of the HH80-81/IRAS 18162–2048 massive protostar, J.M. Girart, in preparation, see discussions in § 4.4.2), where the optical depth effects are most apparent.

For grain properties, we adopt the spherical dust grain model used in Kataoka et al. (2015) and Yang et al. (2016a). It is a composite grain model with abundances consistent with Pollack et al. (1994), which are composed of 8% silicate, 62% water ice and 30% organic by volume. For illustration purposes, we will first consider single-

R_c	79 AU	p	1.064
q	0.43	H_0	16.8 AU
T_0	70 K	R_0	10 AU
T_{s0}	400 K	r_{s0}	3 AU

Table 4.1: Parameters for the disk model.

sized spherical dust grains² with radius $100 \mu\text{m}$ to maximize the effects of scattering at 1 mm; smaller grains that scatter millimeter light less efficiently are considered in § 4.3.2. At 1 mm wavelength, the scattering and absorption opacities are $\kappa_{\text{sca}} = 6.35 \text{ cm}^2/\text{g}$ and $\kappa_{\text{abs}} = 0.738 \text{ cm}^2/\text{g}$, respectively, based on Mie theory (Bohren & Huffman 1983).

Results

In this subsection, we present and discuss the results of integrating the formal solution numerically, focusing on the effects of the optical depth in a disk inclined to the line of sight by 45° , similar to the value obtained for the HL Tau disk (ALMA Partnership et al. 2015; Kwon et al. 2011). To make connection with previous (semi-analytical) work, we start with an optically thin case, with the density scale ρ_0 set to $1.13 \times 10^{-16} \text{ g cm}^{-3}$ (Model A in Table 4.2). This corresponds to a characteristic absorption optical depth vertically through the disk at the characteristic radius $R_c = 79 \text{ AU}$ of $\tau_{\text{c,abs}} = 0.0136$ at 1 mm wavelength; the scattering optical depth is larger ($\tau_{\text{c,sca}} = 0.117$), but still much less than unity. In this case, the total intensity, shown in Fig. 4.4a, appears symmetric between the near- and far-side (to the left and right of

²We only consider single-sized grains in this work. In the limit of Rayleigh scattering under consideration, grains of a range of sizes can be represented by single-sized grains of a certain (equivalent) radius.

Model name	a (μm)	ρ_0 (g/cm^3)	H_0 (AU)
A	100	1.124×10^{-16}	16.8
B	100	1.124×10^{-15}	16.8
C	100	1.124×10^{-14}	16.8
D	37.5	1.124×10^{-14}	16.8
E	10	1.124×10^{-14}	16.8
F	100	1.124×10^{-13}	1.68

Table 4.2: Different models used in this chapter.

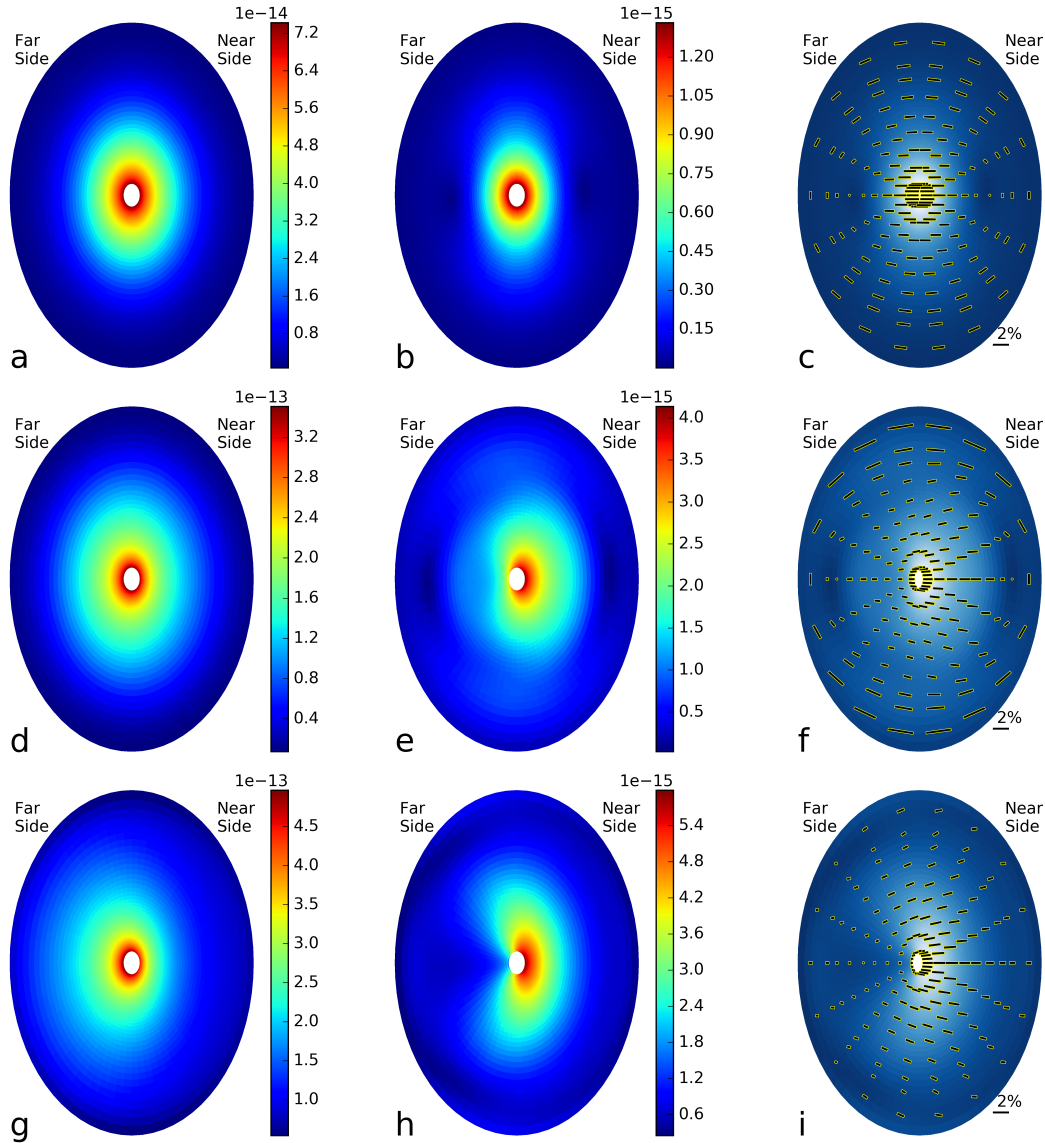


Fig. 4.4.— Distributions of the total intensity (left panels), polarized intensity (middle) and polarization vectors (right panels, with length proportional to the polarization degree) for three disk models with increasing density scale $\rho_0 = 1.13 \times 10^{-16}$ (Model A; top panels), 1.13×10^{-15} (Model B; middle), and $1.13 \times 10^{-14} \text{ g cm}^{-3}$ (Model C; bottom). Intensities are in unit of $\text{erg} \cdot \text{s}^{-1} \cdot \text{sr}^{-1} \cdot \text{cm}^{-2} \cdot \text{Hz}^{-1}$.

the major axis respectively), as expected for an optically thin disk. The polarization pattern, shown in Fig. 4.4b and 4.4c, is very similar to that obtained by Yang et al. (2016a) semi-analytically based on the simplification that the disk is both optically

and geometrically thin (see their Fig. 7). Specifically, the distribution of the polarized intensity is elongated along the major axis and the polarization vectors in the central region are oriented roughly along the minor axis. As discussed in depth in Yang et al. (2016a), both of these features are the consequences of a simple geometric effect: the incident light along the major axis is scattered by 90° into the line of sight and is thus maximally polarized. The polarization degree (about 1.5% here) is also quantitatively consistent with that in Yang et al. (2016a) (slightly bigger than 1%) for the following reason. The grain size a adopted here is about 3 times larger ($100 \mu\text{m}$ vs $36 \mu\text{m}$), which makes the scattering opacity ($\propto a^3$ for Rayleigh scattering) and thus the polarization degree a factor of about $3^3 = 27$ larger. On the other hand, the density scale ρ_0 for this model is about 5% of that in Yang et al. (2016a), which reduces the scattering opacity by a factor of about 20. As a result, we expect the polarization here to be $\sim 27/20 = 1.35$ times that in Yang et al., which is close to our result. The polarization pattern starts to deviate more from that of the optically and geometrically thin case as the optical depth increases, as we show next.

The optical depth can be varied in several ways, including through the disk density, grain properties, and the observing wavelength. Here, we will focus on the effects of varying the optical depth through the density scale ρ_0 , increasing it by a factor of 10 (Model B in Table 4.2) and 10^2 (Model C), respectively. The results are shown in Fig.3, which contrasts the total intensity distributions and polarization patterns for the three cases of different densities. In Model B where the density is increased by a factor of 10 over that of Model A, the characteristic absorption optical depth remains well below unity ($\tau_{\text{c,abs}} = 0.136$), although this is no longer true for the scattering optical depth ($\tau_{\text{c,sca}} = 1.17$). The higher optical depth leads to a drastic asymmetry in the distribution of the polarized intensity, with the near side (to the right of

the major axis) much brighter than the far side (to the left of the major axis; see Fig. 4.4e). This happens despite the fact that the total intensity I is slightly higher on the far side than the near side (Fig. 4.4d), because of the disk geometry, especially the finite angular thickness of the disk (see Fig. 4.6 and associated discussion below). It follows immediately that the light from the near side is much more polarized than that from the far side, as shown in Fig. 4.4f, where the polarization vectors are plotted with the vector length proportional to the polarization degree. Note that most polarization vectors in the central region are no longer parallel to the minor axis as in the optically and geometrically thin case (Yang et al. 2016a): they become significantly rotated with respect to the minor axis direction. The rotation is especially evident at locations along the major axis where the polarization orientation rotates counterclockwise from the minor axis in one direction in the top hemisphere and in the opposite (clockwise) direction in the bottom. This bifurcation in polarization orientation is a major consequence of the higher optical depth in a disk of significant angular thickness. It becomes even more apparent in Model C, where the disk density is increased by another factor of 10 (see Fig. 4.4i), so that both the absorption and scattering optical depths at the characteristic radius exceed unity ($\tau_{c,\text{abs}} = 1.36$ and $\tau_{c,\text{sca}} = 11.7$). In this densest disk that is optically thick to both absorption and scattering, the polarized intensity becomes “kidney” shaped (Fig. 4.4h), showing extreme near-far side asymmetry. The asymmetry in total intensity also becomes more prominent (Fig. 4.4g).

The near-far side asymmetry is further quantified in Fig. 4.5, where the polarization degree along the minor axis is plotted against the distance from the center for all three models in the left panel. A negative value for the polarization degree means that the polarization is along the major axis rather than the minor axis direction.

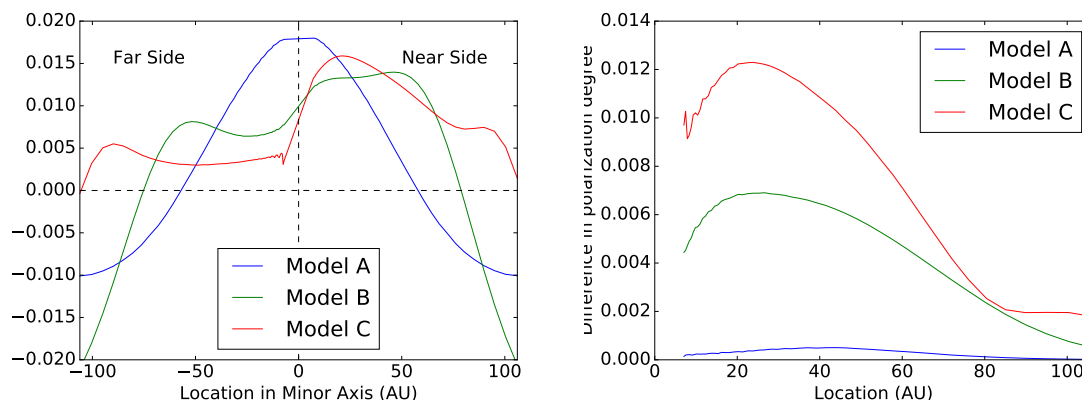


Fig. 4.5.— Left panel shows the polarization degree along the minor axis for the three models with different density scales, with the near side to the right of the central vertical line and the far side to the left. Positive polarization degree indicate a polarization along minor axis, whereas a negative value corresponds to a polarization along major axis. Right panel shows the difference in polarization degree for pairs of points along minor axis plotted against distance from the center of the disk for the same three models. Note the increasing near-far side asymmetry as the density (and thus optical depth) increases.

It is clear that the polarization degree is very symmetric in the most optically thin Model A. As the optical depth increases, the polarization degree on the near side of the disk (the part with positive distance from the center) stays high; indeed, it becomes larger than the optically thin case at some locations. The polarization degree on the far side (the part with negative distance from the center), on the other hand, is significantly reduced, by a factor of ~ 2.5 for the moderately optically thick Model B and ~ 4 for the most optically thick Model C. This increase in asymmetry with optical depth is shown even more explicitly in the right panel of Fig. 4.5, where we plot the difference between the polarization degrees at pairs of symmetric points on the minor axis against the distance from the center. Note that the difference is smaller at larger distances, especially beyond the characteristic radius $R_c = 79$ AU, where the density (and thus column density) drops precipitously. This trend is consistent with the expectation that the asymmetry is controlled mainly by the optical depth for a

given (dust) disk geometry.

We can understand the role of the optical depth in breaking the near-far side symmetry using the semi-infinite analytical model presented in § 4.2.1 in the following way. In the case of a highly optically thick disk, the light observed along any line of sight comes from a thin layer near the disk surface, making the emitting region effectively plane-parallel and semi-infinite locally. In this case, the degree of polarization produced by scattering is sensitive to the inclination of the local disk surface to the line of sight, as illustrated in Fig. 4.2. This local inclination angle is different for the near and far side for any disk of a finite angular thickness, as illustrated in Fig. 4.6. Specifically, for a pair of points located symmetrically on either side of the center along the minor axis, the inclination angle for the point on the near side (i' in the cartoon) is larger than that on the far side (i''). The larger inclination angle leads to a higher degree of polarization, unless the angle is close to 90° . In the latter case, the situation is more complicated, because the light on the near side would come increasingly from the outer (radial) edge of the disk rather than its (top) surface. Note that for the same symmetric pair of points, the one on the far side of the disk surface is closer to the star (see Fig. 4.6), and is thus brighter in total intensity I because of a higher temperature. This naturally explains the near-far asymmetry in the total intensity, which is most prominent in the most optically thick case and is in a sense opposite to that of the asymmetry in the polarized intensity (see Fig.4.4). In other words, the near side of an optically thick disk has a higher polarized intensity despite the fact that its total intensity is lower. These gradients in intensity and polarized intensity together results in much higher polarization fractions on the near side of the disk than the far side of the disk.

Besides the near-far side asymmetry in polarized intensity, another important

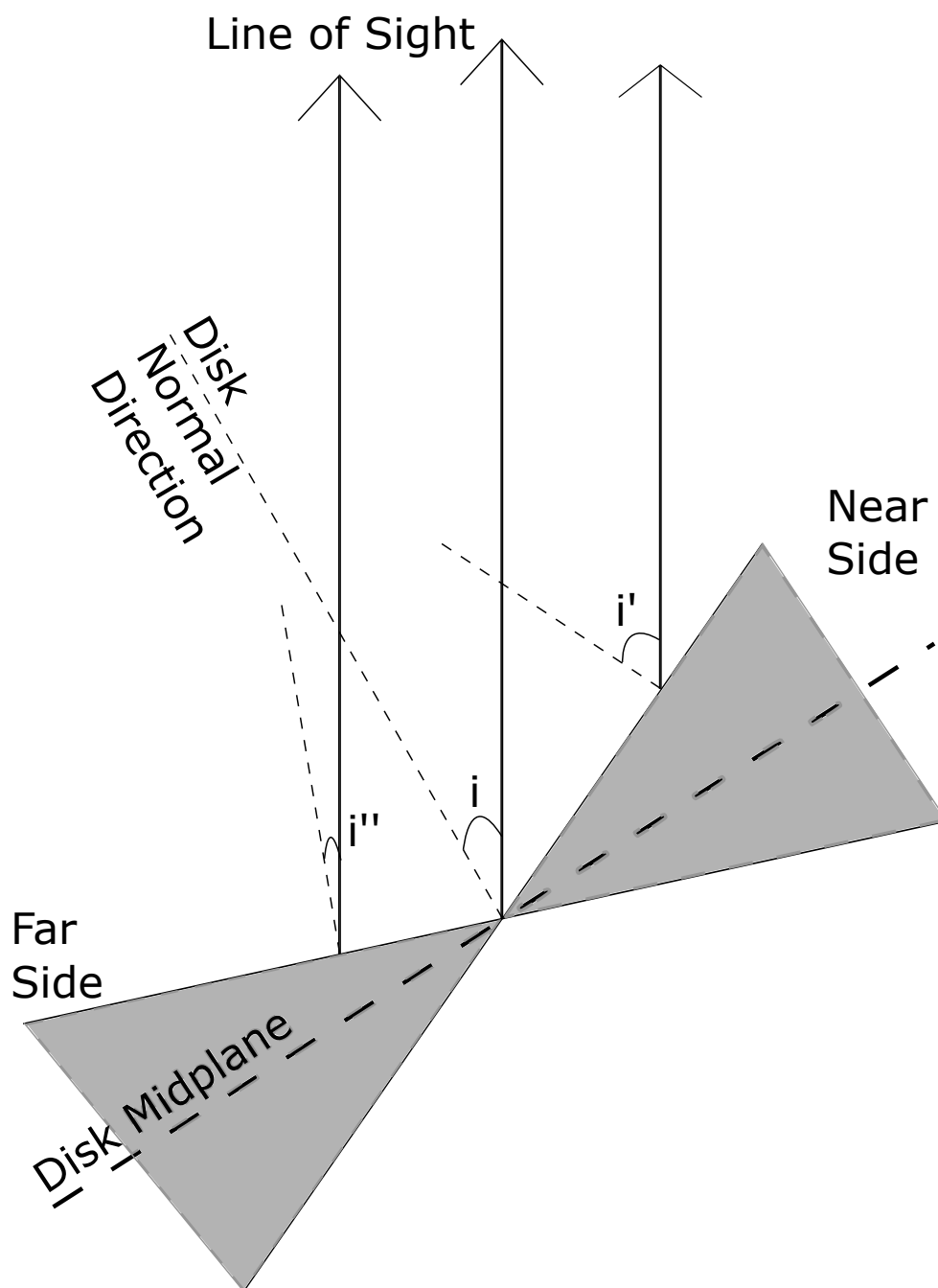


Fig. 4.6.— Illustration of the “local inclination angle” of the disk surface to the line of sight. The gray shaded region represents the disk. The line of sight makes a larger angle to the normal of the disk surface on the near side (denoted by i') than that on the far side (i''). This difference in local inclination angle is the main reason for the near-far side asymmetry in the polarized intensity for optically thick disks.

optical depth effect is the bifurcation in polarization orientation along the major axis. In the geometrically and optically thin case discussed in Yang et al. (2016a), the polarization vectors at locations on the major axis are roughly uni-directional (parallel to the minor axis; see also Fig. 4.4c). As the optical depth increases, the vectors start to rotate more and more away from the minor axis direction and in opposite directions for the upper and lower hemispheres (see Fig. 4.4f and 4.4i). We will denote the angle between the polarization direction and the minor axis by θ_{offset} . This effect is shown more quantitatively in Fig. 4.7, where the offset angle θ_{offset} is plotted against the distance along the major axis for the three models with different density scales. It is clear that θ_{offset} is close to zero for the most optically thin case, but becomes more significant for denser disks. In addition, for each disk, θ_{offset} decreases quickly at large radii, where the surface density also quickly decreases. Both of these trends support the notion that the offset is an optical depth effect. Furthermore, the offset angle is positive in the upper hemisphere (defined as rotating counterclockwise from the west in the right panels of Fig. 4.4) but negative in the lower hemisphere (rotating clockwise from the west), showing explicitly the bifurcation of polarization orientation along the major axis. In other words, the position angle of the polarization vector is inclined in a mirror-symmetric manner with respect to the minor axis of the disk that is assumed to be intrinsically axisymmetric.

This effect can also be understood with the help of the analytical model developed in § 4.2.1, where we showed that, for a semi-infinite slab, the polarization direction is along the local “minor axis” (see Fig. 4.1). As we discussed earlier, in a highly optically thick disk, the light we see along any line of sight comes from a small patch on the disk surface facing the observer that is effectively plane-parallel and semi-infinite. The light from that patch is therefore expected to be polarized along the

direction of the *local* minor axis, which lies at the intersection of the plane of the sky and the plane containing the normal of the local disk surface and the line of sight. For a disk of finite angular thickness, this *local* minor axis is different from the *global* minor axis, which is defined by the normal of the disk *mid-plane* (or the rotation axis of the disk). This is especially true for a flared disk, where the normal of the local disk surface becomes increasingly misaligned with respect to the global (rotation) axis as the radius increases. The increasing misalignment between the local disk normal and the global axis leads to an increasingly large offset angle θ_{offset} between the local minor axis and the global minor axis in the plane of the sky, especially at locations along the global major axis. This is illustrated in Fig. 4.7, where the variation of the offset angle θ_{offset} is plotted as a function of radius (the dashed blue line) as one moves away from the center along the global major axis on a surface one scale height $H(R)$ above the disk mid-plane. The curve agrees remarkably well with that of the most optically thick case inside the characteristic radius $R_c = 79$ AU, which supports our geometric interpretation of the offset. Beyond R_c , the column density drops quickly, making the disk increasingly optically thin and the surface of one scale height increasingly less representative of the $\tau = 1$ surface. The disagreement beyond R_c is therefore to be expected; it strengthens (rather than weakens) our interpretation.

Note that, in Fig. 4.7, we chose to plot the offset angle θ_{offset} only along the major axis, even though the effect is not limited to these locations. There are two reasons for this choice. First, the polarization orientations there are all along the minor axis (i.e., $\theta_{\text{offset}} = 0$) in optically thin limit, which makes it easier to highlight the optical depth effects. Just as importantly, it is easier to check the results with simple geometric disk surface models on the major axis than elsewhere, as we have done in Fig. 4.7 (the dashed blue line). We reiterate that the polarization orientations on the major

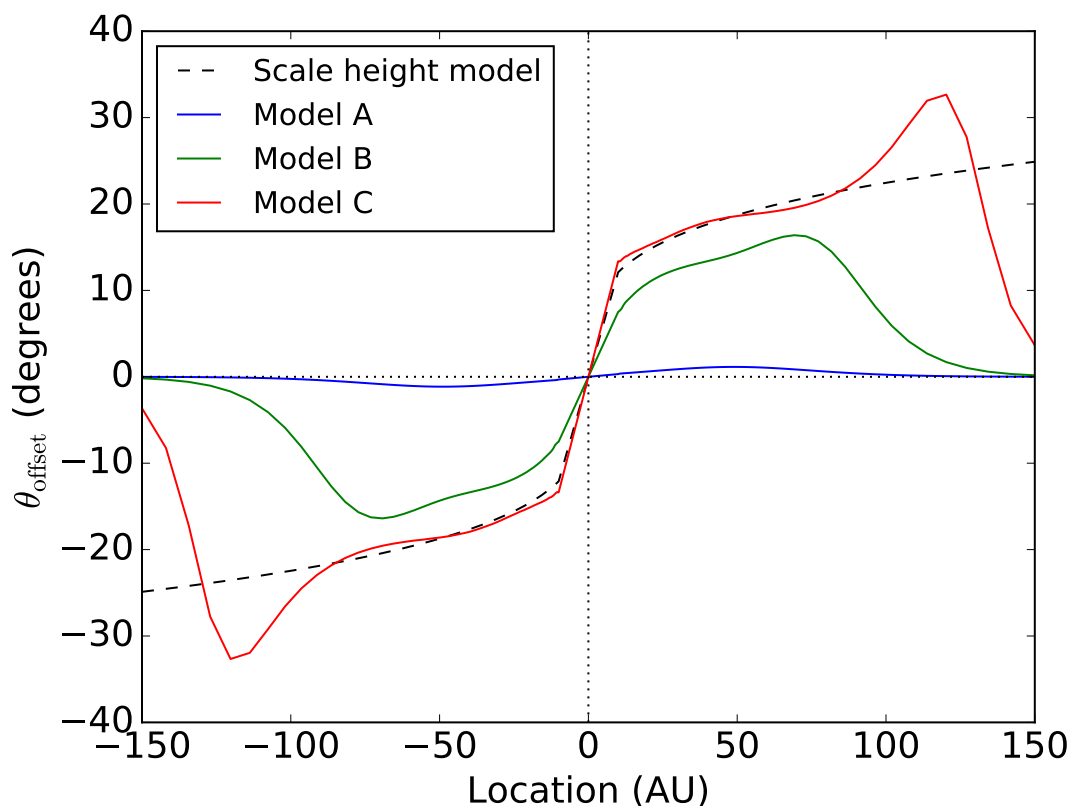


Fig. 4.7.— Bifurcation in polarization orientation along the major axis. Plotted are the offset angle θ_{offset} between the polarization vectors and the direction of the minor axis as a function of distance from the center along the major axis for the three models with different density scales (Models A-C). The blue dashed line shows the expectation based on the shape of the disk surface at one scale height.

axis have mirror symmetry with respect to the minor axis (assuming an intrinsically axisymmetric disk), with the polarization line segments rotating away from the direction of the minor axis by an acute angle counterclockwise in one hemisphere and clockwise in the other (see Fig. 4.4f and i). If such a unique pattern of bifurcation in polarization orientation is observed, we can potentially infer the dependence of the dust scale height on the radius, provided that the disk is optically thick enough.

4.3.2 Monte Carlo radiative transfer and the effects of multiple scattering

So far, we have determined the disk polarization by solving the radiative transfer equation for polarized light using the formal solution under the single scattering approximation. Strictly speaking, the approximation is only valid when the disk is optically thin to scattering. Otherwise, multiple scattering may be important. In this subsection, we gauge the potential effects of multiple scattering on the disk polarization, especially the near-far side asymmetry, through Monte Carlo simulation using the publicly available code `RADMC-3D`³. For the three models presented in this subsection, we allow photons to be polarized between scattering with the scattering phase matrix calculated with Mie theory (Bohren & Huffman 1983). Each model uses 1.28 billions photon packages.

To facilitate comparison with the calculations discussed above, we will adopt the same physical model for the disk as before, focusing in particular on the highest density case of $\rho_0 = 1.13 \times 10^{-14} \text{ g cm}^{-3}$, where the potential effects of multiple scattering are expected to be the largest. We will consider a set of three models with three different (spherical) grain sizes, $10 \mu\text{m}$ (Model E in Table 4.2), $37.5 \mu\text{m}$ (Model D), and also the $100 \mu\text{m}$ (Model C) as before. The grain sizes are chosen so that the scattering opacities span a large range in value (3 orders of magnitude), although the absorption opacities remain rather constant (they differ by $\sim 40\%$ or less). In other words, these models have similar absorption optical depths but vastly different scattering optical depths, with values at the characteristic radius R_c of $\tau_{c,sca} = 1.04 \times 10^{-2}$, 0.56, and 11.7, respectively. The smallest grain size is chosen to provide an independent check on the results of the Monte Carlo simulations, which should be close to those ob-

³`RADMC-3D` is available at <http://www.ita.uni-heidelberg.de/~dullemond/software/radmc-3d/>

tained through the formal solution under the single scattering approximation since the scattering optical depth is much smaller than unity throughout the disk. In the left panels of Fig. 4.8, we plot the distributions of the polarized intensity of the $10\ \mu\text{m}$ grain case (Model E) computed from these two methods in the same column. We can see that they do look very similar qualitatively (and quantitatively, see below), which adds confidence to the results from both methods. Interestingly, there is a significant near-far side asymmetry even in this case of very small scattering optical depth. The implication is that a high *absorption* optical depth is sufficient by itself to generate a strong near-far side asymmetry. This is not surprising since a large absorption optical depth is enough to limit the source region of the polarized (scattered) light to the surface of the disk facing the observer, which has a near-far side asymmetry as viewed by the observer (see illustration in Fig. 4.6). However, in this particular case, the degree of polarization in the region of most interest (within the disk characteristic radius R_c) is of order 2×10^{-4} , which is well below the detection limit of even ALMA.

To obtain a higher degree of polarization, we first increase the grain size to $37.5\ \mu\text{m}$ (Model D), which corresponds to an increase of the scattering optical depth by a factor of ~ 50 . An increase of the polarization degree by a similar factor is expected (to about $\sim 1.0\%$). The actual polarization degree is somewhat less, reaching a value about half of the expected one. The discrepancy is most likely due to the fact that the disk is starting to become optically thick to scattering at the characteristic radius (with $\tau_{c,\text{sca}} = 0.56$) and more so at small radii. As the grain size increases further to $100\ \mu\text{m}$ (Model C), the scattering opacity depth increases by another factor of ~ 20 , to $\tau_{c,\text{sca}} = 11.7$. Even in this most extreme case where the disk is optically thick to both absorption and scattering, the spatial structure of the polarization patterns from the two methods (the formal solution and RADMC-3D) remain qualitatively similar, as

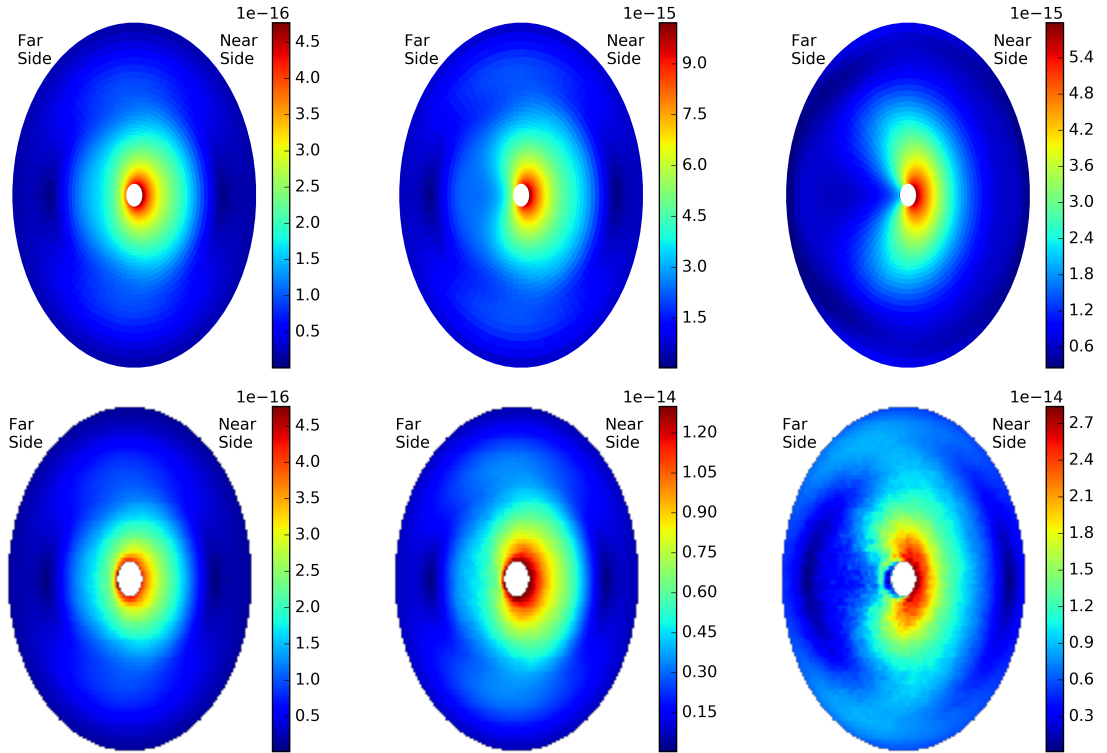


Fig. 4.8.— Comparison of the results from formal solution under single scattering approximation (top panels) and Monte Carlo simulations including multiple scattering (bottom panels). Plotted are the polarized intensity for a representative disk inclined by an angle $i = 45^\circ$ to the line of sight, with three different grain sizes: $10 \mu\text{m}$ (Model E; left panels), $37.5 \mu\text{m}$ (Model D; middle) and $100 \mu\text{m}$ (Model C; right). From left to right, the scattering optical depth at the characteristic radius R_c are 1.04×10^{-2} , 0.56, and 11.7, respectively. Intensities are in unit of $\text{erg} \cdot \text{s}^{-1} \cdot \text{sr}^{-1} \cdot \text{cm}^{-2} \cdot \text{Hz}^{-1}$. The color scales were adjusted to best show the morphology of the polarized intensity.

shown in the right panels in Fig. 4.8. In particular, the inclusion of multiple scattering in the RADMC-3D case does not erase the near-far asymmetry in the distribution of the polarized intensity; the “kidney” shaped distribution broadly resembles that obtained with formal solution without multiple scattering.

To compare the results from the two methods more quantitatively, we plot in Fig. 4.9 the distributions of the total intensity I along both the major and minor axis (top panels), the polarization degree p along the minor axis (middle), and the

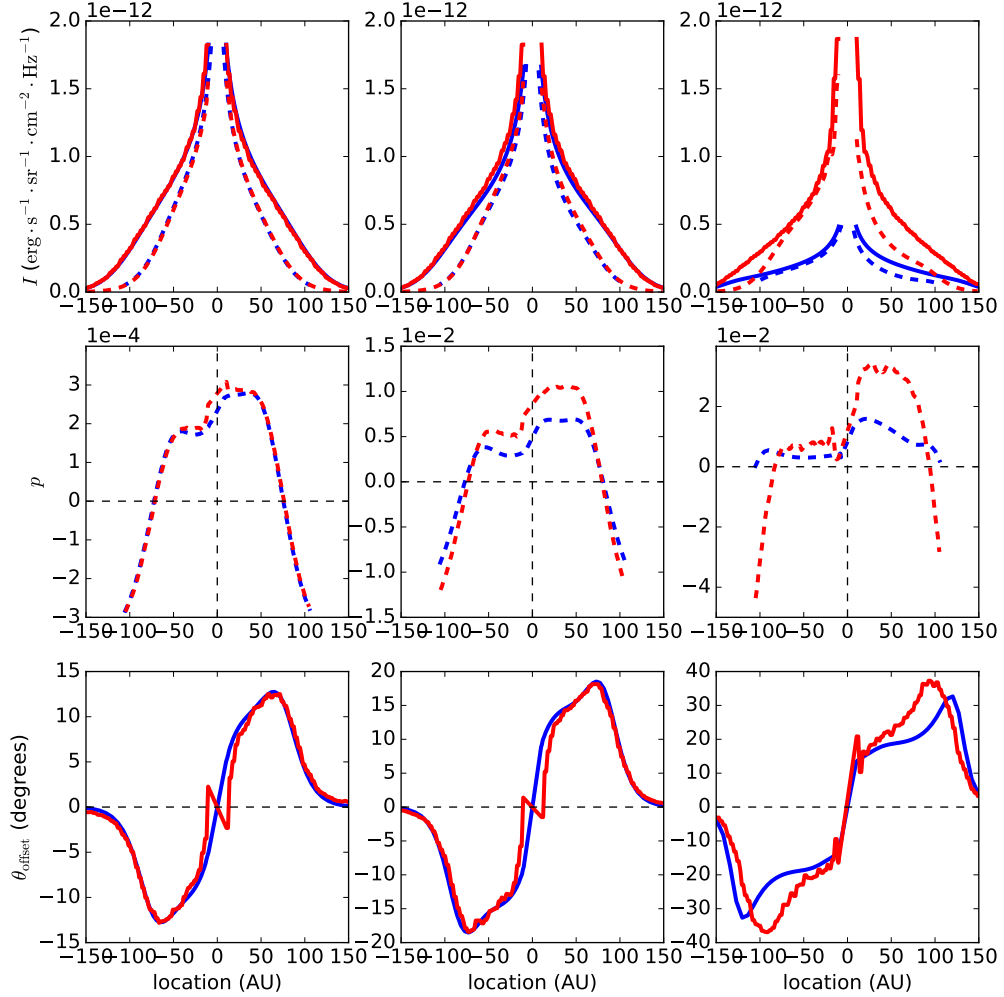


Fig. 4.9.— Quantitative comparison of the results from formal solution under single scattering approximation (blue curves) and Monte Carlo simulations including multiple scattering (red curves). Plotted are the total intensity I along both the major and minor axis (top panels), the polarization degree p along the minor axis (middle), and the offset angle θ_{offset} between the polarization orientation and the minor axis along the major axis (bottom), for three grain sizes: $10\ \mu\text{m}$ (Model E; left panels), $37.5\ \mu\text{m}$ (Model D; middle), and $100\ \mu\text{m}$ (Model C; right). Results on major axis and minor axis are plotted in solid lines and dashed lines, respectively.

offset angle θ_{offset} between the polarization orientation and minor axis along the major axis (bottom). The three columns show models with grain sizes of $10\ \mu\text{m}$ (Model E), $37.5\ \mu\text{m}$ (Model D) and $100\ \mu\text{m}$ (Model C), respectively. Red curves are from RADMC-3D and blue curves from the formal solution. It is clear that there is good agreement in the case of the smallest grain (the left panels; optically thin to scattering) for all three plotted quantities (I , p and θ_{offset}). Multiple scattering does have some effects on the polarization degree p for the case of intermediate grain size (middle column), increasing it by a factor of $\sim 30 - 50\%$ (see the middle panel of the figure). As expected, it affects the case of the largest grain (and the highest scattering optical depth) the most. In particular, multiple scattering increases the total intensity along both the major and minor axes by up to a factor of ~ 4 compared to that obtained under the assumption of single scattering. This is because photons are heavily extinguished due to high scattering optical depth, and the bulk of such extinguished photons would reappear through the disk surface and be observed as (more polarized) scattered photons when multiple scattering is taken into account but not in the single scattering limit. The larger number of (polarized) scattered photons toward the observer naturally explains why the polarization degree is significantly higher with multiple scattering than without, especially on the near side of the inclined disk (see the middle-right panel). In any case, multiple scattering does not erase the near-far asymmetry; if anything, the asymmetry is enhanced by multiple scattering, especially in the case of larger grains. Moreover, multiple scattering events have little effect on the optical depth effect of bifurcation in polarization orientation along the major axis, as measured by the offset angle θ_{offset} , as shown in the bottom panels of Fig. 4.9. This is not too surprising because the orientation of the polarization is expected to be determined mainly by the projected normal direction of the local disk surface in the

plane of the sky in optically thick regime (see § 4.3.1 and Fig. 4.7), which is relatively unaffected by multiple scattering.

4.4 Disk polarization as a probe of dust settling

One of the most striking features of the scattering-induced polarization in an inclined, optically and geometrically thick dust disk is the near-far side asymmetry in polarized intensity. It comes about because (1) the observed photons come from the surface layers of the optically thick disk, and (2) the surface on the near-side is viewed more edge-on than that on the far-side because of the finite angular thickness of the (dust) disk (see Fig. 4.6). Here, we first demonstrate explicitly that the near-far side asymmetry disappears in a geometrically thin dust disk (§ 4.4.1), and then discuss the potential of using the near-far side asymmetry as a probe of the thickness of the dust layer responsible for the scattering (i.e., dust settling; § 4.4.2) and as a way to differentiate dust scattering from other mechanisms for producing disk polarization in (sub)millimeter (such as direct emission from magnetically or radiatively aligned grains, § 4.5).

4.4.1 Dependence of near-far side asymmetry on dust settling

To illustrate the dependence of the near-far side asymmetry on the thickness of the layer of (large) grains responsible for the scattering, we repeat the most optically thick model discussed in § 4.3.1 (Model C in Table 2) but with the (dust) scale height reduced by a factor of 10. The (dust) density is increased by a factor of 10 correspondingly, to keep the column density and thus the optical depth the same (Model F). The

results are shown in Fig. 4.10, where the total intensity, polarized intensity, and po-

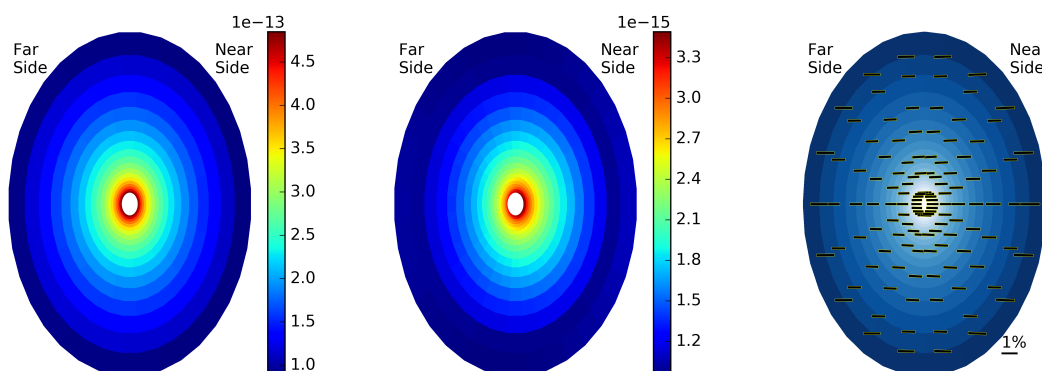


Fig. 4.10.— Total intensity (left), polarized intensity (middle), and polarization vectors (right) for geometrically thin but optically thick disk model (Model F). Intensities are in unit of $\text{erg} \cdot \text{s}^{-1} \cdot \text{sr}^{-1} \cdot \text{cm}^{-2} \cdot \text{Hz}^{-1}$.

larization vectors are plotted. They can be directly compared with the results shown in Fig. 4.4g, Fig. 4.4h, and Fig. 4.4i for the corresponding thicker (dust) disk case (Model C). Several features are immediately apparent from the comparison. First, the two cases have similar scales for the total intensity, which is expected since they have the same distributions of column density and temperature. A major difference is that the disk is nearly symmetric in total intensity and polarized intensity in the geometrically thinner case (Model F) but significantly brighter in total intensity on the far-side and in polarized intensity on the near-side in the geometrically thicker case (Model C). This is not surprising because, as the (angular) thickness of the dust disk shrinks, the surfaces of the near and far sides of the disk become more symmetric with respect to the line of sight (see Fig. 4.6). Furthermore, both surfaces are closer to the disk midplane, reducing the difference between the global minor axis (defined by the disk axis or midplane) and the local minor axis on the disk surface facing the observer, which makes polarization vectors more aligned with the (global) minor axis, as shown in the right panel of Fig. 4.10 (see Fig. 4.4h for comparison). In other

words, the degree of bifurcation in polarization orientation along the major axis is also reduced for a geometrically thin disk. These differences can in principle provide a way to determine whether the large grains responsible for the scattering-induced polarization are settled to the disk midplane or not.

4.4.2 Evidence for evolution of dust settling over time

Dust settling is an important process to study because it tends to increase the local concentration of the dust-to-gas ratio near the midplane and may play a crucial role in the formation of planetesimals and ultimately planets. Physically, whether grains would settle toward the disk midplane or not depends on their sizes, the level of turbulence and the distribution of gas density in the disk, as well as the age of the system. It is expected to occur preferentially for large grains in relatively quiescent, evolved disks. We will first review anecdotal evidence from (unpolarized) dust continuum imaging of edge-on disks that large grains are not yet settled in Class 0 disks, but become more so at later (Class I and II) stages. This is followed by complementary evidence for a similar trend from the currently available disk polarization observations of inclined disks.

Evolution of dust settling in edge-on disks from dust imaging

High resolution observations of (unpolarized) dust continuum, especially with ALMA, have shown that the grains in the two best-studied edge-on Class 0 disks, HH212 and L1527, are vertically distributed. In the case of HH212, the evidence comes from long-baseline ALMA continuum observation in Band 7 (0.85 mm) that resolved the disk vertical structure with a $0.02''$ resolution (Lee et al. 2017). It reveals a dark lane near the disk midplane sandwiched between two brighter regions. Preliminary modeling

of this “hamburger-shaped” continuum indicates that the dust layer responsible for the detected emission at $0.85 \mu\text{m}$ has a scale height of ~ 10 AU at a radius of ~ 40 AU, making the dust disk rather thick geometrically. The dust opacity index β was estimated at 0.6 between 0.85 and 1.4 mm wavelengths, which, taken at the face value, would indicate significant grain growth, possibly to millimeter sizes or larger (Testi et al. 2014). These observations appear to indicate that the grains in the HH212 Class 0 disk have already grown significantly but not yet settled toward the mid-plane. The same picture appears to hold for the edge-on Class 0 disk L1527 as well, which has an estimated (total) thickness (full width at half maximum) of ~ 30 AU at a radius of 50 AU based on ALMA Band 7 continuum observations at 0.8 mm (Sakai et al. 2017; see also Aso et al. 2017 submitted). These two examples provide a strong motivation to study the scattering-induced polarization from dust grains that are yet to settle to the mid-plane, as we have done in § 4.3.

The situation appears different for more evolved disks. For example, for the iconic disk of the Class I/II object HL Tau, Pinte et al. (2016) was able to infer that the large grains responsible for the (sub)millimeter continuum emission are settled to the mid-plane, based on the lack of azimuthal variation of the width of the gaps in the significantly inclined disk (ALMA Partnership et al. 2015). Other possible examples include the disk of the well-studied Class II object HH30, which remains unresolved in the vertical direction by ALMA observations at 1.3 mm (F. Menard et al. 2017, submitted), and the edge-on disk of the so-called “Flying Saucer,” where large grains appear to be settled to the midplane (Guilloteau et al. 2016). Although the number of edge-on disks with high resolution ALMA data remains small, the available evidence is suggestive of a picture where grains responsible for (sub)millimeter continuum emission remain vertically distributed in the youngest (Class 0) disks, but become

more settled at later times.

The tentative trend for the evolution of dust settling is perhaps to be expected, for two reasons. First, it takes time for the grains to grow and settle, which tends to favor dust settling in older sources. Perhaps more importantly, the youngest disks are inferred to accrete at much higher rates than older disks (by one to two orders of magnitude or more, e.g., Yen et al. 2017). If the accretion is driven by turbulence (induced by magneto-rotational instability or some other means), the level of turbulence in the youngest disks must be much higher, which could plausibly stir up the grains enough to prevent them from rapid settling toward the mid-plane (e.g., Fromang & Nelson 2009). If this is indeed true, it would have far-reaching implications for the timing of planet formation: if planetesimals are not formed in earnest until grains have settled, it would be difficult to form planets from planetesimals during the Class 0 phase. A corollary would be that there should not be any planet-induced rings and gaps on Class 0 disks⁴. Given its significance, it is important to probe dust settling using an independent method. We believe that disk polarization has the potential of being developed into one such method.

Evolution of dust settling from polarization of inclined disks

Although the field of disk polarization is poised for rapid growth in the ALMA era, the number of disks with resolved polarization detection remains small. Nevertheless, there is already some indication for the near-far side asymmetry in polarized intensity expected in an optically and geometrically thick (dust) disk. The best example to date is the inclined, optically thick disk of the famous massive protostar HH80-81 (Girart et al. 2018). ALMA observations revealed a well resolved polarization pattern that is

⁴Rings and gaps would be smoothed out quickly by a high level of turbulence in Class 0 disks, potentially making this supposition difficult to test.

roughly parallel to the minor axis close to the center and more azimuthal further out, broadly consistent with the pattern from scattering (Yang et al. 2016a,b; Kataoka et al. 2016a; see Fig. 4.4). Interestingly, the near side of the disk, as inferred from its projection in the plane of the sky on the redshifted jet, is much brighter than the far side in polarized intensity, as expected from scattering-induced polarization with the (large) grains responsible for the scattering not yet settled to the mid-plane.

A similar asymmetry was also observed with ALMA in one of the youngest intermediate mass protostars, OMC3 MM6, with the polarized intensity much brighter on the near side (projected against the redshifted outflow) than the far side (S. Takahashi et al. 2017, submitted). In addition, high-resolution VLA observations revealed that the well-studied low-mass Class 0 protostar NGC 1333 IRAS 4A is significantly polarized at 8 mm, again with the near side brighter than the far side in polarized intensity (Cox et al. 2015; Liu et al. 2016). The source is so bright that it is believed to be optically thick out to 7 mm (Liu et al. 2016), which is consistent with the interpretation that the polarization comes from scattering, at least near the center (see also Yang et al. 2016b). Although it is conceivable that in each of the sources the asymmetry could be produced by an intrinsic feature on the disk, such a dust trap, it is statistically unlikely for such a trap to occur on the near side for all three cases. We conclude that the relatively sparse high-resolution polarization data currently available is consistent with the picture painted by the edge-on disks above, that, during the earliest phase of star formation, grains have already grown significantly to enable detectable polarization from scattering but have yet to settle toward the mid-plane, for both high-mass and low-mass protostars.

For more evolved objects, the situation can be quite different. For example, there is no clear indication of a near-far side asymmetry in the polarized intensity of the

HL Tau (Class I/II) disk from the CARMA observations at 1.3 mm (Stephens et al. 2014), although the spatial resolution is rather limited. The lack of asymmetry is to be expected if the large grains are indeed settled to the mid-plane, as inferred from the shape of the gaps on the disk (Pinte et al. 2016). If the grains in the HL Tau disk have indeed settled, a prediction would be that there would not be any significant near-far side asymmetry even in ALMA Band 7 (the currently shortest wavelength available for polarization observations) where the disk is known to be optically thick. This prediction can readily be tested with ALMA observations. ALMA polarization data is available for the transition disk HD 142527 (Kataoka et al. 2016a), although its interpretation is complicated by the intrinsic asymmetry in the dust distribution. In any case, the observed pattern does not contradict in any obvious way the expectation that the large millimeter-emitting grains have settled in this evolved disk, although more detailed modeling is required to draw a firmer conclusion.

We therefore have two complementary methods of probing dust settling: vertically resolved (non-polarized) continuum imaging of edge-on disks and scattering-produced polarization in inclined disks. The first method is direct and can be interpreted easily with few assumptions but requires nearly edge-on systems (which are rare) and very high spatial resolution. The second method is less demanding in disk inclination (and hence is potentially applicable to more sources) and spatial resolution, but the polarized intensity tends to be much weaker than the non-polarized intensity. It does have the advantage of providing a tighter constraint on the grain size than direct imaging, since the scattering coefficient is much more sensitive to the grain size than the emission coefficient.

4.5 Distinguishing mechanisms of disk polarization

4.5.1 Scattering vs emission by aligned grains

Besides scattering, it is well-known that aligned (non-spherical) grains can also produce polarization through direct emission. Whether large grains responsible for (sub)millimeter emission can be aligned or not inside young star disks remains debated. Hoang (2017) pointed out that, if there are enough iron atoms per cluster inside a grain (i.e., if the grain material is superparamagnetic enough), magnetic fields may align grains with sizes up to a few millimeters. In the case that the number of iron atoms is too small for magnetic alignment, it may still be possible for the grain to be aligned with respect to the direction of anisotropy in the radiation field through radiative torques (Tazaki et al. 2017). The contrast between the polarization patterns from scattering and magnetically aligned grains was already discussed in some depth in Yang et al. (2016b). In this subsection, we will focus on the similarities and differences between those from scattering and radiatively aligned grains.

Both polarization mechanisms depend strongly on the degree of anisotropy in the radiation field: scattering of isotropic radiation does not produce any polarization at all, and radiative torques are far weaker for isotropic radiation field than for anisotropic ones (Lazarian 2007). Radiatively aligned (non-spherical) grains precess around the direction of the radiation flux, with their long axis perpendicular to the flux direction (Tazaki et al. 2017). In the simplest case of a face-on, axisymmetric disk, the radiative flux would be in the radial direction, which would force the grains to align their long axes along the azimuthal direction, producing an azimuthal pattern that is similar to the pattern produced by scattering in a face-on disk (see the upper-left panel of Fig. 2 of Yang et al. 2016a). However, there is substantial dif-

ference between the two mechanisms for significantly inclined (axisymmetric) disks: the radiatively aligned grains would produce a radial polarization pattern, which is similar to the pattern produced by scattering at large distances from the center but not near the center. For scattering, polarization vectors toward the center are more or less parallel to the minor axis, especially for locations on the minor axis. This is an inclination effect caused by the dependence of polarization degree on the scattering angle and thus unique to the scattering-induced polarization (see Fig. 4.4C and the lower-left panel of Fig. 2 of Yang et al. 2016a). High resolution may be required to resolve the central region to find this tell-tale sign for scattering.

It may be possible to distinguish polarization from scattering and radiatively aligned grains even in a face-on disk if the dust distribution is non-axisymmetric (i.e., dust traps). This is because the photons involved in producing the polarization at a given observed wavelength (e.g., (sub)millimeter) are quite different for the two mechanisms. For the scattering-induced polarization, it is the anisotropy of the radiation field at the observed wavelength before the scattering that is responsible for the polarization at the same wavelength after the scattering. This is completely different from the case of radiatively aligned grains where the grain alignment is dominated by the anisotropy of the photons at wavelengths near the peak of the spectral energy distribution (SED) at the grain location, which are usually quite different from the observed wavelength. In particular, the radiation energy density in the bulk of a disk may be dominated by the radiation from the warmer surface layers, which typically have wavelengths much shorter than the mm/sub-mm probed by ALMA. If there is a difference in anisotropy between photons at the observation wavelength and near the SED peak, the polarization patterns produced by the two mechanisms would be different. For illustration, consider the transition disk around Oph-IRS

48. The $440\ \mu\text{m}$ image observed with ALMA in Band 9 shows a “kidney-shaped” concentration of large grains (i.e., a dust trap). The $18.7\ \mu\text{m}$ emission detected by the Very Large Telescope is, on the other hand, much more uniformly distributed in the azimuthal direction (van der Marel et al. 2013). If the radiation field near the SED peak has a distribution closer to that in the mid-infrared than in sub-mm, we would expect the (non-spherical) grains inside the “kidney-shaped” dust trap to be aligned more or less azimuthally, with a corresponding azimuthal polarization pattern from direct thermal dust emission at mm/sub-mm wavelengths. Self-scattering of the mm/submm photons would produce a very different polarization pattern, with polarization vectors switching directions going from inside the dust trap to outside (Kataoka et al. 2016b). High resolution multi-wavelength (mid- and far-IR continuum and (sub)millimeter polarization) observations of this type of sources can help distinguishing these two mechanisms.

We note that aligned grains can produce polarization through both direct emission and scattering. In this chapter, we have limited our treatment to scattering by spherical grains, with the emphasis on the optical depth effects. The combined polarization from both direct emission and scattering by aligned (non-spherical) grains has been considered in Yang et al. (2016b), but only in the optically and geometrically thin limit. These simplifications will be relaxed in a future investigation.

4.5.2 The Near-Far Side Asymmetry as Signpost for Scattering-Induced Polarization

The presence (or absence) and sense of near-far side asymmetry in polarized intensity in inclined, optically and geometrically thick (dust) disks may be the key to distinguish the disk polarization induced by scattering from those by magnetically

or radiatively aligned grains. In the simplest case of (rapidly spinning, effectively) oblate grains aligned with their shortest axes along a purely toroidal magnetic field, large near-far side asymmetry along the minor axis is not expected because the grains there are always viewed edge-on (and thus emit maximally polarized light) independent of the disk inclination angle. In the simplest case of oblate grains radiatively aligned with their shortest axes along a purely (spherically) radial direction, the observer would see the oblate grains located on the minor axis more face-on on the disk surface on the near side than that on the far side (see Fig. 4.6 where the dashed lines on the near and far sides mark the mid-plane of the oblate grains). This would make the intensity of the polarized light emitted by the radiatively aligned grains weaker on the near-side than on the far-side, exactly the opposite of the scattering case. As discussed in § 4.4.2 above, there is already evidence that the polarized intensity is higher on the near side than on the far side in some disks, especially HH80-81. For these sources, the polarization is more likely dominated by scattering than by either magnetically or radiatively aligned grains. This tentative conclusion needs to be strengthened (or refuted) through higher resolution observations of youngest disks (where the dust grains have grown, so that scattering is efficient, but have yet to settle to the midplane), especially at a range of wavelengths where the disk goes from being optically thin to optically thick, with the corresponding increase in the expected degree of near-far side asymmetry.

4.6 Conclusion

Observational progress in disk polarization at (sub)millimeter wavelengths has been rapid in the last few years and is expected to accelerate in the ALMA era. However, the origin of the observed polarization remains uncertain. Part of the reason

is that (sub)millimeter polarization mechanisms such as dust scattering only became widely appreciated very recently and exploration of their basic properties is still at an early stage. In this Chapter, we seek to quantify the effects of optical depth on the scattering-induced polarization through a combination of analytical illustration, approximate semi-analytical modeling using formal solution to the radiative transfer equation, and Monte Carlo simulations, and to evaluate their potential for probing vertical dust settling in the disk and for distinguishing the polarization from scattering from that emitted by aligned grains. The main results are summarized as follows.

- Our analytic, 1D (plane-parallel) slab model demonstrates that scattering can produce a detectable level of polarization, along the direction of the normal to the slab surface projected onto the plane of the sky (i.e., the direction of the “local minor axis” if the slab represents a patch of the disk surface; see Fig. 4.1), even when the optical thickness goes to infinity. The degree of polarization from such a semi-infinite slab increases with the inclination angle (i) of the slab with respect to the line of sight ($i = 0$ means face-on view) until the slab is viewed nearly edge-on (see Fig. 4.2). For a given inclination angle, as the total optical depth of the slab τ_{\max} increases from zero to infinity, the degree of polarization first increases from zero to a maximum value near $\tau_{\max} \sim 1$, before asymptoting to a finite value (see Fig. 4.3). This behavior is very different from that of the aligned grain case, where the polarization degree decreases monotonically with the optical depth τ_{\max} , asymptoting to zero for a semi-infinite, isothermal slab. In addition, in optically thick regions, the degree and orientation of the polarization from direct emission by aligned grains depend strongly on the temperature distribution.

- In an optically thick disk, the observed light comes mainly from the disk surface facing the observer. The shape of that surface has a strong imprint on both the degree and orientation of the scattering-induced polarization in an inclined disk. Specifically, if the scattering dust grains are vertically distributed with a significant angular thickness, the near side of the disk surface would be viewed more edge-on than the far-side (see Fig. 4.6), leading to a higher polarized intensity on the near-side than the far-side, especially along the minor axis. Another consequence of the finite (dust) thickness is that the polarization orientations close to the center are no longer parallel to the minor axis, which is a hallmark of scattering-induced polarization in an optically and/or geometrically thin disk. The deviation is especially clear on the major axis, where the polarization orientations rotate away from the minor axis in one direction on one side of the disk and in the opposite direction on the other side (see Fig. 4.4, right column). The near-far side asymmetry in polarized intensity and bifurcation in polarization orientation are quantified through an approximate semi-analytic solution to the radiative transfer equation under the single scattering approximation (see Fig. 4.4) and Monte Carlo simulations that include multiple scattering (see Fig. 4.8, bottom row).
- Both the near-far side asymmetry in polarized intensity and bifurcation in polarization orientation are unique to the scattering-induced polarization in an optically and geometrically thick (dust) disk. They are produced by simple geometric effects that are not shared by other mechanisms such as direct emission from (non-spherical) grains aligned with either magnetic fields or the direction of radiative flux. As such, they are robust signatures of the scattering-induced polarization, provided that the (dust) disk is both optically and geometrically

thick. Both of these signatures disappear for an optically and/or geometrically thin disk.

- We find anecdotal evidence from high-resolution (unpolarized) dust continuum imaging of edge-on disks that large grains are not yet settled in the youngest, Class 0 disks, but become more so in older (Class I and II) disks (§ 4.4.2). This trend is corroborated by the polarization data in inclined disks that, although still rather limited, appear to indicate that younger sources tend to have brighter polarized emission on the near-side than the far-side and thus less grain settling if scattering is responsible for the polarization (§ 4.4.2). If confirmed, the trend would have far-reaching implications for disk grain evolution, which lies at the heart of the formation of planetesimals and ultimately planets.

Chapter 5

Does HL Tau Disk Polarization in ALMA Band 3 Come from Radiatively or Aerodynamically Aligned Grains?

This chapter is based on a draft of a paper to be submitted before the end of Summer 2018.

Abstract

Disk polarization in (sub)millimeter dust continuum is a rapidly growing field in the ALMA era. It opens up the exciting possibility of detecting and characterizing magnetic fields and grain growth in disks around young stellar objects. However, to use polarization for probing the disk properties, its production mechanism must be ascertained first. To date, the conventional mechanism involving magnetically

aligned grains fails to explain the polarization patterns detected in most disks. This is especially true for the inclined disk of HL Tau in ALMA Band 3 (~ 3 mm), which has an elliptical polarization pattern. The elliptical pattern was taken as evidence for polarized emission by dust grains aligned with their long axes perpendicular the direction of the radiative flux. We show that the radiatively aligned grains produce a circular or concentric, rather than elliptical, polarization pattern even in inclined disks such as HL Tau. An elliptical polarization pattern can be produced if the grains are aligned aerodynamically by the difference in rotation speed between the dust and gas. However, a strong azimuthal variation in polarized intensity is expected for both the radiative and aerodynamic alignment, but not observed in the HL Tau disk in ALMA Band 3. We conclude that neither of these two mechanisms alone can explain the data and the origin of the HL Tau Band 3 polarization remains a mystery. We speculate that this mystery may be resolved by a combination of both direct emission and scattering by aerodynamically aligned grains.

5.1 Introduction

The magnetic field is thought be one of the main drivers behind the dynamics and evolution of protoplanetary disks, through either magnetic-rotational instability (MRI; Balbus & Hawley 1991) or magnetic disk wind (Blandford & Payne 1982; Turner et al. 2014). Firm observational evidence for the magnetic field is therefore one of the most sought-after goals of disk research. One of the most widely used methods for probing magnetic fields is through polarization of thermal dust emission, based on the theory of magnetic alignment of dust grains (Lazarian 2007; Andersson et al. 2015). This method has been applied successfully to a wide range of scales, from molecular clouds (\sim pc or larger; e.g., Planck Collaboration et al. 2015; Fissel et al.

2016) to protostellar envelopes ($\sim 100 \sim 1000$ AU; e.g., Girart et al. 2006; Stephens et al. 2013; Hull et al. 2014; Cox et al. 2018).

On the disk scale ($\lesssim 100$ AU), evidence for the magnetic field has been difficult to obtain from the polarized dust emission. The first spatially resolved polarization in a T Tauri disk was detected in HL Tau through 1.3 mm observations from the Combined Array for Research in Millimeter-wave Astronomy (CARMA; Stephens et al. 2014). It shows a roughly uniform polarization pattern along the disk minor direction which, if interpreted as coming from magnetically aligned grains, would imply an uni-direction magnetic field along the major axis, which is unexpected for a rotating disk. Soon after the appearance of the theory of (sub)millimeter polarization through dust self-scattering (Kataoka et al. 2015), it became clear that the CARMA observed pattern in HL Tau is more consistent with scattering-induced polarization in an inclined disk (Yang et al. 2016a; Kataoka et al. 2016a) than that produced by grains aligned by the widely expected toroidal magnetic fields, although grain alignment with more complex magnetic fields cannot be ruled out (Stephens et al. 2014; Matsakos et al. 2016; see also Alves et al. 2018 for the case of BHB07-11). With polarimetric observations by the Atacama Large Millimeter/submillimeter Array (ALMA), spatially resolved polarization has been detected in an increasing number of circumstellar disks, especially at ALMA Band 7/6 (0.87 mm/1.3 mm). To date, the majority of the observed patterns are consistent with that from self-scattering, e.g., HL Tau (Stephens et al. 2017, Band 7), IM Lup (Hull et al. 2018 Band 7), IRS 63 (Sadovoy et al. in prep, Band 6), HH212 (Lee et al. 2018; Band 7), and HH80/81 (Girart et al. 2018, Band 6).

Besides magnetically aligned grains and dust self-scattering, there are other mechanisms for producing millimeter/submillimeter polarization. One of such mechanisms,

radiative alignment, was recently proposed by Tazaki et al. (2017), based on the earlier work by Lazarian & Hoang (2007). Within the framework of grain alignment by radiative torque, radiative alignment could happen when the magnetic field is weak or absent. In this case, grains will align with their long axes perpendicular to the local radiation flux, or the direction of the local radiation anisotropy, rather than the magnetic field. The mechanisms of radiative alignment and dust self-scattering have in common that both rely on the anisotropy in the radiation field incident on the dust grain to produce polarization, although they have different dependence on wavelength and disk orientation, which makes them distinguishable, especially through multi-wavelength polarization observations and in disks with extreme inclinations (i.e., edge-on).

To date, the strongest support for the mechanism of radiative alignment proposed by Tazaki et al. (2017) comes from the well-resolved polarization pattern detected in HL Tau by ALMA in Band 3 (~ 3 mm; Kataoka et al. 2017; reproduced in Fig. 5.1a). It has a broadly azimuthal pattern that is very different from the more or less uni-directional pattern detected in Band 7 (~ 0.87 mm; Stephens et al. 2017; reproduced in Fig. 5.1b); the latter is a textbook example of what the scattering-induced polarization should look like in an inclined disk (Yang et al. 2016a; Kataoka et al. 2016a). Since the grains responsible for the Band 7 polarization would not produce any detectable polarization through scattering in Band 3 (because the scattering cross-section drops rapidly with wavelength in the Rayleigh limit), it is natural for Kataoka et al. (2017) to attribute the Band 3 polarization to radiative alignment rather than scattering; the conventional interpretation involving magnetically aligned grains would imply a magnetic field that is mostly radial in the disk plane, which is unlikely in a differentially rotating disk). More importantly, since the radiative flux

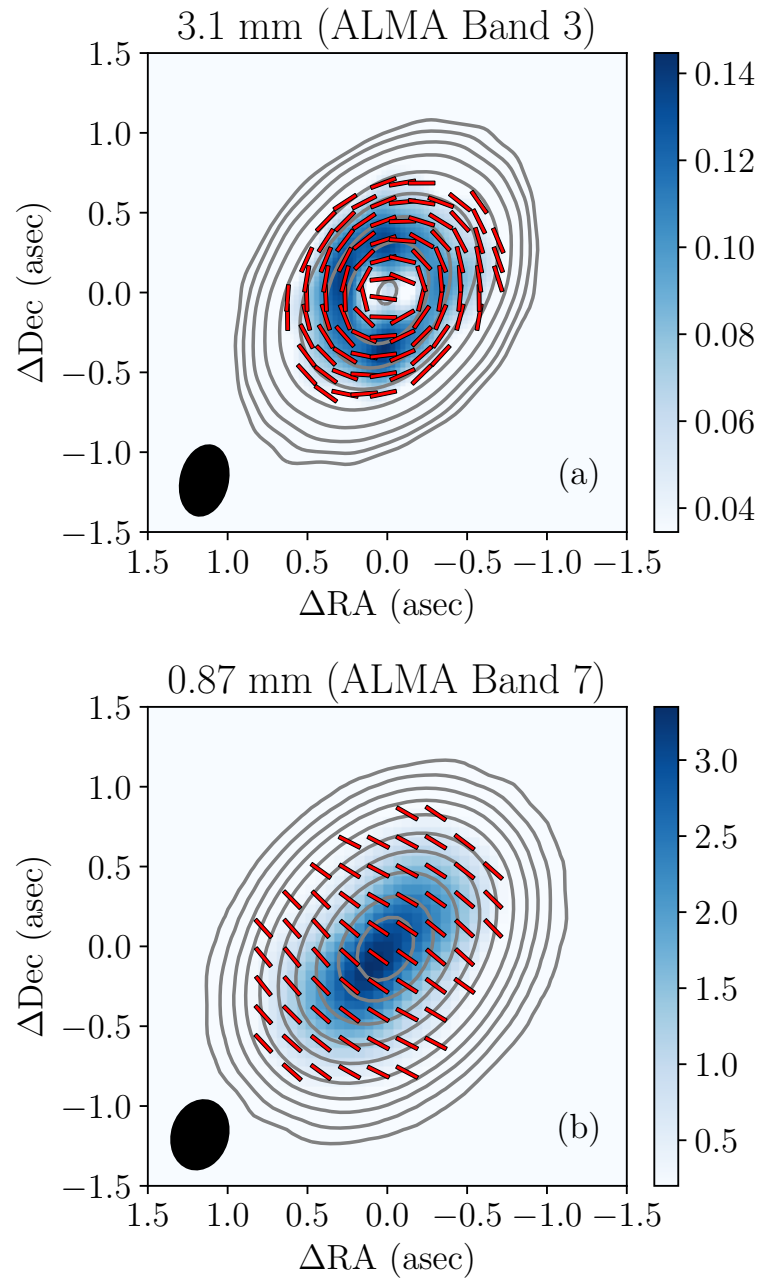


Fig. 5.1.— HL Tau disk polarization detected by ALMA in Band 3 (panel a) and Band 7 (b). The panels are adopted from Kataoka et al. (2017) and Stephens et al. (2017), respectively. Plotted are the polarization orientations (line segments), polarized flux (color map) and total flux (contours).

in an axisymmetric disk is in the radial direction, the radiatively aligned grains are expected to have their long axes in the azimuthal direction in the disk plane, which is thought to produce a polarization pattern in the plane of the sky broadly resembling the observed pattern.

There are, however, two problems with interpreting the Band 3 polarization as coming from radiative alignment. The first problem has to do with the polarization orientation. If the dust grains are aligned with respect to the radiation flux, the situation would be the same as the case where the grains are aligned with respect to a radial magnetic field in the disk plane. In this latter case, it is well known that the polarization is perpendicular to the *plane-of-the-sky* component of the magnetic field, \mathbf{B}_{pos} , which remains radial in the sky plane (i.e., there is no azimuthal component for \mathbf{B}_{pos}). As a result, the polarization pattern from radiative alignment is expected to be *circular* (with the polarization segments tangential to circles in the plane of the sky) rather than *elliptical* (with the polarization segments tangential to ellipses, which are inclined circles projected in the sky plane). The expected circular pattern does not appear to fit the Band 3 data well.

The second, perhaps more serious problem is that the intensity of the polarization from radiatively aligned grains is expected to have a strong azimuthal variation, which is not obvious in the Band 3 data. The azimuthal variation comes from a combination of the effective grain shape and a simple geometric effect. Radiatively aligned grains are expected to spin rapidly around their short axes and are thus effectively oblate (and often represented by oblate spheroids). In a disk inclined to the plane of the sky, such grains would have different projected shapes in the plane of the sky depending on their azimuthal positions in the disk. Specifically, the grains located on the minor axis would appear rounder to the observer than those on the major axis, producing

less polarization; in the extreme case of an edge-on disk, the grains on the minor axis would appear perfectly circular to the observer (because of their fast spin around the line of sight) and thus produce no polarization at all. In contrast, the effectively oblate grains located on the major axis are always viewed by the observer “edge-on,” producing maximum polarization independent of the disk inclination angle.

In this Chapter, we will discuss these two problems associated with the radiative alignment interpretation of HL Tau Band 3 polarization data quantitatively. The problem with polarization orientation is discussed in Sec. 5.2, and that with azimuthal variation in polarized intensity is addressed in Sec. 5.3. We find that the elliptical polarization pattern can be better explained by another grain alignment mechanism (aerodynamic alignment by the differential rotation between gas particles and dust grains) than by radiative alignment and that both alignment mechanisms are expected to produce pronounced azimuthal variation in polarized intensity that should be easily observable. We compute the expected ALMA Band 3 polarization patterns for HL Tau disk based on the radiative and aerodynamic alignment mechanisms taking into account of the finite telescope beam, and compare them with the observational data in Sec. 5.4. We find that both mechanisms fail to match the polarization data and are thus disfavored. In Sec. 5.5, we stress the importance of taking into account beam-averaging in comparing model predictions and observational data and explore plausible ways to improve the model predictions. Additional challenges of aligned grain models in explaining the multi-wavelength observations of the HL Tau disk are briefly discussed. Our main results are summarized in Sec. 5.6.

5.2 Polarization orientation

5.2.1 Polarization pattern from radiative alignment in an inclined disk is circular, not elliptical

A major reason that the HL Tau polarization in ALMA Band 3 was attributed to radiative alignment was that the polarization vectors appear to follow the elliptical contours of constant brightness (which are the circles of constant dust emission in the disk plane projected onto the sky plane; see Fig. 5.1a) and the radiative alignment was thought to produce such an elliptical pattern (see Fig. 3b of Kataoka et al. 2017). The expectation would be true if the grains have their shortest axes aligned by radiative flux along the radial direction in the disk plane *and* their longest axes are preferentially pointing in the disk plane (i.e., parallel to the local tangents to the circles on which the grains locate). In such a case, the long axes of the grains projected in the sky plane would still be aligned with the tangents to the circles projected to the sky plane (i.e., the ellipses), as illustrated by the solid line segments in the left panel of Fig. 5.2. An intuitive way to visualize the situation is to imagine the extreme case where needle-like grains are aligned along circles in the disk plane. When viewed away from the axis of the disk (i.e., in an inclined rather than face-on disk), the “needles” would remain “painted” on the circles, which now become the ellipses in the sky plane, producing an elliptical pattern.

However, this is not what happens in the case of radiative alignment. Even though the shortest axes of the radiatively aligned grains are expected to be in the radial direction in the disk plane, their longest axes will not stay in the disk plane because of the spin around their shortest axes. Even in the absence of any spin, the longest axes would be distributed randomly in the plane perpendicular to the radial direction. In

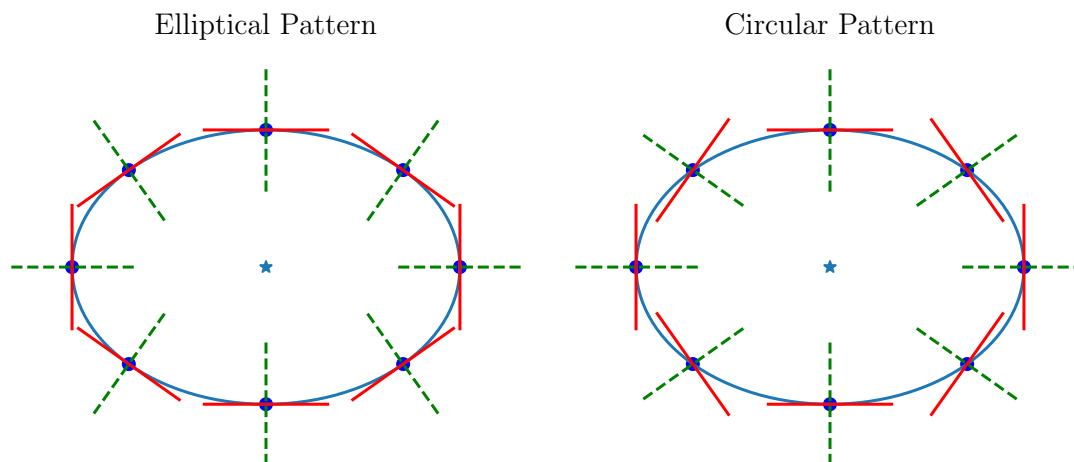


Fig. 5.2.— Elliptical vs circular polarization pattern. The red solid line segments are for polarization orientations, and green dashed line segments for the direction of the required radiative flux projected into the sky plane in the case of radiative alignment.

both cases, the net effect is that the radiatively aligned grains are effectively oblate (due to spin or ensemble average), with their shortest axis (which is also the symmetry axis for the effectively oblate shape) in the radial direction. In this case, the short axis of the projected grain shape in the sky plane remains aligned with a radial line that passes through the center (see the green dashed line segments in the right panel of Fig. 5.2 for illustration). To visualize the situation better, it is again helpful to go to the extreme case, where the effectively oblate grains are infinitely thin “disks” (or “flakes”). In this case, it is easy to show that, when projected to the sky plane, the “disks” become “ellipses” with their short axes along the radial direction in the sky plane and long axes perpendicular to the radial direction, producing a circular (or concentric) polarization pattern as illustrated by the red solid line segments in the right panel of Fig. 5.2. As discussed in the last section, this is consistent with the well-known result of the polarization orientation from magnetically aligned grains in (optically thin) molecular clouds, which is always perpendicular to the B-field

component in the sky plane (e.g., Andersson et al. 2015). If the elliptical pattern shown in Fig.5.1a were to be produced by radiatively aligned grains (as previously envisioned, see Kataoka et al. 2017), the radiative flux would have to be oriented in such directions that, when projected into the sky plane, follow the green dashed lines, which would not go through the center (and thus not in the radial direction), contradicting the expectation in an axisymmetric disk.

5.2.2 Differences between circular and elliptical patterns

In this subsection, we quantify the expected difference in polarization orientation between the elliptical and circular patterns illustrated in Fig. 5.2, and discuss whether such a difference is measurable in the HL Tau ALMA Band 3 data.

For the circular pattern, the polarization angle θ_{cir} at any point in the sky plane is simply the azimuthal angle of that point in the sky plane θ_{sky} rotated by 90° , i.e. the polarization is always perpendicular to the radial direction in the sky plane, namely

$$\theta_{\text{cir}} = \theta_{\text{sky}} + \frac{\pi}{2}. \quad (5.1)$$

For the elliptical pattern, the polarization angle θ_{ell} at a given point depends on the shape of the ellipse, which in turn is controlled by the inclination of the disk i ($i = 0$ for face-on view). It is related to the azimuthal angle θ_{sky} of that point (measured relative to the major axis of the projected disk or ellipse) through

$$\tan(\theta_{\text{ell}}) = -\frac{\cos^2(i)}{\tan(\theta_{\text{sky}})}. \quad (5.2)$$

Fig. 5.3 shows the polarization angle, which goes from 0° to 180° , as a function of azimuthal angle in the sky plane, for the case of a 45° inclined disk (similar to HL

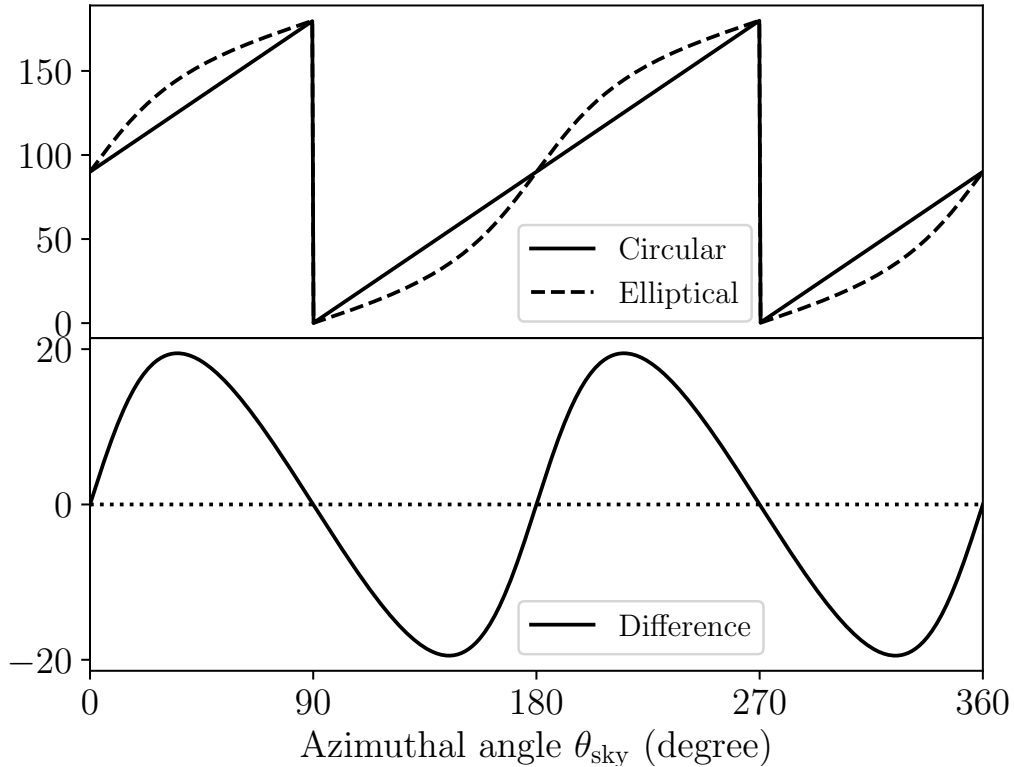


Fig. 5.3.— Upper panel: expected polarization angle for circular (θ_{cir} ; solid line) and elliptical (θ_{ell} ; dashed) pattern as a function of the azimuthal angle θ_{sky} in the sky plane for a disk inclined by 45° to the line of sight. Lower panel: the difference in polarization orientations between the two patterns, which can be as large as $\sim 20^\circ$ for this disk inclination.

Tau disk). The upper panel shows the expected orientation for both circular pattern (solid line) and elliptical pattern (dashed line). The lower panel shows the difference in polarization angle between two patterns. We can see that the difference can be as large as $\sim 20^\circ$. Near the peak of the polarized intensity at the HL Tau Band 3, the signal-to-noise ratio was reported to be 21σ (Kataoka et al. 2017), which roughly corresponds to an error of 2° in polarization angle, so this difference should be easily distinguishable with the current data.

Fig. 5.4 shows the difference in polarization angle between the two polarization

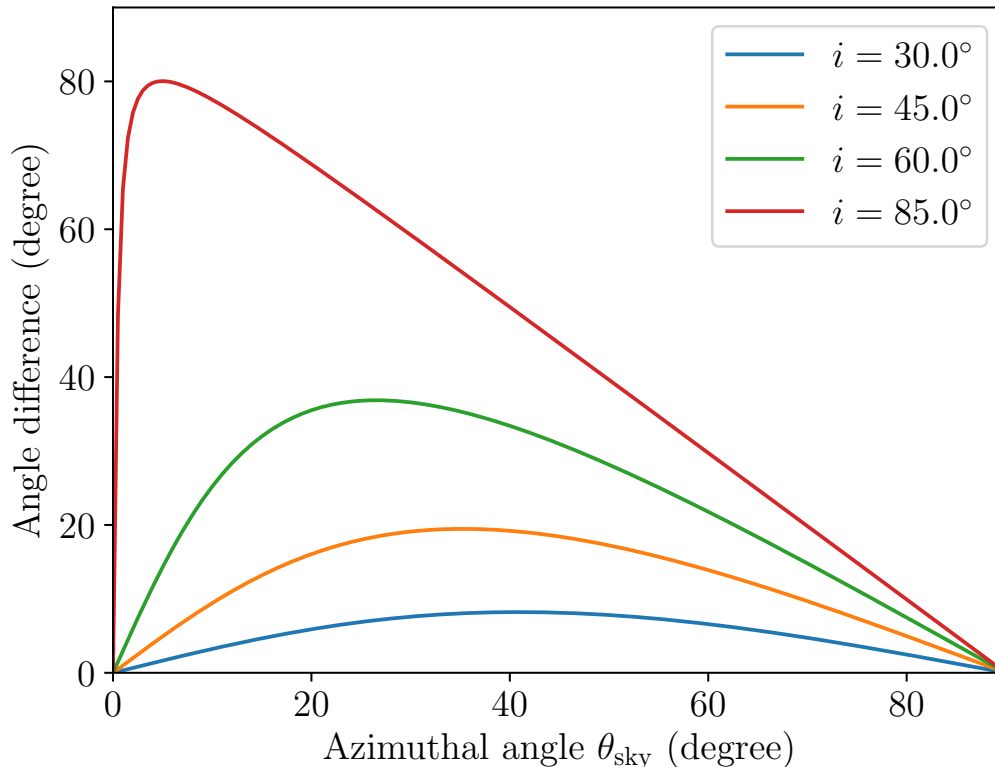


Fig. 5.4.— The difference in polarization angle between the circular and elliptical patterns as a function of the azimuthal angle in the sky plane θ_{sky} between 0° (major axis) and 90° (minor axis), for disks inclined by different angles ($i = 0^\circ$ for face-on view). The difference is larger for a more inclined disk.

patterns for different disk inclination angles. These two patterns are the same for face-on disks ($i = 0^\circ$), as expected. Their difference increases as the disk becomes more inclined to the line of sight, reaching 90° near the major axis (where the azimuthal angle measured from the major axis, θ_{sky} , approaches 0°) for an edge-on disk. For a given inclination angle i (that is not exactly 90°), the difference vanishes on the major ($\theta_{\text{sky}} = 0^\circ$) and minor ($\theta_{\text{sky}} = 90^\circ$) axis, and peaks at a location in the sky plane that is closer to the major axis than the minor axis. Fig. 5.5 illustrates pictorially the nearly edge-on case of $i = 85^\circ$, where the polarization orientations in the elliptical

and circular patterns are almost orthogonal over most of the (narrow, projected) disk. It is in such cases that the difference between the two patterns is most easily distinguishable.

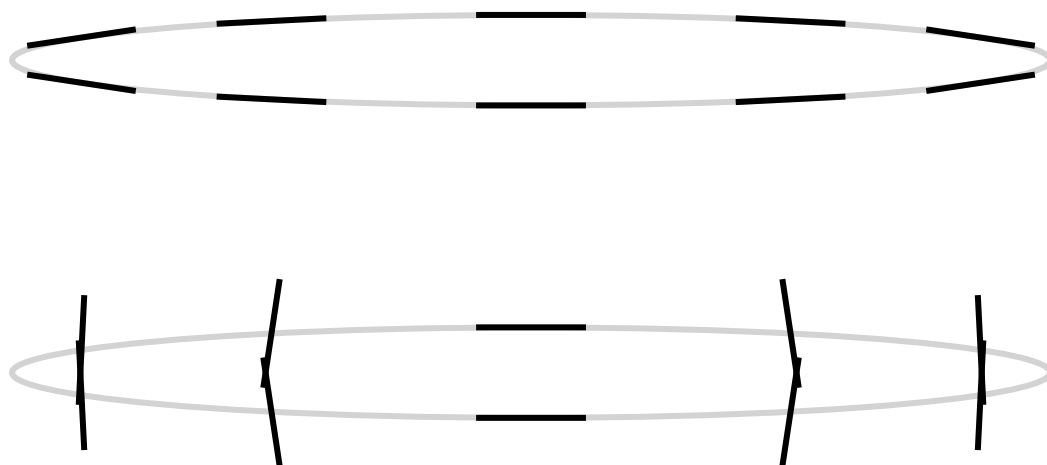


Fig. 5.5.— Large difference in polarization orientation between the elliptical (upper panel) and circular (lower) pattern for a nearly edge-on disk (with an inclination angle $i = 85^\circ$). Such disks are ideal for distinguishing the two patterns.

The difference in polarization orientation between the elliptical and circular patterns translates to a difference in polarization orientation in unresolved disks. This difference is best illustrated by the nearly edge-on case (see Fig. 5.5), where most of the polarization vectors are roughly parallel to the major axis (or the narrow, projected disk) for the elliptical pattern (yielding an averaged polarization along the major axis), but largely perpendicular to it for the circular pattern (yielding an averaged polarization along the minor axis). This difference persists for more moderately inclined disks as well.

To illustrate the difference in averaged polarization more quantitatively, we will

consider the simplest case where the polarization intensity and fraction are spatially uniform across the disk in the sky plane. The disk-averaged polarization fraction for the circular pattern becomes

$$\bar{p}_{\text{cir}} = -p_0 \frac{1 - \cos(i)}{1 + \cos(i)} \quad (5.3)$$

where the subscript “cir” denotes “circular pattern” rather than “circular polarization,” p_0 is the polarization fraction at each point before average, i is the disk inclination angle ($i = 0^\circ$ for face-on), and $\bar{p} < 0$ means polarization along minor axis of the projected disk. Similarly, the disk-averaged polarization fraction for the elliptical pattern is:

$$\bar{p}_{\text{ell}} = p_0 \frac{1 - \cos(i)}{1 + \cos(i)} \quad (5.4)$$

which is positive, and thus along the major (rather than the minor) axis. The opposite sign in the averaged polarization fraction is a generic difference that can in principle be used to distinguish the two patterns. In this particular example, the magnitude of the averaged polarization fraction is the same for the two patterns. This is not true in general, especially when the expected azimuthal variation of the polarization fraction is taken into account (see section 5.3 below).

Nonetheless, Eqs. (5.3) and (5.4) reveal an interesting point. Even though the elliptical and circular polarization patterns have a high degree of symmetry, their disk-averaged polarization fraction \bar{p} is reduced from the intrinsic value p_0 but does not vanish completely in an inclined disk. The reduction factor depends on the disk inclination angle i and the spatial distribution of the polarization intensity. In the simplest case of spatially constant polarization considered above, we have $\bar{p} = (\sqrt{2} - 1)/(\sqrt{2} + 1)p_0 \approx 0.172p_0$ for $i = 45^\circ$. It increases with the inclination angle,

approaching the intrinsic value p_0 in the limit of an edge-on disk.

5.2.3 Aerodynamic alignment can produce elliptical polarization pattern

Besides alignment by radiation field, grains can also be aligned aerodynamically when moving relative to the ambient gas (Gold 1952; Lazarian 1995). This is a strong possibility in circumstellar disks where the gas and dust orbit the central object at different speeds because the former experiences the gas pressure gradient directly but the latter does not. In the simplest case where the gas pressure increases radially inward, the gas would rotate at a sub-Keplerian speed because of the partial pressure support against the stellar gravity. Dust grains would rotate faster, and thus experiencing a “head-wind”¹. The relative speed between the gas and dust depends on several factors, particularly the gas density and grain size. Whether it is fast enough to align the grains emitting in the ALMA Bands through the Gold (1952) mechanism remains to be determined; we will postpone a detailed treatment of this mechanism to a future investigation. In what follows, we will argue that the polarization pattern expected from this mechanism is elliptical rather than circular, unlike the case of radiative alignment.

The aerodynamically aligned grains are expected to have their longest axes along the “streaming direction”, the direction of the relative movement between the gas and dust, which is in the azimuthal direction in the disk plane. If the grains precess rapidly around the streaming direction, they would have an “effective” prolate shape. Even in the absence of any precession, ensemble-averaging of a large number of grains

¹It is also possible for the gas pressure to decrease radially inward, such as near the inner edge of a dense ring. In this case, the gas would rotate faster than the dust, again creating a relative motion between the two that is conducive to aerodynamic grain alignment.

with their long axes preferentially aligned along the same (streaming) direction would also yield an “effective” prolate shape. As discussed earlier in § 5.2, prolate grains with their long axes aligned along the azimuthal direction in the disk plane produce an elliptical rather than circular polarization pattern in the sky plane.

5.3 Azimuthal variation of polarization degree

Besides the polarization orientation, the spatial variation of polarization fraction, especially in the azimuthal direction, is also an important discriminant of different polarization mechanisms. In this section, we will concentrate on the azimuthal variation of the polarization fraction expected from radiative alignment, and contrast it with those from other mechanisms, especially aerodynamic alignment.

5.3.1 Polarization dependence on the inclination of grain alignment axis to the line of sight

The polarization of the thermal emission from aligned non-spherical dust grains depends on the ellipticity of the grains as viewed by the observer in the sky plane. For grains that are effectively “oblate” (or “disk-” or “flake-like” in the extreme case), e.g., when the alignment axis is the shortest axis of the grain (as true for magnetic and radiative alignment), the polarization is maximized when the “disk” is viewed edge-on, with its shortest (alignment) axis in the sky plane. We will denote this maximum polarization fraction by p_0 , and refer to it as the “intrinsic polarization.” When the shortest (alignment, symmetry) axis of the effectively oblate grain is inclined by

an angle i_d to the line of sight, the polarization fraction becomes

$$p(i_d) = \frac{p_0 \sin^2(i_d)}{1 + p_0 \cos^2(i_d)} \quad (5.5)$$

in the dipole regime appropriate for small grains (Lee & Draine 1985b; Yang et al. 2016b). Note that $p(i_d = \pi/2) = p_0$, which recovers the intrinsic polarization fraction for grains viewed edge-on. Since the maximum polarization is observed to be of order 1 – 10% on the disk scale, we have, to a good approximation, $p(i_d) \approx p_0 \sin^2(i_d)$.

For grains that are effectively “prolate” (or “needle-like” in the extreme case), e.g., when the alignment axis is the longest axis, as true for aerodynamic alignment, the polarization is maximized when the longest (alignment) axis of the “needle” is in the sky plane. We again denote this maximum or intrinsic polarization fraction by p_0 . In the more general case, we have

$$p(i_d) = \frac{p_0 \sin^2(i_d)}{1 - p_0 \cos^2(i_d)} \quad (5.6)$$

where i_d is the inclination angle of the longest (alignment, symmetry) axis of the grain to the line of sight. The equation is again derived under the dipole approximation (Lee & Draine 1985b).

5.3.2 Azimuthal variation of polarization degree in inclined disks

With the above background, we can now quantify the azimuthal variation of the polarization degree for aligned grains in inclined disks. We will consider different alignment mechanisms, including magnetic, radiative, and aerodynamic alignment. The results are shown in Fig. 5.6, which plots the polarization degree as a function

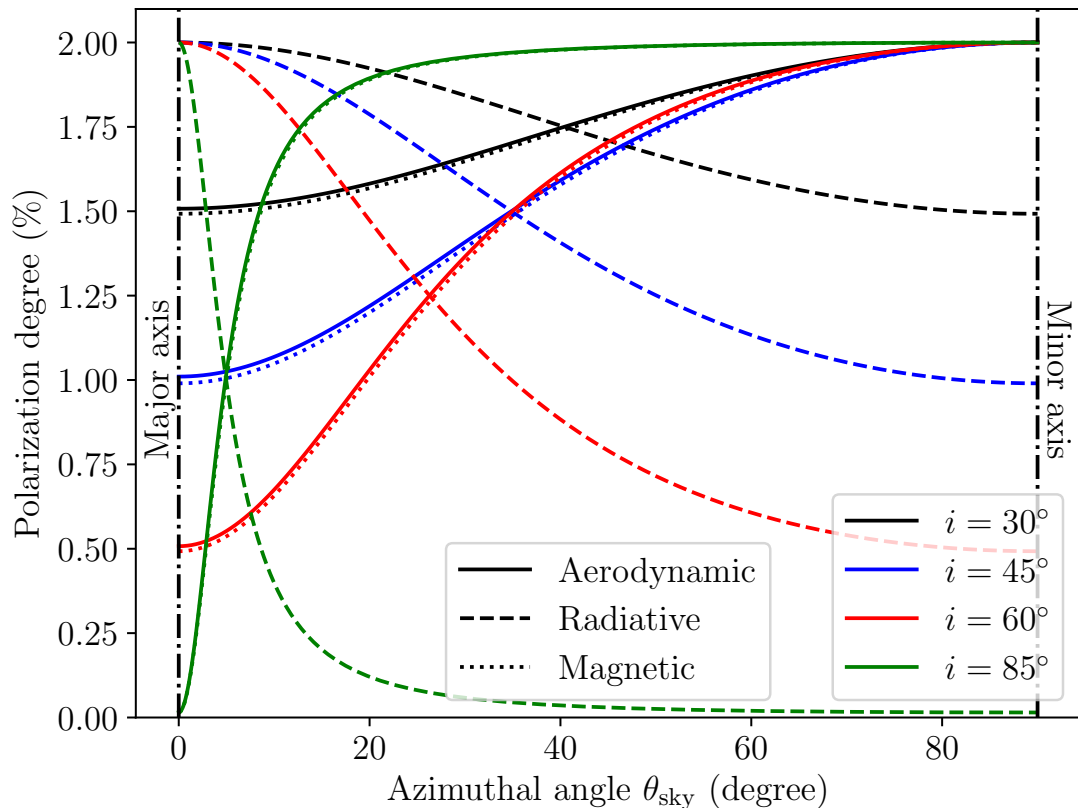


Fig. 5.6.— Polarization degree as a function of the azimuthal angle in the sky plane θ_{sky} for different alignment mechanisms and different inclination angles. The polarization degrees from the magnetic alignment (dotted line) and aerodynamic alignment (solid) have a similar angular dependence, both peaking on the minor axis ($\theta_{\text{sky}} = 90^\circ$). This is opposite to that of the radiative alignment (dashed), which peaks on the major axis ($\theta_{\text{sky}} = 0^\circ$) instead. Different inclination angles are represented by different colors. Note that the polarization degree on the minor axis decreases monotonically with increasing inclination angle for the case of radiative alignment (dashed lines), vanishing completely in the edge-on case with $i = 90^\circ$.

of the azimuthal angle in the sky plane measured from the major axis for each of the three cases, assuming a maximum or intrinsic polarization fraction of $p_0 = 2\%$ for illustration purposes.

For the magnetic alignment case shown in the figure (dotted line), we assume a pure toroidal magnetic field. As discussed earlier, grains with their shortest axes

aligned with the magnetic field are effectively oblate, or “disk-like.” In the simplest case of a “face-on” disk, the effectively oblate grains are viewed “edge-on” everywhere, with the grain alignment (symmetry) axis perpendicular to the line of sight, yielding the maximum polarization. In an inclined disk, the grains on the minor axis remain “edge-on” to the line of sight, but those on the major axis are viewed by the observer more “face-on” and thus rounder, yielding a lower polarization degree. Indeed, the polarization degree on the major axis is simply given by equation (5.5) with the angle i_d between the grain alignment axis and the line of sight given by $i_d = 90^\circ - i$, where i is the disk inclination angle. For the representative case of $i = 45^\circ$ shown in Fig. 5.6 (blue dotted curve), we have $p = 9.09 \times 10^{-2}$ (for the adopted $p_0 = 0.2$) on the major axis. The polarization degrees at intermediate angles between the minor and major axes can be computed using simple geometry (see also Cho & Lazarian 2007, Yang et al. 2016b, Bertrang & Wolf 2017).

For the radiative alignment case shown in the figure (dashed lines), we make the usual assumption that the radiation flux is in the radial direction. Using the same argument as above, it is easy to show that the effectively oblate grains on the major axis remain “edge-on” to the line of sight in an inclined disk (and thus emit maximally polarized light), while those on the minor axis are viewed more “face-on” and thus appear rounder to the observer, yielding a lower polarization degree, given by equation (5.6) with $i_d = 90^\circ - i$.

For the aerodynamic alignment case shown in the figure (solid lines), we assume that the grains have their longest axes aligned with the azimuthal direction in the disk plane. As discussed earlier, such grains are effectively prolate or “needle-like.” On the minor axis of an inclined disk, the aligned grains always have their longest (alignment, symmetry) axes in the sky plane, yielding maximum polarization. Those

on the major axis, on the other hand, have their longest (symmetry) axes inclined by an angle $i_d = 90^\circ - i$ (where i is the disk inclination angle) to the line of sight, and thus appear less elongated (i.e., rounder) to the observer, yielding a lower polarization, given by equation (5.6). For the representative case of $i = 45^\circ$ shown in Fig. 5.6 (blue solid line), the polarization degree on the major axis is $p = 0.11$ (for the adopted $p_0 = 0.2$), which is comparable to, but slightly larger than, that on the major axis for the magnetically aligned grains. Mathematically, the difference comes from the fact that the minus sign in the denominator of equation (5.6) is replaced by a plus sign in equation (5.5). Physically, it is due to the difference in the effective shape of the aligned grains (oblate for magnetic alignment vs prolate for aerodynamic alignment). Nevertheless, the azimuthal variations of the polarization degree for these two cases are very similar, both decreasing monotonically from the minor axis to the major axis. This trend is opposite to the case of radiative alignment, where the alignment axis is along the radial direction in the disk plane, rather than the azimuthal direction (as in the other two cases).

The difference in azimuthal variation of the polarization degree between the case of radiative alignment and those of magnetic and aerodynamic alignment increases with the inclination angle. To illustrate this difference more pictorially, we plot in Fig. 5.7 the polarization pattern in a nearly edge-on disk with $i = 85^\circ$, with the polarization degree proportional to the length of the line segments. This figure drives home the point that edge-on disks are ideal for distinguishing the different polarization mechanisms, from not only the polarization orientation (see also Fig. 5.5 above) but also the azimuthal variation in polarization degree.

Note, in particular, the low polarization fraction near the disk center for the radiative alignment case in the nearly edge-on disk. The physical reason for this

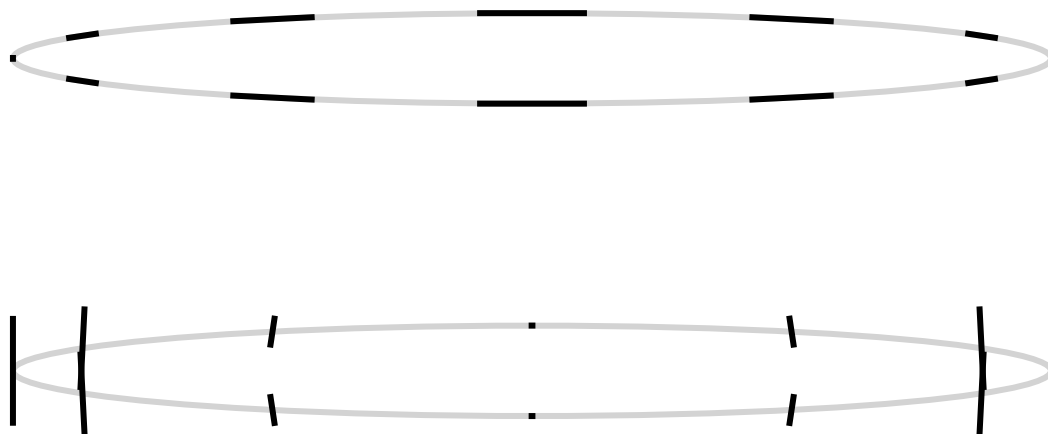


Fig. 5.7.— Large difference in not only polarization orientation but also azimuthal variation of polarization degree between the aerodynamic (upper panel) and radiative (lower) alignment for a nearly edge-on disk (with an inclination angle $i = 85^\circ$). Such disks are ideally suited for distinguishing the two alignment mechanisms.

interesting behavior is that the grains near the center are aligned with radiative flux that is close to the line of sight, which makes the effectively oblate grains appear almost circular in the sky plane, yielding little polarization. This robust feature is especially useful for distinguishing the radiative alignment from other mechanisms, as discussed in Lee et al. (2018) and Harris et al. (2018).

5.4 HL Tau Band 3 polarization: neither radiative nor aerodynamic alignment

Of the three grain alignment mechanisms discussed in the last section, magnetic alignment is the least likely possibility for producing the Band 3 polarization observed

in HL Tau disk (and shown in Fig. 5.1a), because it predicts a polarization orientation perpendicular, rather than parallel, to the elliptical contours of iso-intensity. For the radiative alignment, we have already pointed out one of its potential problems: it predicts a circular, rather than elliptical (Fig. 5.2), polarization pattern that appears different from the observed pattern. The aerodynamic alignment mechanism may do better at matching the observed polarization pattern, but it predicts an azimuthal variation of the polarization degree (see Fig. 5.6) that is not obvious in the data. The same problem is expected for the case of radiative alignment. In this section, we quantify the differences between the data and the model predictions based on the radiative and aerodynamic alignment, taking into account of the finite resolution of the ALMA observations, which is important for properly comparing the data and models because of beam smearing of both the polarization orientation and intensity distribution.

Before convolving with the telescope beam of $0''.445 \times 0''.294$, we adopt for the polarization orientation the circular pattern for the radiative alignment model and the elliptical pattern for the aerodynamic alignment model. For the radial variation of the polarized intensity, we use the much higher resolution ($0''.0853 \times 0''.0611$) ALMA Band 3 continuum data from ALMA Partnership et al. (2015) as the Stokes I model, and assume a maximum (or intrinsic) polarization degree of $p_0 = 2\%$, comparable to the maximum observed value. The azimuthal variation of the polarization degree is then computed based on equations (5.5) and (5.6) for a disk inclination angle of $i = 46.72^\circ$ (ALMA Partnership et al. 2015), as done in the last section. The resulting Stokes Q and U maps are convolved with the beam used for the Band 3 polarization observation. The results are shown in Figs. 5.8 and 5.9.

Fig. 5.8 shows the difference in polarization orientation between the Band 3 data

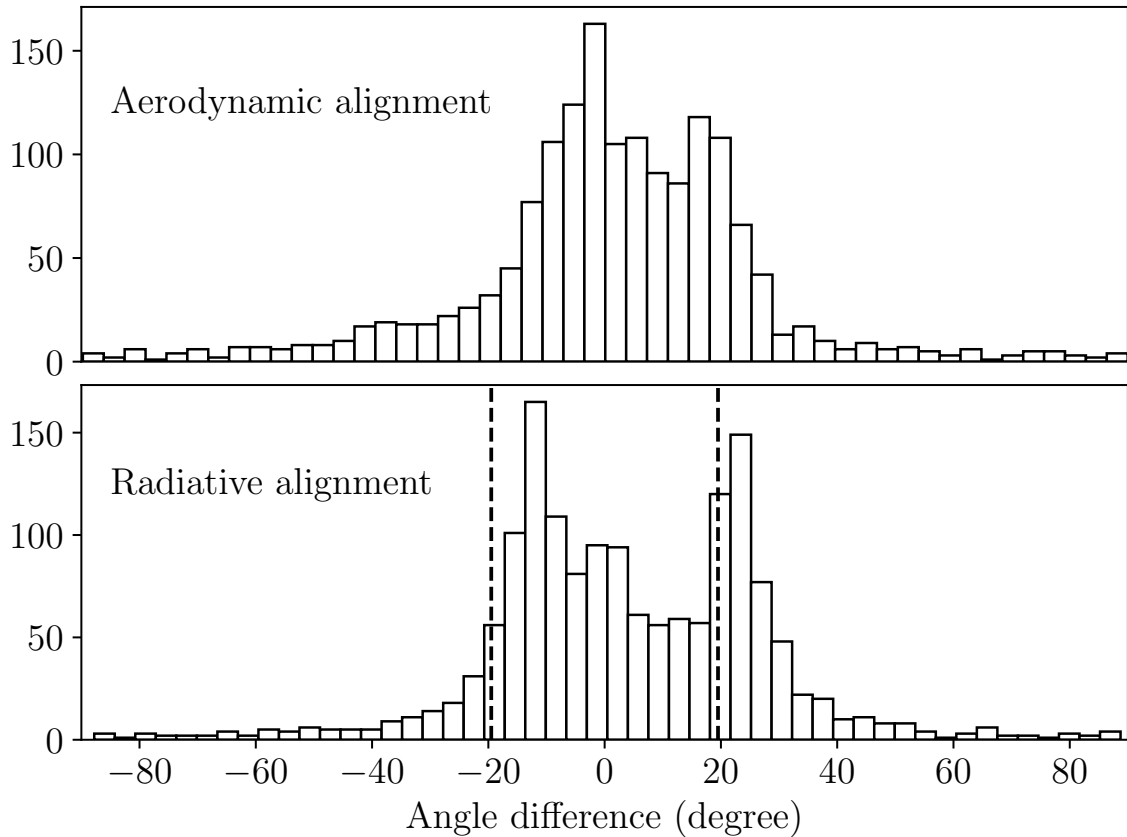


Fig. 5.8.— Histogram of the difference in polarization orientation between the ALMA Band 3 data and the models based on the aerodynamic (upper panel) and radiative (lower) alignment. The two dashed vertical lines are at $\pm 19.5^\circ$, the maximum difference expected between the circular and elliptical polarization pattern for an inclined disk of $i = 45^\circ$, as shown in Fig. 5.3.

and the model predictions at all locations on the disk where the polarization is detected at at least 5σ level. As expected, the aerodynamic alignment model reproduces the observed polarization orientations better, with the distribution of the angle difference centered around 0° . The relatively large dispersion around 0° comes from beam smearing coupled with significant azimuthal variation of the polarized intensity (see discussion in the last section and Fig. 5.9 below). In contrast, the angle difference between the data and the radiative alignment model has a bimodal distribution, peaking at two angles that are close to the maximum values ($\pm 19.5^\circ$) expected between

the elliptical and circular pattern for an inclination angle $i = 45^\circ$ (see Fig. 5.3, lower panel). This is additional evidence that the polarization pattern observed in ALMA Band 3 is closer to elliptical than circular and that the radiative alignment model is disfavored based on the polarization orientation.

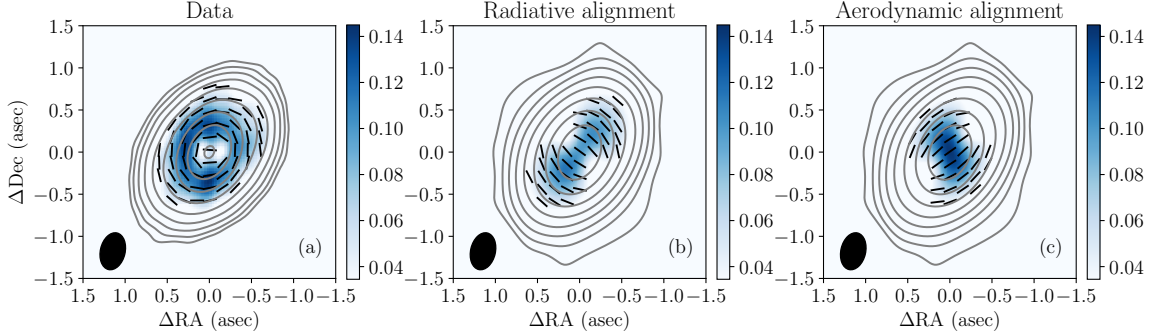


Fig. 5.9.— Comparison between the ALMA Band 3 data (left panel) and the models based on radiative (middle) and aerodynamic (right) alignment. The colormap shows the polarized flux, in mJy/beam, and the contours are for Stokes I, with a logarithmic scale. The line segments denote the polarization orientations. They are plotted only in regions with polarized intensity above $34.5 \mu\text{Jy}/\text{beam}$, which corresponds to 5σ noise level in Kataoka et al. (2017). The ellipse at the lower corner represents the interferometric beam.

Unfortunately, both the radiative and aerodynamic alignment models are disfavored based on the distribution of the polarized intensity, which is shown in Fig. 5.9. The radiative alignment model produces more polarization at locations along the major axis than along the minor axis, and the opposite is true for the aerodynamic alignment model. These patterns are in line with the expectations discussed in the last section based on the variation of the inclination of the grain alignment (symmetry) axis to the line of sight at different locations on the disk. Specifically, the higher polarization at locations along the major axis in the case of radiative alignment is because the effectively oblate grains there are viewed edge-on; those on the minor axis are viewed more face-on and thus appear rounder to the observer, yield-

ing a lower polarization. In contrast, the effectively prolate grains in the case of aerodynamic alignment are viewed edge-on at locations along the minor axis (yielding maximum polarization) and more pole-on (and thus appear rounder) at locations along the major axis (yielding a lower polarization). Beam averaging modifies the patterns somewhat, but not fundamentally. In particular, it does not average out the polarization near the center because the polarization degree varies substantially in the azimuthal direction in both models, which contradicts the observation that shows a low-polarization “hole” near the center (see Fig. 5.1a). The strong discrepancy between the data and the models suggests that, by itself, neither radiative nor aerodynamic alignment explains well the observed data. In the next section, we will speculate on whether more complex models can explain the data better.

5.5 Discussion

5.5.1 More complex models for HL Tau Band 3 polarization: scattering by aerodynamically aligned grains?

In the last section (§ 5.4), we have shown that the aerodynamic alignment model can explain the orientation of the polarization observed in HL Tau at Band 3 reasonably well (see Fig. 5.8, top panel). However, it predicts a strong polarization parallel to the major axis at the center despite beam smearing and a lack of polarization at locations along the major axis, neither of which is observed. These two problems have the same origin: the decrease of polarization degree going from the minor axis to the major axis (see Fig. 5.6). In order to make the model agree better with the data, one needs to find a way to increase the polarization degree for locations on the major axis relative to those on the minor axis without changing the polarization orientation. One natural

way to meet this requirement, at least qualitatively, is through scattering.

Previous studies have established that scattering in the Rayleigh limit produces a stronger polarization at locations on the major axis of an inclined disk than those on the minor axis (Yang et al. 2016a, see their Fig. 2; Kataoka et al. 2016a). Although the details of this azimuthal variation depend on the properties of the incident radiation, especially its anisotropy, it can be understood easily in the extreme case where most of the incident radiation is emitted by the brightest central region. In such a case, the incident radiation moving radially outward would be scattered by the grains located on the major axis by 90° into the line of sight and thus be maximally polarized, but by an angle $90^\circ \pm i$ (where i is the disk inclination angle) by the grains located on the minor axis in the disk plane, yielding a lower polarization. This tendency is broadly similar to that of the radiative alignment case, and the opposite of that of the aerodynamic alignment case. It is therefore reasonable to expect that when both direct emission and scattering by aerodynamically aligned grains are taken into account, the opposite tendencies for the polarization produced by direction emission and scattering should cancel each other at least to some extent, making the combined polarization less dependent on the azimuthal angle than that produced by direct emission alone.

Whether the expected reduction in the degree of azimuthal variation of the polarization intensity can reproduce the observed data quantitatively remains to be determined. A self-consistent computation of the polarization from both direct emission and scattering by aerodynamically aligned grains is beyond the scope of this work. As an illustration of the basic principles, we carry out two numerical experiments. First, we reconsider the aerodynamic alignment model discussed in the last section, but with the azimuthal variation of the polarized intensity removed. We also normal-

ize the polarization intensity so that the maximum value is close to the maximum observed value. The results are shown in Fig. 5.10a,c. Compared to the unmodified

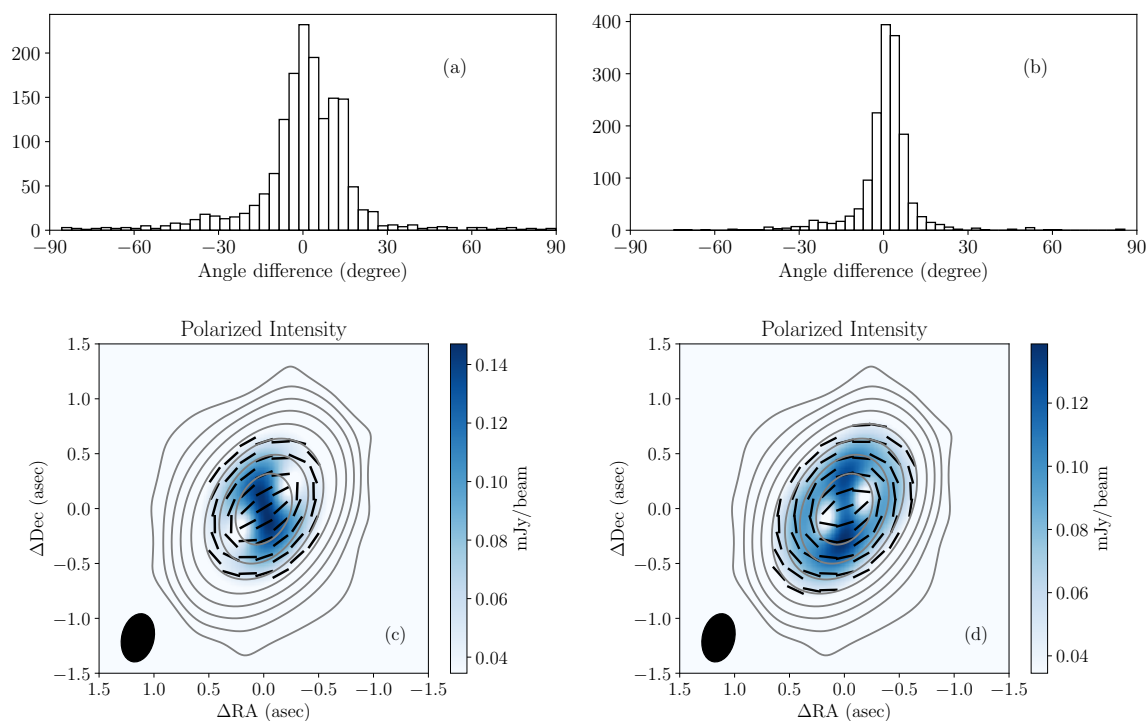


Fig. 5.10.— Two intrinsically elliptical polarization models with different azimuthal variations. The left column assumes uniform azimuthal polarization fraction, whereas the right column has polarization peaking at major axis, in the same way as the radiative alignment model. The upper panels show the histogram of the difference in polarization orientation with data for the two models, and the lower panel show the simulated polarization observation.

case, the beam-convolved polarization orientations agree with the observed values somewhat better (compare Fig.5.10c to Fig.5.9a), although there is still a substantial spread in their difference around 0° . Interestingly, even though the polarized intensity is set to be azimuthally uniform intrinsically, it has pronounced azimuthal variation after beam-convolution. Specifically, there are two low polarization “bays” located near the major axis (one on each side of the center). These are the regions where the polarization orientations in the intrinsically elliptical pattern change rapidly from one

location to another. As a result, their polarized intensity is lowered more by beam-averaging compared to, e.g., the regions near the minor axis where the polarization orientations are more spatially uniform. This example demonstrates clearly the strong interplay between the spatial distribution of polarized intensity and the spatial variation of polarization orientation in the presence of significant beam-averaging; the effects of beam-convolution need to be evaluated carefully when comparing models and observations.

In order to produce a more uniform azimuthal distribution after beam-averaging for an intrinsically elliptical polarization orientation, the polarized intensity needs to have an intrinsic azimuthal distribution that is higher along the major axis than along the minor axis. As an illustration, we adopt the azimuthal variation for the radiative alignment model for an inclination angle $i = 45^\circ$ (shown in Fig. 5.6 as blue dashed line), where the polarization degree is about a factor of 2 higher on the major axis than on the minor axis. The results are shown Fig. 5.10b,d. We have again normalized the maximum polarized intensity to the observed maximum value. Compared to the modified model with an intrinsically uniform azimuthal distribution of polarized intensity, there is a drastic improvement in the agreement between the modeled polarization orientations and the observed ones (compare Fig. 5.10b to Fig. 5.10a). The spatial distribution of polarized intensity also agrees better with observation, although a nearly vertical region of relatively high polarized intensity remains near the center, which is absent from the data; the polarization near the center could in principle be reduced by a higher optical depth there, although the optical depth effects remain to be quantified.

In any case, we have demonstrated that a combination of an intrinsic elliptical polarization pattern and an intrinsic azimuthal variation of polarization intensity that

favors the major axis over the minor axis improves the model fit to the observed data in ALMA Band 3. Whether this combination can be achieved by direct emission and scattering by aerodynamically aligned grains or some other physical mechanisms remains to be determined.

5.5.2 Polarization spectrum of HL Tau disk: a potential problem for aligned grains?

We have argued that it is difficult for the radiative alignment to explain the polarization observed in the HL Tau disk in ALMA Band 3, because it predicts a circular polarization pattern and substantial azimuthal variation of polarized intensity that are not observed. Potentially, there is one additional difficulty, namely, the radiatively aligned grains is expected to at least contribute to, if not dominate, the polarization in other ALMA bands, especially Band 7 (see Fig. 5.1b). In particular, under the oft-adopted dipole or electrostatic approximation (Bohren & Huffman 1983; Yang et al. 2016b), the polarization fraction changes little with wavelength, as long as the dielectric constants of the grains are well behaved, which is generally the case in the (sub)millimeter regime (Draine & Lee 1984; Kataoka et al. 2014). If this is true, it would contradict the ALMA Band 7 polarization data on the HL Tau disk: the $\sim 1.8\%$ polarization detected in Band 3 (Kataoka et al. 2017) is well above the $\sim 0.6\%$ polarization detected in Band 7 and has a completely different pattern (Stephens et al. 2017); the Band 7 polarization pattern is a textbook example of scattering-induced polarization in an inclined disk (Yang et al. 2016a; Kataoka et al. 2016a). The apparent lack of contamination from aligned grains in Band 7 posts a challenge to not only the radiative alignment mechanism but also aligned grain interpretation in general, including aerodynamically aligned grains. For aligned grain

models to be compatible with the existing multi-wavelength data in HL Tau, their polarization fraction has to drop by at least a factor of 3 going from ALMA Band 3 (~ 3 mm) to Band 7 (~ 0.87 mm). Whether such a large drop is physically feasible remains to be determined.

5.6 Summary and conclusions

In this chapter, we have discussed the polarization expected from different grain alignment mechanisms, especially the radiative and aerodynamic alignment and compared the model predictions with the HL Tau ALMA Band 3 data. The main results are:

1. Unlike generally assumed previously, the polarization pattern from radiative alignment is circular or concentric rather than elliptical for an axisymmetric disk. The circular polarization expected of radiative alignment is not consistent with the pattern observed in the HL Tau disk in ALMA Band 3, as shown in Fig. 5.8b.
2. An intrinsically elliptical pattern can be produced if the grains are aligned aerodynamically by the relative motions between the dust and gas in the azimuthal direction in the disk plane. The polarization orientations from the elliptical pattern are in better agreement with the Band 3 data, although a significant scatter remains because of beam-averaging in the simplest case where the polarization intensity does not have any intrinsic azimuthal variation (see Fig. 5.10a).
3. Strong intrinsic azimuthal variation is expected in an inclined disk for all grain alignment models, as shown in Fig. 5.6. In particular, the polarization is higher at locations on the minor axis for both the magnetic and aerodynamic alignment than those on the major axis, and the opposite is true for the radiative

alignment. The differences in both the polarization orientation and azimuthal variation of polarized intensity increase with the disk inclination angle to the line of sight, making edge-on disks ideally suited for distinguishing the different alignment mechanisms.

4. The strong azimuthal variation in polarized intensity expected in the radiative and aerodynamic alignment is not observed in the ALMA Band 3 polarization data of the HL Tau disk (see Fig. 5.9), which is evidence against interpreting the data using either of these two mechanisms alone.
5. We showed that beam-averaging introduces a strong interplay between the polarization orientation and azimuthal variation of the polarized intensity that needs to be accounted for when comparing models and data. In particular, a polarization pattern that is intrinsically elliptical without any intrinsic azimuthal variation in polarized intensity shows a pronounced azimuthal variation when beam-averaged (see Fig. 5.10c). To reduce the azimuthal variation after beam-averaging (for a better match to observation), an intrinsic azimuthal variation with higher polarization along the major axis than along the minor axis is needed (see Fig. 5.10b,d). Such an intrinsic variation is qualitatively expected of the polarization produced by dust scattering in an inclined disk. Whether a combination of both direct emission and scattering by aligned grains in general, and aerodynamically aligned grains in particular, can explain the ALMA Band 3 data remains to be determined.
6. We note that the polarization fraction detected in the HL Tau disk is three times higher in Band 3 than Band 7. Any grain alignment-based mechanism for explaining the Band 3 data will need to address the question of why the Band

7 data appears to be consistent with pure scattering, with little contamination from emission by aligned grains, which are expected to produce a polarization fraction that varies little with wavelength in the simplest dipole or electrostatic regime. More work is needed to resolve this potentially serious discrepancy.

We conclude that although the origin of the HL Tau disk polarization in ALMA Band 3 remains a mystery, the flood of ALMA data and relatively early stage of theoretical development should make the field of disk polarization an exciting area of research that is poised for rapid growth.

Chapter 6

Conclusions and outlook

In this thesis, we have studied the (sub)millimeter polarization of disks around young stellar objects, and made several contributions to this emerging field. Firstly, we helped establishing scattering as a potential alternative mechanism to the magnetic alignment as an origin of disk polarization at (sub)millimeter wavelengths, and showed that it can be a powerful tool to probe grain sizes in protoplanetary disks. Secondly, we calculated the scattering by aligned grains by adopting electrostatic approximation and studied the interplay between the polarization produced by the scattering and that by the magnetic alignment. Thirdly, we studied the behavior of scattering in the optically thick regime of an inclined disk, and discovered the near-far side asymmetry in the polarized intensity. The near-far side asymmetry requires the dust disk to be optically thick and, just as importantly, geometrically thick. As such, it has the potential to study the settling of large dust grains responsible for the scattering in protoplanetary disks, which is otherwise hard to accomplish. Last but not the least, we studied the potential mechanism behind the ALMA observed HL Tau Band 3 polarization. We pointed out that the radiative alignment is not a satisfactory explanation, and showed that yet another mechanism, aerodynamic alignment, may

be required to explain the data. The aerodynamic alignment has so-far been ignored in the disk polarization literature; it deserves more attention in the future. Our major achievements are summarized in Sec. 6.1. In Sec. 6.2, we discuss outstanding open questions and present an outlook of the field.

6.1 Major Achievements

In this subsection, we summarize the major achievements of this thesis, which are based on the summary sections of Chapters 2–5.

6.1.1 Scattering-induced polarization in inclined disks

Motivated by the first resolved (sub)millimeter disk polarization observation toward the classical T Tauri star system, HL Tau (Stephens et al. 2014), we developed a simple semi-analytic model for the dust scattering-induced polarization in the limit of optically and geometrically thin disc and Rayleigh scattering, with an emphasis on the effects of the disc inclination to the line of sight. The main results are summarized below.

1. We showed that scattered light illuminated by isotropic coplanar radiation will be polarized, when viewed from an inclined angle, and the polarization is perpendicular to both the normal axis of the plane (disk) and the line of sight. This is the *minor* axis of the disk in the sky plane. We found a simple analytical expression for the polarization degree (Eq. 2.18), which increases monotonically with increasing inclination angle and can be polarized up to $1/3$ in the extreme edge-on case.
2. We developed an efficient approximate model for computing disk polarization

from dust scattering by dividing the source region of the millimeter radiation to be scattered at a location inside the disk into two conceptually distinct parts: a near-field region centered on the location with a size comparable to the local dust scale height, and a far-field region outside. Radiation from the near-field region is more or less isotropic, and does not contribute significantly to the polarization of the scattered light, only to decrease the overall polarization fraction. Radiation from the far-field region is concentrated towards the disk plane. It is strongly polarized after scattering in an inclined disk.

3. We adopted a simple model for the HL Tau disk, based on the model fitted by Kwon et al. (2011). The case with a 45° inclination angle (see Fig. 2.5) naturally reproduces the two main features observed by CARMA in the HL Tau disk: (1) the region of high polarized intensity is elongated along the major axis, and (2) the polarization is uniformly orientated along the directions parallel to the minor axis of the disk. Both features come from simple geometric effects.
4. Through carefully investigation of the contribution from the local direct thermal emission, we identified the scattering optical depth as one of the key factors that control the degree of polarization. The scattering optical depth is determined, in part, by the scattering optical depth, which strongly depends on the sizes of the dust grains responsible for the scattering (see e.g. Fig. 3.7). In order to reproduce the 1 percent polarization observed by Stephens et al. (2014) at 1.3 mm, we inferred a maximum grain sizes to be about $70 \mu\text{m}$, which is consistent with Kataoka et al. (2016a)'s independent work based on Monte Carlo simulations. The polarization can thus become a powerful tool to probe grain sizes independent of other methods, such as the power-law index β for the dust grain absorption opacities.

5. We applied our theory to another system, the disk around Class II star, IM Lup. We adopted the fitted model by Cleeves et al. (2016) and carried out Monte Carlo radiative transfer simulations with varying grain sizes. Our results agree well with the data (see Fig. 2.8 and 2.9). We inferred the maximum grain sizes in this system to be about $60 \mu\text{m}$.

In summary, we led the effort in establishing scattering as a major mechanism in producing polarization at (sub)millimeter wavelengths in disks around young stellar objects. The scattering-induced polarization allows us to probe the grain growth in protoplanetary disks, which is a crucial first step towards the formation of planetesimals and ultimately planets.

6.1.2 Interplay between scattering and magnetic alignment

In order to understand the interplay between the two known mechanisms¹, we employed the electrostatic approximation to calculate the scattering off aligned small ellipsoids. Together with our thin-disk approximation developed in our previous work and the unpolarized incoming radiation assumption, we calculated the potential polarization with different disk inclinations, including both scattering and direct thermal emission from magnetically aligned grains. We found that the interplay between the two mechanisms strongly depends on the following factors:

1. Grain sizes. Since scattering is very sensitive to the grain sizes, scattering models favor grains with size parameter $2\pi a/\lambda$ on the order of unity. If the grains are too small, the polarization will easily be overwhelmed by direct thermal emission from magnetically aligned grains.

¹At the time of our paper Yang et al. (2016b).

2. Inclination. It is very hard for a face-on disk geometry to produce detectable polarization through scattering, even though we found some special scattering-induced polarization features that appear only for non-spherical grains (see Fig. 3.1). Moderately inclined disk systems, such as HL Tau (Stephens et al. 2017) and IM Lup (Hull et al. 2018), are better suited to study the polarization from scattering. At the same time, polarization from face-on disks, such as HD 142527 (Kataoka et al. 2016b) and TW Hya (A-rank Cycle 4 proposal led by T. Muto and C-rank Cycle 5 proposal led by H. Yang), if detected, is more likely due to some sort of alignment-based mechanisms.
3. Alignment efficiency and axis ratio of the aspherical dust grains. Polarization degree from magnetic aligned grains will be higher if grains are better aligned or are more nonspherical.
4. Local radiation field. The most important quantity for determining the relative importance of scattering and direct emission is the ratio between the local black body intensity, which determines the strength of the direct thermal emission, to the local mean intensity, which determines the strength of the scattered radiation. Near the center of the disk, the mean intensity is usually higher than the outer part of the disk. As a result, for certain cases, it is possible to have scattering being more important near the center of the disk, producing a roughly uniform polarization pattern. At the same time, the direct thermal emission is expected to dominate at the outer part of the disk, forming a fan-like radial polarization pattern. The transition between these two regimes produces a butterfly-shaped polarized intensity map and two “null” points (see middle right panel in Fig. 3.3).

Observationally, the two mechanisms, scattering and magnetic alignment, pro-

duce distinguishable polarization patterns. By comparing the models with the real observation, we can get some handles on the aforementioned factors.

With our illustrative models, we found suggestive evidence that the polarization pattern observed in NGC 1333 IRAS 4A1 at 8 mm is shaped by a combination of direct emission and scattering. The scattering and direct emission naturally account for, respectively, the relatively uniform polarization directions observed in the central region and the roughly radial pattern at larger distances (see Fig. 3.4). Most interestingly, there is clear evidence for at least one “null” point in the observed polarization map, which can naturally be interpreted as the location on the major axis of an inclined disc where the polarization from the scattering and direct emission cancel each other. The implied disk orientation matches that required for launching the observed molecular outflows.

If both direct emission and scattering from the same magnetically aligned grains indeed contribute significantly to the polarization observed in IRAS 4A1, it would imply not only that a magnetic field exists on the disk scale, but that it is strong enough to align large, possibly millimeter-sized, grains, at least in this source, with potentially far reaching consequences for the disk dynamics and evolution as well as grain alignment theory.

6.1.3 The near-far side asymmetry in optically thick disks

Our thin-disk approximation model relies on the disk being optically thin. In order to relax this constraint and quantify the effects of optical depth on the scattering-induced polarization in disks, we solved the radiation transfer problem using both the approach of formal solution under the single-scattering approximation and Monte Carlo simulations with the RADMC-3D code. The main results are summarized

below.

1. We developed an analytic 1D (plane-parallel) slab model with the single scattering approximation and demonstrated that scattering can produce a detectable level of polarization, even in the case with an infinite optical depth. The direction is perpendicular to both the normal direction of the local surface, and the line of sight. This direction coincides with the minor axis of a thin disk, so our theory is consistent with our previous results.
2. In a slab model, the polarization degree depends on both the optical depth and the inclination angle. The polarization degree increases with increasing optical depth until $\tau_{\max} \sim 1$, where τ_{\max} is the maximum optical depth of the slab (see Fig. 4.3). It then decreases and approaches asymptotically the infinitely thick result. The polarization degree also increases with increasing inclination angle (see Fig. 4.2), except for the extreme edge-on cases.
3. We also studied analytically the expected polarization from alignment-based mechanisms². With this, we pointed out that in the optically thick regime, polarization from aligned grains can be reversed if the temperature is increasing along line of sight away from us. The net polarization will be along the short axis of the dust grains, which coincides with the external alignment axis, such as the magnetic field. This direction is the opposite of the canonical direction and care must be exercised when interpreting polarization in optically thick systems.
4. We studied a disk model similar to the one used by Kwon et al. (2011), but in the optically thick regime. We found two outstanding features, namely the

²This analytic expression is not an original piece of work.

near-far side asymmetry and the bifurcation of polarization orientation. Both of them come from the fact that for an optically thick disk, the local surface is more important than the global disk. The difference in the inclination of the local surface between the near side and the far side causes the near-far side asymmetry (see the illustration in Fig. 4.6). The variation of the normal vector across the whole disk for a flared disk causes the bifurcation of polarization orientation.

Both of these features, namely the near-far side asymmetry and the bifurcation of polarization orientation, apply only to dust disks with a finite geometric thickness and disappear when dust grains are well settled. As such, they can potentially be used to study the settling of big dust grains responsible for scattering at (sub)millimeter wavelengths. We find suggestive evidence for such features in the disk around massive star forming region HH 80-81. Detailed comparison with the data by Girart et al. (2018) shows that our model can explain the polarization degree and orientation very well at the southwest part of the disk. See Sec. 6.2.2 in the outlook section for a more discussion on this.

6.1.4 The radiative alignment mechanism in HL Tau Band 3

We studied in detail the expected polarization from the radiative alignment mechanism, proposed by Tazaki et al. (2017). We simulated the polarimetric observations based on different alignment mechanisms and compared the model predictions with the HL Tau Band 3 data, which was originally attributed to radiative alignment (Kataoka et al. 2017). The main results are summarized below.

1. Unlike generally assumed previously, the polarization pattern from radiative alignment is circular or concentric rather than elliptical for an axisymmetric

disk. The circular polarization expected of radiative alignment is not consistent with the pattern observed in the HL Tau disk in ALMA Band 3, which is closer to an elliptical pattern. An intrinsically elliptical pattern can be produced if the grains are aligned aerodynamically by the relative motions between the dust and gas in the azimuthal direction in the disk plane.

2. We found a strong intrinsic azimuthal variation in polarization degree based on the radiative alignment mechanism. In particular, the polarization is higher at locations on the major axis. Azimuthal variation also exists for other alignment-based mechanisms, such as aerodynamic alignment and magnetic alignment. For the two later mechanisms, polarization is higher at locations on the minor axis, which is the opposite of that from radiative alignment. Such variation, however, is not seen in the HL Tau Band 3 polarimetric observation.
3. We simulated HL Tau Band 3 observation based on both radiative alignment and aerodynamic alignment. We generated theoretically expected Stokes I, Q, U maps in high resolution and convolved them with the actual beam used in Kataoka et al. (2017). We found that the aerodynamic alignment can fit the polarization orientation slightly better than the radiative alignment. That being said, both aerodynamic alignment and radiative alignment failed to reproduce the observed polarization. The difference between the model and the data likely comes from the fact that both models predict a strong azimuthal variation, which doesn't show up in the data.
4. We showed that models with an elliptical polarization pattern, with no azimuthal variation or stronger polarization at locations on the major axis, can reproduce the data better. These treatments, however, are not physically self-

consistent. We proposed that scattering off aerodynamically aligned grains can potentially be able to produce the observed polarization in HL Tau Band 3.

We also pointed out that edge-on disks are better suited for testing the radiative alignment. On the one hand, radiative alignment predicts polarization mostly perpendicular to the edge-on disk, which is perpendicular to the prediction by the aerodynamic alignment (which is an elliptical pattern). On the other hand, radiative alignment predicts strong polarization at locations on the major axis, and has little to no polarization near the center of the edge-on disk. This unique distribution can easily be distinguished from other mechanisms³.

We conclude that although the origin of the HL Tau disk polarization in ALMA Band 3 remains a mystery, the flood of ALMA data and relatively early stage of theoretical development should make the field of disk polarization an exciting area of research that is poised for rapid growth.

6.2 Discussions and outlook

Spatially resolved polarimetric observation at (sub)millimeter wavelengths is a brand new field of research being revolutionized by ALMA. Since the first resolved polarization observation toward the classical T Tauri system, HL Tau (Stephens et al. 2014), we have been deeply involved in the development of the theory on origins of such polarization. We help established the scattering as one of the most important mechanisms in producing (sub)millimeter polarization. We studied various aspects of scattering-induced polarization, such as its interplay with other mechanisms and its

³Some edge-on systems, such as L1527 (Harris et al. 2018) and HH212 (Lee et al. 2018), already have resolved polarization observations. The polarization distribution predicted by radiative alignment is not seen in these cases.

behaviour in the optically thick regime. Despite all these advances, many open questions remain. In this section, we will discuss some of the most important outstanding questions and give an outlook of the field.

6.2.1 Probing grain sizes and the tension with other methods

We have shown that the scattering-induced polarization can be a powerful tool to probe grain sizes in protoplanetary disks, thanks to the strong dependence of the scattering opacity of dust grains on their grain sizes. This is especially true for IM Lup, which has the best fitted scattering model to date (see Sec. 2.5). Our model reproduces well the observed polarized intensity, polarization degree, and the variations of polarization degree along both the major and minor axis (see Hull et al. 2018 for more detail). We found that an MRN-size distribution with a maximum grain size of $61 \mu\text{m}$ fits the data the best. At the same time, models with slightly smaller ($50 \mu\text{m}$) or slightly bigger ($70 \mu\text{m}$) maximum grain sizes will significantly under or over produce the polarization degree. This sensitivity comes from the strong dependency of the scattering opacity on the maximum grain size ($\kappa_{sca} \propto a^3$). This is a double-edged sword. On the one hand, we can provide a very precise constraint on the grain size. On the other hand, this leads to a severe fine-tuning problem since only grains with a narrow range of sizes can produce the observed polarization.

The grain sizes predicted from scattering models are all about $\sim 10\text{--}100 \mu\text{m}$ (Yang et al. 2016a; Kataoka et al. 2016a; Hull et al. 2018). These predictions are in strong tension with the grain sizes predicted independently based on the spectral index β of the dust absorption opacity $\kappa \propto \nu^\beta$, where ν is the frequency. Draine (2006) suggested that if the value of β is inferred to be less 1 at a certain wavelength λ , it would indicate that the dust grains responsible for the emission at this wavelength be at least 3λ in

size. In the HL Tau system, the derived β is between 0 and 1 for most part of the disk (ALMA Partnership et al. 2015). One thus concludes that the dust grains need to be at least about 4 mm. This is 1–2 orders of magnitude bigger than the value we inferred for the HL Tau disk based on the scattering-induced polarization. This tension need to be solved before one can fully trust the dust grain size estimates from either method.

There are some potential ways to resolve this tension. On the β -method side, one needs to be very careful. The direct observable is the spectral energy distribution, which is usually parametrize as $F_\nu \propto \nu^\alpha$, where α is the standard spectral index. The canonical relation $\beta = \alpha - 2$ used to derive the value for β requires the system to be optically thin. In the optically thick regime, this relation will naturally produce a small β (since the radiation field approaches the Planck function with an intensity $\propto \nu^2$ in the Rayleigh-Jeans limit), which would lead to a mistaken conclusion of big dust grains, even though big grains are not required.

On the scattering side, the biggest caveat is the use of the Mie theory for computing the dust optical properties. It assumes solid spherical dust grains, which may not be appropriate, especially for porous grains. There is some possibilities that large porous grains may behave in a way similar to small solid grains in the terms of scattering, while preserving their ability to produce a small β . Another drawback of the Mie theory is that it cannot treat irregular grains. We showed, in Fig. 2.7, that the scattering-induced polarization can be very complex for large spherical grains. It is caused by an ill-behaved polarization phase function for large spherical grains, shown as the red curve in Fig. 2.6. Fig. 6.1 shows the scattering optical properties of an ensemble of randomly-oriented large irregular grains (Shen et al. 2009). These grains are clusters of monomers created through a Monte Carlo method (Shen et al. 2008).

Comparing Fig. 6.1 with the red curve in Fig. 2.6, we can see that even though the polarization at 90° is only about 40% (as opposed to the 100% for the Rayleigh scattering), the overall polarization phase function is well-behaved and close to that of the Rayleigh scattering. It can thus potentially produce uniform polarization pattern, observed in HL Tau and IM Lup, as well as having a small β index. Even though Shen et al.'s method is not directly applicable to millimeter-sized grains (since it would take too long to assemble such large grains using the Monte Carlo method), their results indicate that randomly-oriented irregular grains can potentially resolve the tension between scattering and β -based method.

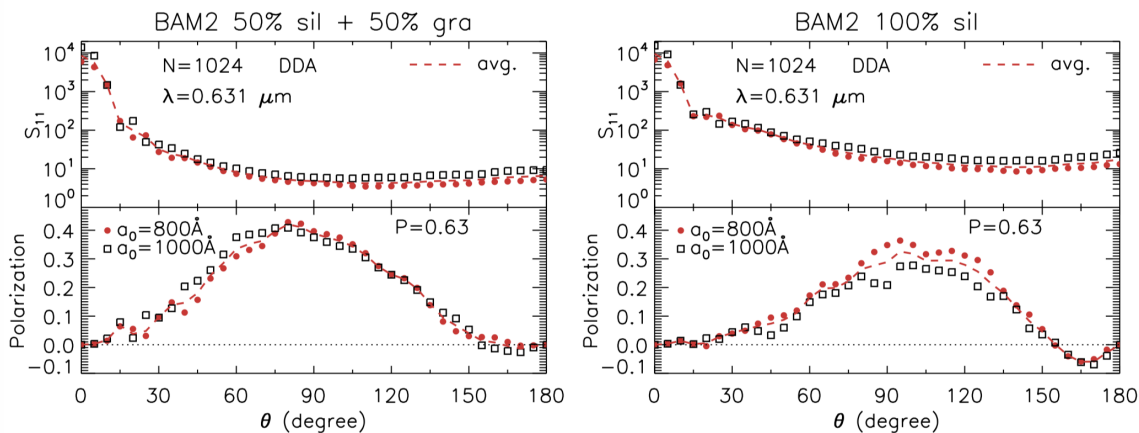


Fig. 6.1.— Scattering properties for aggregates resembling cometary dust, taken from Shen et al. (2009). The size parameters $2\pi a/\lambda$ is about $10 \sim 15$. The bottom panels are to be compared with Fig. 2.6. Unlike the scattering phase functions for large *spherical* grains calculated with Mie theory, represented with the red curve in Fig. 2.6, the large aggregates have a better behaved scattering phase function. See Shen et al. (2008) and Shen et al. (2009) for details.

6.2.2 The near-far side asymmetry and dust settling in protoplanetary disks

In Chap. 4, we showed that when a disk is both optically thick and has finite geometric thickness, the scattering-induced polarization from such a disk will have two distinct features, namely the near-far side asymmetry and the bifurcation of polarization orientations. These features can be potential powerful tools to probe the settling of large dust grains responsible for the scattering at (sub)millimeter wavelengths.

Girart et al. (2018) compared our model with the polarimetry observation towards the massive protostellar system HH 80-81. They found agreement in most part of the disk, except for the northeast part, where the polarization could be contaminated by the envelope, which could provide an extra, more or less uni-directional component. Based on our theory, we can infer that the massive disk around the massive HH 80-81 protostar has potentially unsettled large dust grains. The lower-mass HH 111 system, observed by Lee et al. (2018), shows a very similar polarization pattern. As a Class I source, HH 111 likely has unsettled dust grains as well. It is very interesting that large dust grains already exist in these sources in their early evolution stages.

On the other hand, the polarization in HL Tau Band 7 (Stephens et al. 2017), IM Lup (Hull et al. 2018), IRS 63 (Sadavoy et al. in prep), etc., doesn't have the near-far side asymmetry predicted for unsettled disks. Since HL Tau and IRS 63 are Class I/II systems and IM Lup is a Class II system, they are all thought to be older than HH 80-81 and HH 111. Based on our theory, this means that as protoplanetary disks evolve to later stages, the dust grains in disks are more and more settled. As a result, older disks will lose the near-far side asymmetry. This tentative trend is shown with a collection of observations in Fig. 6.2. My collaborator S. Sadavoy is proposing an ALMA polarization survey in the Ophiuchus and Perseus clouds in Cycle 6, with me

as a Co-I, to search for the near-far side asymmetry in more systems. If this trend is confirmed, we will be able to answer important questions such as how long it takes for dust grains to settle to the midplane. The settling is important for dust dynamics and evolution in the disk, and is difficult to probe observationally through other means.

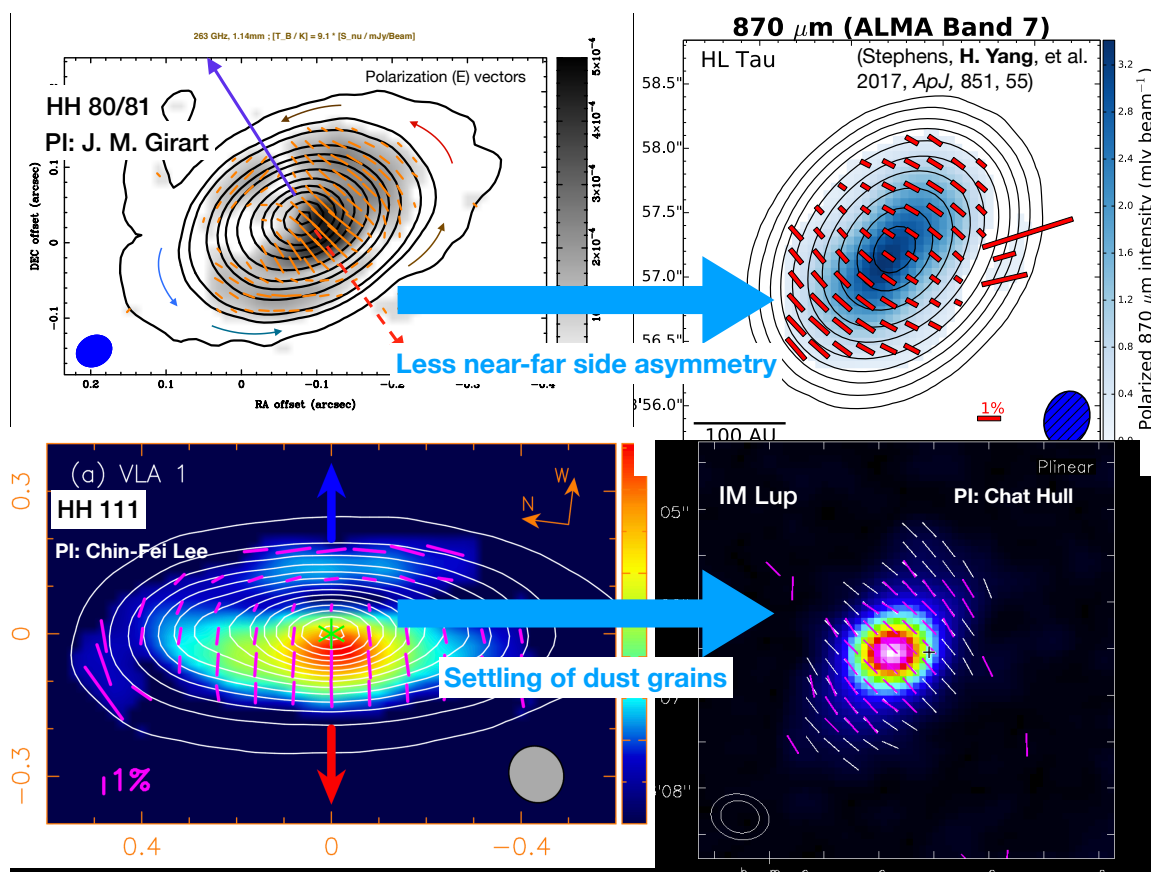


Fig. 6.2.— Dust evolution and near-far asymmetry. Upper left: HH 80-81 (Girart et al. 2018), a massive protostar. Lower left: HH 111 (Lee et al. 2018), a deeply embedded Class I source. Upper right: HL Tau (Stephens et al. 2017), Class I/II source. Lower right: IM Lup (Hull et al. 2018), a weak-line T Tauri star and Class II source. We see a tentative trend that younger systems to the left show a prominent near-far side asymmetry, which disappears in the older systems to the right. This is an indication of dust settling based on our theory of scattering-induced polarization.

6.2.3 Radiative alignment: open questions and observational test

Recently, Tazaki et al. (2017) proposed another mechanism that can potentially align dust grains in protoplanetary disks. Grains aligned this way will have their long axis perpendicular to the local radiation flux direction. Even though its initial idea was proposed a decade earlier by Lazarian & Hoang (2007), the observational support for this new mechanism, to the best of my knowledge, hasn't been found yet. Whether it works in the protoplanetary disk still remains an open question.

The best evidence for radiative alignment is the azimuthal polarization pattern observed in the HL Tau at Band 3 (Kataoka et al. 2017). However, as we have pointed out in Chap. 5, the radiative alignment explanation is not satisfactory. Aside from the two problems we stressed in Chap. 5, there is another problem with radiative alignment and alignment-based mechanisms in general. If the 1.8% polarization at Band 3 is due to alignment of dust grains, why such a high polarization doesn't exist at Band 7, where polarization is mostly uni-directional? The polarization at Band 7 is only $0.6 \sim 0.8\%$, which will easily be overwhelmed by the polarized thermal emission from aligned grains that are contributing the 1.8% polarization at Band 3. Does this mean that smaller grains that emit more strongly at the shorter (Band 7) wavelength are less aligned? A comprehensive model involving both the optical properties of dust grains and the alignment theory of dust grains is needed to understand the multi-wavelength behavior of the polarization in the HL Tau system.

We also need better observational test for the radiative alignment mechanism. As discussed in Chap. 5, we found that *edge-on systems* are better suited for this task. On the one hand, it can tell apart the radiative and aerodynamic alignment. In edge-on disks, these two mechanisms will produce perpendicular polarization. If

we see polarization perpendicular to an optically thin edge-on disk, that will rule out the aerodynamic alignment. Conversely, radiative alignment can be ruled out if the polarization is parallel to the optically thin edge-on disk. Note that one need to be careful about the optical depth. In the optical thick regime, the polarization reversal discussed in Chap. 4 may come in and complicate the interpretation. Furthermore, the radiative alignment has a very distinctive distribution of the polarized intensity along the edge-on disk. It has little to no polarization near the center of the disk, due to the coincidence of the line of sight and the radiation flux direction. This is the opposite of all other mechanisms, including aerodynamic alignment, magnetic alignment, and scattering. This unique feature can easily be tested in edge-on systems. In fact, the observation towards the L1527 system by Harris et al. (2018) already shows a stronger polarized intensity near the center of the disk. One case, however, is not enough to rule out the radiative alignment in general. More observations toward edge-on systems are needed to test this newly proposed mechanism more stringently.

A difficulty in distinguishing the polarization from the radiative alignment from that by scattering is the degeneracy between these two mechanisms. They both depend on the anisotropy of the radiation field. The scattered light will be polarized in the direction perpendicular to the anisotropy of radiation field. At the same time, radiatively aligned grains will have their long axis perpendicular to the anisotropy of the radiation field, producing polarization perpendicular to the anisotropy as well. We found that there is one key difference that can break the degeneracy, the wavelength of the photons involved. The scattering mechanism only cares about the radiation at the observing wavelength, e.g. (sub)millimeter wavelength. On the other hand, the radiative alignment cares about the radiation at the peak of the spectrum energy distribution, which is usually about $\sim 10\text{--}100\ \mu\text{m}$, since such photons contribute

most to the grain alignment. To take advantage of this difference, we proposed for ALMA polarization observation toward the ρ Oph IRS 48 system (PI: H. Yang; ALMA Cycle 5 B-ranked proposal). This system is known to have grains of different sizes concentrating in regions of different shapes and sizes. In particular, the smaller μm -sized grains are azimuthally uniformly distributed, whereas the bigger mm-sized grains have a lob-sided structure. If such a difference manifests itself in a difference in the anisotropy of the radiation field at different wavelengths, we would expect scattering and radiatively aligned grains to have different polarization features, even though both of them depend on the radiation anisotropy. The ρ Oph IRS 48 system (and other similar systems) thus serves as a good test for the radiative alignment mechanism.

Appendix A

Radiative transfer of polarized light

In this appendix, we will discuss the radiative transfer of polarized light. I will focus on the formal solution type method, which is used throughout this thesis. The formal solution calculates the radiation through a line integral. It is similar to the Ray tracing method, which is one major branch of the radiative transfer methods. The other branch, Monte Carlo methods, also uses the line integral to propagate photon packages between scattering events. The Monte Carlo code, RADMC-3D (Dullemond et al. 2012), is also used in the IM Lup modeling in Chap. 2 and in Chap. 4 for sanity check of our method. Readers are referred to Dullemond et al. (2012) and the excellent review by Whitney (2011) for detailed discussion of the Monte Carlo radiative transfer method, which will not be covered here.

A.1 Formulation of the vector radiative transfer problem

To describe a polarized light, one needs a full set of Stokes parameters, (I, Q, U, V) (see Eq. B.6 for one way to define Stokes parameters). The Stokes I describes the intensity of the light. The Stokes Q and U describe the linear polarization of the light. The circular polarization is quantified with the Stokes V . As a result, the radiative transfer of polarized light requires the propagation and transportation of the full set of Stokes parameters, or the Stokes vector $\mathbf{S} \equiv (I, Q, U, V)$.

The basic vector radiative transfer equation can be written as (see e.g. Tsang et al. 1985, Chap. 3):

$$\hat{\mathbf{n}} \cdot \nabla \mathbf{S}(\mathbf{r}, \hat{\mathbf{n}}) = -N \mathbf{C} \mathbf{S}(\mathbf{r}, \hat{\mathbf{n}}) + N \mathbf{C}_{\text{abs}} B_\nu(T(\mathbf{r})) + N \int d\Omega Z(\hat{\mathbf{n}}, \hat{\mathbf{n}}') \mathbf{S}(\mathbf{r}, \hat{\mathbf{n}}'). \quad (\text{A.1})$$

In the above equation, \mathbf{C} is the extinction matrix, and \mathbf{C}_{abs} is absorption cross section, which is written as a vector because the thermal emission from asymmetric dust grains can be polarized. $Z(\hat{\mathbf{n}}, \hat{\mathbf{n}}')$ is the phase matrix for scattering from direction $\hat{\mathbf{n}}'$ to $\hat{\mathbf{n}}$, and $\mathbf{S}(\mathbf{r}, \hat{\mathbf{n}}')$ is the Stokes parameters for the corresponding incoming radiation. The detailed calculation of the scattering phase matrix will be discussed in App. B.

The scattering part, i.e. the third term on the right hand side, makes this equation non-linear and very hard to solve in general. In this part of the appendix, we seek to find a simple formal solution by making the assumption that no radiation is added to the integration line through scattering, so we can drop this term for now; the treatment of this term will be discussed later. The transfer equation now reads:

$$\hat{\mathbf{n}} \cdot \nabla \mathbf{S}(\mathbf{r}, \hat{\mathbf{n}}) = -N \mathbf{C} \mathbf{S}(\mathbf{r}, \hat{\mathbf{n}}) + N \mathbf{C}_{\text{abs}} B_\nu(T(\mathbf{r})). \quad (\text{A.2})$$

One way to solve this equation numerically is to start from infinitely far away where there is no radiation at all, and then integrate along the light path until location \mathbf{r} . In practice, when solving for the Stokes vector $\mathbf{S}(\mathbf{r}, \hat{\mathbf{n}})$ at location \mathbf{r} along $\hat{\mathbf{n}}$ direction, one need to go backward along $-\hat{\mathbf{n}}$ direction until effectively infinity and integrate from there. This will be very inefficient if the medium is optically thick. In this appendix, we provide a formal solution to the problem, which allows the user to integrate from \mathbf{r} backward to infinity. The contribution along this line of integration is guaranteed to decrease as one moves farther away from the point of interest and one may truncate after some optical depth, say $\tau \sim 10$.

A.2 The formal solution to the problem

Along a given direction, the equation A.2 is of the following general type:

$$\frac{d\mathbf{A}(x)}{dx} = \mathbf{M}(x)\mathbf{A}(x) + \mathbf{u}(x), \quad (\text{A.3})$$

where x is the distance along the light path. To solve this equation formally, let us first solve the special problem with $\mathbf{u}(x) = 0$ and $\mathbf{M}(x) = \mathbf{M}$, a constant. The equation becomes:

$$\frac{d\mathbf{A}(x)}{dx} = \mathbf{M}\mathbf{A}(x) \quad (\text{A.4})$$

The solution to this equation is simply:

$$\mathbf{A}(x) = e^{\mathbf{M}x} \mathbf{A}_0 \quad (\text{A.5})$$

Now let's put back the $\mathbf{u}(x)$ term. We can solve this through variation of constants. Let $\mathbf{A}(x) = e^{\mathbf{M}x} \mathbf{B}(x)$, we have:

$$\begin{aligned}
e^{Mx} \frac{d\mathbf{B}}{dx} + \mathbf{M}e^{Mx} \mathbf{B} &= \mathbf{M}e^{Mx} \mathbf{B} + \mathbf{u}(x) \\
\frac{d\mathbf{B}}{dx} &= e^{-Mx} \mathbf{u}(x) \\
\mathbf{B}(x) &= \int e^{-Mx'} \mathbf{u}(x') dx' \tag{A.6}
\end{aligned}$$

This corresponds to:

$$\mathbf{A}(x) = \int e^{M(x-x')} \mathbf{u}(x') dx' \tag{A.7}$$

In radiative transfer, the integral goes from $-\infty$ to x and we have $\mathbf{A}(-\infty) = \mathbf{0}$. This sets the constant and we finally get:

$$\mathbf{A}(x) = \int_{-\infty}^x e^{M(x-x')} \mathbf{u}(x') dx' \tag{A.8}$$

This would be the final solution if the orientation of dust grains along $\hat{\mathbf{n}}'$ doesn't change and \mathbf{M} is a constant. However, that's usually not the case. The problem gets a lot harder when allowing \mathbf{M} to change. Without \mathbf{u} , the equation now reads:

$$\frac{d\mathbf{A}(x)}{dx} = \mathbf{M}(x)\mathbf{A}(x) \tag{A.9}$$

Naively, we might consider a solution of the following form:

$$\mathbf{A} = \exp\left(\int \mathbf{M}(x) dx\right) \mathbf{A}_0$$

However, this won't work. Here we introduce an exponential function that con-

serves the orders of matrix, denoted by $T[\exp(\dots)]$:

$$\mathbf{A} = T \left[\exp \left(\int_{x_0}^x \mathbf{M}(x') dx' \right) \right] \mathbf{A}_0 \quad (\text{A.10})$$

where the orders-conserved integral is defined as¹:

$$T \left[\exp \left(\int_{x_0}^x \mathbf{M}(x') dx' \right) \right] \equiv 1 + \int_{x_0}^x \mathbf{M}(x') dx' + \int_{x_0}^x dx_1 \int_{x_0}^{x_1} dx_2 \mathbf{M}(x_1) \mathbf{M}(x_2) + \dots \quad (\text{A.11})$$

It can be easily verified that under this definition, solution in Eq. (A.10) satisfies Eq. (A.9).

Now let's seek the solution to the full solution Eq. (A.3). The trial solution is

$$\mathbf{A}(x) = T \left[\exp \left(\int_{x_0}^x \mathbf{M}(x') dx' \right) \right] \mathbf{B}(x) \quad (\text{A.12})$$

Plugging this into Eq. (A.3), we get:

$$\mathbf{M}\mathbf{A}(x) + T \left[\exp \left(\int_{x_0}^x \mathbf{M}(x') dx' \right) \right] \frac{d\mathbf{B}(x)}{dx} = \mathbf{M}\mathbf{A}(x) + \mathbf{u}(x)$$

$$T \left[\exp \left(\int_{x_0}^x \mathbf{M}(x') dx' \right) \right] \frac{d\mathbf{B}(x)}{dx} = \mathbf{u}(x)$$

The formal solution to this is then:

$$\mathbf{B}(x) = \int T \left[\exp \left(\int_{x_0}^x \mathbf{M}(x') dx' \right) \right]^{-1} \mathbf{u}(x) dx \quad (\text{A.13})$$

¹This is very similar to the Tyson time-ordering operator in Quantum Mechanics. The two problems are also mathematically the same. We need Tyson time-ordering operator when solving systems with time-dependent Hamiltonian. Here we have the extinction matrix varying along the light path.

Note that unlike the previous case, we have:

$$\mathbf{T} \left[\exp \left(\int_{x_0}^x \mathbf{M}(x') dx' \right) \right]^{-1} \neq \mathbf{T} \left[\exp \left(\int_{x_0}^x -\mathbf{M}(x') dx' \right) \right] \quad (\text{A.14})$$

which makes this formal solution harder to apply directly.

Putting all these together, we get the formal solution to the full ODE as:

$$\mathbf{A}(x) = \mathbf{T} \left[\exp \left(\int_{-\infty}^x \mathbf{M}(x') dx' \right) \right] \int_{-\infty}^x \mathbf{T} \left[\exp \left(\int_{-\infty}^{x'} \mathbf{M}(x'') dx'' \right) \right]^{-1} \mathbf{u}(x') dx' \quad (\text{A.15})$$

We can check that the orders-conserved integral satisfies:

$$\mathbf{T} \left[\exp \left(\int_{x_1}^{x_2} \mathbf{M}(x') dx' \right) \right] = \mathbf{T} \left[\exp \left(\int_{x_0}^{x_2} \mathbf{M}(x') dx' \right) \right] \mathbf{T} \left[\exp \left(\int_{x_1}^{x_0} \mathbf{M}(x') dx' \right) \right] \quad (\text{A.16})$$

where $x_2 \leq x_0 \leq x_1$.

With this, we have

$$\mathbf{A}(x) = \int_{-\infty}^x \mathbf{T} \left[\exp \left(\int_{x'}^x \mathbf{M}(x'') dx'' \right) \right] \mathbf{T} \left[\exp \left(\int_{-\infty}^{x'} \mathbf{M}(x'') dx'' \right) \right] \mathbf{T} \left[\exp \left(\int_{-\infty}^{x'} \mathbf{M}(x'') dx'' \right) \right]^{-1} \mathbf{u}(x') dx' \quad (\text{A.17})$$

$$\mathbf{A}(x) = \int_{-\infty}^x \mathbf{T} \left[\exp \left(\int_{x'}^x \mathbf{M}(x'') dx'' \right) \right] \mathbf{u}(x') dx' \quad (\text{A.18})$$

Plugging in $\mathbf{M} = -N\mathbf{C}$, $\mathbf{u} = N\mathbf{C}_{\text{abs}}B_\nu(T(\mathbf{r}))$, and replace $\mathbf{A}(x)$ with $\mathbf{S}(\mathbf{r}, \hat{\mathbf{n}})$, we get the formal solution to the vector radiative transfer equation, Eq. A.2. Note that the integrand at location x' only depends on the source function at the current location $\mathbf{u}(x')$ and the propagator between x' and x , $\mathbf{T} \left[\exp \left(\int_{x'}^x \mathbf{M}(x'') dx'' \right) \right]$. One can easily integrate from x backward towards $-\infty$ and truncate at a suitable location in

between.

A.3 Non-grid based numerical calculation with single scattering approximation

Eq. A.18 would be an exact solution if we didn't have any radiation added to the light path through scattering. If we somehow know all the incoming radiation at locations along the light path, we will know how to evaluate the third term, the scattering term, in Eq. A.1. We can then replace $\mathbf{u}(x')$ with the following source term:

$$\mathcal{S}_{\text{full}} = N C_{\text{abs}} B_{\nu}(T(\mathbf{r})) + N \int d\Omega Z(\hat{\mathbf{n}}, \hat{\mathbf{n}}') \mathbf{S}(\mathbf{r}, \hat{\mathbf{n}}'), \quad (\text{A.19})$$

to get the end result.

One way to calculate the incoming radiation at locations along the light path is the single scattering approximation. In order to solve for $\mathbf{S}(\mathbf{r}_0, \hat{\mathbf{n}})$, we integrate from the location \mathbf{r}_0 going backward along direction $-\hat{\mathbf{n}}$. At any point \mathbf{r} , we use the full source term $\mathcal{S}_{\text{full}}$. In this source term, we encounter the Stokes parameters of incoming radiation at location \mathbf{r} , $\mathbf{S}(\mathbf{r}, \hat{\mathbf{n}}')$, which requires another integration of the formal solution. This time, when solving for $\mathbf{S}(\mathbf{r}, \hat{\mathbf{n}}')$, we will drop the scattering term in the full vector radiative transfer equation and take the following partial source term instead:

$$\mathcal{S}_{\text{part}} = N C_{\text{abs}} B_{\nu}(T(\mathbf{r})). \quad (\text{A.20})$$

This treatment is effectively assuming single scattering. This is because we allow scattering to add to our light path, but we don't allow any addition from scattering to our "secondary light path", the integration path to solve for $\mathbf{S}(\mathbf{r}, \hat{\mathbf{n}}')$. All photons

at the very end are scattered at most once during our full calculation.

This formal solution method also doesn't depend on grid structures. To evaluate the integral numerically, one needs to choose a step δr while integrating along any light path, and two steps in angles $(\delta\theta, \delta\phi)$ while integrating over the solid angles in the third term, the scattering term, of the full vector radiative transfer equation, Eq. A.1. One also needs an analytic form describing the extinction matrix $\mathbf{C}(\mathbf{r}, \hat{\mathbf{n}})$, the absorption cross section $\mathbf{C}_{\text{abs}}(\mathbf{r}, \hat{\mathbf{n}})$, the temperature distribution $T(\mathbf{r})$, the number density distribution $N(\mathbf{r})$, and the scattering phase matrix $\mathbf{Z}(\mathbf{r}; \hat{\mathbf{n}}, \hat{\mathbf{n}}')$. The last one is especially hard to calculate and very important. Its detailed calculation will be discussed in App. B.

In Chap. 4, we used this method to calculate the polarization from an optically thick disk. We also compared our result with the Monte Carlo code, RADMC-3D (see Fig. 4.9). We found that the results are qualitatively similar even in the extremely optically thick case, where multiple scattering must have occurred. Quantitatively, our flux is a factor of a few smaller than that from the Monte Carlo method in the extremely optically thick case, and agrees reasonably well in less optically thick cases.

Appendix B

Calculation of optical properties of dust grains

Throughout the thesis, the optical properties of dust grains are needed to carry out radiation transfer calculations. In this appendix, I will briefly introduce the three methods employed to calculate these properties.

Here we shall assume uniform dust grains with no structures. The material is uniform and isotropic¹. Let the dielectric constant² of the material in question be ϵ (this is the same as permittivity in Gaussian units). The dielectric constant, in general, is a complex number. It is related to the complex refraction index m as:

$$\epsilon = m^2 \tag{B.1}$$

For arbitrarily complicated dust grains, we cannot calculate the optical properties exactly. For different regimes, different approximations and methods apply. In this

¹This assumption works for silicate dust. For graphite dust, we need a matrix (or at least two complex scalars) to represent the dielectric constants.

²This is sometimes, or maybe better, referred to as *dielectric function*, due to the nature of its wavelength dependence.

thesis, we used three different methods: the electrostatic approximation, the Mie theory, and the Discrete Dipole Approximation.

B.1 Conventions and basic definitions

Before discussing the three methods in detail, let's introduce some terminology and two important quantities in the scattering problem: the amplitude scattering matrix and the scattering matrix. In what follows, I will follow mostly Bohren & Huffman (1983)'s convention. Readers are encouraged to refer to Chap. 3 in Bohren & Huffman (1983) to learn more about the basics of the absorption and scattering of light by small particles.

B.1.1 The amplitude scattering matrix

The most basic scattering problem is the scattering of an incoming plane wave. The incident electric field can be decomposed as:

$$\mathbf{E}_i = (E_{10}\hat{\mathbf{e}}_{1i} + E_{20}\hat{\mathbf{e}}_{2i})e^{i\mathbf{k}\cdot\mathbf{r}-i\omega t} = E_{1i}\hat{\mathbf{e}}_{1i} + E_{2i}\hat{\mathbf{e}}_{2i}, \quad (\text{B.2})$$

where $k = 2\pi/\lambda$ is the wave number. $\hat{\mathbf{e}}_{1i}$ and $\hat{\mathbf{e}}_{2i}$ are two unit vectors perpendicular to the propagation direction \mathbf{k}^3 . At a sufficiently large distance from the scattering particle (the far-field), the scattered electric field \mathbf{E}_s is a transverse and spherical wave, which follows the asymptotic form:

$$\mathbf{E}_s \sim \frac{e^{ikr}}{-ikr} \mathbf{A} \quad (\text{B.3})$$

³The convention I usually adopt in a spherical coordinates system is to let $\hat{\mathbf{e}}_1$ be $\hat{\mathbf{e}}_\theta$ and $\hat{\mathbf{e}}_2$ be $\hat{\mathbf{e}}_\phi$. This way the two unit vectors are determined solely by the light propagation direction $\hat{\mathbf{k}}$. The degenerate pole directions with $\theta = 0, \pi$ are assumed to have $\phi = 0$.

where \mathbf{A} is an arbitrary vector perpendicular to $\hat{\mathbf{e}}_r$. We can also decompose \mathbf{E}_s as:

$$\mathbf{E}_s = E_{1s}\hat{\mathbf{e}}_{1s} + E_{2s}\hat{\mathbf{e}}_{2s}. \quad (\text{B.4})$$

The relation between the incident and scattered electric field is then readily expressed in a matrix form:

$$\begin{pmatrix} E_{1s} \\ E_{2s} \end{pmatrix} = \frac{e^{ikr}}{-ikr} \begin{pmatrix} S_2 & S_3 \\ S_4 & S_1 \end{pmatrix} \begin{pmatrix} E_{1i} \\ E_{2i} \end{pmatrix}, \quad (\text{B.5})$$

This matrix is called the *amplitude scattering matrix*, which depends, in general, on both the scattering angle and the azimuthal angle.

B.1.2 The scattering matrix

Eq. B.5 describes the relation between the amplitudes of the incident and scattered electric fields, which are not directly observable. We need a relation between the Stokes parameters, the direct observable quantities, of the incident and scattered light. The Stokes parameters can be defined as:

$$\begin{aligned} I &= \langle E_1 E_1^* + E_2 E_2^* \rangle, \\ Q &= \langle E_1 E_1^* - E_2 E_2^* \rangle, \\ U &= \langle E_1 E_2^* + E_2 E_1^* \rangle, \\ V &= i \langle E_1 E_2^* - E_2 E_1^* \rangle, \end{aligned} \quad (\text{B.6})$$

where $\langle \dots \rangle$ denotes the time-averaged quantities. Following this definition, we find that the relation between incident and scattered Stokes parameters is the following:

$$\begin{pmatrix} I_s \\ Q_s \\ U_s \\ V_s \end{pmatrix} = \frac{1}{k^2 r^2} \begin{pmatrix} S_{11} & S_{12} & S_{13} & S_{14} \\ S_{21} & S_{22} & S_{23} & S_{24} \\ S_{31} & S_{32} & S_{33} & S_{34} \\ S_{41} & S_{42} & S_{43} & S_{44} \end{pmatrix}, \begin{pmatrix} I_i \\ Q_i \\ U_i \\ V_i \end{pmatrix} \quad (\text{B.7})$$

where the matrix elements can be calculated with the elements in the amplitude scattering matrix in the following way:

$$\begin{aligned} S_{11} &= \frac{1}{2}(|S_1|^2 + |S_2|^2 + |S_3|^2 + |S_4|^2) \\ S_{12} &= \frac{1}{2}(|S_2|^2 - |S_1|^2 + |S_4|^2 - |S_3|^2) \\ S_{13} &= \text{Re}\{S_2 S_3^* + S_1 S_4^*\} \\ S_{14} &= \text{Im}\{S_2 S_3^* - S_1 S_4^*\} \\ S_{21} &= \frac{1}{2}(|S_2|^2 - |S_1|^2 - |S_4|^2 + |S_3|^2) \\ S_{22} &= \frac{1}{2}(|S_2|^2 + |S_1|^2 - |S_4|^2 - |S_3|^2) \\ S_{23} &= \text{Re}\{S_2 S_3^* - S_1 S_4^*\} \\ S_{24} &= \text{Im}\{S_2 S_3^* + S_1 S_4^*\} \\ S_{31} &= \text{Re}\{S_2 S_4^* + S_1 S_3^*\} \\ S_{32} &= \text{Re}\{S_2 S_4^* - S_1 S_3^*\} \\ S_{33} &= \text{Re}\{S_1 S_2^* + S_3 S_4^*\} \\ S_{34} &= \text{Im}\{S_2 S_1^* + S_4 S_3^*\} \\ S_{41} &= \text{Im}\{S_2^* S_4 + S_3^* S_1\} \\ S_{42} &= \text{Im}\{S_2^* S_4 - S_3^* S_1\} \\ S_{43} &= \text{Im}\{S_1 S_2^* - S_3 S_4^*\} \\ S_{44} &= \text{Re}\{S_1 S_2^* - S_3 S_4^*\} \end{aligned} \quad (\text{B.8})$$

This 4×4 matrix is called the *scattering matrix*, and is arguably the most important quantity in any scattering theory.

B.2 The electrostatic approximation

The electrostatic approximation is also known as the dipole approximation. It applies to small dust grains in the Rayleigh limit. In general, when the dust grain experiences the incoming sinusoidal electromagnetic radiation, it will respond to it with some oscillating electromagnetic fields inside the dust grain. The typical length scale for this oscillation is the wavelength of the electromagnetic radiation λ . When the grain size a is much smaller than λ , the phase difference across the whole grain is negligible and the electrostatic approximation applies.

B.2.1 The spherical case

The simplest case is when the dust grain is spherical. For a sphere with dielectric constant ϵ and radius a , we can calculate the internal electric field when exposed to a uniform constant external electric field \mathbf{E}_0 . We find that the sphere will excite a dipole in response to this external field \mathbf{E}_0 , with a dipole moment:

$$\mathbf{p} = a^3 \frac{\epsilon - 1}{\epsilon + 2} \mathbf{E}_0 \equiv \alpha \mathbf{E}_0, \quad (\text{B.9})$$

where α is called the polarizability.

When the incident radiation is oscillating, we assume the particle will build up a dipole moment corresponding to the instantaneous electric field strength. This introduces an oscillating dipole, which will then radiate the following dipole radiation

(in the far field):

$$\mathbf{E}_s = \frac{k^2 e^{i(kr - \omega t)}}{r} (\hat{\mathbf{r}} \times \mathbf{p}) \times \hat{\mathbf{r}} \quad (\text{B.10})$$

which is essentially in the direction of \mathbf{p} projected to the plane defined with $\hat{\mathbf{r}}$, the propagation direction, as the normal direction (the transverse plane).

Let $\mathbf{E}_0 = E_0 \hat{\mathbf{e}}_0$, $\mathbf{E}_s = E_s \hat{\mathbf{e}}_s$, Eq. B.10 may be rewritten, after plugging in Eq. B.9, as:

$$E_s = \frac{k^2 e^{i(kr - \omega t)}}{r} E_0 [\alpha(\hat{\mathbf{e}}_0 \cdot \hat{\mathbf{e}}_s)] \quad (\text{B.11})$$

We can see that the angle dependence simply comes from the dot product between the unit vector in the incident electric field direction and the unit vector in the scattered electric field direction. Comparing this with the definition of the amplitude scattering matrix, we find that the elements are given by:

$$\begin{aligned} S_2 &= -ik^3 [\alpha(\hat{\mathbf{e}}_{1i} \cdot \hat{\mathbf{e}}_{1s})] & S_3 &= -ik^3 [\alpha(\hat{\mathbf{e}}_{2i} \cdot \hat{\mathbf{e}}_{1s})] \\ S_4 &= -ik^3 [\alpha(\hat{\mathbf{e}}_{1i} \cdot \hat{\mathbf{e}}_{2s})] & S_1 &= -ik^3 [\alpha(\hat{\mathbf{e}}_{2i} \cdot \hat{\mathbf{e}}_{2s})] \end{aligned} \quad (\text{B.12})$$

where $\hat{\mathbf{e}}_{1i}$, $\hat{\mathbf{e}}_{2i}$, $\hat{\mathbf{e}}_{1s}$, and $\hat{\mathbf{e}}_{2s}$ are the base unit vectors of the incident and scattered light of your choice.

The scattering cross section derived from the amplitude scattering matrix is then:

$$C_{\text{sca}} = \frac{8k^3}{3} |\alpha|^2 = \pi a^2 \frac{8}{3} x^4 \left| \frac{\epsilon - 1}{\epsilon + 2} \right|^2 \quad (\text{B.13})$$

where $x \equiv 2\pi a/\lambda$ is called “the size parameter.” We can see that the scattering cross section goes roughly as a^6/λ^4 .⁴ The strong size dependency is why we can use scattering-induced polarization to probe grain sizes.

⁴Note that this is not the exact wavelength dependence, since there is also a wavelength dependence in ϵ .

To compare with the scattering cross section, we can calculate the absorption cross section through optical theorem⁵:

$$C_{\text{abs}} = 4\pi k \text{Im}\{\alpha\} = \pi a^2 4x \text{Im}\left\{\frac{\epsilon - 1}{\epsilon + 2}\right\} \quad (\text{B.14})$$

In practice, we also need the scattering matrix, which can be calculated with Eq. B.8 and Eq. B.12.

B.2.2 The ellipsoid case

The above calculation is based on the exact solution of a small spherical particle under a uniform external electric field. It turns out that the problem with a spheroid can also be solved exactly with a formal integral solution. The full solution requires a coordinate transformation into the ellipsoidal coordinates and finding the eigenfunctions to the Laplace equations in the new coordinates, which will not be covered here. Readers are encouraged to refer to Sec. 5.3 in Bohren & Huffman (1983) for more details.

In the special case of ellipsoids (two of the three principle axes being equal), the formal integral yields some simpler analytic expressions. In this case, the polarizability is no longer a simple scalar, and we need a matrix to represent it:

$$\mathbf{p} = \bar{\alpha}\mathbf{E}. \quad (\text{B.15})$$

⁵Note that the optical theorem gives the extinction cross section rather than the absorption extinction. It gives the absorption cross section instead. This is because the amplitude scattering matrix is incorrect due to the ignorance of back reaction of the scattered field on the dipole. This back reaction will manifest itself, to the leading order, as a phase delay between the dipole and the incident radiation, which was ignored in the electrostatic approximation. It turns out that in this case, the optical theorem will give absorption cross section instead (van de Hulst 1957; Bohren & Huffman 1983).

In the principle coordinates of the ellipsoidal particle, the polarizability is a diagonal matrix $\bar{\alpha} = \text{diag}\{\alpha_1, \alpha_2, \alpha_3\}$. The eigen polarizabilities are:

$$\alpha_i = r_e^3 \frac{\epsilon - 1}{3 + 3L_i(\epsilon - 1)}, \quad (\text{B.16})$$

where r_e is the radius of the sphere with the same volume. The $L_i (i = 1, 2, 3)$ is a geometric parameter determined solely by the shape of the particle, subjected to the constraint $L_1 + L_2 + L_3 = 1$. We can see that in the spherical case with $L_1 = L_2 = L_3 = 1/3$, we recover the polarizability we obtained before.

Following the convention $L_1 \leq L_2 \leq L_3$ (which corresponds to $a_1 \geq a_2 \geq a_3$ and $|\alpha_1| \geq |\alpha_2| \geq |\alpha_3|$), we have for a prolate spheroid ($a_1 > a_2 = a_3$):

$$L_1 = \frac{1 - e^2}{e^2} \left(-1 + \frac{1}{2e} \ln \frac{1 + e}{1 - e} \right), \quad e^2 = 1 - s^2, \quad (\text{B.17})$$

where $s = a_2/a_1 < 1$ is the axis ratio. The other two geometric parameters are both equal to $(1 - L_1)/2$.

For an oblate spheroid ($a_1 = a_2 > a_3$), we have:

$$\begin{aligned} L_1 &= \frac{g(e)}{2e^2} \left[\frac{\pi}{2} - \tan^{-1} g(e) \right] - \frac{g^2(e)}{2}, \\ g(e) &= \left(\frac{1 - e^2}{e^2} \right)^{1/2}, \quad e^2 = 1 - \frac{1}{s^2}, \end{aligned} \quad (\text{B.18})$$

where the axis ratio is defined as $s = a_1/a_3 > 1$. The other two geometric parameters are given by $L_2 = L_1$ and $L_3 = 1 - 2L_1$.

Substituting in the new dipole moment in Eq. B.15, we get the elements of the

amplitude scattering matrix as given by:

$$\begin{aligned} S_2 &= -ik^3[\hat{\mathbf{e}}_{1i}^T \bar{\alpha} \hat{\mathbf{e}}_{1s}] & S_3 &= -ik^3[\hat{\mathbf{e}}_{2i}^T \bar{\alpha} \hat{\mathbf{e}}_{1s}] \\ S_4 &= -ik^3[\hat{\mathbf{e}}_{1i}^T \bar{\alpha} \hat{\mathbf{e}}_{2s}] & S_1 &= -ik^3[\hat{\mathbf{e}}_{2i}^T \bar{\alpha} \hat{\mathbf{e}}_{2s}] \end{aligned} \quad (\text{B.19})$$

where the superscript T denotes the transpose of the vector.

To sum up, the electrostatic approximation gives us a simple analytic form to calculate the amplitude scattering matrix given the E vectors of both incoming radiation and outgoing radiation. The whole process only requires some simple linear algebra.

B.3 The Mie theory

Although the electrostatic, or dipole, approximation, gives a very simple and fast way to calculate the scattering matrix, it only applies to small particles where the phase is roughly the same across the whole particle. It turns out that the absorption and scattering by a sphere of arbitrary radius with a uniform and arbitrary refractive index can be calculated exactly with a formal solution. This formal solution was originally discovered by Mie (1908). The calculation of absorption and scattering by spheres through this formal solution is commonly referred to as the Mie theory⁶.

The full derivation of the formal solution to this problem is too lengthy and not original work of my own. Readers are encouraged to refer to Chap. 4 in Bohren & Huffman (1983) for more details. Here I will outline some important steps.

For a system with spherical symmetry, it can be shown that the eigenfunctions to

⁶Note that Gustav Mie may not be the first to construct such a solution. Peter Debye and Ludvig Lorenz are both strong contenders for this honor (Bohren & Huffman 1983). We shall follow the common term and refer to this as the Mie theory.

the problem are:

$$\begin{aligned} \mathbf{M}_{\text{emn}} &= \frac{-m}{\sin\theta} \sin m\phi P_n^m(\cos\theta) z_n(\rho) \hat{\mathbf{e}}_\theta \\ &\quad - \cos m\phi \frac{dP_n^m(\cos\theta)}{d\theta} z_n(\rho) \hat{\mathbf{e}}_\phi, \end{aligned} \quad (\text{B.20})$$

$$\begin{aligned} \mathbf{M}_{\text{omn}} &= \frac{m}{\sin\theta} \cos m\phi P_n^m(\cos\theta) z_n(\rho) \hat{\mathbf{e}}_\theta \\ &\quad - \sin m\phi \frac{dP_n^m(\cos\theta)}{d\theta} z_n(\rho) \hat{\mathbf{e}}_\phi, \end{aligned} \quad (\text{B.21})$$

$$\begin{aligned} \mathbf{N}_{\text{emn}} &= \frac{z_n(\rho)}{\rho} \cos m\phi n(n+1) P_n^m(\cos\theta) \hat{\mathbf{e}}_r \\ &\quad + \cos m\phi \frac{dP_n^m(\cos\theta)}{d\theta} \frac{1}{\rho} \frac{d}{d\rho} [\rho z_n(\rho)] \hat{\mathbf{e}}_\theta \\ &\quad - m \sin m\phi \frac{P_n^m(\cos\theta)}{\sin\theta} \frac{1}{\rho} \frac{d}{d\rho} [\rho z_n(\rho)] \hat{\mathbf{e}}_\phi, \end{aligned} \quad (\text{B.22})$$

$$\begin{aligned} \mathbf{N}_{\text{omn}} &= \frac{z_n(\rho)}{\rho} \sin m\phi n(n+1) P_n^m(\cos\theta) \hat{\mathbf{e}}_r \\ &\quad + \sin m\phi \frac{dP_n^m(\cos\theta)}{d\theta} \frac{1}{\rho} \frac{d}{d\rho} [\rho z_n(\rho)] \hat{\mathbf{e}}_\theta \\ &\quad + m \cos m\phi \frac{P_n^m(\cos\theta)}{\sin\theta} \frac{1}{\rho} \frac{d}{d\rho} [\rho z_n(\rho)] \hat{\mathbf{e}}_\phi, \end{aligned} \quad (\text{B.23})$$

where z_n is any of the four spherical Bessel functions j_n , y_n , $h_n^{(1)}$, or $h_n^{(2)}$.

With quite some work, it can be shown that a plane wave propagating in x -direction, $\mathbf{E}_i = E_0 e^{ikr \cos\theta} \hat{\mathbf{e}}_x$ can be expanded in the above spherical harmonics as:

$$\mathbf{E}_i = E_0 \sum_{n=1}^{\infty} i^n \frac{2n+1}{n(n+1)} (\mathbf{M}_{o1n}^{(1)} - i\mathbf{N}_{e1n}^{(1)}), \quad (\text{B.24})$$

where the superscript (1) denotes spherical harmonics generated by the spherical Bessel functions of the first kind j_n (see Eq. B.20, B.21, B.22, B.23).

In the scattering problem, we care mostly about the scattered field, which can be expanded as:

$$\mathbf{E}_s = \sum_{n=1}^{\infty} E_n (ia_n \mathbf{N}_{e1n}^{(3)} - b_n \mathbf{M}_{o1n}^{(3)}), \quad (\text{B.25})$$

where the superscript (3) denotes spherical harmonics generated by $h_n^{(1)}$. Asymptotically, we have $h_n^{(1)}(kr) \sim (-1)^n e^{ikr}/(ikr)$, so the above expression can indeed represent an outgoing spherical scattered field.

The coefficients a_n 's and b_n 's can then be solved exactly. The full expressions are not included in this appendix. Readers are encouraged to refer to Eq. (4.53) in Bohren & Huffman (1983), Sec. 4.3, Page 100 for the full expressions.

With these, we can calculate the scattering cross section as:

$$C_{\text{sca}} = \frac{2\pi}{k^2} \sum_{n=1}^{\infty} (2n+1) (|a_n|^2 + |b_n|^2), \quad (\text{B.26})$$

and the extinction cross section as:

$$C_{\text{ext}} = \frac{2\pi}{k^2} \sum_{n=1}^{\infty} (2n+1) \text{Re}\{a_n + b_n\}. \quad (\text{B.27})$$

Another useful quantity is the scattering matrix. In the far field, the scattered radiation can be obtained by substituting the asymptotic expression for $h_n^{(1)}$. The resulting transverse components of the scattered electric field are:

$$E_{s\theta} \sim E_0 \frac{e^{ikr}}{-ikr} \cos \phi S_2(\cos \theta), \quad (\text{B.28})$$

$$E_{s\phi} \sim -E_0 \frac{e^{ikr}}{-ikr} \sin \phi S_1(\cos \theta), \quad (\text{B.29})$$

where

$$S_1 = \sum_{n=1}^{\infty} \frac{2n+1}{n(n+1)} (a_n \pi_n + b_n \tau_n), \quad (\text{B.30})$$

$$S_2 = \sum_{n=1}^{\infty} \frac{2n+1}{n(n+1)} (a_n \tau_n + b_n \pi_n), \quad (\text{B.31})$$

where $\pi_n \equiv P_n^1/(\sin \theta)$, $\tau_n \equiv dP_n^1/d\theta$, and P_n^m is the associated Legendre function.

The scattering amplitude matrix is then:

$$\begin{pmatrix} E_{\parallel s} \\ E_{\perp s} \end{pmatrix} = \frac{e^{ik(r-z)}}{-ikr} \begin{pmatrix} S_2 & 0 \\ 0 & S_1 \end{pmatrix} \begin{pmatrix} E_{\parallel i} \\ E_{\perp i} \end{pmatrix}. \quad (\text{B.32})$$

The derived scattering matrix, which relates the incident and scattered Stokes parameters follows from this is:

$$\begin{pmatrix} I_s \\ Q_s \\ U_s \\ V_s \end{pmatrix} = \frac{1}{k^2 r^2} \begin{pmatrix} S_{11} & S_{12} & 0 & 0 \\ S_{12} & S_{11} & 0 & 0 \\ 0 & 0 & S_{33} & S_{34} \\ 0 & 0 & -S_{34} & S_{33} \end{pmatrix} \begin{pmatrix} I_i \\ Q_i \\ U_i \\ V_i \end{pmatrix}, \quad (\text{B.33})$$

with:

$$S_{11} = \frac{1}{2} (|S_2|^2 + |S_1|^2), \quad (\text{B.34})$$

$$S_{12} = \frac{1}{2} (|S_2|^2 - |S_1|^2), \quad (\text{B.35})$$

$$S_{33} = \frac{1}{2} (S_2^* S_1 + S_2 S_1^*), \quad (\text{B.36})$$

$$S_{34} = \frac{i}{2} (S_1 S_2^* - S_2 S_1^*). \quad (\text{B.37})$$

This concludes the most important formulae in the Mie theory. Practically, the summation can be truncated at sufficiently large series number n to achieve arbitrarily

small error.

Even though the full formal solution was known in early 20th century, it wasn't until 1980s before the Mie theory was used practically when the computers were good enough to calculate the coefficients numerically. The most popular Mie theory code `bhmie` was developed by Bohren & Huffman (1983) and was attached as an appendix of the book. The most common version and the version I used is the one improved by Bruce T. Draine, together with some wrapper functions written by Thomas P. Robitaille⁷.

B.4 The Discrete Dipole Approximation

The discrete dipole approximation (DDA) is a powerful method to calculate the absorption and scattering by particles with arbitrary sizes⁸ and shapes. The DDA theory was initially proposed by Purcell & Pennypacker (1973). It was further developed by Draine (1988) and Draine & Goodman (1993). Draine & Flatau (1994) provides an excellent review on this topic and describes the implementation of the fortran DDA code, DDSCAT⁹. In this section, I will briefly introduce the idea behind DDA. Readers are encouraged to refer to Draine & Flatau (1994) to learn about the mathematical foundation and implementation details. Readers may refer to Draine & Flatau (2013) to learn about the applicability and usage of the DDSCAT code.

Given a target of arbitrary geometry, the phase may be varying substantially across the whole particle, so we cannot treat the whole particle as a dipole. At the same time, we don't have any symmetry to the problem. In this case, exact

⁷Available online at: <https://github.com/hyperion-rt/bhmie>

⁸Note that in reality, it may take very long for DDA to converge, so it's not quite for arbitrary sizes. Practically, when the size parameter $x = 2\pi a/\lambda$ is on the order of a few or smaller, the convergence is fast. For grains on order of $x \sim 10$ or bigger, it will take longer time to converge.

⁹Available online: <http://ddscat.wikidot.com/>

solution is not possible. DDA attacks this problem by replacing the whole particle as an array of point dipoles. The response of each dipole to the local radiation field is essentially the same as the one described in Sec. B.2, except for the modification on the polarizability of each dipole to include back reaction and thus to satisfy the optical theorem. The local electric field at each dipole consists of not only the incoming external electromagnetic radiation, but also the sum of the electric field contributions from all other dipoles in the particle, or the array. As a result, the calculation requires the inversion of an $N \times N$ matrix, where N is the number of point dipoles. The approximated problems with an array of point dipoles are thus solved, essentially exactly.

In order for the replacement to be valid, we need individual dipoles to be smaller than the wavelengths (inside the material). We then ask for the separation between dipoles d to satisfy:

$$|m|kd < 1, \tag{B.38}$$

where m is the complex refractive index, $k = 2\pi/\lambda$ is the wave number in vacuum. In practice, it is suggested to carry out multiple calculations with different number of dipoles N and extrapolate to $N \rightarrow \infty$ to get a much more reliable result.

References

- Alcala, J. M., Krautter, J., Schmitt, J. H. M. M., Covino, E., Wichmann, R., & Mundt, R. 1995, *A&AS*, 114, 109
- ALMA Partnership, Brogan, C. L., Pérez, L. M., Hunter, T. R., Dent, W. R. F., Hales, A. S., Hills, R. E., Corder, S., Fomalont, E. B., Vlahakis, C., Asaki, Y., Barkats, D., Hirota, A., Hodge, J. A., Impellizzeri, C. M. V., Kneissl, R., Liuzzo, E., Lucas, R., Marcelino, N., Matsushita, S., Nakanishi, K., Phillips, N., Richards, A. M. S., Toledo, I., Aladro, R., Brogiere, D., Cortes, J. R., Cortes, P. C., Espada, D., Galarza, F., Garcia-Appadoo, D., Guzman-Ramirez, L., Humphreys, E. M., Jung, T., Kamenno, S., Laing, R. A., Leon, S., Marconi, G., Mignano, A., Nikolic, B., Nyman, L.-A., Radiszcz, M., Remijan, A., Rodón, J. A., Sawada, T., Takahashi, S., Tilanus, R. P. J., Vila Vilaro, B., Watson, L. C., Wiklind, T., Akiyama, E., Chapillon, E., de Gregorio-Monsalvo, I., Di Francesco, J., Gueth, F., Kawamura, A., Lee, C.-F., Nguyen Luong, Q., Mangum, J., Pietu, V., Sanhueza, P., Saigo, K., Takakuwa, S., Ubach, C., van Kempen, T., Wootten, A., Castro-Carrizo, A., Francke, H., Gallardo, J., Garcia, J., Gonzalez, S., Hill, T., Kaminski, T., Kurono, Y., Liu, H.-Y., Lopez, C., Morales, F., Plarre, K., Schieven, G., Testi, L., Videla, L., Villard, E., Andreani, P., Hibbard, J. E., & Tatematsu, K. 2015, *ApJ*, 808, L3
- Alves, F. O., Girart, J. M., Padovani, M., Galli, D., Franco, G. A. P., Caselli, P.,

- Vlemmings, W. H. T., Zhang, Q., & Wiesemeyer, H. 2018, ArXiv e-prints
- Alves, J., Lombardi, M., & Lada, C. J. The Pipe Nebula: A Young Molecular Cloud Complex (The Southern Sky ASP Monograph Publications), 415
- Andersson, B.-G., Lazarian, A., & Vaillancourt, J. E. 2015, ARA&A, 53, 501
- André, P., Di Francesco, J., Ward-Thompson, D., Inutsuka, S.-I., Pudritz, R. E., & Pineda, J. E. 2014, Protostars and Planets VI, 27
- Andrews, S. M., Wilner, D. J., Hughes, A. M., Qi, C., & Dullemond, C. P. 2009, ApJ, 700, 1502
- Armitage, P. J. 2015, ArXiv e-prints:1509.06382
- Balbus, S. A. & Hawley, J. F. 1991, ApJ, 376, 214
- Balsara, D. S., Tilley, D. A., Rettig, T., & Brittain, S. D. 2009, MNRAS, 397, 24
- Bertrang, G. H.-M. & Wolf, S. 2017, MNRAS, 469, 2869
- Bickel, W. S., Davidson, J. F., Huffman, D. R., & Kilkson, R. 1976, Proc Natl Acad Sci U S A, 73, 486, 813228[pmid]
- Birnstiel, T., Klahr, H., & Ercolano, B. 2012, A&A, 539, A148
- Blandford, R. D. & Payne, D. G. 1982, MNRAS, 199, 883
- Blum, J. & Wurm, G. 2008, ARA&A, 46, 21
- Bohren, C. F. & Huffman, D. R. 1983, Absorption and scattering of light by small particles (New York: Wiley)
- Calvet, N. & Gullbring, E. 1998, ApJ, 509, 802

- Canovas, H., Ménard, F., Hales, A., Jordán, A., Schreiber, M. R., Casassus, S., Gledhill, T. M., & Pinte, C. 2013, *A&A*, 556, A123
- Carrasco-González, C., Henning, T., Chandler, C. J., Linz, H., Pérez, L., Rodríguez, L. F., Galván-Madrid, R., Anglada, G., Birnstiel, T., van Boekel, R., Flock, M., Klahr, H., Macias, E., Menten, K., Osorio, M., Testi, L., Torrelles, J. M., & Zhu, Z. 2016, *ApJ*, 821, L16
- Chandrasekhar, S. 1960, *Proceedings of the National Academy of Sciences*, 46, 253
- Chandrasekhar, S. 1987, *Ellipsoidal figures of equilibrium* (New York : Dover)
- Chandrasekhar, S. & Fermi, E. 1953, *ApJ*, 118, 113
- Chiang, E. & Youdin, A. N. 2010, *Annual Review of Earth and Planetary Sciences*, 38, 493
- Chiang, E. I. & Goldreich, P. 1997, *ApJ*, 490, 368
- Chiang, E. I., Joungh, M. K., Creech-Eakman, M. J., Qi, C., Kessler, J. E., Blake, G. A., & van Dishoeck, E. F. 2001, *ApJ*, 547, 1077
- Ching, T.-C., Lai, S.-P., Zhang, Q., Yang, L., Girart, J. M., & Rao, R. 2016, *ApJ*, 819, 159
- Cho, J. & Lazarian, A. 2007, *ApJ*, 669, 1085
- Chokshi, A., Tielens, A. G. G. M., & Hollenbach, D. 1993, *ApJ*, 407, 806
- Cleeves, L. I., Öberg, K. I., Wilner, D. J., Huang, J., Loomis, R. A., Andrews, S. M., & Czekala, I. 2016, *ApJ*, 832, 110

- Cox, E. G., Harris, R. J., Looney, L. W., Li, Z.-Y., Yang, H., Tobin, J. J., & Stephens, I. 2018, *ApJ*, 855, 92
- Cox, E. G., Harris, R. J., Looney, L. W., Segura-Cox, D. M., Tobin, J., Li, Z.-Y., Tychoniec, L., Chandler, C. J., Dunham, M. M., Kratter, K., Melis, C., Perez, L. M., & Sadavoy, S. I. 2015, *ApJ*, 814, L28
- Crutcher, R. M., Nutter, D. J., Ward-Thompson, D., & Kirk, J. M. 2004, *ApJ*, 600, 279
- Draine, B. T. 1988, *ApJ*, 333, 848
- . 2006, *ApJ*, 636, 1114
- Draine, B. T. & Flatau, P. J. 1994, *J. Opt. Soc. Am. A*, 11, 1491
- Draine, B. T. & Flatau, P. J. 2013, ArXiv e-prints
- Draine, B. T. & Goodman, J. 1993, *ApJ*, 405, 685
- Draine, B. T. & Lee, H. M. 1984, *ApJ*, 285, 89
- Dullemond, C. P. & Dominik, C. 2004, *A&A*, 421, 1075
- Dullemond, C. P., Juhasz, A., Pohl, A., Sereshti, F., Shetty, R., Peters, T., Commercon, B., & Flock, M. 2012, RADMC-3D: A multi-purpose radiative transfer tool, *Astrophysics Source Code Library*
- Fernández-López, M., Stephens, I. W., Girart, J. M., Looney, L., Curiel, S., Segura-Cox, D., Eswaraiah, C., & Lai, S.-P. 2016, *ApJ*, 832, 200
- Feynman, R. P. 1965, *Feynman lectures on physics. Volume 3: Quantum mechanics* (MA : Addison-Wesley)

- Finkenzeller, U. & Basri, G. 1987, *ApJ*, 318, 823
- Fissel, L. M., Ade, P. A. R., Angilè, F. E., Ashton, P., Benton, S. J., Devlin, M. J., Dober, B., Fukui, Y., Galitzki, N., Gandilo, N. N., Klein, J., Korotkov, A. L., Li, Z.-Y., Martin, P. G., Matthews, T. G., Moncelsi, L., Nakamura, F., Netterfield, C. B., Novak, G., Pascale, E., Poidevin, F., Santos, F. P., Savini, G., Scott, D., Shariff, J. A., Diego Soler, J., Thomas, N. E., Tucker, C. E., Tucker, G. S., & Ward-Thompson, D. 2016, *ApJ*, 824, 134
- Flock, M., Ruge, J. P., Dzyurkevich, N., Henning, T., Klahr, H., & Wolf, S. 2015, *A&A*, 574
- Fosalba, P., Lazarian, A., Prunet, S., & Tauber, J. A. 2002, in *American Institute of Physics Conference Series*, Vol. 609, *Astrophysical Polarized Backgrounds*, ed. S. Cecchini, S. Cortiglioni, R. Sault, & C. Sbarra, 44–50
- Fromang, S. 2013, *EAS Publications Series*, 62, 95
- Fromang, S. & Nelson, R. P. 2009, *A&A*, 496, 597
- Gaia Collaboration, Brown, A. G. A., Vallenari, A., Prusti, T., de Bruijne, J. H. J., Mignard, F., Drimmel, R., Babusiaux, C., Bailer-Jones, C. A. L., Bastian, U., & et al. 2016, *A&A*, 595, A2
- Girart, J. M., Fernández-López, M., Li, Z.-Y., Yang, H., Estalella, R., Anglada, G., Áñez-López, N., Busquet, G., Carrasco-González, C., Curiel, S., Galvan-Madrid, R., Gómez, J. F., de Gregorio-Monsalvo, I., Jiménez-Serra, I., Krasnopolsky, R., Martí, J., Osorio, M., Padovani, M., Rao, R., Rodríguez, L. F., & Torrelles, J. M. 2018, *ApJ*, 856, L27
- Girart, J. M., Rao, R., & Marrone, D. P. 2006, *Science*, 313, 812

- Gold, T. 1952, *MNRAS*, 112, 215
- Goldreich, P. & Kylafis, N. D. 1981, *ApJ*, 243, L75
- . 1982, *ApJ*, 253, 606
- Goldreich, P. & Ward, W. R. 1973, *ApJ*, 183, 1051
- Goodman, J. & Pindor, B. 2000, *Icarus*, 148, 537
- Greene, T. P., Wilking, B. A., Andre, P., Young, E. T., & Lada, C. J. 1994, *ApJ*, 434, 614
- Guidi, G., Tazzari, M., Testi, L., de Gregorio-Monsalvo, I., Chandler, C. J., Pérez, L., Isella, A., Natta, A., Ortolani, S., Henning, T., Corder, S., Linz, H., Andrews, S., Wilner, D., Ricci, L., Carpenter, J., Sargent, A., Mundy, L., Storm, S., Calvet, N., Dullemond, C., Greaves, J., Lazio, J., Deller, A., & Kwon, W. 2016, *A&A*, 588, A112
- Guilloteau, S., Piétu, V., Chapillon, E., Di Folco, E., Dutrey, A., Henning, T., Semenov, D., Birnstiel, T., & Grosso, N. 2016, *A&A*, 586, L1
- Gullbring, E., Calvet, N., Muzerolle, J., & Hartmann, L. 2000, *ApJ*, 544, 927
- Hall, J. S. 1949, *Science*, 109, 166
- Harris, R. J., Cox, E. G., Looney, L. W., Li, Z.-Y., Yang, H., Fernández-López, M., Kwon, W., Sadavoy, S., Segura-Cox, D., Stephens, I., & Tobin, J. 2018, *ArXiv e-prints*
- Hartmann, L., Calvet, N., Gullbring, E., & D'Alessio, P. 1998, *ApJ*, 495, 385

- Hildebrand, R., Davidson, J., Dotson, J., Dowell, C., Novak, G., & Vaillancourt, J. 2000, *PASP*, 112, 1215
- Hildebrand, R. H. & Dragovan, M. 1995, *ApJ*, 450, 663
- Hiltner, W. A. 1949a, *ApJ*, 109, 471
- . 1949b, *Nature*, 163, 283
- Hoang, T. 2017, *ArXiv e-prints*
- Hoang, T. & Lazarian, A. 2009, *ApJ*, 697, 1316
- . 2012, *Advances in Astronomy*, 2012, 208159
- Hughes, A. M., Hull, C. L. H., Wilner, D. J., & Plambeck, R. L. 2013, *AJ*, 145, 115
- Hughes, A. M., Wilner, D. J., Cho, J., Marrone, D. P., Lazarian, A., Andrews, S. M., & Rao, R. 2009, *ApJ*, 704, 1204
- Hull, C. L. H., Girart, J. M., Tychoniec, L., Rao, R., Cortés, P. C., Pokhrel, R., Zhang, Q., Houde, M., Dunham, M. M., Kristensen, L. E., Lai, S.-P., Li, Z.-Y., & Plambeck, R. L. 2017a, *ApJ*, 847, 92
- Hull, C. L. H., Mocz, P., Burkhart, B., Goodman, A. A., Girart, J. M., Cortés, P. C., Hernquist, L., Springel, V., Li, Z.-Y., & Lai, S.-P. 2017b, *ApJ*, 842, L9
- Hull, C. L. H., Plambeck, R. L., Bolatto, A. D., Bower, G. C., Carpenter, J. M., Crutcher, R. M., Fiege, J. D., Franzmann, E., Hakobian, N. S., Heiles, C., Houde, M., Hughes, A. M., Jameson, K., Kwon, W., Lamb, J. W., Looney, L. W., Matthews, B. C., Mundy, L., Pillai, T., Pound, M. W., Stephens, I. W., Tobin, J. J., Vaillancourt, J. E., Volgenau, N. H., & Wright, M. C. H. 2013, *ApJ*, 768, 159

- Hull, C. L. H., Plambeck, R. L., Kwon, W., Bower, G. C., Carpenter, J. M., Crutcher, R. M., Fiege, J. D., Franzmann, E., Hakobian, N. S., Heiles, C., Houde, M., Hughes, A. M., Lamb, J. W., Looney, L. W., Marrone, D. P., Matthews, B. C., Pillai, T., Pound, M. W., Rahman, N., Sandell, G., Stephens, I. W., Tobin, J. J., Vaillancourt, J. E., Volgenau, N. H., & Wright, M. C. H. 2014, *ApJS*, 213, 13
- Hull, C. L. H., Yang, H., Li, Z.-Y., Kataoka, A., Stephens, I. W., Andrews, S., Bai, X., Cleeves, L. I., Hughes, A. M., Looney, L., Pérez, L. M., & Wilner, D. 2018, ArXiv e-prints
- Jackson, J. D. 1999, *Classical electrodynamics*, 3rd edn. (New York, NY: Wiley)
- Kataoka, A., Muto, T., Momose, M., Tsukagoshi, T., & Dullemond, C. P. 2016a, *ApJ*, 820, 54
- Kataoka, A., Muto, T., Momose, M., Tsukagoshi, T., Fukagawa, M., Shibai, H., Hanawa, T., Murakawa, K., & Dullemond, C. P. 2015, *ApJ*, 809, 78
- Kataoka, A., Okuzumi, S., Tanaka, H., & Nomura, H. 2014, *A&A*, 568, A42
- Kataoka, A., Tsukagoshi, T., Momose, M., Nagai, H., Muto, T., Dullemond, C. P., Pohl, A., Fukagawa, M., Shibai, H., Hanawa, T., & Murakawa, K. 2016b, *ApJ*, 831, L12
- Kataoka, A., Tsukagoshi, T., Pohl, A., Muto, T., Nagai, H., Stephens, I. W., Tomisaka, K., & Momose, M. 2017, *ApJ*, 844, L5
- Kirchschlager, F. & Wolf, S. 2014, *A&A*, 568, A103
- Kwon, W., Looney, L. W., & Mundy, L. G. 2011, *ApJ*, 741, 3
- Kwon, W., Looney, L. W., Mundy, L. G., & Welch, W. J. 2015, *ApJ*, 808, 102

- Lada, C. J. 1987, in IAU Symposium, Vol. 115, Star Forming Regions, ed. M. Peimbert & J. Jugaku, 1–17
- Lazarian, A. 1995, ApJ, 451, 660
- Lazarian, A. 2007, Journal of Quantitative Spectroscopy and Radiative Transfer, 106, 225, {IX} Conference on Electromagnetic and Light Scattering by Non-Spherical Particles
- Lazarian, A. & Hoang, T. 2007, MNRAS, 378, 910
- Lazarian, A., Pogosyan, D., & Esquivel, A. 2002, in Astronomical Society of the Pacific Conference Series, Vol. 276, Seeing Through the Dust: The Detection of HI and the Exploration of the ISM in Galaxies, ed. A. R. Taylor, T. L. Landecker, & A. G. Willis, 182
- Lee, C.-F., Li, Z.-Y., Ching, T.-C., Lai, S.-P., & Yang, H. 2018, ApJ, 854, 56
- Lee, C.-F., Li, Z.-Y., Ho, P. T. P., Hirano, N., Zhang, Q., & Shang, H. 2017, Science Advances, 3
- Lee, H. M. & Draine, B. T. 1985a, ApJ, 290, 211
- . 1985b, ApJ, 290, 211
- Li, D., Pantin, E., Telesco, C. M., Zhang, H., Wright, C. M., Barnes, P. J., Packham, C., & Mariñas, N. 2016, ApJ, 832, 18
- Li, Z.-Y., Banerjee, R., Pudritz, R. E., Jørgensen, J. K., Shang, H., Krasnopolsky, R., & Maury, A. 2014, Protostars and Planets VI, 173
- Liu, H. B., Lai, S.-P., Hasegawa, Y., Hirano, N., Rao, R., Li, I.-H., Fukagawa, M., Girart, J. M., Carrasco-González, C., & Rodríguez, L. F. 2016, ApJ, 821, 41

- Lynden-Bell, D. & Pringle, J. E. 1974, MNRAS, 168, 603
- Martin, E. L., Rebolo, R., Magazzu, A., & Pavlenko, Y. V. 1994, A&A, 282, 503
- Mathis, J. S., Rumpl, W., & Nordsieck, K. H. 1977, ApJ, 217, 425
- Matsakos, T., Tzeferacos, P., & Königl, A. 2016, MNRAS, 463, 2716
- Mie, G. 1908, Ann. Phys, 25, 337
- Min, M., Hovenier, J. W., & de Koter, A. 2005, A&A, 432, 909
- Murakawa, K. 2010, A&A, 518, A63
- Murakawa, K., Preibisch, T., Kraus, S., Ageorges, N., Hofmann, K.-H., Ishii, M., Oya, S., Rosen, A., Schertl, D., & Weigelt, G. 2008, A&A, 488, L75
- Okuzumi, S., Tanaka, H., Kobayashi, H., & Wada, K. 2012, ApJ, 752, 106
- Pérez, L. M., Carpenter, J. M., Chandler, C. J., Isella, A., Andrews, S. M., Ricci, L., Calvet, N., Corder, S. A., Deller, A. T., Dullemond, C. P., Greaves, J. S., Harris, R. J., Henning, T., Kwon, W., Lazio, J., Linz, H., Mundy, L. G., Sargent, A. I., Storm, S., Testi, L., & Wilner, D. J. 2012, ApJ, 760, L17
- Pinte, C., Dent, W. R. F., Ménard, F., Hales, A., Hill, T., Cortes, P., & de Gregorio-Monsalvo, I. 2016, ApJ, 816, 25
- Pinte, C., Padgett, D. L., Ménard, F., Stapelfeldt, K. R., Schneider, G., Olofsson, J., Panić, O., Augereau, J. C., Duchêne, G., Krist, J., Pontoppidan, K., Perrin, M. D., Grady, C. A., Kessler-Silacci, J., van Dishoeck, E. F., Lommen, D., Silverstone, M., Hines, D. C., Wolf, S., Blake, G. A., Henning, T., & Stecklum, B. 2008, A&A, 489, 633

- Planck Collaboration, Ade, P. A. R., Aghanim, N., Alina, D., Alves, M. I. R., Armitage-Caplan, C., Arnaud, M., Arzoumanian, D., Ashdown, M., Atrio-Barandela, F., & et al. 2015, *A&A*, 576, A104
- Pohl, A., Kataoka, A., Pinilla, P., Dullemond, C. P., Henning, T., & Birnstiel, T. 2016, *A&A*, 593, A12
- Pollack, J. B., Hollenbach, D., Beckwith, S., Simonelli, D. P., Roush, T., & Fong, W. 1994, *ApJ*, 421, 615
- Pringle, J. E. 1981, *Annual Review of Astronomy and Astrophysics*, 19, 137
- Purcell, E. M. & Pennypacker, C. R. 1973, *The Astrophysical Journal*, 186, 705
- Rao, R., Girart, J. M., Lai, S.-P., & Marrone, D. P. 2014, *ApJ*, 780, L6
- Rao, R., Girart, J. M., Marrone, D. P., Lai, S.-P., & Schnee, S. 2009, *ApJ*, 707, 921
- Ricci, L., Trotta, F., Testi, L., Natta, A., Isella, A., & Wilner, D. J. 2012, *A&A*, 540, A6
- Rodriguez, L. F., Loinard, L., DAlessio, P., Wilner, D. J., & Ho, P. T. P. 2005, *The Astrophysical Journal Letters*, 621, L133
- Sadavoy, S. I., Myers, P. C., Stephens, I. W., Tobin, J., Commercon, B., Henning, T., Looney, L., Kwon, W., Segura-Cox, D., & Harris, R. 2018, *ArXiv e-prints*
- Sakai, N., Oya, Y., Higuchi, A. E., Aikawa, Y., Hanawa, T., Ceccarelli, C., Lefloch, B., López-Sepulcre, A., Watanabe, Y., Sakai, T., Hirota, T., Caux, E., Vastel, C., Kahane, C., & Yamamoto, S. 2017, *MNRAS*, 467, L76

- Santangelo, G., Codella, C., Cabrit, S., Maury, A. J., Gueth, F., Maret, S., Lefloch, B., Belloche, A., André, P., Hennebelle, P., Anderl, S., Podio, L., & Testi, L. 2015, *A&A*, 584, A126
- Schlichting, H. E., Fuentes, C. I., & Trilling, D. E. 2013, *AJ*, 146, 36
- Segura-Cox, D. M., Harris, R. J., Tobin, J. J., Looney, L. W., Li, Z.-Y., Chandler, C., Kratter, K., Dunham, M. M., Sadavoy, S., Perez, L., & Melis, C. 2016, *ApJ*, 817, L14
- Segura-Cox, D. M., Looney, L. W., Stephens, I. W., Fernández-López, M., Kwon, W., Tobin, J. J., Li, Z.-Y., & Crutcher, R. 2015, *ApJ*, 798, L2
- Shakura, N. I. & Sunyaev, R. A. 1973, *A&A*, 24, 337
- Shen, Y., Draine, B. T., & Johnson, E. T. 2008, *ApJ*, 689, 260
- . 2009, *ApJ*, 696, 2126
- Shu, F. H., Adams, F. C., & Lizano, S. 1987, *ARA&A*, 25, 23
- Slipher, V. M. 1912, *Lowell Observatory Bulletin*, 2, 26
- Stephens, I. W., Looney, L. W., Kwon, W., Fernández-López, M., Hughes, A. M., Mundy, L. G., Crutcher, R. M., Li, Z.-Y., & Rao, R. 2014, *Nature*, 514, 597
- Stephens, I. W., Looney, L. W., Kwon, W., Hull, C. L. H., Plambeck, R. L., Crutcher, R. M., Chapman, N., Novak, G., Davidson, J., Vaillancourt, J. E., Shinnaga, H., & Matthews, T. 2013, *ApJ*, 769, L15
- Stephens, I. W., Yang, H., Li, Z.-Y., Looney, L. W., Kataoka, A., Kwon, W., Fernández-López, M., Hull, C. L. H., Hughes, M., Segura-Cox, D., Mundy, L., Crutcher, R., & Rao, R. 2017, *ApJ*, 851, 55

- Tanaka, H., Himeno, Y., & Ida, S. 2005, *The Astrophysical Journal*, 625, 414
- Tazaki, R., Lazarian, A., & Nomura, H. 2017, *ApJ*, 839, 56
- Testi, L., Birnstiel, T., Ricci, L., Andrews, S., Blum, J., Carpenter, J., Dominik, C., Isella, A., Natta, A., Williams, J. P., & Wilner, D. J. 2014, *Protostars and Planets VI*, H. Beuther, R. S. Klessen, C. P. Dullemond, and T. Henning (eds.), University of Arizona Press, Tucson, 339
- Tobin, J. J., Dunham, M. M., Looney, L. W., Li, Z.-Y., Chandler, C. J., Segura-Cox, D., Sadavoy, S. I., Melis, C., Harris, R. J., Perez, L. M., Kratter, K., Jørgensen, J. K., Plunkett, A. L., & Hull, C. L. H. 2015, *ApJ*, 798, 61
- Tobin, J. J., Hartmann, L., Chiang, H.-F., Wilner, D. J., Looney, L. W., Loinard, L., Calvet, N., & D'Alessio, P. 2013, *ApJ*, 771, 48
- Tsang, L., Kong, Jin Au, ., & Shin, R. T. 1985, *Theory of microwave remote sensing* (New York : Wiley), "A Wiley-Interscience publication."
- Turner, N. J., Fromang, S., Gammie, C., Klahr, H., Lesur, G., Wardle, M., & Bai, X. N. 2014, *Protostars and Planets VI*, Henrik Beuther, Ralf S. Klessen, Cornelis P. Dullemond, and Thomas Henning (eds.), University of Arizona Press, Tucson, 411
- van de Hulst, H. C. 1957, *Light Scattering by Small Particles* (New York: John Wiley & Sons)
- van der Marel, N., van Dishoeck, E. F., Bruderer, S., Birnstiel, T., Pinilla, P., Dullemond, C. P., van Kempen, T. A., Schmalzl, M., Brown, J. M., Herczeg, G. J., Mathews, G. S., & Geers, V. 2013, *Science*, 340, 1199

- Velikhov, E. 1959, *J. Expt. Theor. Phys. (USSR)*, 36, 1398
- Verhoeff, A. P., Min, M., Pantin, E., Waters, L. B. F. M., Tielens, A. G. G. M., Honda, M., Fujiwara, H., Bouwman, J., van Boekel, R., Dougherty, S. M., de Koter, A., Dominik, C., & Mulders, G. D. 2011, *A&A*, 528, A91
- Whitney, B. A. 2011, *Bulletin of the Astronomical Society of India*, 39, 101
- Williams, J. P. & Cieza, L. A. 2011, *ARA&A*, 49, 67
- Yang, H., Li, Z.-Y., Looney, L., & Stephens, I. 2016a, *MNRAS*, 456, 2794
- Yang, H., Li, Z.-Y., Looney, L. W., Cox, E. G., Tobin, J., Stephens, I. W., Segura-Cox, D. M., & Harris, R. J. 2016b, *MNRAS*, 460, 4109
- Yang, H., Li, Z.-Y., Looney, L. W., Girart, J. M., & Stephens, I. W. 2017, *MNRAS*, 472, 373
- Yen, H.-W., Koch, P. M., Takakuwa, S., Krasnopolsky, R., Ohashi, N., & Aso, Y. 2017, *ApJ*, 834, 178
- Youdin, A. N. & Goodman, J. 2005, *ApJ*, 620, 459
- Zapata, L. A., Loinard, L., Rodriguez, L. F., Hernandez-Hernandez, V., Takahashi, S., Trejo, A., & Parise, B. 2013, *The Astrophysical Journal Letters*, 764, L14
- Zeeman, P. 1897, *ApJ*, 5, 332